PREPARATION AND CHARACTERIZATION OF NANOCRYSTALLINE METAL-OXIDE POWDERS

A thesis submitted

by

Bhagaban Kisan

to

Indian Institute of Technology Guwahati

in

Partial fulfillment of the requirement for the award of the degree of

Doctor of Philosophy in Physics

Department of Physics
Indian Institute of Technology Guwahati
Guwahati 781 039, Assam, India
September 2017

PREPARATION AND CHARACTERIZATION OF NANOCRYSTALLINE METAL-OXIDE POWDERS

A thesis submitted

by

Bhagaban Kisan

to

Indian Institute of Technology Guwahati

in

Partial fulfillment of the requirement for the award of the degree of
Doctor of Philosophy in Physics

Department of Physics
Indian Institute of Technology Guwahati
Guwahati 781 039, Assam, India
September 2017

Statement

The work contained in the thesis entitled “Preparation and characterization of nanocrystalline metal-oxide powders” has been carried out by me under the supervision of Prof. Perumal Alagarsamy at the Department of Physics, Indian Institute of Technology Guwahati. This work has not been submitted elsewhere for the award of any degree.

September 2017

(Bhagaban Kisan)
Roll No: 10612115
Department of Physics
Indian Institute of Technology Guwahati
Guwahati – 781039
India.

Certificate

It is certified that the work contained in the thesis entitled “Preparation and characterization of nanocrystalline metal-oxide powders” submitted by Bhagaban Kisan, a Ph.D. student of the Department of Physics, Indian Institute of Technology Guwahati for the award of degree of Doctor of Philosophy has been carried out under the supervision of Prof. Perumal Alagarsamy. This work has not been submitted elsewhere for the award of any degree.

September 2017

(Prof. Perumal Alagarsamy)
Professor
Department of Physics
Indian Institute of Technology Guwahati
Guwahati – 781039
India.

Dedicated to my

beloved brothers and parents

Acknowledgements

Pursuing a PhD is an enjoyable as well as a throbbing experience. I considered this process as climbing a big mountain, step by step, accompanied with hardships, bitterness, enthusiasm, trust, encouragement and support from many people. Hence, I would still like to give my heartfelt thanks to all the members who helped me.

First of all, I would like to express the deep sense of gratitude to my thesis supervisor Prof. Perumal Alagarsamy for his resourceful guidance, constructive criticisms and careful supervision throughout my research work. His continuous encouragements and intellectual discussions have been a driving force for me to excel in my work. I have learned a lot from him and his advice on research as well as on career has been priceless.

I am grateful to my doctoral committee members, Prof. S. B. Santra, Prof. S. Kanagaraj and Dr. D. Pamu for reviewing my research work regularly and providing valuable comments & suggestions for the improvement of my research work. I am thankful to current HOD, Department of Physics, Prof P. Poulose, and Prof. S. Basu, and Prof. S. Ravi, the former HODs, Department of Physics for their immense support. I extend my whole hearted thanks to all the faculty members of Physics department, who supported me in several ways during my research life in IIT Guwahati (IITG). I am thankful to IITG for providing me financial assistantship during the research period.

I express my sincere thanks to Dr. Sidananda Sarma, scientific officer in the department of physics, for guiding me to handle various high precision instruments in the department of physics. Also, I thank Mr. Chandan Borgohain, Dr. Kula Kamal Senapati, Mr. Madhurjya Borah and Mr. Kesho Singh, the scientific officers of CIF, who have patiently and enthusiastically extended their expertise in handling various instruments that I have used for my research work.

I am fortunate to have my seniors Dr. Akhilesh Kumar Singh, Dr. P.C. Shyni, Dr. Bharagab and Dr. Rahul Das, who helped me in various ways during my PhD period. Dr. Sunita Mohanty, Dr Tribedi Bora, Dr. Santhosh, Dr. Batakrushna, Dr. Bhargab, Anabil, Ravi Patta, Aneeta, Camelia, Gobinda, Arnab, Dr. Nisha, Rajkumar, Buddhadeb, Ranganadha, Bipul, Bibhuti, Ranjan, Junmoni, Dr. Mahesh, Ramesh, Biswajit, Obaidulla, and all other research scholars of physics department always be remembered for the wonderful time we have shared together. I thank my football team Ramesh, Biswajit, Arnab, Anabil for their company during the initial days of IITG which made me to feel comfortable here.

A special thanks to Dr. Akhilesh Kumar Singh, Dr. Shyni, Dr. Bhargab for playing the dual role of a senior and a good friend with memorable life in IITG campus. The hours long chit-chats we had sometimes 'under the sky' were a great relief from the busy schedule of PhD life for all of us and the funny moments we shared during those times will remain as unforgettable moments of my IITG life. The encouragement, advices, trust and care they extended, helped me a lot to cross all the hurdles and to emerge with enhanced courage and confidence. They made me to laugh even in the midst of thousands of problems. Big thanks to my ever best buddies for being the source of my positive energy and inspiration.

Words cannot express how grateful I am to my family for all the sacrifices they have made on my behalf. The prayers, support, love and care they have shed on me was what sustained me this far. I am so fortunate to have such great parents who had taught me the value of education and given me the freedom to continue my studies as long as I wished. Countless thanks to my elder brothers and sisters who took all the family responsibilities on their shoulder in my absence without any complaints. They always provided unconditional love, trust, support and encouragement which motivated me to work harder and do my best in my career. My family is the origin of my happiness and the backbone of my success.

I am thankful to all my school and college friends for their well wishes and to my teachers for their kind blessings which motivated me to complete this voyage. Also, my sincere thanks to all those, who have been helped me in whatever manner and bring me to this position, some of whom I may have inadvertently forgotten to mention in this acknowledgement. Finally and foremost I thank the almighty God for giving me the good times which I enjoyed a lot and the bad times from which I learned many lessons. I remain thankful to the God for the courage and ability given to face all the adverse situations to come out with flying colors.

Bhagaban Kisan

PREFACE

Spintronics (also termed as spin electronics) at the interface between the magnetism and electronics is a new field of research in multidisciplinary level and emerging out technology. This exploits both intrinsic spin of the electron and its associated magnetic moment in addition to its fundamental electronic charge. In particular, the spintronics based on diluted magnetic semiconductors (DMS) provides a new technology that transforms reading and writing information for many uses by spin rather than by typical electronic charge. Hence, DMS materials are considered as one of the new kind of materials for spintronic applications, especially those materials whose Curie temperature (T_C) is above room temperature. However, the practical applications of these materials are strongly challenged by its low reproducibility of room temperature ferromagnetism (FM) and controversial observations concerning over the origin of FM in DMS materials. Nevertheless, extensive studies on high T_C ferromagnetic DMS including NiO, ZnO, TiO_2, SnO_2, ZnTe, In_2O_3, Cu_2O, etc., have been reported after the discovery of the room temperature FM in Co doped TiO_2 thin films. In addition, the effect of doping using selective elements such as Mn, Co, Ni and V in metal-oxide has been studied to induce FM beyond room temperature. However, Sundaresan et al proposed that FM behavior in nanoparticles of non-magnetic oxides is a universal feature and FM was confined to the surface of the nanoparticles.

On the other hand, the study of fine nanocrystalline metal-oxide particles has become a subject of increasing interest and intense research in the myriad of different fields such as catalysis, magnetic resonance imaging contrast agents, targeted drug delivery, sensors, energy conversion, electrochromics, etc. These nanoparticles lie between clusters whose properties are strongly dependent on its size and submicron sized particles which have almost the properties same as bulk materials. In particular, the study of magnetism and magnetic interactions in various types of metal-oxide nanoparticles has generated much attention due to size and/or defect induced magnetic properties and their potential applications in biomedical, magnetoelectronic device, catalysis, spintronics, etc. There has been a profusion of recent work on the magnetic properties of nanosized antiferromagnetic (AFM) particles and most of the reports demonstrate the existence of FM moment on the nanoparticles. This was mainly instigated from Néel's suggestion that fine nanoparticles of AFM nature should exhibit either a weak FM or superparamagnetism. Richardson et al reported the first investigation on size dependent properties of NiO system. Subsequently, the effect of size dependent magnetic

properties and the competition between finite sizes versus surface effects on the room temperature magnetic crossover of NiO were reported. Out of these studies, a common theory put forward to discuss the unusual FM properties is a form of core-shell model, where the core spins are antiferromagnetically aligned and the shell spins give rise to FM moment. In addition, several other models such as two-sublattice model and multi-sublattice model were also proposed to account for the observation of large moment in NiO nanoparticles. Some theoretical calculation and experimental data have shown that NiO nanoparticles ranging from 1 to 50 nm can have both AFM and FM couplings. Furthermore, there exists controversial reports on the nature of the temperature dependent magnetic properties. For instance, Duan et al and Rinaldi-Montes et al reported the existence of two peaks in zero-field-cooled (ZFC) curves corresponding to two blocking processes, while Tiwari et al observed only the signature of spin glass freezing without any low temperature freezing or blocking.

Similarly, wide band gap DMS have gained enormous attention recently as a promising route to realize semiconductor based spintronics. Sharma et al reported the first experimental evidence of showing room temperature FM in Mn doped ZnO. The recent studies on ZnO system revealed realization of room temperature FM in either pure nanostructured ZnO without transition metal doping or ZnO doped with non-magnetic ions such as C and K. However, a careful analysis of the literature reveals contradictory results on the development of room temperature FM in pure ZnO system. Bartolomé et al showed that the preparation of ZnO based particles using ball milling technique resulted in a drastic reduction in the average size of the crystals without any induced FM. In addition, Sanyal et al reported that the ball mill processed ZnO did not show FM despite the creation of Zn vacancy during the ball milling process. On the other hand, Potzger et al reported an easy mechanical way to create FM defective ZnO and correlated to flake like structures in planar compressed pieces of the powder. Xing et al suggested that the oxygen vacancies induce characteristic photoluminescence and boost the room temperature FM in ZnO nanowires. Banerjee et al reported the enhancement of FM in pure ZnO powder upon thermal annealing due to the formation of oxygen vacancy clusters. Very recently, Phan et al and Ghose et al proposed that mechanical milling can be used to produce defect-related FM in ZnO nanoparticles. These studies revealed that the development of FM in un-doped ZnO was attributed to the defect density of either oxygen or Zn.

The other metal-oxide having many industrial uses as DMS, photocatalyst and strong stability in UV light is a Titanium dioxide (TiO_2), a non-toxic oxide semiconductor. TiO_2 has drawn wide attention over the years because of its interesting optical, photocatalytic, electronic and magnetic properties. The anatase phase has been used for photocatalyst of photo-

decomposition and solar energy conversion because of its high photoactivity. In addition, there are controversial results among different research groups in studying the magnetic properties of TiO_2 nanoparticles. Pandey et al argued that oxygen vacancies lead to electron doping in TiO_2 system, but does not induce appreciable FM using *ab-initio* electronic structure calculation. Hoa et al reported enhanced FM in un-doped TiO_2 nanowire as compared to Ni doped TiO_2 nanowire.

A careful literature noticeably reveals that the observed magnetic properties in DMS materials are critically dependent on fabrication methods, growth conditions, doping agents and the form of the materials. Several preparation methods such as chemical process, hydrothermal technique, sonochemical and microwave, vapor transport method, sputtering, pulsed laser deposition, etc., were used to prepare these metal-oxide materials. Most of the reported investigations are bottom to top approach on selected size of the particles, which reveal that the resulting magnetic properties in these oxide materials are complex due to the interplay between finite size, surface effects and interface effects, etc. On the other hand, the approach of top to bottom method for studying the magnetic properties of pure NiO, ZnO and TiO_2 powders without any impurity phases is still limited and/or missing. This motivated us to adopt an alternative and inexpensive technique called ball milling process using a high-energy planetary ball mill under dry milling conditions in an argon atmosphere to prepare nanoscale NiO, ZnO and TiO_2 powders. The ball milling process is a solid state method in which the materials undergo repeated cold welding and fracturing. This produces final materials in powder form with nanosized crystals, which can be tailored in various shapes and dimensions by compacting and giving proper heat treatment for availing commercially.

Therefore, this thesis work aims (i) to understand the evolution of crystal structure, nanocrystalline microstructure and resulting vibrational, electronic, magnetic, resonance properties and optical properties as a function of milling time in milled NiO, ZnO and TiO_2 powders prepared using a high-energy planetary ball mill under dry milling conditions in an argon atmosphere, (ii) to study the effect of annealing at different temperatures and to understand the origin of room temperature FM in these nanocrystalline powders and (iii) to investigate the correlation between structural and other resulting properties of these ball milled powders and to explore the possibility to enhance their magnetic properties. In addition, the physical properties of NiO nanoparticles prepared by sol-gel method with different molar concentrations and annealed at different annealing temperatures are reported for comparative study.

Chapter 1 presents a brief introduction to the content of the thesis along with a detailed review of the literature relevant to the present thesis work. The motivations and objectives of the thesis work are also explained in this chapter. In Chapter 2, the crystal structures, understanding of various types of defects, intrinsic and extrinsic origin of FM in NiO, ZnO and TiO_2 and optical properties are discussed. In addition, the fundamental aspects of magnetism and various theoretical methods employed in the analysis of the data of the presently investigated samples are summarized. Chapter 3 describes the experimental methods including the sample preparation methodologies used in the present study. The basic principle and theory behind the experiments, the experimental set up and measurement/methodology used for the determination of the physical properties are also briefly discussed here.

In Chapter 4, the effects of milling time period on the evolution of nanocrystalline microstructure and the resulting vibrational, electronic, magnetic, resonance and optical properties of NiO powders prepared by ball milling process are reported. Structural properties reveal the formation of single phase face centered cubic (*fcc*) nanosized NiO powders without any impurities within the detection limit of the techniques utilized. The average crystal size decreases and effective strain increases rapidly for the initial period of milling up to 10 hrs. NiO powders milled more than 10 hrs exhibit fine nanosized crystals with the size of around 11 nm. The strain decreases slightly for NiO powders milled above 20 hrs. Lattice volume decreases almost linearly with decreasing inverse of crystal size. Vibrational properties characterized by Raman study show the disappearance of two-magnon (2M) band immediately, broadening and enhancement of one-phonon (1P) longitudinal optical (LO) band and decrease of two-phonon (2P) LO and 2P TO vibration frequency with decreasing NiO crystal size. The color of the NiO powder changes from the pale green for pure NiO to dark green for milled NiO powders. This can be attributed to the existence of non-stoichiometry in the milled NiO powders, caused by the defects, size reduction, oxidization of Ni^{2+} to Ni^{3+} due to breaking of Ni^{2+}-O^{2-}-Ni^{2+} super-exchange interaction, as evidenced clearly from X-ray photoelectron spectroscopy (XPS) spectra. The pure NiO powder exhibits AFM nature, which transforms into FM gradually at room temperature. The magnitude of induced FM in milled NiO powders depends on the milling time period. A maximum magnetization of 1.08 emu/g at 12 kOe applied field and a coercivity of about 160 Oe are obtained at room temperature for 30 hrs milled NiO powder. The exchange bias decreases almost linearly with decreasing crystal size. Annealing of as-milled NiO powders (i) results in a large reduction in magnetization, but the rate of reduction strongly depends on the milling conditions and (ii) confirms the origin of FM as intrinsic one. Temperature dependent magnetization (*M-T*) measurements in the low

temperature range between 4 K and 300 K exhibit two peaks corresponding to freezing of surface spin and spin glass like phase. The presence of spin glass like phase verified through de Almedia-Thouless (AT) line plot provides additional anisotropy and enhances exchange bias under field-cooling condition. High temperature *M-T* measurements show the presence of mixed magnetic phases for the initial period of milling and on-set of FM behavior with a well-defined magnetic phase transition (T_C) at around 780 K. Electron paramagnetic resonance (EPR) study discloses a close correlation between the EPR results and magnetic properties. Photoluminescence (PL) study shows blue-shifting of band edge emission peak, which confirms the finite size effect in milled NiO powders. These nanoscale NiO powders with cubic structure, moderate magnetization at room temperature and high T_C would be useful for spintronic devices.

In Chapter 5, we report systematic investigations on the evolution of nanostructured ZnO, room temperature FM and temperature dependent magnetic properties, and tunable vibrational, electronic and optical properties of ZnO powders undergone size reduction by ball milling process. Structural studies reveal that both un-milled and as-milled ZnO powders exhibit single phase hexagonal wurtzite structure without any detectable impurities. The average crystallite size decreases and the effective strain increases for the initial periods of milling and then both saturate at higher milling periods. Vibrational properties show that bulk ZnO yields six Raman-active modes including two B_1 silent modes. Upon milling, the development of E_1(LO) vibration mode attributed to defects due to oxygen vacancies and/or Zn interstitials in ZnO powders has been observed. XPS spectra of bulk ZnO powder exhibit two strong peaks centered around 1022 and 1045 eV, which are in agreement with the binding energies of Zn $2p_{3/2}$ and Zn $2p_{1/2}$, respectively, with a spin-orbital-splitting of 23 eV. This confirms that Zn is present as Zn^{2+}. In addition, the O 1s spectrum exhibits a broad asymmetric feature indicating the presence of multi-component oxygen species: (i) low binding energy peak at 530.3 eV due to O^{2-} ions on the wurtzite structure of the hexagonal Zn^{2+} ion array, which are surrounded by zinc atoms with their full complement of nearest-neighbor O^{2-} ions, (ii) intermediate binding energy peak at 531.5 eV associated with O^{2-} ions that are in oxygen deficient regions within the matrix of ZnO and higher binding energy peak at 532.7 eV due to absorbed H_2O or O_2 molecules on the surface. With increasing milling time, the peaks at 531.5 eV and 532.7 eV increase at the expense of the peak at 530.3 eV, indicating the increase in oxygen vacancies with milling. Paramagnetic (PM) nature observed in un-milled ZnO gradually unveils room temperature FM with modest magnetization and coercivity. A maximum magnetization of 0.92 emu/g at 12 kOe applied field and a coercivity of 172 Oe were obtained for 40 hrs milled ZnO

powder. Annealing of the as-milled ZnO powders displays a drastic reduction in room temperature magnetization signifying the observed FM properties as intrinsic one. High temperature *M-T* data show a clear magnetic phase transition from FM to PM state around 500 °C, which shifts slightly towards higher temperature with increasing milling period up to 20 hrs. EPR study shows that FM order increases with increasing milling time due to the increase in oxygen and zinc vacancies. A close correlation between EPR results and magnetic properties has been observed. The optical studies reveal a blue-shifting of excitonic absorption peak with crystal size reduction. This results in an increase in band gap with size reduction in milled ZnO powders. These ZnO powders with tunable magnetic and optical properties are promising to find applications in multifunctional spintronic and photonic devices.

Chapter 6 discusses the evolution of nanocrystalline microstructure and the resulting vibrational, electronic, magnetic, resonance and optical properties of TiO_2 powders prepared by ball milling process as a function of milling period. Structural studies show that with increasing milling time, peak broadening in XRD peaks along with the development of new phases corresponding to oxygen deficient $TiO_{2-\delta}$ and rutile phases occurs. Vibrational studies support the formation of news phases with increasing milling period. XPS spectra of pure TiO_2 powder show that in Ti 2p spectra, two peaks centered around binding energy of 459 and 465 eV, assignable to $2p_{3/2}$ and $2p_{1/2}$, respectively, of Ti^{4+} in TiO_2. This suggests the identical chemical state of Ti atoms in pure TiO_2. However, with increasing milling period, a significant Ti^{3+} signals could be observed in Ti 2p spectra providing the evidence of oxygen vacancies in the milled powders. In addition, O 1s signal of milled powders depicts three contributions at 530.7, 532.9 and 534.3 eV after peak modeling. The main peak at 530.7 eV could be ascribed to lattice oxygen in TiO_2, while the signal at 532.9 eV could be associated to surface hydroxyl groups. The calculated spectrum exhibits additional feature at 534.3 eV arising from the O atom of the water molecule. Paramagnetic nature observed in pure anatase phase of TiO_2 transforms into induced FM with crystal size reduction. A maximum magnetization of 0.16 emu/g is obtained for 60 hrs milled TiO_2 powder. EPR study show that the nature of EPR signals changes with milling time due to the increase in oxygen and Ti vacancies and exhibit a good agreement with magnetic properties. Optical studies reveal two major peaks around 395 nm and 470 nm due to band-to-band direct transitions in pure TiO_2 powders. Upon milling, additional peaks are observed due to surface recombination, oxygen vacancies and surface defects. The lattice strain and defects reduce the bandgap slightly.

In Chapter 7, we report the structural, vibrational, optical, magnetic and resonance properties of the NiO nanoparticles prepared by sol-gel method with different molar concentrations and annealed at different temperatures. NiO nanoparticles have single phase *fcc* structure with negligible strain and without any detectable impurity phases, but the average crystallite size increases and lattice constant decreases with increasing annealing temperature. The shape of NiO particles changes from spherical to non-spherical in nature with increasing annealing temperature. Vibrational properties exhibit a new Raman band at 500 cm^{-1} associated with magnetic origin induced by strong phonon-magnon interaction. This peak shows red-shift with increasing molar concentration for the samples annealed at 350 °C. The presence of 2M mode was not observed in the presently investigated samples. The optical properties exhibit a strong UV emission around 350 nm, which depicts blue-shift for NiO nanoparticles as compared to bulk. Low temperature *M-T* curves in 350 °C annealed samples display peaks in ZFC curves, which shift to lower temperature with increasing applied magnetic fields. The existence of spin glass like phase due to freezing of the uncompensated surface spins has been verified through AT line plot. The presence of spin glass like phase provides additional anisotropy between the freezing surface spins and the compensated spins at the core under field cooling condition, which results in a larger exchange bias variation at lower temperatures. However, the samples annealed at 500 °C with molar concentration more than 0.1 M neither show spin glass nor exhibit large exchange bias. A well-defined magnetic phase transition due to induced FM nature is observed at high temperature around 610 K, but the phase transition temperature increases slightly from 610 K to 618 K with increasing molar concentration up to 0.3 M. EPR results are in good agreement with the observed magnetic properties. The observed results make these nanoparticles as an excellent model system not only for the better understanding of various properties but also to enhance the magnetic surface contribution in nanostructured system.

The above results have been used to understand the evolution of nanocrystalline microstructure with fine crystallites of NiO, ZnO and TiO_2 and the resulting vibrational, electronic, magnetic, resonance and optical properties on the basis of milling time period and annealing conditions in shaping the properties of milled nanocrystalline metal-oxide powders. Furthermore, the conclusions have been drawn on the basis of finite size effect, defect density and oxidation/reduction and uncompensated spins at the surfaces. Chapter 8 provides a summary of the results obtained in the thesis and suggests possible directions of future work.

CONTENTS

Chapter 1

Prologue

1.1. Introduction

Spintronics is a rapidly growing field of research in multidisciplinary level and intensified by a strong synergy between breakthroughs in basic science and industrial applications in the fields of magnetic recording, nonvolatile memories, magnetic field sensors, semiconductor spintronics, etc [SATO2015, XUY2015, BAND2016, SCHA2016]. Spintronics, also termed as spin electronics, at the interface between magnetism and electronics, exploits both intrinsic spin of the electron and its associated magnetic moment in addition to its fundamental electronic charge. Hence, the operation principle of spintronic devices is based on completely different physical phenomena as compared to their charge-based counterparts. The addition of the spin degree of freedom to the conventional electronic devices has several advantages like non-volatile, increased data processing speed, decreased electric power consumption and increased integration densities. A proposed technology tree for spin-based devices is shown in Figure 1.01 [PEAR2003].

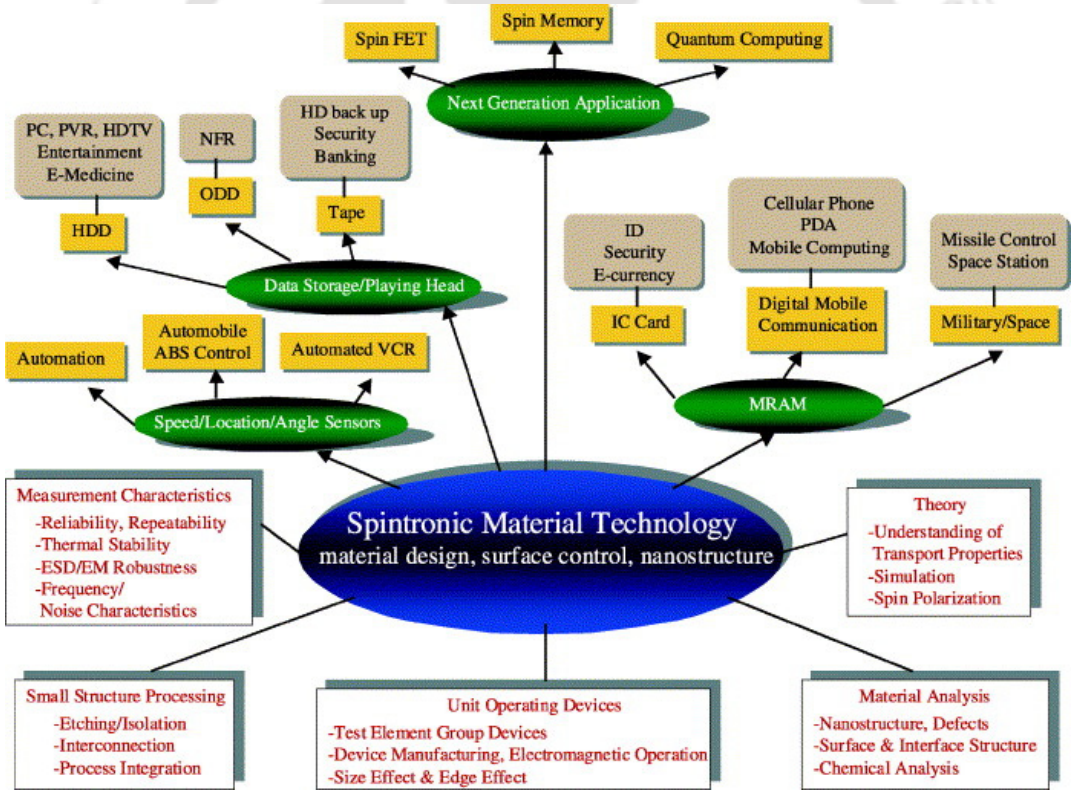

Figure 1.01: Technology tree for spin-based devices and their potential applications [PEAR2003].

Particularly, in the area of semiconductor spintronics, the realization of materials that combine semiconducting behavior with robust magnetism has long been a dream of material

physics. One of the precondition for semiconductor spintronics is the use of ferromagnetic semiconductors (FMSC) with large Curie temperature (T_C) above room temperature [JUND2006]. Since the magnetic properties of FMSCs are a function of carrier concentration in the material in many cases, then it will be possible to have electrically or optically-controlled magnetism through field-gating of transistor structures or optical excitation to alter the carrier density. Such novel control of magnetism has already been realized electronically and optically in different FMSCs [OHNO2000, OIWA2002, PARK2002]. The current interest in FMSCs can be traced to difficulties in injecting spins from a ferromagnetic (FM) metal into a semiconductor [BAND2016] due to the dissimilar materials properties of a metal and semiconductor. Therefore, an efficient spin injection in the diffusive transport regime is difficult unless the magnetic material is nearly 100 % spin-polarized, i.e., half-metallic [RASH2000]. Although there have been recent reports of successful and efficient spin injection from a metal to a semiconductor by ballistic transport at room temperature [TSYM2016], the realization of functional spintronic devices requires materials with ferromagnetic ordering at operational temperatures compatible with existing semiconductor materials. Thus, the topic of diluted magnetic semiconductors (DMS) has received extensive interest.

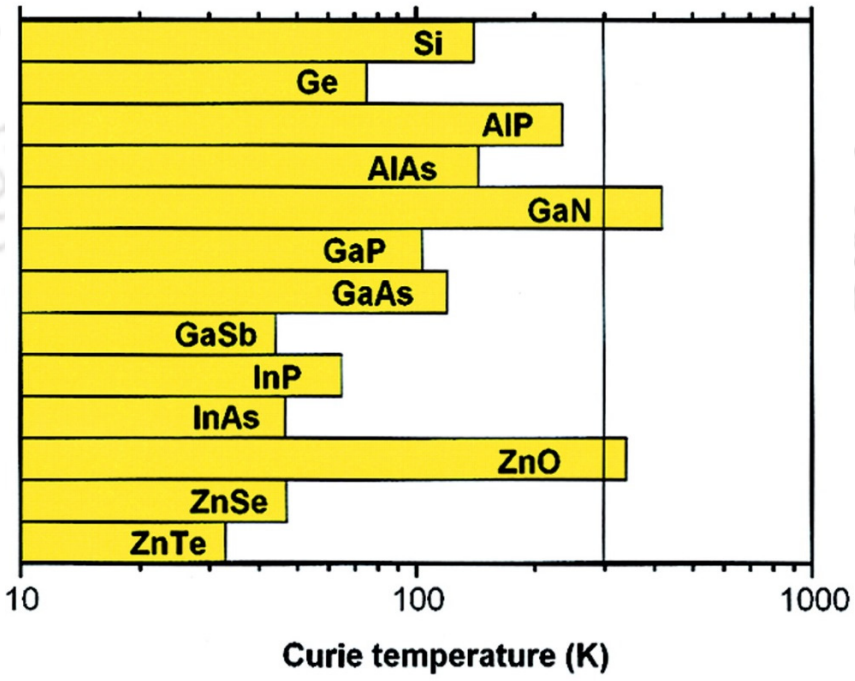

Figure 1.02: T_C values for 5 % Mn doped compound semiconductors [DIET2000].

The spintronics based on DMS provides a new technology that transforms reading and writing information for many uses by spin rather than by typical electronic charge [DIET2000,

LIUC2005]. In addition, DMS of nanocrystalline oxides are especially attractive due to their unique properties and find applications in catalysis, sensor, optoelectronic devices, etc [OHNO1998, DIET2000, MATS2001, UEDA2001, RODE2003, SHAR2003, SHIN2003, WUJB2003, COEY2004, RAMC2004, SHIN2004, LINY20061]. Therefore, DMS materials are considered as one of the new kind of materials for spintronic applications, especially those materials exhibiting high T_C above room temperature. Figure 1.02 displays the computed values of T_C using theoretical model for various semiconductors containing 5 % of Mn and 3.5×10^{20} holes per cm^3 [DIET2000]. It is clear from the figure that the compounds GaN-Mn exhibit room temperature FM with T_C of nearly 6 % larger than the one predicted for ZnO having wurtzite structure. This resulted in extensive studies on high T_C FM DMS materials including NiO, ZnO [RODE2003, SHAR2003, SCHW20041], TiO_2 [MATS2001, SHIN2003, SHIN2004], SnO_2 [OGAL2003], ZnTe [SAIT2003], In_2O_3 [HEJ2005], Cu_2O [WEIM2005], etc., after the discovery of the room temperature FM in Co doped TiO_2 [MATS2001]. In addition, the effect of doping using selective elements such as Mn [SHAR2003], Co [SHAR2003, SCHW20041], Ni [RADO2003] and V [SAEK2001] in metal-oxide has been studied to induce FM beyond room temperature.

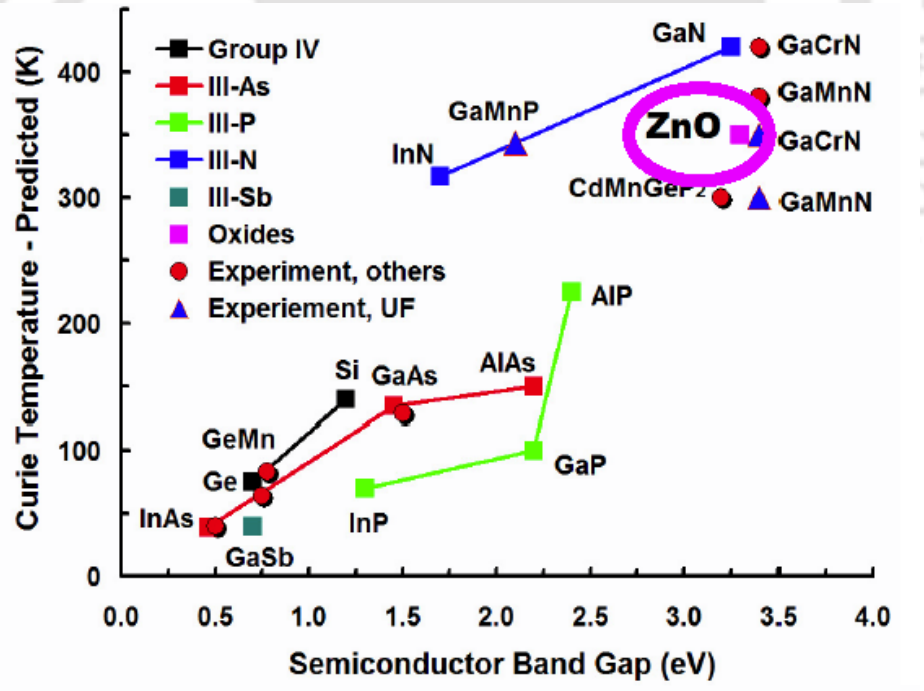

Figure 1.03: Predicted T_C as a function of bandgap (after [DIET2000]) along with some experimentally reported values in the literature [PEAR2003].

However, the exact contributions of various factors to the FM properties in these systems are still debatable. In order to find a correlation between FM and semiconducting properties, compilation of predicted T_C using mean-field approximation [PEAR2003] for different semiconducting materials as a function of bandgap is displayed in Figure 1.03. To support the prediction, some of the experimentally reported values in the literature are also displayed in Figure 1.03. It is clear from the figure that the materials such as GaMn and GaMnN, GaCrN, exhibit T_C above room temperature. Interestingly, the oxide based material (ZnO) also shows T_C above room temperature with large bandgap. But, the practical applications of these oxide materials are strongly challenged by its low reproducibility of room temperature FM and controversial observations concerning over the origin of FM in DMS materials. Nevertheless, Sundaresan et al proposed that FM behavior in nanoparticles of non-magnetic oxides is a universal feature and confined to the surface of the nanoparticles [SUND2006, SUND2009].

1.2. Motivation behind the work with historical perspective from the literature

With the recent interests in the development of various spintronic devices based on the DMS materials, it is very much important to study the properties of oxide materials that are commonly used in such applications. Therefore, the study of fine nanocrystalline metal-oxide particles has become a subject of increasing interest and intense research in the myriad of different fields such as catalysis, batteries, supercapacitors, magnetic resonance imaging contrast agents, targeted drug delivery, sensors, energy conversion, electrochromics, etc. These nanoparticles lie between clusters whose properties are strongly dependent on its size and submicron sized particles which have almost the properties same as bulk materials. In particular, the study of magnetism and magnetic interactions in various types of metal-oxide materials, as listed in Table 1.01, has generated much attention due to size and/or defect induced magnetic properties and their potential applications in biomedical, magnetoelectronic device, catalysis, spintronics, etc.

Table 1.01: Room temperature FM NiO, ZnO and TiO_2 with different preparation methods.

Materials	**Processing**	H_C **(Oe)**	M_S	**References**
NiO nanoparticles	Chemical method	100 (5.3 nm)	---	[MAKH1997]
NiO nanoparticles	Ball milling	259 (7-3 nm)	0.06 emu/g	[MISH2004]

Ni doped ZnO Thin film	Sputtering	100	0.11 μ_B	[SCHW20042]
CuO nanoparticles	Sol-gel	200 (13-17 nm)	10 emu/mol	[RAOG2005]
NiO nanorods	Sol-gel method	620 at 5 K (5 nm)	---	[SEEH2005]
Fe doped NiO nanoparticles	Chemical method	30 (100-200 nm)	0.38 μ_B/Fe	[WANG20051]
NiO nanoparticles	Chemical method	933 (24-50 nm)	---	[LIL2006]
Li and Fe doped NiO Thin film	Sputtering	---	16 emu/cc	[LINY20062]
Ni doped TiO_2	Ball milling	40-60 (20-50 nm)	0.008 emu/g	[UHMY2006]
Co doped ZnO	Solid state reaction	200-350	0.04 μ_B/Co	[ZHUT2006]
Ni and Ni-NiO nanoclusters	Cluster beam deposition	562 (2-5 nm)	0.9 emu/g	[ZHOU2007]
Fe doped NiO nanoparticles	Co-precipitation method	110-350 (15-60 nm)	0.2 emu/g	[HEJH2008]
NiO doped on Fe_2O_3	Mechanical alloying	600 at 200 K (10 nm)	10-30 emu/g at 5 K	[LIUX20081]
Fe doped NiO nanorods	Hydrothermal method	614 (50-100 nm)	0.6 emu/g	[MANN2008]
Mn doped ZnO nanorods	Chemical vapor deposition	50 (150 nm)	0.39 μ_B/Mn	[YANH2008]
Fe and Li doped NiO Thin film	Pulse laser deposition	--- (80-100 nm)	0.67 μ_B/Fe	[YANW2008]
C doped ZnO nanoneedles	Cathodic vacuum arc technique	30 (600 nm)	2.16 emu/cc	[HERN2009]
NiO nanoparticles	Sol gel	40 (7-30 nm)	---	[JAGO2009]
$Ni(OH)_2$ nanoparticles	Sol-gel method	200-500 (2-5 μm)	20-50 emu/g $T < 300$ K	[LIUX2010]

NiO nanoparticles	Co-precipitation method	250 (5.8 nm)	1.5 emu/g	[MENE2010]
NiO nanoparticles	Precipitation method	130-770 (16-25 nm)	0.04 emu/g	[KART2011]
Fe doped NiO nanoparticles	Sol-gel method	372 (18-98 nm)	5.32 emu/g	[KHEM2011]
NiO & (Ni, Zn)O nanoparticles	Chemical method	--- (8-30 nm)	1-3 emu/g $T < 300$ K	[PECK2011]
CuO nanoparticles	Ball milling	90-2360 $T < 300$ K (24-76 nm)	0.08 emu/g	[BIAN2012]
NiO nanoparticles	Thermal decomposition	433 at 5 K (3.5-12 nm)	12 emu/g	[DUAN2012]
NiO nanoparticle	Hydrothermal method	--- (300-500 nm)	12.5 emu/g	[KHAI2012]
Li and Fe doped NiO nanofibers	Electrospining method	--- (30-50 nm)	0.7 emu/g	[LUOY2012]

There has been a profusion of recent work on the magnetic properties of nanosized antiferromagnetic (AFM) particles and most of the reports demonstrate the existence of FM moment on the nanoparticles [KHAD2003, BHOW2004]. This was mainly instigated from Néel's suggestion that fine nanoparticles of AFM nature should exhibit either a weak FM or superparamagnetism (SPM) [NEEL1962]. Richardson et al [RICH1956] reported the first investigation on size dependent properties of NiO system. Subsequently, the effect of particle size dependent magnetic properties [KODA1997, TIWA2005, THOT2007, MAKH2008] and the competition between finite sizes versus surface effects [MAND2011] on the room temperature magnetic crossover of NiO, prepared by chemical process [WINK2005, LIL2006, THOT2007, COPP2013, ALSE2014, ROYA2014], pulse laser deposition [HONG2006], sputtering [LUOX2015] and hydrothermal [WANG20052, WANG2011] techniques, were reported. Sundaresan et al proposed that FM behavior in nanoparticles of non-magnetic oxides is a universal feature [SUND2006, SUND2009]. Out of these studies, a common theory put forward to discuss the unusual FM properties is a form of core-shell model, where the core spins are antiferromagnetically aligned and the shell spins give rise to FM moment

[TIWA2005, JAGO2009]. In addition, several other models such as two-sublattice model and multi-sublattice model were also proposed to account for the observation of large moment in NiO nanoparticles [KODA1997]. Some theoretical calculation and experimental data have shown that NiO nanoparticles ranging from 1 to 50 nm can have both AFM and FM couplings [YIJB2007]. Furthermore, there exists controversial reports on the nature of the temperature dependent magnetic properties. Makhlouf et al [MAKH2008] reported that exchange bias obtained under zero-field-cooled (ZFC) and field-cooled (FC) conditions for different sized particles decreases and the magnetization increases rapidly below 30 nm. The nature of temperature dependent coercivity, $H_C(T)$, is strongly dependent on the particle size and varies from linear to non-linear behavior with decreasing particle size. Proenca et al [PROE2011] shown that effective magnetic anisotropy increases with decreasing NiO particle size and number of uncompensated spins per nanoparticles was found to be proportional to $n_s^{1/3}$ (n_s is total number of spins). Similarly, Duan et al [DUAN2012] reported that larger saturation magnetization and H_C in fine NiO nanoparticles are mainly resulting in from surface spins and explained using core-shell model. While Ghosh et al [GHOS2006] reported that spin freezing temperature increases from 10 to 15 K with increasing particle size of NiO from 3 to 7 nm, respectively, Winkler et al [WINK2008] showed larger spin freezing temperature of 17 K for 3 nm particles. On the other hand, Proenca et al [PROE2011] and Duan et al [DUAN2012] reported SPM properties at room temperature. Similarly, Duan et al [DUAN2012] and Rinaldi-Montes et al [RINA2014] reported the existence of two peaks in ZFC curves corresponding to two blocking processes, while Tiwari et al [TIWA2005] observed only the signature of spin glass freezing, which decreases with increasing particle size, but no low temperature freezing or blocking was observed. The above literature reports clearly reveal that the results from different groups are inconsistent and difficult to compare due to the differences in the defects and surface effects of the studied particles prepared by different preparation techniques. Furthermore, the resulting magnetic properties of NiO particles are very complex due to temperature dependent interplay between finite size core effects, surface effects, interface effects and defects or oxygen vacancies.

Similarly, wide band gap DMS have gained enormous attention recently as a promising route to realize semiconductor based spintronics [DIET2000, PEAR2003]. Sharma et al reported the first experimental evidence of showing room temperature FM in Mn doped ZnO [SHAR2003]. The recent studies on ZnO system revealed realization of room temperature FM in either pure nanostructured ZnO without transition metal doping or ZnO doped with non-magnetic ions such as C and K [HONG2007, AKBA2011, GHOS2011]. However, a careful

analysis of the literature reveals contradictory results on the development of room temperature FM in pure ZnO system. Bartolomé et al [BART2007] showed that the preparation of ZnO based particles using ball milling technique resulted in a drastic reduction in the average size of the crystals without any induced FM. Similarly, Sanyal et al [SANY2008] reported that the ball milling processed ZnO did not show FM despite the creation of Zn vacancy during the ball milling process. On the other hand, Potzger et al [POTZ2008] reported an easy mechanical way to create FM defective ZnO and correlated to flake like structures in planar compressed pieces of the powder. Xing et al [XING2010] suggested that the oxygen vacancies induce characteristic photoluminescence and boost the room temperature FM in ZnO nanowires synthesized using vapor transport method. Banerjee et al [BANE2007] reported the enhancement of FM in pure ZnO powder upon thermal annealing due to the formation of oxygen vacancy clusters. Podila et al [PODI2010] reported the formation of room temperature FM in ZnO films depending on the sample preparation and annealing conditions. The observation of FM was also supported with *ab-initio* calculations exploring the role of surface defects on the magnetic behavior of nanoscale ZnO. Very recently, Phan et al [PHAN2013] and Ghose et al [GHOS2013] proposed that mechanical milling can be used to produce defect-related FM in ZnO nanoparticles. These studies revealed that the development of FM in un-doped ZnO was attributed to the defect density of either oxygen or Zn. However, there are no detailed reports summarizing the stability of FM above room temperature in ZnO nanoparticles and the size effect on the development of room temperature FM. Furthermore, ZnO is an optically transparent II-VI semiconductor, electro-optical and well known piezoelectric material with hexagonal wurtzite structure. It exhibits wide band gap (3.27 – 3.42 eV) and expected to show possible size dependent properties.

The other metal-oxide having many industrial uses as DMS, photocatalyst and strong stability in UV light is a Titanium dioxide (TiO_2), a non-toxic oxide semiconductor [MATS2001, SHIN2003, HONG2004, KIMD2004, SHIN2004]. TiO_2, especially in bulk or thin film form, has drawn wide attention over the years because of its interesting optical, photocatalytic, electronic and magnetic properties [KHAT2012, BARA2016]. The anatase phase has been used for photocatalyst of photo-decomposition and solar energy conversion because of its high photoactivity [ZHOU1996, PIER2003]. However, there are controversial results among different research groups in studying the magnetic properties of TiO_2 nanoparticles. Some reports suggested that segregation and the formation of transition metal clusters are the origin of FM signal [KIMJ2003, XUJ2010], while other reports hinted as intrinsic nature of FM mediated by carriers or defects [GRIF2008, MOHA2012]. Pandey et al

[PAND2011] argued that oxygen vacancies lead to electron doping in TiO_2 system, but does not induce appreciable FM using *ab-initio* electronic structure calculation. Hoa et al [HOAN2013] reported enhanced FM in un-doped TiO_2 nanowire as compared to Ni doped TiO_2 nanowire. Theoretical and experimental evidences showed that the magnetic ordering of un-doped TiO_2 is strongly related to oxygen vacancy [HONG2006, RUMA2007, KIMD2009, SUND2009, LIH2012, MOHA2012] and thus it was thought to be the source of room temperature FM in un-doped semiconducting oxides. However, there are no detailed reports summarizing the size effect on the development of room temperature FM in TiO_2.

The above literature noticeably reveals that the observed magnetic properties in DMS materials are critically dependent on fabrication methods, growth conditions, doping agents and the form of the materials. Several preparation methods such as chemical process, hydrothermal technique, sonochemical and microwave, vapor transport method, sputtering, pulsed laser deposition, etc., were used to prepare these metal-oxide materials. Most of the reported investigations are bottom to top approach on selected size of the particles, which reveal that the resulting magnetic properties in these oxide materials are complex due to the interplay between finite size, surface effects and interface effects, etc. On the other hand, the approach of top to bottom method for studying the magnetic properties of pure NiO, ZnO and TiO_2 powders without any impurity phases is still limited and/or missing. This motivated us to adopt an alternative and inexpensive technique called ball milling process using a high-energy planetary ball mill under dry milling conditions in an argon atmosphere to prepare nanoscale NiO, ZnO and TiO_2 powders. The ball milling process is a solid state method [SURY2001, KOCH2006] in which the materials undergo repeated cold welding and fracturing. This produces final materials in powder form with nanosized crystals, which can be tailored in various shapes and dimensions by compacting and giving proper heat treatment for availing commercially. Also, the reports on magnetic materials demonstrated that T_C can be enhanced moderately by introducing stress through ball milling process [GORR2009].

1.3. Objective of the thesis work

- To prepare nanocrystalline powders of pure NiO, ZnO and TiO_2 by ball milling process in a planetary ball mill under dry milling conditions and at argon gas atmosphere with different milling time periods (t_m = 0 - 60 hrs).
- To understand the evolution of crystal structure and nanocrystalline microstructure in pure NiO, ZnO and TiO_2 powders as a function of milling time periods.

- To study the resulting vibrational, electronic, magnetic, resonance properties and optical properties of pure and milled NiO, ZnO and TiO_2 powders as a function of milling time periods.
- To investigate the effect of annealing on the modification of microstructure and to study the origin of induced ferromagnetism in NiO, ZnO and TiO_2 powders.
- To study temperature (at low/high temperatures) and field dependent magnetic properties of as-prepared and annealed powders.
- To analyze the correlation between the structural, microstructure and physical properties of nanocrystalline powders both in the as-prepared and annealed conditions.
- For comparative study, NiO nanoparticles are prepared by sol-gel method with different molar concentrations and annealed at different annealing temperatures, and studied structural, vibrational, optical, magnetic and resonance properties.

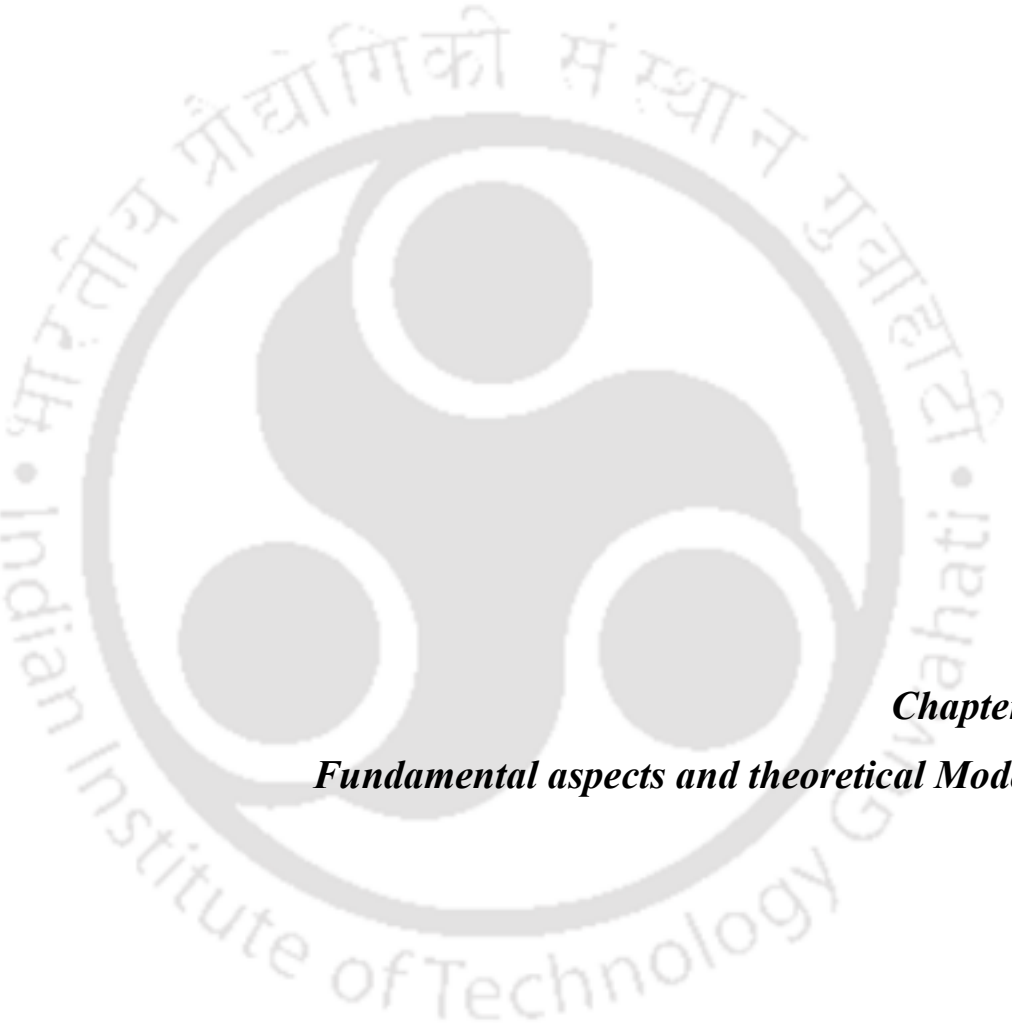

Chapter 2

Fundamental aspects and theoretical Models

2.1. Introduction

Magnetism is a physical phenomenon known for thousands of years by which materials shows an attractive or repulsive force. The history of magnetism is coeval with the history of science. However, the underlying principles and mechanisms that explain the magnetic properties of the materials are still complex and mysterious. It is well-known that most of the modern technological devices such as electrical power generator, transformer, electric motor, sensor, computer, and components of sound and video reproduction system rely on magnetism and magnetic materials. Hence, during last few decades, extensive studies on various types of magnetic materials have been carried out from both fundamental and application points of views. Recently, the tendency of miniaturization of electronic devices has created a demand for the search of new materials such as thin films and dilute magnetic semiconductors (DMS) and their production by different simple and inexpensive synthesis methods. In particular, the development of DMS exhibiting room temperature magnetism with and without additional elements doping has received enormous interest in the scientific community due to their dual characteristics of semiconductor and ferromagnetism (FM). Such materials facilitate one more degree of freedom, i.e., spin polarization of charge carriers, to tune and control electrical transport in devices. Therefore, the devices, having such extra degree of freedom, are called spintronic devices and they have potential applications in electronic circuit for high speed signal processing, low power consumption, magneto-optic device, etc. Hence, over last few decades, large number of studies on various nanoparticles, thin films and new DMS material have been carried out. In this regard, the understanding of development of magnetic properties in new types of materials and optimization of the magnetic properties for different applications are very much essential. This chapter provides a brief description of structure of metal-oxide materials, the origin of magnetism, different types of magnetism, the phenomenon of FM in oxide materials and the various phenomena affecting the ferromagnetic properties of materials prepared by different techniques for suitable applications.

2.2. Structural properties

The crystal structure of various wide band gap oxide materials such as NiO, ZnO and TiO_2 taken in the present investigations are discussed. Other structural effects such as crystal field effect and Jahn-Teller distortion are also briefly introduced.

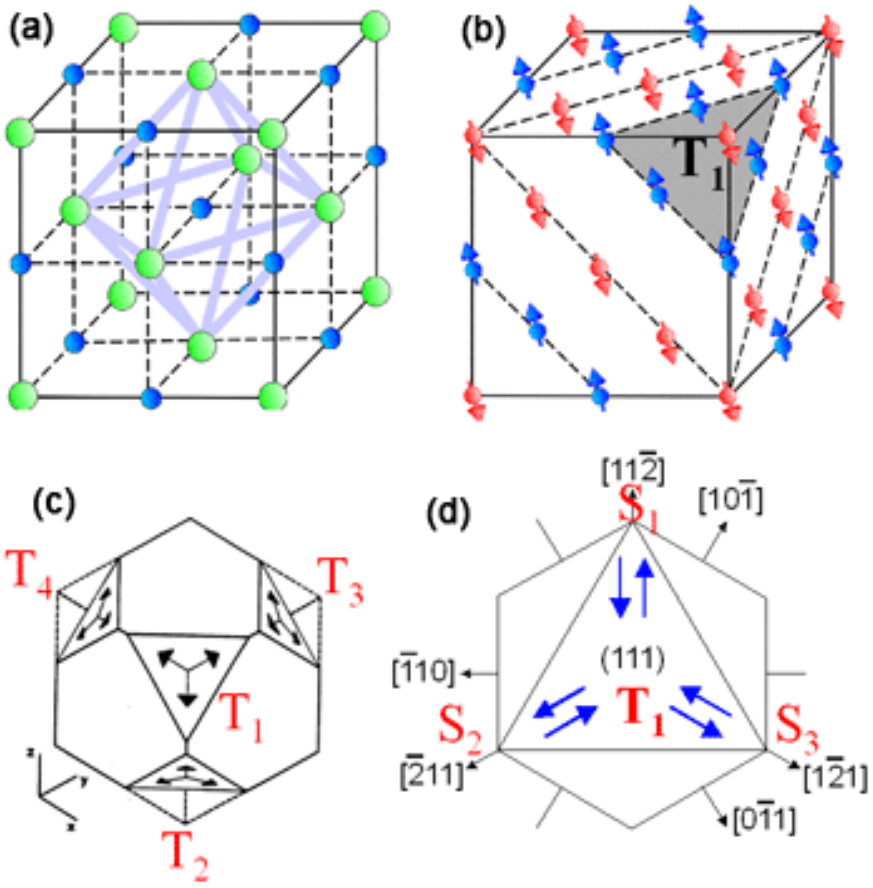

Figure 2.01: Schematic representation of collinear arrangement of magnetic (a) cation of NiO, (b,c) T_1 domains and (d) S_1 domain.

2.2.1. Crystal Structure

Nickel (II) oxide is the chemical compound with the formula NiO. It is an important transition metal (TM) oxide and attracted increasing attention owing to potential use in a variety of applications such as catalysis [DOOL1994], battery cathodes [YANG1999, HOTO2000], gas sensors [MILL1997], electrochromic films [WANG20121] and magnetic materials [MAKH1997, ICHI2003]. It adopts the NaCl structure as shown in Figure 2.01(a) with octahedral Ni(II) and O^{2-} sites and crystallizes in face structure cubic (*fcc*) structure (space group *Fm3hm* [225]) with the bulk lattice constant of NiO at 0 K is (a =) 4.1705 Å. The simple NiO structure is known as the rock salt structure exhibiting green color when the Ni and O ratio is stoichiometrically correct. NiO is type II antiferromagnetic (AFM) and the magnetic unit cell is found to be close to cubic with a doubled lattice parameter in order to accommodate the AFM spin arrangement as shown in Figure 2.01(b). In fact, the spins were found to be parallel on cubic (111) planes, but antiparallel on neighboring (111) planes. The relative orientation of

the spins with respect to each other is determined by exchange interactions. The main factor responsible for this particular AFM arrangement is the 180° super-exchange interaction. Assuming a collinear spin structure, a trigonal distortion restricts the number of possible spin structures to the four experimentally observed *T*-domains. These are characterized by AFM domains (*T* domains), in which the moments form FM foils parallel to one of the four equivalent (111) planes of the *fcc* lattice [KEFF1957, DUOL2010] with the spin aligned in the plane of the foil. This type of AFM ordering is further stabilized by a rhombohedral distortion in the direction perpendicular to the foils caused by magnetostriction. Inside each (111) foil, the spin is driven to align along one of the three equivalent $[11\bar{2}]$ directions by sources of smaller anisotropy as shown in Figure 2.01(b,c,d). This gives three equivalent so-called *S*-domains. With increasing temperature, they transform into paramagnetic (PM) state having space group *Fm3m* above the Néel temperature (T_N) of 523 K [ROTH1958].

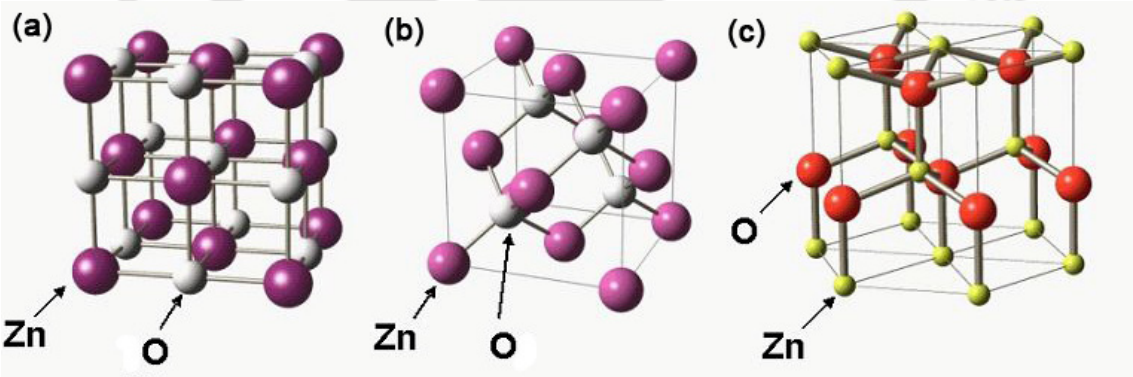

Figure 2.02: Representation of ZnO crystal structures: (a) Rock salt, (b) Zinc blende and (c) Wurtzite.

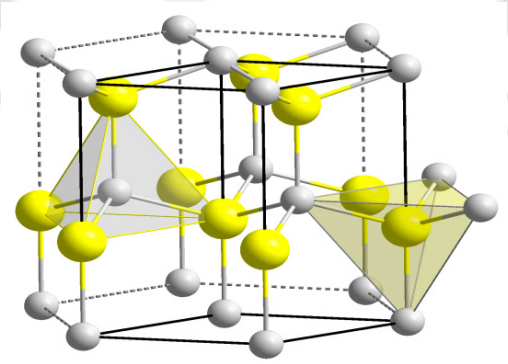

Figure 2.03: Hexagonal wurtzite structure.

Similarly, the other oxide system as a semiconducting materials received great interest among the researchers is zinc oxide (ZnO) due to its interesting prospects in the field of

optoelectronic applications owing to its wide and direct bandgap (~3.437 eV at 8 K [NAGA2017]. Most of the II-VI binary compound semiconductors crystallize as either zinc blende or hexagonal wurtzite structure where each anion is surrounded by four cations or vice versa. ZnO crystallizes in three different structures: Wurtzite, Zinc blende and rock salt as demonstrated in Figure 2.02. Among these, wurtzite structure is the thermodynamically stable phase in ambient conditions, while zinc blende structure is stabilized only by growth on cubic structures and rock salt structure can be obtained at high pressure [OZGU2005]. The wurtzite structure has a hexagonal unit cell with lattice parameters, $a = b = 3.250$ Å and $c = 5.206$ Å [ABRA1969]. It belongs to *P63mc* space group with Zn atoms occupying the (0.667, 0.333, 0.000) position having a multiplicity factor of 2 and oxygen atom occupying the (0.667, 0.333, 0.380) site with multiplicity factor 2. Thus, there are two formula units per unit cell as shown in Figure 2.03. In both the cases, Zn and O atoms have tetrahedral co-ordination.

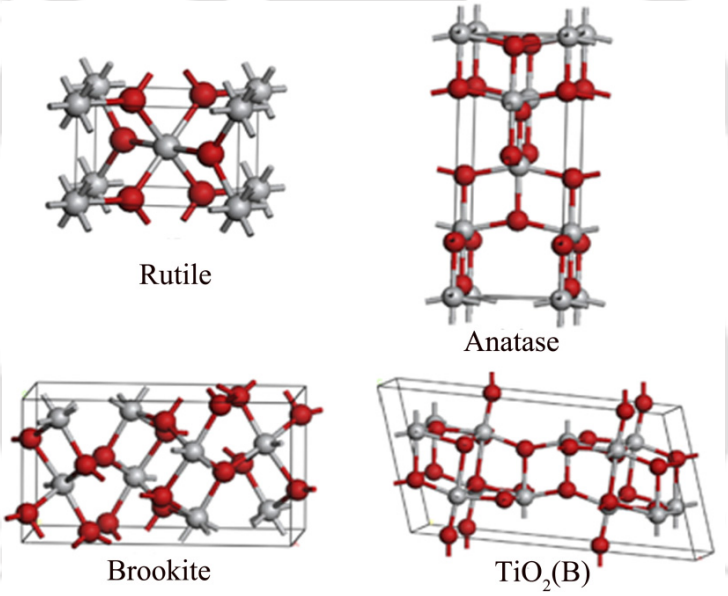

Figure 2.04: Schematic representation of different Structure of TiO_2 Red ball: O atom, Grey ball: Ti atom [DING2014].

On the other hand, titanium dioxide, also known as titanium (IV) oxide or titania, is the naturally occurring oxide of titanium (TiO_2), which mainly crystallizes into three different forms: rutile, anatase and brookite structures as shown in Figure 2.04. In addition, the pressure induced monoclinic baddeleyite and orthorhombic forms like TiO_2(B) [see Figure 2.04(d)] are found recently at the Ries Crater in Bavaria. The rutile state is found to be the most stable state. Upon heating, the anatase and brookite phases are converted into rutile form. The rutile and anatase phases belong to the tetragonal crystal structure and brookite structure exhibits

orthogonal cell. The rutile phase belongs to the $P4_2/mnm$ space group with lattice parameters $a = b = 4.594$ Å and $c = 2.959$ Å and $z = 2$ [HOWA1991]. The anatase phase belongs to the $I4_1/amd$ space group with lattice parameters $a = b = 3.785$ Å and $c = 9.514$ Å and the number of formula units per unit cell $z = 4$ [HOWA1991]. The brookite phase belongs to the *Pbca* space group with $z = 8$ and $a = 5.456$ Å, $b = 9.182$ Å and $c = 5.143$ Å. TiO_2(B) phase belongs to space group C2/*m* with a =12.173 Å, $b = 3.732$ Å and $c = 6.537$ Å.

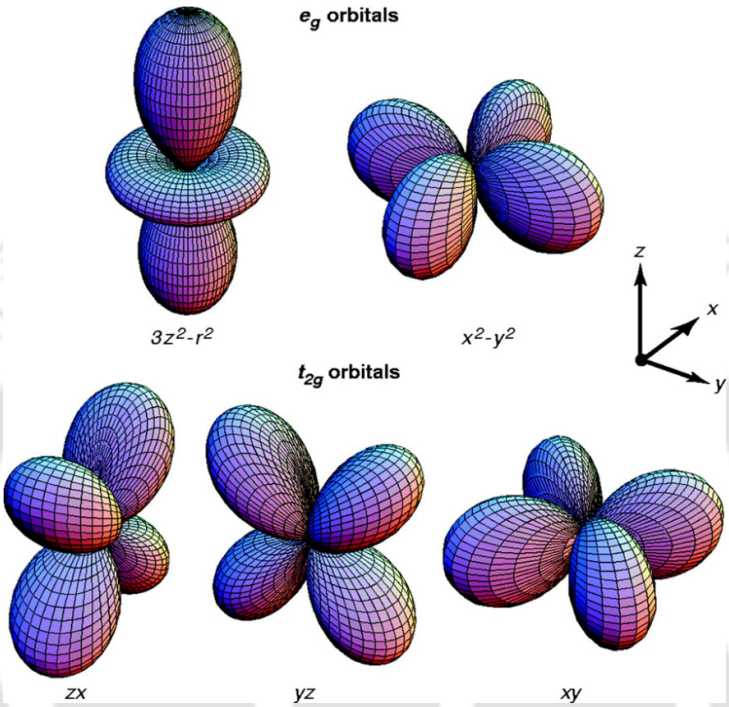

Figure 2.05: The electronic distribution of *3d* orbitals. In the cubic crystal field, the fivefold degeneracy is lifted to two e_g orbitals ($d_{3z^2-r^2}$ and $d_{x^2-y^2}$) and three t_{2g} orbitals (*zx*, *yz* and *xy*) [TOKU2000].

2.2.2. Crystal field effect

Atoms in a solid with a regular crystal structure are influenced by the electric field of the neighboring atoms. Such electric fields are called crystal field [BLUN2003]. Crystal field depends upon the local environments such as the nature of atomic co-ordination. The crystal field effect on *d* orbitals can be illustrated by moving a set of negative point charges close to a metal ion, owing to the Coulomb repulsion between the *d* orbital electrons and the surrounding charges. The *d* shell has five orbitals, the first three are called t_{2g} orbitals, namely, d_{xy}, d_{yz} and d_{zx} and last two are called e_g orbitals namely $d_{3z^2-r^2}$ and $d_{x^2-y^2}$. The electronic distributions of *d* orbitals are shown in Figure 2.05. In the absence of crystal field, all the five levels are

degenerate. The t_{2g} orbitals point along in between *x*, *y* and *z* axes, but the e_g orbitals point along the direction of *x*, *y* and *z* axes. In case of surrounding negative charge is spherically symmetric, all five *d* orbitals are equally affected. In practical cases, the surrounding negative charge is never spherically distributed, because the charge is associated with specific ions that occupy specific positions. The consequence is that each *d* orbital is affected differently, and however a particular *d* orbital is affected depends upon the geometry of the surrounding point charges. This effect is clearly seen in the splitting of the energy levels for the five *d* orbitals. The crystal field effects are summarized in the chart shown in Figure 2.06. Each geometry of point charges (linear, square, planar, tetrahedral or octahedral) produces a characteristic splitting pattern for the five *d* orbitals (*xy*, *yz*, *zx*, x^2-y^2 and z^2).

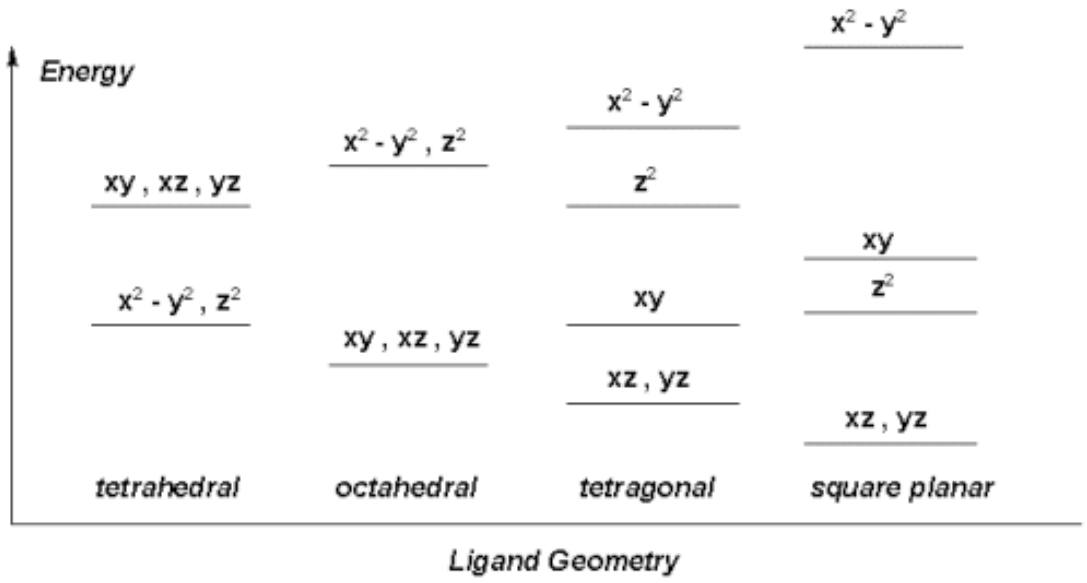

Figure 2.06: Schematic representation splitting of *d*-orbitals in presence of different anion configurations [BASO1964].

2.2.3. High spin and low spin arrangement

In the case of octahedral environment as shown in Figure 2.07, the 3*d* electrons will first fill up the t_{2g} level before filling e_g. However, the competition between the crystal field energy and pairing energy will decide the manner in which each orbital is filled up. In the presence of weak crystal field, the electrons filling in the orbitals will take place as per Hund's rule, i.e., electrons will singly occupy in each orbital followed by pairing of electrons with opposite spin in each orbital. On the other hand, the presence of strong crystal field, where the crystal field energy dominates the Hund's energy, electrons will doubly occupy in some of the orbitals (t_{2g} or e_g) before the electrons are filled in the higher energy orbitals. For example, Figure 2.08 shows the

electronic arrangement in 3*d* shell of Co^{2+} ion under weak and strong crystal field cases. The net spin quantum number for the weak field case is found to be $S = 3/2$, whereas $S = 1/2$ for the strong field case.

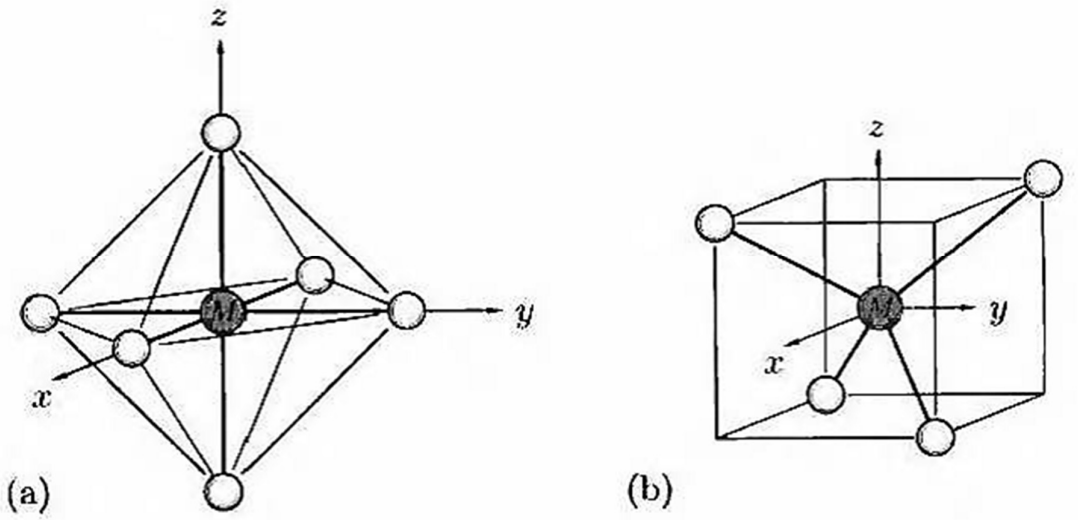

Figure 2.07: Schematic representation TM ion in (a) octahedral (b) tetrahedral configurations [BASO1964].

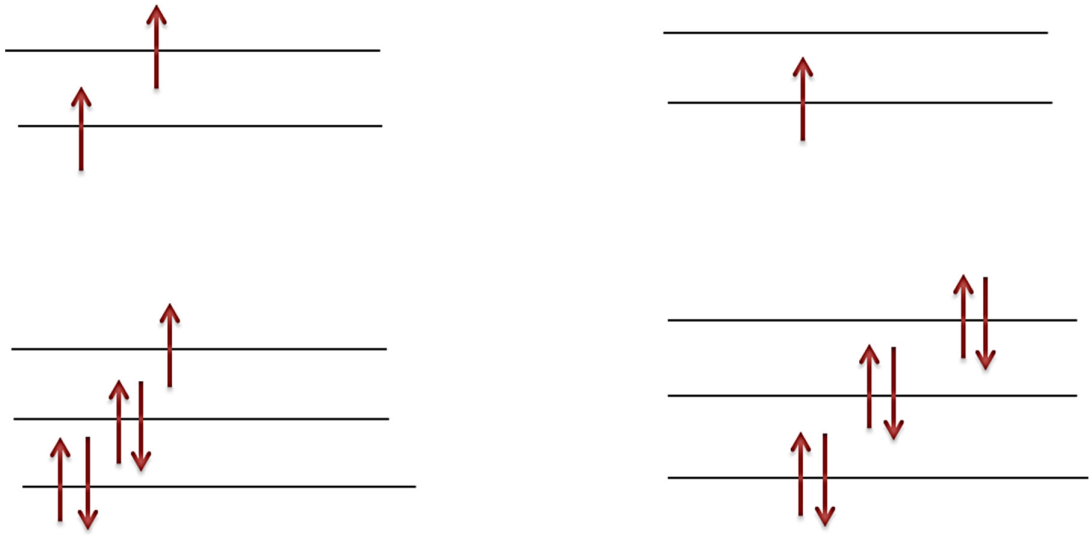

Figure 2.08: Electronic configuration of (left) high-spin (weak field) (right) low-spin (strong field) cation $3d^7$ shell of TM ion.

2.2.4. Orbital quenching

In general, the effective magnetic moment of an ion is calculated by following the Hund's rule and taking the values of *S*, *L* and *J*. The formula is given by

$$\mu_{eff} = g\mu_B\sqrt{J(J+1)} \qquad (2.01)$$

where μ_{eff} is the effective magnetic moment per magnetic ion, g is the Landé g-factor whose value is equal to $g = 1 + [J(J+1) + S(S+1) - L(L+1)]/(2J(J+1))$ and $J = L + S$ is the total angular momentum quantum number. L and S are the orbital and spin angular momentum number, respectively. In 3*d* shell of TM ions, the crystal field interaction is much stronger than the spin-orbit coupling interaction and as a result, the system chooses a ground state, such that $L = 0$. This is called quenching of orbital momentum and it leads to $J = S$ and $g = 2$. Thus, eqn.(2.01) modifies to the following form.

$$\mu_{eff} = 2\mu_B\sqrt{S(S+1)} \qquad (2.02)$$

The theoretically calculated μ_{eff} values for a few TM ions by considering total angular momentum number, J (P1) and independently by taking only spin quantum number S (P2) are tabulated in Table 2.01.

Table 2.01. Theoretical effective magnetic moment by considering Hund's coupling (P1) and orbital quenching (P2) along with experimental values for selected TM ions [BLUN2003].

Ion	Shell	S	L	J=L+S	g	P1=$g\sqrt{J(J+1)}$ (μ_B)	P2=$2\sqrt{S(S+1)}$ (μ_B)	$P_{Expt.}$ (μ_B)
Fe^{2+}, Co^{3+}	$3d^6$	2	2	4	3/2	6.70	4.9	4.82
Fe^{3+}	$3d^5$	5/2	0	5/2	2	5.92	5.92	5.82
Co^{2+},Ni^{3+}	$3d^7$	3/2	3	9/2	1.33	6.63	3.87	4.90
Ni^{2+}	$3d^8$	1	3	4	5/4	5.59	2.83	3.12
Zn^{2+}	$3d^{10}$	0	0	0		0	0	0
Ti^{3+}	$3d^1$	½	2	3/2		1.55	1.73	1.70

2.2.5. Jahn-Teller Distortion

The observed degeneracy in crystal field splitting can be further broken by the lattice distortion. For example, in MnO_6 octahedral environment, the electrons in the 3*d* shell of Mn ions are under the Coulomb interaction of electrons from the 2*p* shell of O ions. Since the p_x, p_y, p_z orbitals of O point along *x*, *y* and *z* directions, respectively, there will be overlapping with e_g orbitals of Mn ions ($d_{x^2-y^2}$, $d_{3z^2-r^2}$). So, the energy of e_g orbitals is raised compared to t_{2g} orbitals.

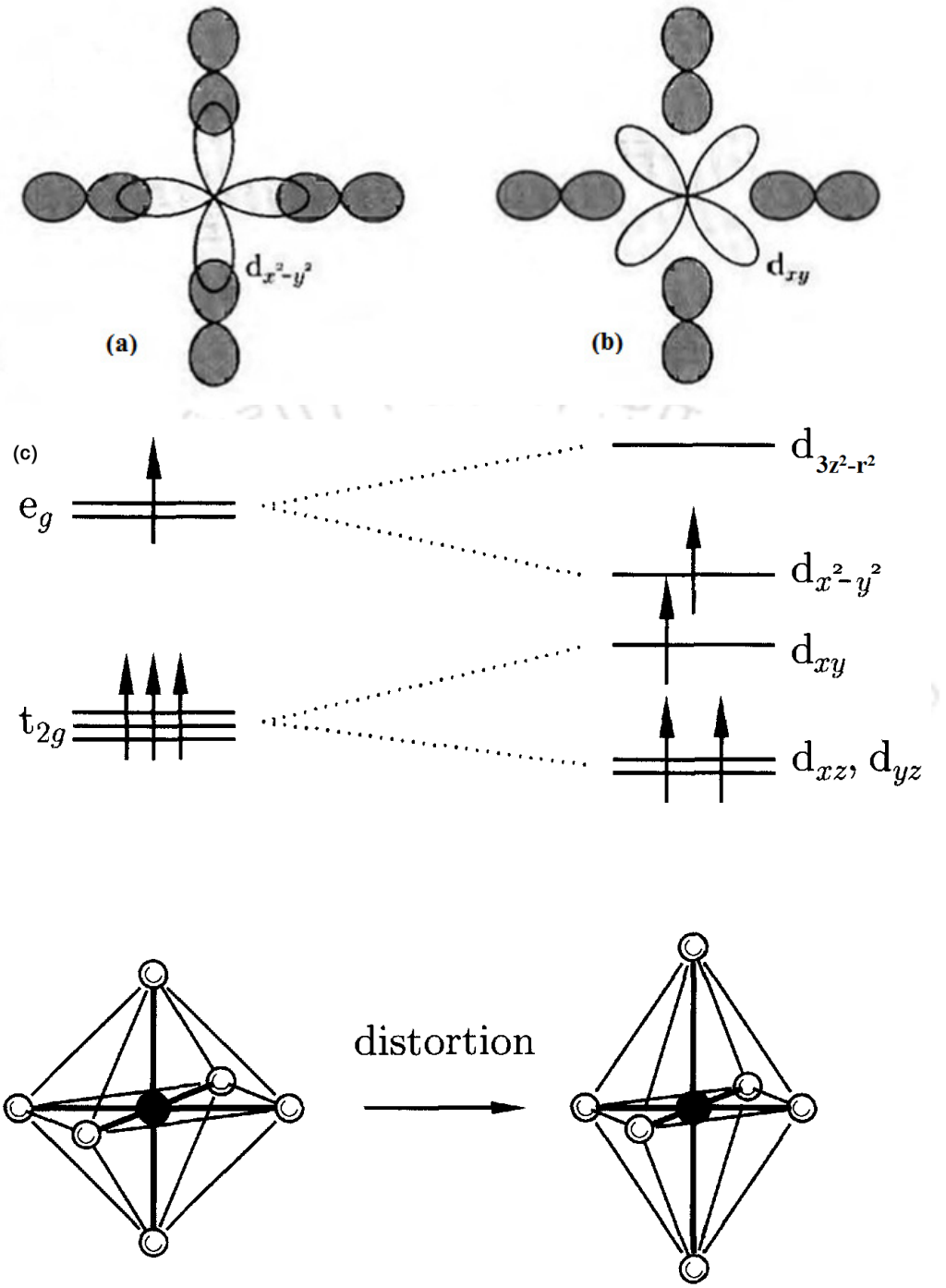

Figure 2.09: (a) Overlapping of one of the e_g orbitals ($d_{x^2-y^2}$) with p orbital of neighboring O in a two dimensional diagram (b) One O of the t_{2g} orbitals with p orbital. (c) The crystal field splitting of d shell in octahedral environment and Jahn-Teller distortion leads to a further splitting of both t_{2g} and e_g states.

Figure 2.09(a) shows a two dimensional diagram of typical overlapping of one of the e_g orbitals ($d_{x^2-y^2}$) with p orbitals of neighboring O ions. On the other hand, we can see no such

overlapping with a typical t_{2g} orbitals (d_{xy}) as shown in Figure 2.09(b). In view of the above crystal field effect, the degeneracy in e_g orbitals and t_{2g} orbitals of *d*-shell are lifted as shown in Figure 2.09(c) for octahedral coordination [BLUN2003]. Thus, in addition to the splitting of *d*-orbitals into t_{2g} and e_g orbitals due to crystal field, there is further splitting of orbital within t_{2g} and e_g due to Jahn-Teller (JT) effect. The oxygen ions are surrounded by Mn^{3+} ions. The readjustment of position of oxygen ions in MnO_6 octahedra can lead to asymmetry in MnO_6 octahedra. The above lattice symmetry lifts the degeneracy of t_{2g} and e_g orbitals. The lifting of degeneracy due to orbital-lattice interaction is known as JT distortion. This JT distortion is significant for partially filled orbitals, where there is a net energy gain. This distortion leads to an increase in elastic energy and decrease in electronic energy such that there is a net reduction in energy. Mn^{3+} ions have one e_g electron and decrease in electronic energy such that there is a net reduction in energy. Mn^{3+} ions are JT active, while Mn^{4+} ions are inactive for JT distortion in octahedral environment. Mn^{3+} ions have one e_g electron out of two e_g orbitals namely, ($d_{3z^2-r^2}$) and ($d_{x^2-y^2}$). The elongation of MnO_6 octahedra along *z*-axis gives rise to reduction in ($d_{3z^2-r^2}$) level compared to ($d_{x^2-y^2}$) level. Since there is only one e_g electron, which occupies the ($d_{3z^2-r^2}$) level, there is reduction in electronic energy. The splitting of e_g and t_{2g} orbitals due to JT distortion is shown in Figure 2.09(c). On the other hand, Mn^{4+} ion does not have any e_g electron, so reduction in electronic energy is not feasible and hence no JT distortion. The TM ion un-doped and doped semiconductors are also affected by the JT distortion as estimated theoretically in Cr-doped Group II-VI based DMS by Blinowski et al [BLIN1996]. The susceptibility data obtained by Brumage et al [BRUM2001] on Cu-doped ZnO samples could be explained based on the crystal field effect and by incorporation the JT distortion, where the doped Cu was in Cu^{2+} state with electronic configuration $3d^9$.

2.3. Defects

Defect engineered NiO, ZnO and TiO_2 nanocrystalline materials have received unprecedented attention because intrinsic as well as extrinsic defects in the materials play a very crucial and fundamental role in enhancing the materials/device performance. The types, concentration and spatial distribution of intrinsic point defects such as vacancies and interstitial atoms influence the performance of metal-oxides in gas sensing, electronics, photonics, solar-induced photochemistry for fuel production and environmental cleanup, and the realization of room temperature FM. In particular, recent studies revealed that physical and chemical properties of TiO_2, such as light absorption, photocatalytic activity, gas sensing properties, electrical

conductivity and magnetic properties etc. can be modulated by the defect/disorder. [LIM2000, TIWA2005, HONG2006, JING2006, BANE2007, SANY2008, PODI2010, WANG2011, DUAN2012, KISA2012, ACHA2013, CHEN2013, LIUX2013, PANX2013, SUJ2013]. Before going into the details of the defects, let us first introduce the types of defects and related modification in the properties of NiO, ZnO and TiO_2 nanocrystalline materials. Any form of deviation from perfect crystal can be treated as a defect. Interestingly, the perfect metal-oxide material will not have a clear crystal structures, i.e., even in a single crystal of NiO, ZnO and TiO_2, one finds point defects (misplaced lattice atoms/ ions, vacancies, foreign atoms/ ions) and/ or extended defects such as dislocations. This will affect the band structure of the materials, which in-turn changes the properties of the materials. For example, the single crystal of cubic NiO, wurtize ZnO and rutile TiO_2 shows different colors due to defects. Point defects as shown in Figure 2.10 are further classified into native defects and external impurity defects (dopants) which can be found either on the lattice (substitutional site) or at the interstitial positions. Dislocations are the kind of defects that an extra line of atoms inserted or removed in/ from the crystal which does not extend throughout the crystal.

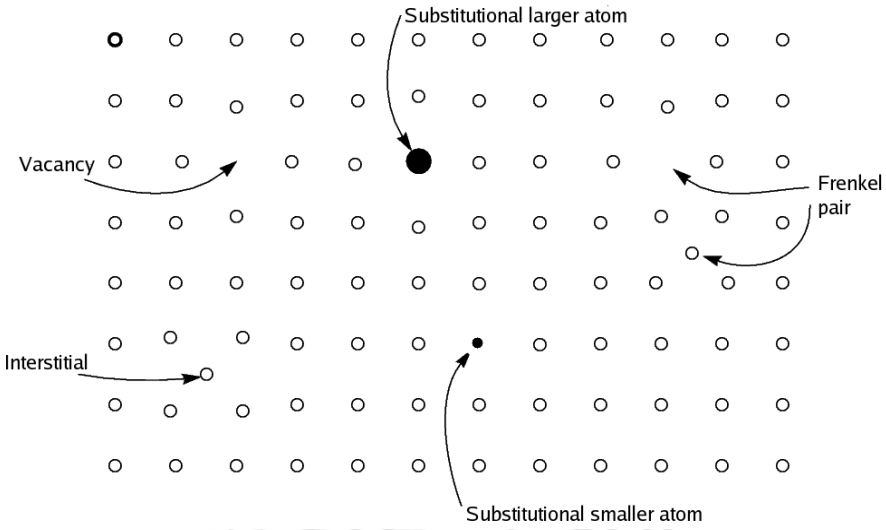

Figure 2.10: Schematic illustration of some simple point defect types in a solid.

2.3.1. Intrinsic defects

The understanding of defect mechanism is very essential in metal-oxide system to improve the gas-sensing performance of the metal-oxide semiconductors. Roberts et al [ROBE1984] reported that high binding energy components of O 1s spectra at 531.4 eV and Ni $2p_{3/2}$ spectra at 856.1 eV obtained from XPS spectra can be correlated with the oxide defect structure. Jang et al [JANG2009] reported that nickel vacancy is the dominant point defect, which results in

the electrical conductivity of NiO thin films. Similarly, Zhang et al [ZHAN2016] also reported that the nickel vacancies are the dominant defect type determining the electrical properties of NiO samples. Thus, intrinsic defects alter the lattice parameters in NiO, TiO_2 and have some effects on the width of the band gap [EKUM2011]. The oxygen interstitial O_i is the O-excess defect and is observed as a surface defect, when NiO is heat treated in O-rich environment. Vacancies and interstitial atoms are responsible for the occurrence of nonstoichiometric compounds. NiO is a good example of a compound with somewhat variable stoichiometry. When NiO is prepared at relatively low temperature (1100 K) by partial oxidation of excess nickel, its composition is $Ni_{1.0}O_{1.0}$ exhibiting pale green color and insulating properties. If the same substance is treated with excess oxygen at 1500 K, the cation vacancies occur and the composition approaches to $Ni_{0.97}O_{1.0}$ and changes the color of the powder into black with semiconducting properties. The deficiency of positive charge that would otherwise accompany cation vacancies is compensated by the presence of the appropriate amount of Ni^{3+}. This is majorly responsible for the electrical conductivity of non-stoichiometric NiO. If a Ni^{3+} ion exists at some point, an electron from elsewhere in the lattice may jump to it, converting it to Ni^{2+} and simultaneously creating a Ni^{3+} ion at a new lattice point. By a series of such electron jumps, charge can migrate through the crystal and producing properties different than the stoichiometric one.

Similarly, in ZnO materials, Lin et al [LINB2001] and Djurisic et al [DJUR2007] identified several oxygen and zinc related intrinsic defects and also some complex defect states which were probed by PL spectroscopy. Liu et al [LIUJ2009] demonstrated that PL of the ZnO nanowires can be tuned from UV to green by controlling the native defects, either by the gas flow during growth process or post–growth annealing in O_2. Some reports show that the most commonly observed green emission is caused by the presence of Zn vacancy [KOHA2000, JANO2007]. In contrast, other groups reported that it is not caused by Zn vacancy, however oxygen vacancy is responsible [VANH1996, LINB2001]. Therefore, a systematic generalized correlation of the defects and the corresponding emission need to be done for the improvement of UV PL intensity. Hence, obtaining highly efficient UV emission from the ZnO nanostructures is one of most important issues for optoelectronic applications of ZnO. The first–principle calculation on ZnO nanostructures shows the possible formation of six types of native point defects in ZnO: oxygen and zinc vacancies (V_O and V_{Zn}), interstitials (O_i and Zn_i), and antisites (O_{Zn} and Zn_O) [JANO2009]. The calculation shows that there is also a possibility of formation of three types of oxygen vacancy defects according to their charge states namely, neutral (V_O^O), singly ionized (V_O^+) and doubly ionized (V_O^{++}).

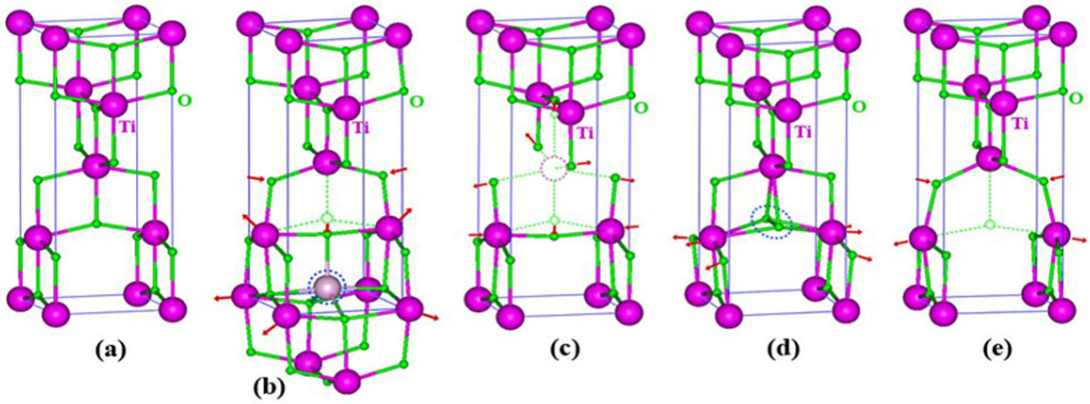

Figure 2.11: Atomic structure of (a) stoichiometric TiO_2, (b) Ti^{4+}, (c) Ti_v^{4-}, (d) O_i^{2-} and (e) O_v^{2+} defects. Relaxation directions of neighboring atoms are indicated by arrows [NAPH2006].

On the other hand, native defects in TiO_2 are widely investigated by using density functional theory calculations. All the fundamental native defects such as oxygen vacancy (O_V), O interstitial (Oi), Ti vacancy (Ti_V), and Ti interstitial (Ti_i) have low formation energy depending upon the O-rich or Ti-rich growth environments and easily appear in non-stoichiometric TiO_2 material [NAPH2006, MORG20101, LEEH2012]. While the antisite defects, namely, Ti-antisite and O-antisite, have high formation energies and hence unstable [NAPH2006]. Reduced TiO_2 with a Ti excess can be accommodated as O_V and Ti_i. Both of these defect species are likely to be present in the reduced TiO_2 samples with competition between defect types determined by synthesis conditions and sample history. If the electronic state of the defect (i.e., its charge and distribution) is different from its host TiO_2, it will introduce energy states in the band gap [gap between valence band (VB) and conduction band (CB)]. For example, Morgan et al [MORG20101] reported using GGA+U calculation that the oxygen vacancies and Ti interstitial defects give rise to states within the band gap in both anatase and rutile TiO_2, corresponding to the electrons localized at the Ti^{3+} centers. Both experimental studies and theoretical calculations revealed the presence of defect states within the band gap of TiO_2 and identified that the band gap is shifted to visible region due to O_V and Ti_i defects which is beneficial for visible-light photocatalytic applications [WEND2008, FINA2009, MORG20101, LEEH2012, CHEN2013, LIUX2013]. The presence of defects thus alters the electronic band structure which influences the operating efficiency of photocatalytic and photovoltaic applications. Recently, Liu et al [LIUX2013] reported the enhanced visible-light photocatalysis in Ti^{3+} (originated from O_V) self-doped TiO_2 materials. Moreover, the conductive track in the on-state in resistive switching mechanism (resistive switching random

access memory device) is believed to be arising from a percolation path of oxygen vacancies or similar defects across the thin films of TiO_2 material [ACHA2013]. Thus, the behavior of extra electron and associated defects is critical to the performance of TiO_2 as a catalyst and electronics. The crystal lattice distortions are also expected due to the presence of defects. The lattice relaxation of anatase TiO_2 due to various native defects was reported by Na-Phattalung et al [NAPH2006]. The atomic structure of stoichiometric and defective anatase TiO_2 is shown in Figure 2.11. This indicates that intrinsic defects may also alter the lattice parameters in TiO_2, which may cause lattice strain and influences band gap [EKUM2011]. The oxygen interstitial O_i is the O-excess defect and is observed as a surface defect when TiO_2 is heat treated in O-rich environment.

2.3.2 Extrinsic defects

Doping is a process of adding small amount of foreign atoms/ions (dopant) into a parent material (host matrix) without forming any secondary phases. When a large amount of the dopant material is added, there is formation of either different oxides or a secondary phase, which may or may not be the mixed oxide, depending on the mutual solubility limit of the two components. This can be referred as mixed oxide or cluster formation rather than the doping. The distribution of the dopant in the crystals/ grains of the matrix material may be homogeneous or heterogeneous. Doping in NiO, ZnO and TiO_2 is performed with the aim of the enhancing the properties of the parent NiO, ZnO and TiO_2 for potential applications. For instance, doping causes the band gap narrowing in TiO_2 nanostructure by introducing the defect states (as either donor or accepter level, depending on dopants) within the band gap. This helps to improve the photocatalytic reaction in two ways: (i) decrease the band gap energy (red-shift of optical absorption edge), enabling photocatalytic activity under visible light illumination, i.e., photocatalyst under sunlight and eliminating the use of UV lamps; (ii) increase the quantum efficiency, i.e., increase the number of photons effectively used for the catalyzed redox reaction. This can only be done by increasing the lifetime of the separated charge carriers (electron and hole) by inducing trap sites.

2.4. Optical band gap

The electronic band gap of a semiconductor is the energy spacing between its valence band maximum and conduction band minimum. In all semiconductors the band gap transition can be facilitated with light, i.e., these materials are photo-activated. Upon the illumination of light, the electrons are excited from valence band to conduction band and the band gap of a

semiconductor results in the resonance absorption of light at a particular wavelength λ_{bg} which corresponds to at least E_{bg}. There are two main types of band gap transition in semiconductors, i.e., (i) direct band gap and (ii) indirect band gap transition.

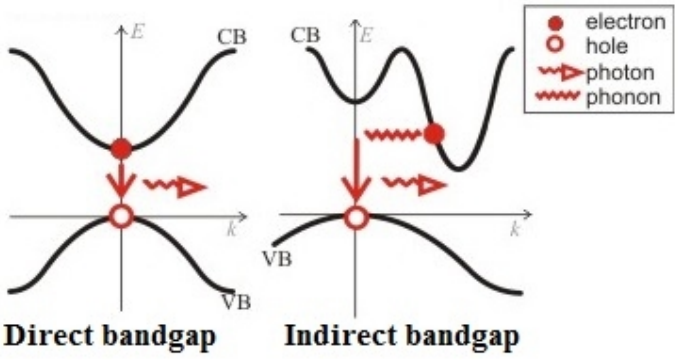

Figure 2.12: Direct and indirect transition semiconductors.

2.4.1. Direct band gap transition

In this case, the transition of the electrons from the bottom of the conduction band to the top of the valence band. A semiconductor, in which the bottom of the conduction band and the top of the valence band are placed at a common wave vector, k, is the direct transition semiconductor, as shown in Figure 2.12. In this transition, the energy and the momentum are conserved. Therefore, the phonons do not take part in direct transitions.

2.4.2. Indirect band gap transition

A semiconductor, in which the bottom of the conduction band and the top of the valence band have different k values, is the indirect transition semiconductors. In this case, the electronic transition from valance band to conduction band is electrically dipole forbidden and the transition is phonon assisted, where both energy and momentum of the created electron-hole pair are changed in the transition. Therefore, absorption and emission of light are weaker as compared to those of direct band gap semiconductors.

2.4.2.1. Calculation of the band gap

The dependence of the band gap energy (E_{bg}) and absorption coefficient (α) of optical absorption is given by eqn.(2.03) [BARD1954]

$$\alpha h\upsilon = A(h\upsilon - E_{bg})^{\gamma} \qquad (2.03)$$

where A is a constant, γ represents the optical transition mode and $h\upsilon$ is the photon energy (in eV). In other words, α is always proportional to the difference between the photon energy and

the band gap to some exponent γ. γ depends on the optical transition mode whose values are listed in Table 2.02. Fitting the experimental absorption data with correct choice of γ reveals the band gap and the nature of transition. From the optical absorption spectra, the band gap can be calculated by extrapolating the tangent of $(\alpha h\upsilon)^{1/2}$ versus $h\upsilon$ plot to $(\alpha h\upsilon)^{1/2} = 0$ for indirect allowed band gap and $(\alpha h\upsilon)^2$ versus $h\upsilon$ plot to $(\alpha h\upsilon)^2 = 0$ for direct allowed band gap. This plot is known as Tauc's plot [TAUC1966].

Table 2.02: γ values with respect to different optical transition modes for eqn. (2.03).

γ	Transition mode
$^1/_2$	Direct allowed
$^3/_2$	Direct forbidden
2	Indirect allowed
3	Indirect forbidden

2.4.3. Band gap transition

NiO is a direct wide band gap semiconductor having band gap of ~3.42 eV. ZnO is a II–VI group direct wide bandgap semiconductor having bandgap of ~3.37 eV and high excitonic binding energy (60 meV) at room temperature. The different phases of TiO_2 exhibit different nature of band gap transition. According to the experimental results and theoretical calculations, rutile TiO_2 exhibits both direct and indirect band gap [PASC1978, DAUD1997]. Kavan et al [KAVA1996] reported that rutile TiO_2 has a direct band gap of 3.0 eV, while Tang et al [TANG1994] determined an indirect band gap of 3.0 eV based on their experimental results. Most of the experimental studies [TANG1994, KAVA1996] suggested that anatase TiO_2 has an indirect band gap of 3.2 eV. Welte et al [WELT2008] reported indirect band gap of 3.19 and 3.25 eV for anatase TiO_2, respectively. The experimental studies on band gap energy of brookite TiO_2 suggested a band gap ranging between 3.1 and 3.4 eV [STEN2011, PAOL2013].

The band gaps of all the main polymorphs of TiO_2 are in UV region of light irrespective of the nature of optical transition. The optical absorption properties of TiO_2 can be manipulated by the defect engineering. The oxygen vacancy and Ti interstitial defect states give rise to localized states within the band gap of the TiO_2 materials [WEND2008, LIUX2013]. So, the light absorption is tuned from UV to visible light by introducing the native defects.

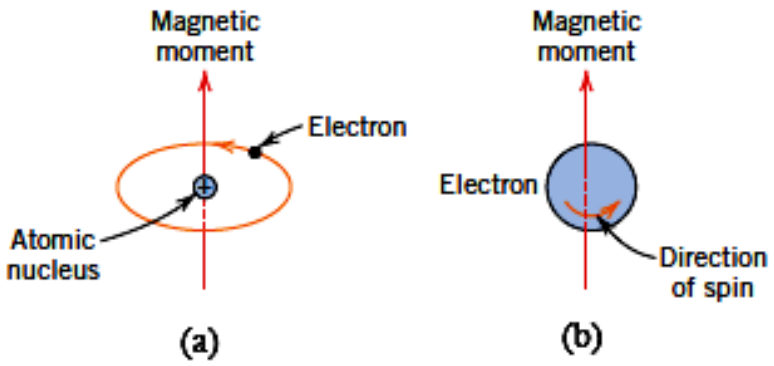

Figure 2.13: Schematic representation of the magnetic moment associated with (a) an orbiting electron and (b) a spinning electron.

2.5. Magnetic ordering

2.5.1 Origin of magnetism

The macroscopic magnetic properties of materials are the consequence of magnetic moments associated with individual electrons in an atom [OHAN2000, KITT2004]. Each electron in an atom has magnetic moment originating from two different sources: (a) One is orbital motion of electron around the nucleus, generating a small magnetic field and having magnetic moment along the axis of rotation [see Figure 2.13(a)] and (b) Other magnetic moment originates from the electron spin, which is directed along the spin axis either up or down depending on the mode of rotation [see Figure 2.12(b)]. This reveals that the each electron in an atom may be thought of as being a small magnet having permanent orbital and spin magnetic moments. Furthermore, in an atom, electrons are occupied according to the Pauli's Exclusion Principle and Hund's rule. The net magnetic moment for an atom is the sum of the magnetic moments of the each of constituting electrons, including both orbital and spin contributions and taking into the account of moment cancellation. For an atom having completely filled electron shells or subshells, when all electrons are considered, there is a total cancellation of both the moments. Thus, materials composed of atoms having completely filled electron shells are not capable of being permanently magnetized.

Based on number of unpaired electrons in an atom, their orientation in the orbitals and the spin-orbit interaction between the electron orbital angular momentum and spin angular momentum and their response in the external applied field, materials are classified into diamagnetic, paramagnetic, ferromagnetic, antiferromagnetic and ferrimagnetic [KRON2003].

2.5.2. Diamagnetism

Diamagnetism is a fundamental property of materials and it is a manifestation of Lenz law, i.e., if one applies a field to a system of moving charges, then their motions change in such a way that they create a magnetization that opposes the original applied field [OHAN2000]. Such effect is present in all the materials, but is often obscured by other types of magnetism. It generally occurs in materials having completely filled electronic configuration. The atoms and molecules of diamagnetic substances do not possess any net magnetic moments (i.e., all the orbital shells are filled and there is no unpaired electron). However, when exposed to a magnetic field, the electrons orient themselves such that they try to oppose the applied magnetic field and hence they register negative magnetization and negative susceptibility. Most of semiconductor material likes ZnO, SnO_2 etc. are diamagnetic in nature.

2.5.3. Paramagnetism

For some solid materials, each atom possesses a permanent dipole moment by virtue of incomplete cancellation of electron spin and/or orbital magnetic moments. The orientations of these atomic magnetic moments are random in the absence of an external magnetic field and result no net macroscopic magnetization. However, these atomic dipoles are free to rotate and paramagnetism (PM) occurs when they preferentially align, by rotation, with an external field [KITT2004]. Some of the atoms or ions in this class of materials have a net magnetic moment due to unpaired electrons in partially filled orbital. However, the individual magnetic moments do not interact electrons in magnetically. In the presence of an applied magnetic field, there is a partial alignment of atomic magnetic moments in the direction of the applied field, resulting in a net positive magnetization and hence positive susceptibility. Both diamagnetic and PM materials are generally considered to be non-magnetic because they exhibit magnetization only under the application of an external field. The tendency of alignment of magnetic moments along the field direction is opposed by the thermal energy, which tries to randomize the spin orientation. So they exhibit a temperature (T) dependent susceptibility, χ known as the Curie Law,

$$\chi = \frac{c}{T} \tag{2.04}$$

with a Curie constant C [BLUN2003]. In classical theory, each atomic moment is considered as magnetic dipole alignment in a particular direction with an angle θ with respect to applied field and average magnetic moment along the field direction, z is written as

$$< \mu^z > = \mu L(y) \tag{2.05}$$

Here, μ is the magnetic moment of each dipole and $L(y)$ is the Langevin function, $L(y)=\text{Coth}y-1/y$ and $y = \mu_B/(k_BT)$. This function explains the magnetization of small particles made up of atomic clusters. For low applied field or at high temperature, such that y is small, $L(y)$ tends to $y/3$. So

$$< \mu^z > = \frac{\mu y}{3} = \frac{\mu^2 B}{3k_B T} \tag{2.06}$$

or the magnetization

$$M = N < \mu^z > = \frac{N\mu^2 B}{3k_B T} \tag{2.07}$$

So, the susceptibility

$$\chi = \frac{M}{H} = \frac{\mu^2 N\mu_0}{3k_B T} = \frac{C}{T} \tag{2.08}$$

and the Curie law is obtained by the classical theory. According to quantum mechanical treatment and by considering the quantization of total angular momentum of each atom, the average magnetic moment per atom aligned along the magnetic field direction (i.e., z direction) of any PM sample can be written as [JILE1997, GUIM1998, BLUN2003].

$$< \mu_J{}^z > = g\mu_B J B_J(x) \tag{2.09}$$

Here g is Landgé g-factor and it depends on spin-orbit coupling of electrons in each atom. J is the total angular momentum quantum number. $\mu_B = 9.27\times10^{-24}$ J/T is Bohr magnetron. $B_J(x)$ is Brillouin function, which can be written as,

$$B_J(x) = \frac{1}{J}\left[\left(J+\frac{1}{2}\right) Coth\left(J+\frac{1}{2}\right)x - \frac{1}{2} Coth\frac{x}{2}\right] \tag{2.10}$$

Here, the variable $x = (g\mu_B B)/(k_B T)$, where k_B is the Boltzmann constant and T is the temperature. If N is the number of atoms per unit volume, the volume magnetization M can be written as,

$$M = N < \mu_J{}^z > = Ng\mu_B J B_J(x) \tag{2.11}$$

For the selection of magnetic field B and temperature T such that x is small, $B_J(x) \sim [J(J+1)/3]x$. Such assumption holds true for PM sample in a wide temperature region and for low applied field. So

$$< \mu^z > = Ng\mu_B J \frac{(J+1)}{3} x = \frac{Ng^2\mu_B^2 B}{3kT} J(J+1) \tag{2.12}$$

Or the susceptibility

$$\chi = \frac{\mu_0 Ng^2\mu_B^2}{3kT} J(J+1) \tag{2.13}$$

It is in the form of Curie law, C/T. Thus the magnetic susceptibility based on Brillouin function expression reduces to Curie-law. The examples of PM materials are W, Ce, Al, Li, Mg, etc. with typical χ value of 6.8×10^{-5}, 5.1×10^{-5}, 2.2×10^{-5},1.4×10^{-5},1.2×10^{-5} respectively in SI units [BLUN2003].

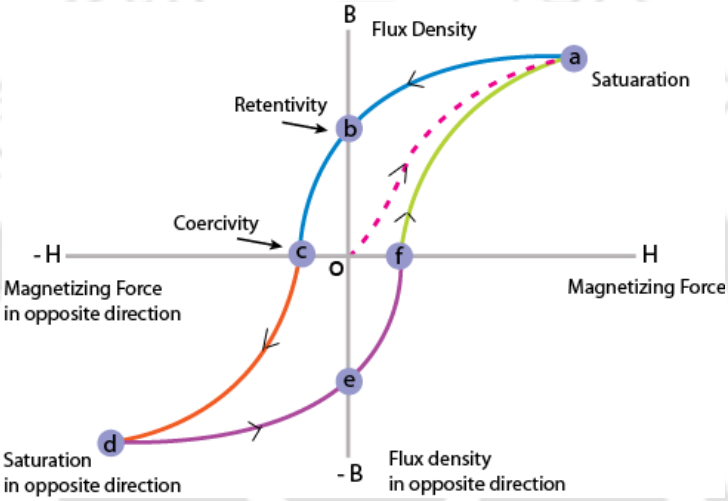

Figure 2.14: Magnetic hysteresis loop of a ferromagnetic material.

2.5.4. Ferromagnetism

Certain materials possess a permanent magnetic moment resulting from strong interaction between the magnetic moments even in the absence of an external field. This dominates over the thermal energy and reveals an alignment of magnetization in a particular direction. Such behaviors are displayed by the transition metals and some of the rare earth metals. In FM material, there are two distinct characteristics: (1) their spontaneous magnetization and (2) existence of magnetic ordering temperature. Spontaneous magnetization is the net magnetization that exists inside a uniformly magnetized microscopic volume even in the absence of external magnetic field. The magnitude of this magnetization at absolute temperature depends on the spin magnetic moments of electrons. The atomic moments in FM materials align either a parallel or an antiparallel arrangements showing very strong interactions, which are produced by electronic exchange forces. As a result, a large net magnetization even after removing the external applied magnetic field exists in FM materials.

All FM materials exhibit magnetic hysteresis loop (*M-H* loop) under the application of magnetic field as displayed in Figure 2.14. By studying its hysteresis loop we can get information about the magnetic properties of a FM material. The loop is generated by measuring the magnetic flux of a FM material while the magnetizing field is changed continuously. FM materials in virgin states follow the dashed line (starting from the origin 'o') as applied field is increased and reach the point 'a' where almost all of the magnetic domains are aligned to field direction and an additional increase in the magnetizing field produces a very little or no increase in magnetic flux. The magnetization obtained at this point is called saturation magnetization (M_S). When the field is reduced to zero, the curve moves from point 'a' to 'b'. At this point, some magnetic flux remains in the material even at zero magnetic field. This is called as retentivity and indicates the remanence or level of residual magnetism in the material. As the magnetic field is reversed, the curve moves to point 'c', where the magnetization reaches to zero. This point is called as coercivity (H_C) or coercive force. On further increasing the field in the negative direction, materials become magnetically saturated but in the opposite direction (point 'd'). Reducing the field to zero brings the curve to point 'e'. At this point, the level of residual magnetism is almost equal to that achieved in the other direction (point 'b'). Increasing the field back in the positive direction returns the magnetization to zero. Subsequently, the curve takes a different path from point 'f' back to the saturation point (point 'a'), where it completes the loop. From the *M-H* loop, the following magnetic parameters can be determined: (i) Retentivity: the material's ability to retain a certain amount of magnetization when the magnetizing field is removed after achieving saturation, (ii) Residual magnetism or Residual flux: The magnetic flux density that remains in a material when the magnetic field is zero. Note that residual magnetism and retentivity are the same when the material has been magnetized to the saturation point. However, the level of residual magnetism may be lower than the retentivity value if the magnetic field did not reach the saturation level, (iii) Coercivity: The magnitude of reverse magnetic field is required to make the magnetization to zero; (iv) Permeability: A property of a material that describes the ease with which a magnetic flux is established in the component. These hysteresis parameters are not solely intrinsic properties but are dependent on various parameters such as grain size, domain state, internal stresses and temperature. Since the hysteresis parameters are dependent on grain size, they are useful for magnetic grain sizing of natural samples. The elements Fe, Ni, and Co and their alloys are typical examples of FM materials. FM materials are mainly divided into two groups: (a) hard FM materials which exhibit very high H_C (> 1000 Oe). These materials are mainly used as permanent magnets and media for data storage and (b) soft FM

materials with low H_C (< 100 Oe) are used for transformer core, read head and magnetic sensor applications.

Another important parameter is the magnetic induction [$B = \mu_0 (H + M)$], where μ_0 is the permeability of free space], which is the total flux of magnetic field lines through a unit cross sectional area of the material. From the initial magnetization curve, the initial magnetic permeability μ_I (= B/H), for very small applied magnetic field and maximum permeability μ_{max} [=$(B/H)_{max}$] can be obtained. These parameters indicate the amount of induction generated by the material in a given magnetic field and are useful in characterizing magnetic materials. μ_I and H_C have a reciprocal relationship. So, materials exhibiting low H_C necessarily have a high μ_I. When increasing temperature, a transition from FM state to PM state occurs at a temperature called Curie temperature (T_C) that is due to thermal energy eventually overcomes the exchange energy and produces a randomizing effect leading to PM.

The phenomenon of FM can often be described by mean field or molecular field model. The molecular field model simply assumes that all the interactions from the neighboring magnetic species can be described in terms of an effective internal or molecular field B_m, which is proportional to the magnetization, i.e., $B_m = \lambda M$, where λ is the Weiss molecular field constant. So the total magnetic field experienced by each dipole is the sum of applied field B and the molecular field B_m. The expression for magnetization can be written by following eqn.(2.11) with the modification that

$$M = \frac{Ng^2\mu_B^2 J(J+1)}{3kT}(B_a + \lambda M) \qquad (2.14)$$

2.5.5. Antiferromagnetism

In antiferromagnetic materials, the spins of electrons align in a regular pattern with neighboring spins pointing in opposite directions, below a certain temperature called Néel temperature. Above the Néel temperature, the material is typically PM. The magnetic susceptibility of AFM material will appear to go through a maximum as the temperature is lowered. The AFM ordering is possible based on different type of magnetic unit cell structure as shown in Figure 2.15 except for *B* type, which is a FM one. In *A* type structure, the magnetic ions are coupled ferromagnetically in each (001) plane but with alternate planes aligned in opposite spin orientation such that it they exhibit net AFM interaction. *B* type structure is a FM one with all six nearest neighbor magnetic ions coupled ferromagnetically. In *C* type structure, the atoms in (101) and (110) planes are ferromagnetically aligned. Each atom has two ferro and four AFM nearest neighbors such that there is net AFM unit cell.

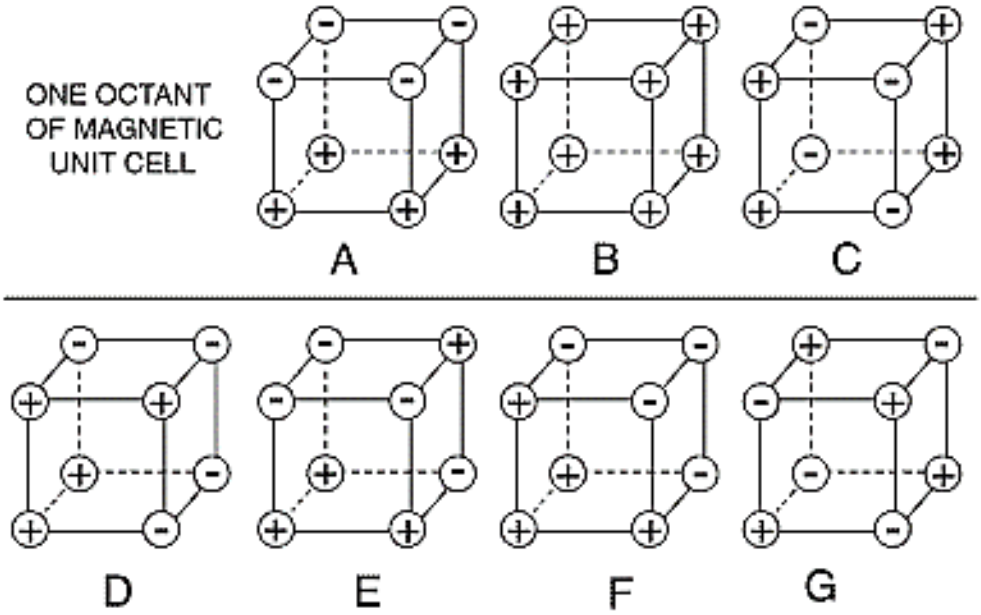

Figure 2.15: Different type of antiferromagnetic arrangement in a unit cell.

In *G* type structure, each ion is coupled antiferromagnetically to all its six nearest neighbors. Hence the atoms of positive and negative number of FM and AFM bonds are shown in Figure 2.15. Some of the materials follow a structure which is a result of coupling of two types of magnetic structures. One such example is *CE* type, where there is coherent stacking of octants of *C* and *E* type structures. The examples of AFM materials are MnF_2, MnO, CoO, FeO, Cr_2O_3, α-Fe_2O_3 with Néel temperature of 67 K, 116 K, 292 K, 116 K, 307 K, and 950 K with θ_C of -80 K, -510 K, -330 K, -610 K, -485 K, -2000 K respectively [BLUN2003].

2.6. Intrinsic properties of magnetic materials

Intrinsic properties of FM materials are M_S, T_C and magnetocrystalline anisotropy (MCA). These properties describe the equilibrium properties of the material on the atomic scale.

2.6.1. Exchange Interaction

Weiss (1907) reported that in addition to any externally applied field *H*, there is an internal molecular field or exchange field in a FM proportional to its magnetization.

$$\overrightarrow{B_E} = \lambda \vec{M} \qquad (2.15)$$

where, λ is a constant independent of temperature. According to eqn.(2.15), each spin sees the average magnetization of all the other spins. This molecular field is not really a magnetic field

and therefore does not enter into the Maxwell equations. For example, there is no current density $\vec{j}$ related to $\overrightarrow{B_E}$ by $\vec{\nabla} \times \vec{H} = 4\pi\vec{j}/c$. The magnitude of the molecular field may be as high as 1000 Tesla. Now the question is what is the origin of such huge internal molecular field? For instance, the magnetic field at distance *r* due to a magnetic dipole of dipole moment *m* is [KITT2004],

$$\overrightarrow{B_{dip}} = \left(\frac{\mu_0 M}{4\pi r^3}\right)[2cos\theta\overrightarrow{e_r} + sin\theta\overrightarrow{e_\theta}] \tag{2.16}$$

The order of magnitude of B_{dip} (= $\mu_0 H_{dip}$) is $\mu_0 M/4\pi r^3$ and taking m = 1 μ_B and r = 0.1 nm provides $B_{dip} \approx$ 1 Tesla or 10 kG only. This reveals that the huge molecular field is not due to the magnetic dipole interaction. This lingered as a mystery until Heisenberg introduced the concept of exchange interaction in 1928 [HEIS1928]. The origin of the Heisenberg exchange interaction is electrostatic, but the explanation involves quantum mechanics. The charge distribution of a system of two spins depends on whether the spins are parallel or antiparallel. Pauli's exclusion principle dismisses that no two identical electrons occupy the same quantum state simultaneously. However, it does not exclude two electrons of opposite spin. Therefore, the electrostatic energy of a system depends on the relative orientation of the spins: the difference in energy defines the exchange energy. The energy of interaction between the atoms *i* and *j* bearing electron spins S_i and S_j is defined from the Heisenberg model as [OHAN2000],

$$E_{exch} = -2\sum_{i<j} J_{ij} S_i . S_j \tag{2.17}$$

where, J_{ij} is the exchange integral and is related to the overlap of the charge distribution of the atoms *i* and *j*. Assuming that the exchange interaction is the same for each nearest-neighbor pair, eqn.(2.17) turns out to be

$$E_{exch} = -2J\sum_{i<j}^{nn} S_i . S_j \tag{2.18}$$

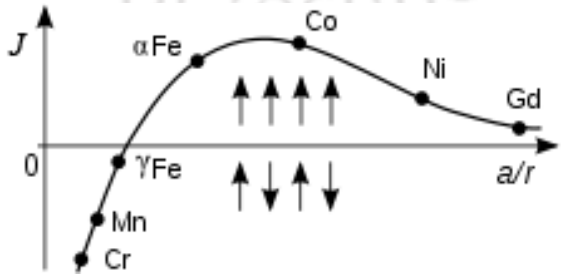

Figure 2.16: Bethe-slater curve: Elements above (below) the horizontal axis are ferromagnetic (antiferromagnetic).

For parallel orientation of the magnetization (ferromagnet), J should be positive and for antiparallel alignment of spins, J should be negative. The variation of J with respect to inter-atomic distance is shown in Figure 2.16. This curve is also known as the Bethe-Slater curve. It is clear from the Figure 2.16 that the value of J and hence the short-range exchange interaction depends strongly on the inter-atomic distance. The eqn.(2.18) can further be simplified by considering the energy of a particular atom i interacting with its j nearest neighbor:

$$E_{exch}^{i} = -2JS_i \sum_j S_j \tag{2.19}$$

while for the entire material,

$$E_{exch} = -\frac{1}{2}\sum_j E_{exch}^{i} \tag{2.20}$$

Thus, the discrete, pairwise interaction can be replaced by assuming that the magnetic moment $\mu_m^i = g\mu_B S_i$ at site i interact with a molecular field. H_{eff} given by the net effect of the z nearest neighbor spins:

$$E_{exch}^{i} = -\mu_0 \mu_m^i H_{eff} = -g\mu_0\mu_B S_i H_{eff} \tag{2.21}$$

where, g is the landé g-factor, μ_B is Bohr magneton and μ_0 is the permeability of the free space (= $4\pi\times10^{-7}$ H/m or 1.256×10^{-6} H/m). Comparing eqn.(2.21) with eqn.(2.19) provides the effective field as,

$$H_{eff} = \frac{2J}{g\mu_0\mu_B}\sum_j S_j \cong \frac{2zJ}{g\mu_0\mu_B}\langle S_j\rangle \tag{2.22}$$

Here, the sum over z neighboring spins has been replaced by z times the average spin value $\langle Sj\rangle$. Using $M = N_v g\mu_B\langle S_j\rangle$, eqn.(2.22) gives,

$$H_{eff} \cong \frac{2zJ}{N_v g^2 {\mu_B}^2 \mu_0} M \tag{2.23}$$

From eqn.(2.23), it can be seen that H_{eff} is the Weiss molecular field defined as $H_{mol} = \lambda$M, provided

$$\lambda = \frac{2zJ}{N_v g^2 {\mu_B}^2 \mu_0} \tag{2.24}$$

Using the value of molecular field coefficient λ as 10^3, J is calculated to be 2×10^{-21} J or 0.01 eV/atom. Exchange interactions are weaker than the Coulomb interactions that distinguish

levels of different principal and orbital quantum numbers, but stronger than spin-orbit interaction. Following the treatment of Weiss molecular field that $T_C = \lambda C$ with $C = N_v {\mu_m}^2 \mu_0 / 3k_B$, the expression for T_C can be obtained from eqn.(2.24) as

$$T_C = \frac{2zJ{\mu_m}^2}{g^2{\mu_B}^2 3k_B} = \frac{2zJs(s+1)}{3k_B} \tag{2.25}$$

where, $\mu_m = \sqrt{g\mu_B s(s+1)}$. Another important relation between exchange energy and the magnetization is defined as,

$$\frac{E_{exch}^{ij}}{V} = \frac{s^2 a^2 J N_v'}{2}\left(\frac{\nabla M}{M}\right)^2 = A\left(\frac{\nabla M}{M}\right)^2 \tag{2.26}$$

where, a is the distance between the spins, A is called the exchange stiffness constant having 1-2×10^{-11} J/m for most ferromagnets, and N_v' is number of nearest neighbor atoms per unit volume. Therefore, it is clear from the above equations that the exchange energy or the Heisenberg exchange interaction depends strongly on temperature due to the dependence of interatomic distance on temperature. In particular, the disorder FM system is the subject of low T_C due to the low value of J.

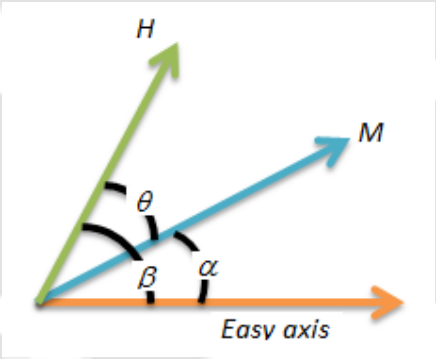

Figure 2.17: Schematic diagram of magnetization, applied field, and easy axis for a given material.

2.7. Anisotropy

When a physical property of any materials depends on the direction that property is said to exhibit anisotropy. In magnetism, the preference of magnetization to lie in a particular direction of sample is called magnetic anisotropy. As anisotropy plays an important role in tuning the nature of *M-H* loop, it is much essential to understand the various possible sources of the magnetic anisotropy and its influence on the control of the magnetic properties. Figure 2.17 displays a typical situation where for zero applied field, the magnetization would point along the easy axis shown (α = 0). When a field is applied, the magnetization is pulled towards the

field direction and approaches closer to the field direction with increasing the applied field. For any intermediate values of α, the magnetization is being attracted in opposite directions, i.e., up by the field and down by the anisotropy.

Let us assume that all the magnetization is pointing in the same direction in a magnetic material and the material exhibits an easy axis of magnetization. In such scenario, we can describe the energy per unit volume of the magnetization of this material by

$$E = K\,sin^2\alpha \tag{2.27}$$

where, K is called anisotropy constant with an unit of energy per unit volume (J/m^3). Hence, the energy term, E, is also energy per unit volume. In general, the magnitude of uniaxial anisotropy is described in terms of the anisotropy field, which is defined as the field needed to saturate the magnetization of a uniaxial crystal in the hard axis direction, as given in eqn.(2.28)

$$H_k = \frac{2K}{\mu_0 M} \tag{2.28}$$

In general, the energy of the magnetization is given by,

$$E = K\,sin^2\alpha - \mu_0 MH\,cos(\beta - \alpha) \tag{2.29}$$

where, the first term is anisotropy energy. The second term is due to the magnetic field and the difference in the angle (β - α) is the angle between H and M. In order to get equilibrium, we required first derivative to be zero. Therefore, taking derivative of eqn.(2.29) with respect to the angle results,

$$\frac{dE}{d\alpha} = 2K \sin\alpha \cos\alpha - \mu_0 MH\,sin(\beta - \alpha) = 0 \tag{2.30}$$

Taking the value of β as 90° for the equilibrium angle for the magnetization relative to the easy axis and considering the eqn.(2.28) gives

$$\sin\alpha = \frac{H}{H_k} \tag{2.31}$$

2.7.1. Magnetocrystalline anisotropy

Figure 2.18 shows initial magnetization curves of single crystals of different 3*d* FM elements. It could be clearly seen that the magnetization approaches to saturation in different ways when magnetized in different directions. Iron displays [100] as easy direction and [111] as hard direction, while nickel exhibits [111] as easy axis and [100] as hard directions. This behavior can be understood by analyzing the development of anisotropy energy in different symmetries as given below

For hexagonal:

$$E_a = K_1 \sin^2\theta + K_2 \sin^4\theta + K_3 \sin^6\theta + K_3' \sin^6\theta \sin 6\phi \quad (2.32)$$

For tetragonal:

$$E_a = K_1 \sin^2\theta + K_2 \sin^4\theta + K_2' \sin^4\theta \cos 4\phi + K_3 \sin^6\theta + K_3' \sin^6\theta \sin 6\phi \quad (2.33)$$

For cubic:

$$E_a = K_{1c}(\alpha_1^2\alpha_2^2 + \alpha_2^2\alpha_3^2 + \alpha_3^2\alpha_1^2) + K_{2c}(\alpha_1^2\alpha_2^2\alpha_3^2) \quad (2.34)$$

where, α_i are the direction cosines of the magnetization. K_{1c} term is equivalent to $K_{1c}(\sin^2\theta\, cos^2\phi \sin^2\phi + \cos^2\theta \sin^2\theta)$. When, $\theta = 0$, $\phi = 0$, this term reduces to eqn.(2.27) [COEY2010].

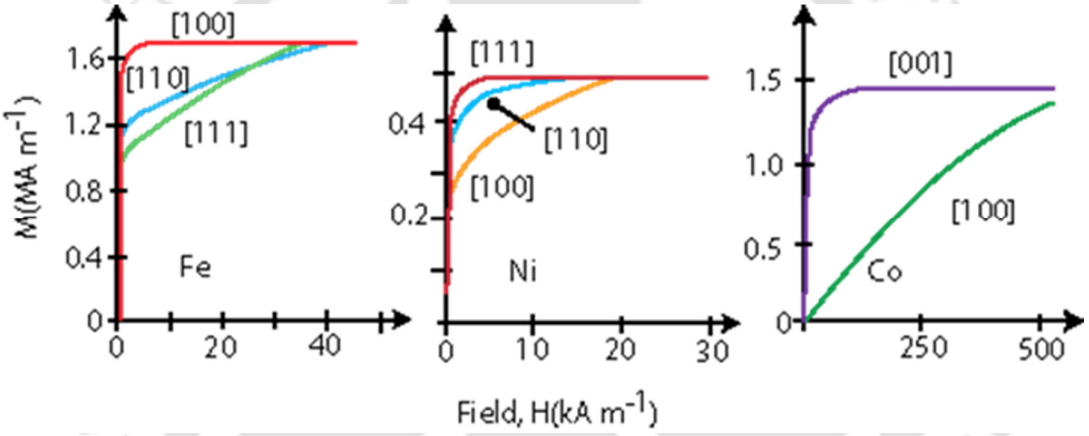

Figure 2.18: Magnetization of single crystals of Iron, Nickel and Cobalt.

Figure 2.19: Schematic drawing of broadside and head-to-tail configurations for a pair of ferromagnetically coupled magnetic moments.

2.7.1.1. Origin of magnetocrystalline anisotropy

There are two distinct sources of magnetocrystalline anisotropy: (i) single-ion contributions and (ii) two-ion contributions. The first one is essentially due to the electrostatic interaction of the orbitals containing the magnetic electrons with the potential created at the atomic site by the rest of the crystal. This crystal field interaction stabilizes a particular orbital and by spin-orbit interaction, the magnetic moment is aligned in a particular crystallographic direction. For

example, a uniaxial crystal having 2×10^{28} ions/m^3 described by a spin Hamiltonian DS^2 with D/k_B = 1 K and S = 2 will have anisotropy constant $K_1 = nDS^2 = 1.1\times10^6$ J/m^3. On the other hand, the later contribution replicates the anisotropy of the dipole-dipole interaction. Considering the broadside and head-to-tail configurations of two dipoles each with moment m, as shown in Figure 2.19, the energy of the head-to-tail configuration is lower by $3\mu_0 m^2/(4\pi r^3)$ and hence the magnets tend to align head-to-tail. In non-cubic lattices, the dipole interaction is an appreciable source of FM anisotropy. The samples are new kinds of materials that are very important to notice to that the NiO, TiO_2 and ZnO with the potential created at the atomic site by the rest of the crystal. This crystal field interaction stabilizes a particular orbital and by spin-orbit interaction, the magnetic moment is aligned in a particular crystallographic direction.

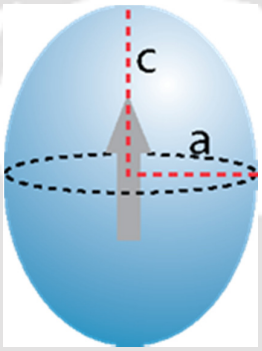

Figure 2.20: Magnetization of a prolate ellipsoid of revolution with $c > a$ and no magnetocrystalline anisotropy. c-axis is the easy direction of magnetization.

2.7.2. Shape anisotropy

Shape anisotropy arising due to the asymmetric shape of the material is important for thin films where one dimension is very short as compared to other dimensions. The demagnetization field inside the material or the stray field outside the magnetic material depends on the magnetization and shape of the material [JILE1997, OHAN2000, BLUN2003]. The magnetostatic energy of a ferromagnetic ellipsoid as shown in Figure 2.20 with magnetization M_S is given as

$$E_m = \frac{1}{2}\mu_0 VNM_S^2 \qquad (2.35)$$

The anisotropy energy is related to the difference in energy ΔE when the ellipsoid is magnetized along its hard and easy directions. N is the demagnetization factor tensor for the easy direction. N'=(1/2)(1-N) is the demagnetization factor tensor for the hard directions. Hence,

$$\Delta E_m = \frac{1}{2}\mu_0 V M_S^2 \left[\frac{1}{2}(1-N) - N\right]$$

$$\Delta E_m = \frac{1}{4}\mu_0 V M_S^2 [1-3N]$$

$$K_{sh} = \frac{1}{4}\mu_0 M_S^2 [1-3N] \tag{2.36}$$

In addition, the demagnetization factor tensor that relates the demagnetization field with a specimen magnetization as a function of position is given by [NEAL1994],

$$N(r) = -\frac{1}{4\pi}\iiint d^3r'\nabla'\left(\nabla'\left(\frac{1}{r-r'}\right)\right) \tag{2.37}$$

Table 2.03: Demagnetization factors (in Gaussian units) of selected shapes.

Shape	N_1	N_2	N_3
Sphere	4π/3	4π/3	4π/3
Long Cylinder along z-axis	2π	2π	0
Infinite plate normal to *z*-axis	0	0	4π
Strip film normal to *z*-axis (with t – thickness, W – Width, L – Length; $t \le W \le L$)	0	$8t/W$	4π

This tensor is given by an integral over the object volume and can be evaluated either inside or exterior to the body. The value of tensor N significantly depends on the specimen shape, which is difficult to obtain in closed-form. It may be calculated exactly for an ellipsoidal shape only. In many symmetrical materials such as any ellipsoids of revolution, the demagnetization factor tensor only has three principal components, i.e.,

$$\begin{pmatrix} H_1 \\ H_2 \\ H_3 \end{pmatrix} = -\begin{pmatrix} N_1 & 0 & 0 \\ 0 & N_2 & 0 \\ 0 & 0 & N_3 \end{pmatrix}\begin{pmatrix} M_1 \\ M_2 \\ M_3 \end{pmatrix} \tag{2.38}$$

where, $N_1 + N_2 + N_3 = 1$ (in SI) and $N_1 + N_2 + N_3 = 4\pi$ (Gaussian). The demagnetization factors for the selected shapes are summarized in Table 2.03. A detailed calculation of demagnetization factor for various objects can be found in [NEAL1994]. The shape anisotropy is zero for a sphere, as $N = 1/3$. Shape anisotropy is fully effective in samples which are so small that they do not break up into domains [COEY2010].

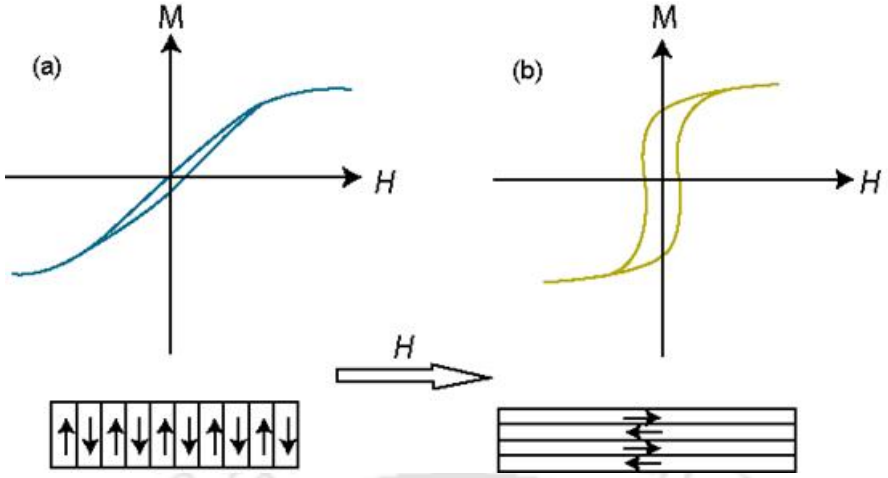

Figure 2.21: Magnetization of a thin film with induced anisotropy created by annealing in a magnetic field. The sheared (a) and open (b) loops are observed when the measuring field *H* is applied perpendicular and parallel to the annealing field direction, respectively.

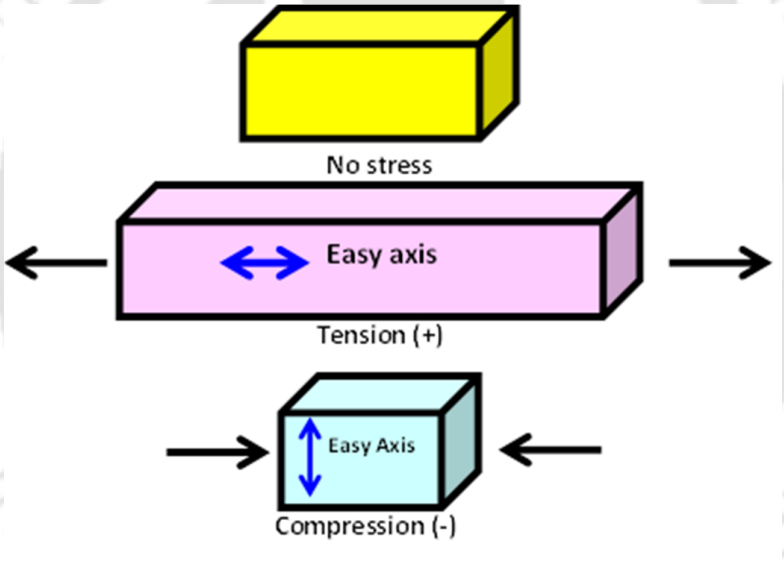

Figure 2.22: Schematic drawing of bars to demonstrate inducing an easy-axis in a material with the positive magnetostriction.

2.7.3. Induced anisotropy

In some materials, the magnetic anisotropy can be induced by many ways: (i) fabricate a nanoparticles in the presence of a magnetic field, (ii) heat treat the materials in the presence of external applied magnetic field and (iii) apply uniaxial stress. In the first two cases, after such treatment, the material may exhibit an easy axis of magnetization that points in the direction of the magnetic field. This induced anisotropy is certainly independent of any crystalline anisotropy or any other form of anisotropy that might be present. Figure 2.21 shows the typical

example of inducing the anisotropy in FM materials by field annealing. In the last case, the uniaxial anisotropy is induced by applying uniaxial stress (σ) in a ferromagnetic solid [KRON2003]. The magnitude of the stress-induced anisotropy is

$$K_{u\sigma} = \frac{3}{2}\sigma\lambda_S \tag{2.39}$$

where, λ_S is the saturation magnetostriction. Both the single-ion and two-ion anisotropy contribute to the stress induced anisotropy. The highest values of uniaxial anisotropy are found in hexagonal and other uniaxial crystals. Smallest values are found in cubic alloys and amorphous ferromagnets.

2.7.4. Magnetostrictive anisotropy

Another important form of anisotropy in magnetic materials is due to magnetostriction, a change of volume of an isotropic crystal due to magnetic order. Magnetostriction relates the stress in a magnetic material to an anisotropy created by that stress. Figure 2.22 shows schematic views of bars with different applied stress conditions. If λ is positive, then application of a tensile stress to the bar creates an easy axis in the direction of the applied stress. If a compressive stress is applied, then the direction of the easy axis created will be perpendicular to the stress direction. On the other hand, if the magnetostriction constant for the material is negative, then the above phenomena would be reversed: a tensile stress will create an easy axis perpendicular to the stress direction and a compressive stress will create an easy axis in the direction of the applied stress.

2.8. Surface effects

The nanoparticles have small size and hence large fraction of all the atoms in a nanoparticle are surface atoms [BATL2002]. Since the ratio of surface atoms to the bulk atoms is large, surface contribution to magnetization becomes significant. In general, the magnetic nanoparticles are considered to consist of single domain particles with uniaxial anisotropy. The orientation of its magnetic moment points either up or down in a zero field along the easy axis. However, the surface atoms experience different environments than those in the core of the particles. As discussed earlier, there are several types of defects that exist on the surface. These defects result in uncompensated disordered spins at the surface of the nanoparticle leading to surface magnetization (FM or AFM). The surface magnetization is contributed by the surface uncompensated spins, which depend on the size of the particle and on the degree of surface disorder [DOBR2005, HOCH2006]. Because of surface effects, FM could be a universal

feature of nanoparticles and their oxides, as reported by Sundaresan et al [SUND2006]. For example, nanoparticles of non-magnetic materials such as cerium oxide and aluminum oxide were found to display *M-H* loops at room temperature. Nanoparticles of metal nitrides, such as niobium nitride were also found to exhibit FM. Nanoparticles of some superconductors in the normal state were found to show FM. The smaller the nanoparticle, the larger is the FM. High field hysteresis and relaxation of the magnetization could result due to irreversible reorientations of the surface spins [KODA19991]. Nunes et al [NUNE1998] considered the structural relaxation of spinel ferrite nanoparticles using molecular dynamic modelling. They predicted non-uniform strains in the surface layers, with an average expansion of a few percent compared to bulk. They suggested that such an expansion might result in a stress-induced anisotropy field of up to 70 kOe, which could account for some of the anomalous magnetic behavior of ferrite nanoparticles. Kodama et al proposed that the canted spins in ferrite nanoparticles freeze into a spin glass-like phase at temperatures below 50 K [KODA1997, KODA19991, MORU2013]. Thus, the surface spins have multiple configurations for any orientation of the core magnetization. Nevertheless, several models such as two-sublattice model, multi-sublattice model [KODA1997] and core-shell model [TIWA2005, JAGO2009] have been proposed by considering different types of particle interactions [MENE2010] on the complexity of the magnetic properties of NiO nanoparticles and the observed results were explained on the basis of competition among core size effects, surface anisotropy and interface interaction. The nature of temperature dependence of coercivity of such particles is strongly dependent on the particle size and the nature varies from linear behavior to non-linear behavior with decreasing particle size. Proenca et al [PROE2011] shown that the effective magnetic anisotropy increases with decreasing particle size and the number of uncompensated spins per nanoparticles was found to be proportional to $n_s^{1/3}$ (n_s = total number of spins), indicating the random distribution on the nanoparticle surface. This leads to unidirectional anisotropy between ferromagnetically coupled uncompensated surface spins and AFM cores and provides additional pinning force resulting a shift of the hysteresis loop. Similarly, Duan et al [DUAN2012] reported that the larger saturation magnetization and coercivity in fine NiO nanoparticles is mainly resulting from the surface spins and explained using core-shell model. It is well understood that the changes in the physical properties can be directly related to their microscopic origin and theoretical studies are required to confirm the surface effects. Several magnetic effects could also result from the finite size effect of nanoparticles. These could include:

(i) Random oriented uncompensated surface spins.

(ii) Canted spins.

(iii) Spin glass like behavior of the surface spins.

(iv) Magnetically dead layer at the surface.

(v) Enhancement of the magnetic anisotropy which result for surface anisotropy.

However, surface effects can lead to a decrease or an increase in the magnetization of the nanoparticle. It was reported that magnetization of oxide nanoparticles decreases up to creation size for some oxide nanoparticle [KODA19992]. On the other hand, the magnetization of some metallic nanoparticles (cobalt) was reported to increase [RESP1998]. The reduction of magnetization of oxide nanoparticles was attributed to the existence of a magnetically dead layer on the particle's surface and the existence of canted spins or the existence of a spin glass-like behavior of the surface spins [KODA19992]. Several experimental studies reported an increase in the effective magnetic anisotropy due to surface effects [BODK1994, JAME2001, LUIS2002, JAME2004]. Computational studies also reported different anisotropy and magnetic moment at the surface of magnetic clusters embedded in matrices [XIEY2004]. Binns et al reported that both spin and orbital moments at the surface are different from those of the bulk counterparts using Synchrotron radiation [BINN2002]. These studies suggest that the total magnetization of the nanoparticle is composed of two components: a component due to the surface spins and a component due to the core of the particle. This led to the development of model of core-shell to describe interaction between the core and the shell. In nanoparticles of AFM or ferrimagnetic materials, this interaction occurs at the interface between the FM surface and AFM (or ferrimagnetic) core. In some FM nanoparticles, the surface of the metal usually oxidizes in air and forms an AFM metal-oxide shell around the FM metal core. Thus, there will be an interaction between the core and the shell, called exchange bias or exchange coupling, which provides an additional magnetic anisotropy to help aligning the FM spins in certain directions.

Core-shell exchange interaction and surface anisotropy were found to play significant roles in determining some magnetic properties of nanoparticles. The structural modifications at the boundaries of FM or ferrimagnetic nanoparticles, such as vacancies, broken bonds, may induce enough frustration, which leads to different canted magnetic structures [MAKO2009]. The canted surface spins may freeze giving rise to a glassy state at low temperatures. One of the important features characterizing the surface spin glass state in nanoparticles is the flattening of the field-cooled magnetization at low temperatures [LABA2005]. The main origin of spin glass-like behavior in nanoparticles could be due to strong inter-particle interactions or due to surface spin effects within individual particles.

2.9. Spin glass

The transition from disordered spin state to metastable frozen disorder state due to competing magnetic interactions undergoes a transition below certain temperature, called as spin glass temperature (T_{sg}) [HUAN1985, BIND1986, MYDO1993, GING1994, DIEP2004]. The frozen disordered state is known as spin glass. Here, each spin is under the competing magnetic interactions with the nearest spins or next nearest spins. Therefore, the spin cannot find a ground state by simultaneously minimizing their energy with each neighboring spins. Thus, they are frozen in a metastable random direction to minimize the total energy. Unlike the other phase transitions, where a system undergoes transition from disorder to order state, here, the system undergoes transition from one disordered state to another disordered state. Hence, the debate is where it is really a thermodynamic phase transition. More or less, it is agreed that spin glass is a phase transition because the high temperature magnetic disorder is due to random thermal fluctuations without any interaction between magnetic spins, while the low temperature disorder state is due to long range magnetic interaction of opposite signs. Conventional spin glass materials are CuMn, AgMn, AuFe [BIND1986, DIEP2004] and some oxide materials.

DC susceptibility data of conventional spin glass materials exhibit bifurcation between zero-field-cooled (ZFC) and field-cooled (FC) curves at T_{sg} [NAGA1979]. Similarly, some research groups have reported that NiO nanoparticles exhibit superparamagnetism [BODK2000, BAHL2006] or spin glass behavior [TIWA2005]. While Ghosh et al [GHOS2006] reported that T_{sg} increases from 10 to 15 K with increasing particle size of NiO from 3 to 7 nm, respectively, Winkler et al [WINK2008] showed much higher T_{sg} of 17 K for 3 nm particles. Spin glass transition was also reported in un-doped and TM doped DMS materials [TIWA2005, YIJB2007, GRUY2009]. Nagata et al [NAGA1980] found a spin glass behavior on (Hg,Mn)Te based DMS material below 11 K. Similarly, Chen et al [CHEN1995] found that Fe doped HgSe, ZnSe, CdS and ZnS group II-VI based DMS materials exhibit typical spin glass behavior. The stability of the Sherrington-Kirkpatrick solution of a spin glass model [SHER1975, SHER1978] given by de Almeida et al [ALME1978] could be fitted using de Almeida-Thouless (AT) line described as

$$H_{AT}(T) \propto \left(1 - \frac{T_{peak}}{T_{sg}}\right)^{1.5} \tag{2.40}$$

2.10. Magnetic interaction

2.10.1. Direct exchange interaction

Two neighboring magnetic moments can interact with each other directly without the aid of any intermediate molecules or ions. This interaction is known as direct exchange. In reality, there is hardly seen any interesting magnetic phenomenon that could be explained based on the direct exchange. As there is insufficient overlapping of the participating magnetic dipoles, direct exchange is not an important mechanism in controlling the magnetic properties.

2.10.2. Magnetic dipole-dipole interaction

Magnetic dipole-dipole interaction [BLUN2003] or dipolar coupling refers to the direct interaction between two magnetic dipoles. The energy of the interaction is given as

$$H = -\frac{\mu_0}{4\pi r_{ij}^3}[3(\mu_i.\hat{r}_{ij})(\mu_j.\hat{r}_{ij}) - (\mu_i.\mu_j)] \qquad (2.41)$$

where $\hat{r}_{ij}$ is a unit vector parallel to the line joining the centers of the two dipoles, μ_i, μ_j are the moments of two dipoles separated by a distance $|r_{ij}|$. This interaction is important in the properties of those materials, which order at milli-Kelvin temperature. The magnetic dipolar interaction is too weak to account for the ordering of most of the magnetic materials. There is a built in anisotropy to the dipolar interaction which can orient the spins either parallel (FM) or antiparallel (AFM). If the spins are oriented along r_{ij}, they couple ferromagnetically. Otherwise, they couple antiferromagnetically.

2.10.3. RKKY Interaction

It is a special kind of indirect exchange commonly seen in metals having localized magnetic moments and the interaction is mediated via the itinerant electrons. The localized magnetic moment of an ion spin-polarizes the conduction electrons and this spin-polarized electrons couple to the neighboring localized magnetic moment at a distance r away. The Ruderman-Kittel-Kausya-Yosida (RKKY) model [RUDE1954, KASU1956, YOSI1957, BLUN2003] explains the magnetic interaction between the localized single magnetic ions and the delocalized conduction electrons band. The exchange interaction is thus indirect because it does not involve direct coupling between magnetic moments. The coupling takes the form of an r dependent exchange interaction $J_{ex}(r)$ given by

$$J_{ex}(r) = \frac{4\pi^2 m^* k_F^4}{r^2} F(2k_F r) \qquad (2.42)$$

m^* is effective mass, k_F is the Fermi wave vector of the electron gas. The oscillating function is given as $F(x) = (xcosx - sinx)/x^4$ and is plotted in Figure 2.23 as a function of x.

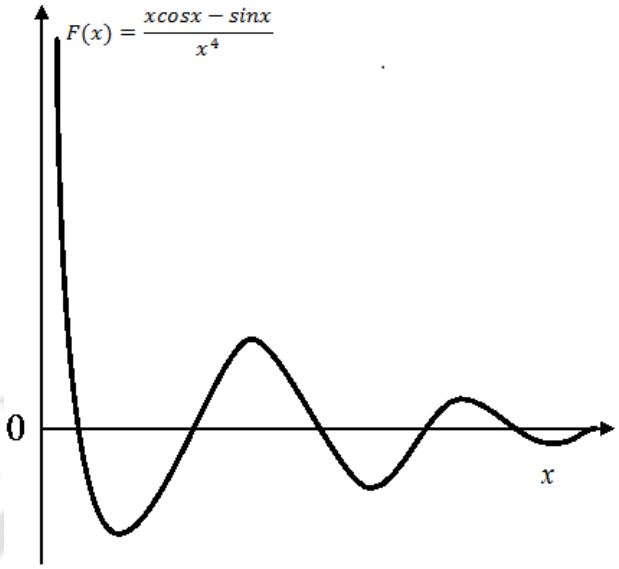

Figure 2.23: The Oscillatory part of RKKY interaction energy. $F(x)$ is proportional to the product of the Fermi wave vector and the distance from the localized moment.

It is a long range interaction with oscillatory dependence on the distance between the magnetic ions. Hence depending on the separation it may be either FM or AFM [VEGA2001]. RKKY interaction is also found to play a major role in many DMS materials when the solubility of carrier level is quite high [STOR1986, DIET1997, NADO2002]. The carrier concentration in such case is found to be quite high, i.e., on the order of 10^{19} cm^{-3} to 10^{21} cm^{-3} and it correspond to about 60 at% of carrier doping in Group IV-VI based DMS [STOR1986, NADO2002]. In DMS materials, doping of extra charge carrier along with magnetic ions gives rise to enhanced ferromagnetism [RISB2003, LIN2004, SLUI2005, THEO2006, LIX2007, GOPI2008]. (GaMn)As and (Ge,Mn) alloys exhibit FM due to exchange interaction between Mn atoms with distance larger than the average nearest Mn and Mn distance. In addition, the exchange interactions exhibit oscillatory character and are exponentially damped by disorder. However, isolated Mn impurities in the semiconductor host with same number of valence holes exhibit undamped RKKY type behavior [BOUZ2003, BERG2004, KUDR2004].

2.10.4. Super-exchange interaction

Kramer [KRAM1934], Anderson and his group [ANDE1955, ANDE1958], Goodenough [GOOD1995] and Kanamori [KANA1959] pointed out that FM and AFM interactions are

possible by a mechanism called super-exchange interactions. Here, two magnetic ions interact through an intermediate non-magnetic ion. This is a common interaction in insulating magnetic oxides, where the intermediate ion is O^{2-}.

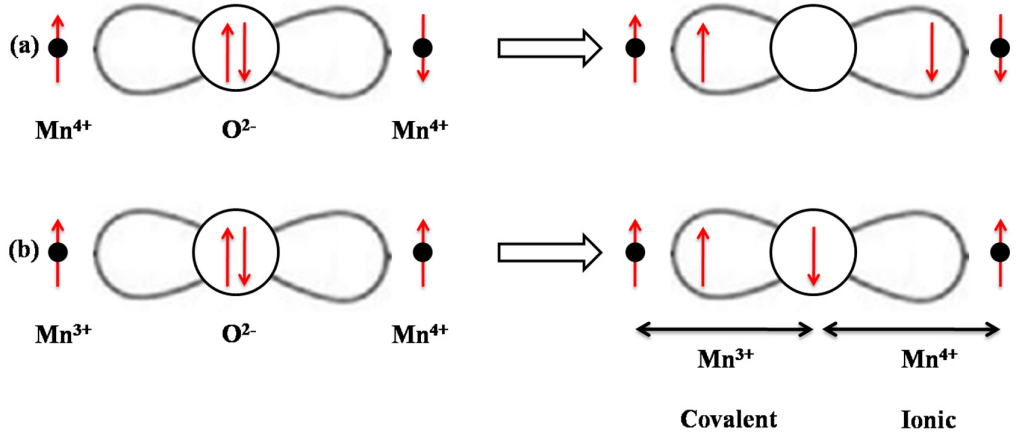

Figure 2.24: Arrangement of spins and orbitals in (a) an antiferromagnetic super-exchange interaction, and (b) a ferromagnetic super-exchange interaction.

A schematic representation of super-exchange interaction producing AFM and FM is shown in Figure 2.23 (a) and (b), respectively. Figure 2.23 (a) shows the situation where the 3*d* orbitals are pointing towards the O-2*p* orbital. The overlapping between the 3*d* and *p* orbitals facilitates the simultaneous covalent bond formation between the cations (Mn^{4+}) and anions (O^{2-}) on both sides since the electrons of O^{2-} anion are shared with the 3*d* electrons. Here, out of two valence electrons of oxygen, the up spin electron spends some time with the cation in one side having up spin configuration and the down spin electron spends some time with other cation having down spin configuration to satisfy the Hund's rule. In this process, each cation-anion pair has FM (parallel) alignment of electrons and the net cation-cation interaction is AFM.

According to Goodenough [GOOD1995], the above covalent bonding is not permissible if the core spins of magnetic cations are aligned parallel as shown in Figure 2.23 (b). Under this situation, out of two valence electrons of O^{2-}, the spin up electron form covalent bonding with left side cation (Mn^{3+}) having spin up electron, while the spin down electron of oxygen forms ionic bond with right side cation (Mn^{4+}). The direct exchange between oxygen and the right side cation is AFM. So, overall FM interaction prevails between Mn^{3+} and Mn^{4+} ions. In many DMS materials, the super-exchange interaction comes into picture at large concentrations of TM-ion. The first principles study of the super-exchange interaction in (Ga, Mn)V, (V=N, P, As and Sb) by Chang et al [CHAN2007] reports that short-range super-exchange interaction

is found to be AFM in nature and is found to be quite strong in (Ga,Mn)N and weak in (Ga,Mn)As and (Ga,Mn)Sb. The significant super-exchange interaction at large TM concentrations plays an important role in reducing Curie temperature.

2.10.5. Anisotropic exchange interaction

Dzyaloshinskii [DZYA1958] postulated a contribution to the exchange interaction between two neighboring spins, which was later identified by Moriya [MORI1960] as spin-orbit coupling between the spins. The excited state of one of the participating ions is not connected with oxygen ion but is produced by the spin-orbit coupling in one of the magnetic ions. Hence, there is an interaction between the excited states of one ion with the ground state of other ion. This interaction is known anisotropic exchange interaction and is mathematically represented as

$$H_{DM} = D(S_1 \times S_2) \tag{2.43}$$

where S_1 and S_2 are two neighboring spins and D is Dzyaloshinskii-Moriya constant. The Dzyaloshinskii-Moriya interaction tries to align the vectors S_1 and S_2 at right angles in a plane perpendicular to the vector D. Its very effect is to cant the spins by a small angle. The Dzyaloshinskii-Moriya interaction is responsible for the observation of small ferromagnetic moment for antiferromagnetic samples.

Chapter 3

Experimental Methods

3.1. Introduction

In the course of present investigations, several experimental techniques were used for the preparation and characterization of the samples. This chapter provides a brief description of these experimental techniques.

3.1. Techniques used for sample preparation

Material processing in the present thesis were carried out in two steps viz., high-energy planetary ball milling of the pure metal-oxide powders followed by heat treatment of as-milled powders under different atmospheres and preparation of pure samples using sol-gel method with different molar concentrations and annealed at different temperatures. A brief discussion on both the techniques is given below.

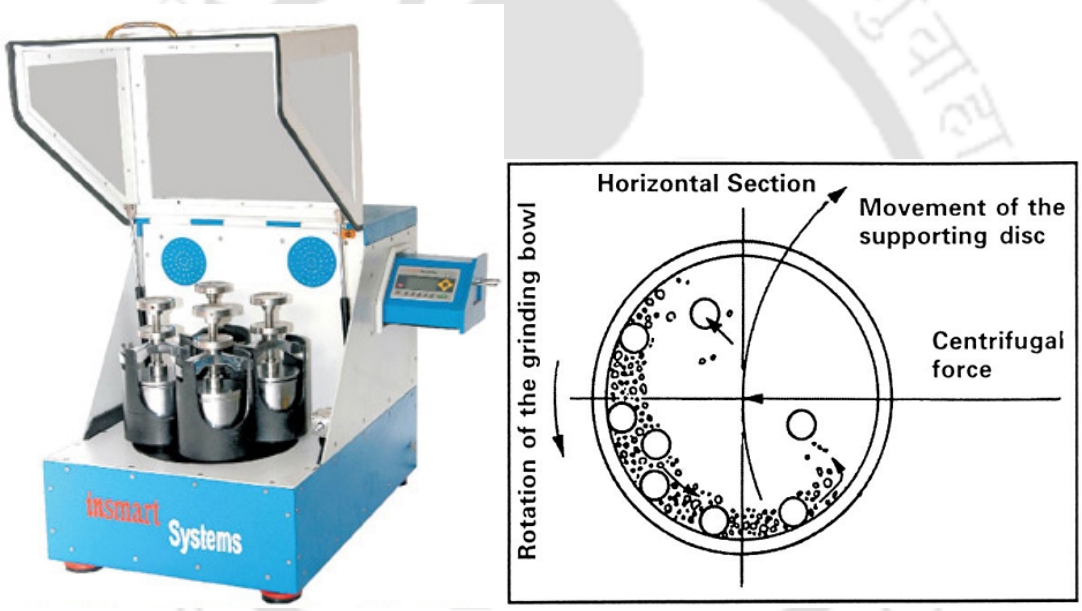

Figure 3.01: (left) Photographic view of the planetary ball mill used and (right) Schematic diagram of the horizontal section of a vial depicting the movement of the balls inside the vial due to its planet like movement.

3.1.1. Ball milling technique

Milling of pure oxide powders was carried out by high-energy ball milling in a planetary ball mill (Insmart, India) under dry milling conditions in an argon (Ar) gas atmosphere. The photographic view of the planetary ball comprising of a horizontal support disc on which vials are mounted and the schematic view of milling process are depicted in Figure 3.01. The vials mounted on the horizontal disc rotates in a direction opposite to that of the disc and thereby simulating a planetary like motion. This results in a large centrifugal force acting on the balls

kept inside the vial and causes the balls to collide with themselves and to the wall of the vial with high impact. When the metal-oxide powders are placed in the vial along with the balls, the powders are subjected to repeated cold welding and fracture at the surfaces of the balls and the vial. This process leads to disintegration of the powders, resulting first in refinement of crystallite size to produce nanocrystalline alloys along with large number of defects in the parent powders [SONI2001, SURY2001, KOCH2002, SURY2004]. Hence, crystallite size refinement is a natural consequence of a ball milling process. As the milling time progresses the alloy becomes amorphous. The refinement and alloying processes are determined by the milling parameters such as powder to ball weight ratio, ball size, rotation speed, milling time, etc. Nature of the milling vial and balls also plays an important role in the process along with the milling media.

In the present thesis work, dry milling of high purity oxide powders has been carried out under high purity Ar gas atmosphere. Hardened steel vial and hardened steel balls were used for milling of all the powders. After a careful and systematic investigations, the ball to powder weight ratio was fixed at 10:1 and the rotating speed was 500 rotations per minute for milling process. Prolonged milling under dry conditions results in a temperature rise inside the vial which usually deteriorates the final product. Thus, the milling process was programmed to pause for 15 minutes after every 15 minutes of continuous milling to avoid excessive heating. In addition, Ar gas was periodically filled inside the vial to avoid oxidation.

3.1.2. Sol-gel method

The sol-gel process is a wet-chemical technique that uses either a chemical solution (sol short for solution) or colloidal particles (sol for nanoscale particle) to produce an integrated network (gel). The method is used for the fabrication of metal-oxides, glass materials, etc [BAAB2015, MISH2017]. Nickel acetate tetrahydrate ($(CH_3COO)_2Ni.4H_2O$) received from Merck was dissolved first in doubly distilled deionized water with different molar concentrations of 0.1, 0.2, 0.3 and 0.5 under constant stirring for 2 hrs at moderate temperatures of 40 to 50 °C to obtain a light greenish sol. Subsequently, 2 to 3 ml of ethylene glycol (from Merck) was added slowly to the warm sol to obtain a greenish thick gel. A clear gel of 0.1 M, 0.2 M, 0.3 M and 0.5 M solution was achieved. The gel product was eventually dried at 120 °C for 12 hrs. As-made powders without annealing exhibit nickel hydroxide structure. The dried powders were subsequently subjected to air annealing at different temperatures (350 °C and 500 °C) for 3 hrs to produce fine NiO powders.

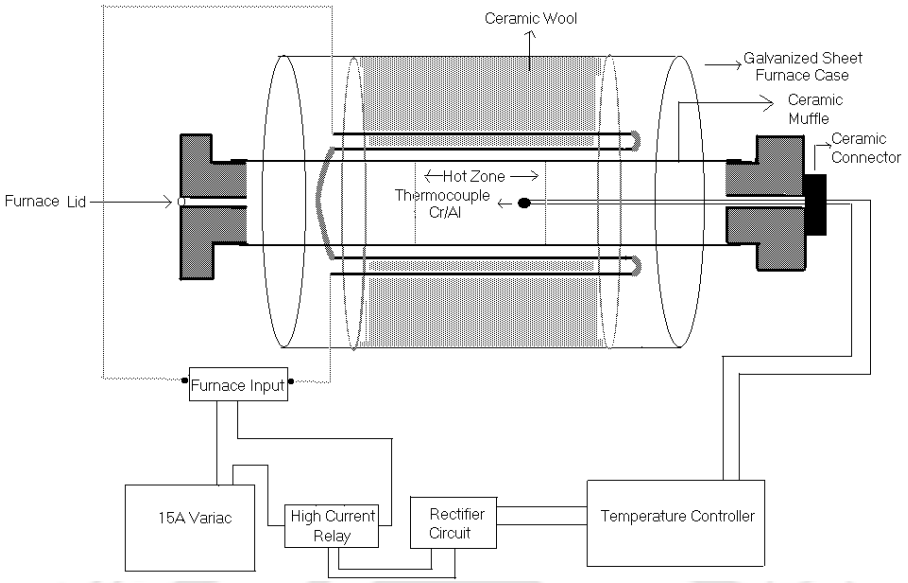

Figure 3.02: Block diagram of the high temperature furnace.

3.1.3. Heat treatment at elevated temperatures

In order to optimize nanocrystalline microstructure and to release defects (strain) created during the milling process, the selected as-milled powders were undergone heat treatment at elevated temperatures (annealing) in an air atmosphere using a resistive tubular furnace (Okay, India). The block diagram of the high temperature furnace is shown in Figure 3.02. This tubular furnace could be used up to a temperature of 1600 °C. The temperature of the constant temperature heat zone at the center of the furnace extends to 150 mm. The annealing temperature was controlled to ± 2 °C using a commercial temperature controller. The annealing temperature and annealing time were optimized based on the development of nanocrystalline microstructure, release of defects (strain) and magnetic properties of the nanocrystalline powders.

3.2. Structural characterization

3.2.1. X-ray diffraction

Powder X-ray diffraction (XRD) is the most widely used non-destructive technique for general crystalline material characterizations. Two different powder X-ray diffractometers viz. Seifert 3003 T/T and high-power (18 kW) Rigaku TTRAX III were used in the thesis work depending upon the availability. Cu-K_α X-ray radiation with a wavelength of 1.54056 Å was used in all the cases. Figure 3.03 displays the typical photographic view of the Rigaku high-power (18 kW) TTRAX III X-ray diffractometer and Bragg-Brentano geometry of powder X-ray

diffractometer. The theta-theta (θ–θ) goniometer was used in the reflection (Bragg-Brentano) geometry [CULL2001].

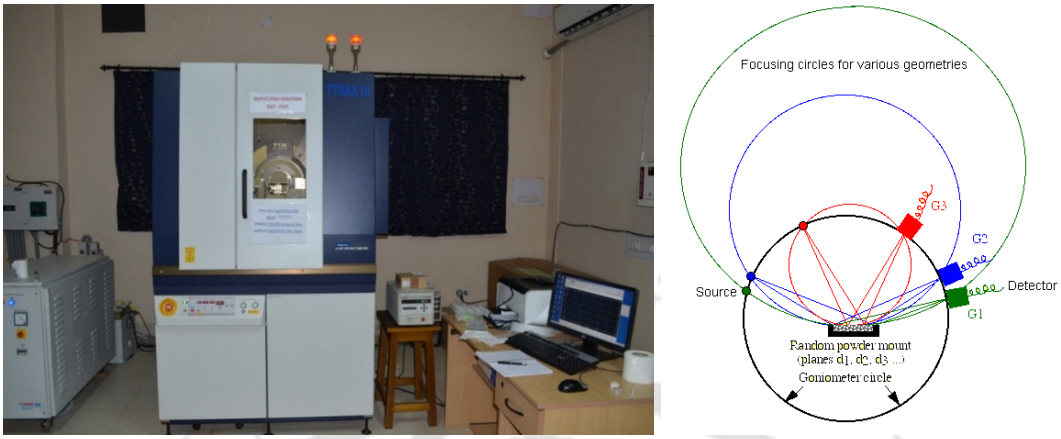

Figure 3.03: (left) Photographic view of Rigaku TTRAX III 18 kW X-ray diffractometer and (right) Bragg-Brentano diffraction geometry of a powder X-ray diffractometer.

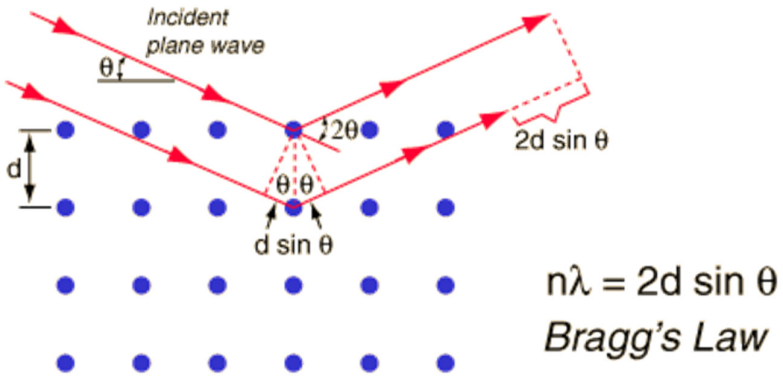

Figure 3.04: Diffraction of X-ray by a crystal.

XRD technique allows identification of various crystalline phases present in the material and provides other structural information such as the size of the crystallites, strain present inside the crystallites, lattice constant, etc. It is well-known that an ideal crystal has a periodic arrangement of atoms as shown in Figure 3.04. Diffraction of X-ray occurs through constructive interference of X-ray scattered from atoms of a set of parallel planes in crystal lattice at a particular angular positions of the incident wave known as Bragg angles [CULL2001]. This condition for obtaining constructive interference is known as Bragg's law given by the relation [CULL2001],

$$2d_{hkl}\sin\theta = n\lambda \qquad (3.01)$$

where, d_{hkl} is inter-planer spacing, θ is the angle of incidence of the X-ray beam with the atomic plane, λ is wavelength of the X-ray and n is order of diffraction (we consider only the first order

diffraction, n =1, because the second order peaks are mostly difficult to detect experimentally). A series of these angles can be used to determine the Miller indices (*hkl*) and the crystal structure can be identified from the systematic behavior of these indices. Figure 3.04 shows the diffraction of X-ray from crystal lattice planes illustrating Bragg's law. The structural parameters such as the average size of the crystallites, *d*-spacing, lattice constant and strain present inside the crystallites, etc. can be determined by a careful analysis of the XRD patterns using various models [CULL2001]. All measurements were carried out at an accelerated voltage of 50 kV and current of 200 mA. XRD data were collected at a slow scan rate of 0.005 °/s. The exact peak position and full width half maxima (FWHM) of the XRD peak is obtained using Gaussian fitting to the experimental data. The crystallite size and the strain present in the crystallites can be estimated from the width of the diffraction peaks. This is analogous to the diffraction of light from a grating where the line width is proportional to the number of diffracting grooves in the grating. The broadening $\Delta\theta_{size}$ due to crystallite size can be quantified by Scherrer's formula [CULL2001],

$$\Delta\theta_{size} = \frac{k\lambda}{D\cos\theta} \tag{3.02}$$

where $\Delta\theta_{\text{size}}$ size is broadening due to crystallite size and D is the average size of the crystals. Presence of strain also broadens the peak which can be quantified as [CULL2001],

$$\Delta\theta_{strain} = 4\eta\tan\theta \tag{3.03}$$

where $\Delta\theta_{\text{strain}}$ is broadening due to strain and η is the lattice strain. Williamson and Hall plot (WHP) method is used to estimate the effects of crystallite size and strain due to the broadening [WILL1953], which is the combination of both equations (3.02) and (3.03) for a set of Bragg peaks. This method is a linear representative of the total broadening effect expressed as

$$\Delta\theta = \frac{k\lambda}{D_{WHP}\cos\theta} + 4\eta\tan\theta \tag{3.04}$$

or

$$\Delta\theta\cos\theta = \frac{k\lambda}{D_{WHP}} + 4\eta\sin\theta \tag{3.05}$$

In case of elastically anisotropic materials, certain Bragg peaks are more affected by strain than other peaks. In such cases, the use of WHP method for the analysis of size and strain is questionable, as the data extracted from XRD do not fall into straight line. In order to consider the different strain contribution to different peaks, Modified Williamson-Hall Plot (MWHP)

method [UNGA1991, UNGA1992] can be used to analyze the diffraction peaks. According to this model, the individual contribution to the broadening of XRD peaks can be expressed as

$$(\Delta K)^2 = \left(\frac{0.9}{D}\right)^2 + \left(\frac{\pi b^2 \rho}{2B}\right) K^2 C_{hkl} \qquad (3.06)$$

where ΔK [$= (2\cos\theta\Delta\theta)/\lambda$], $\Delta\theta$ is full width at half maximum (FWHM) of the Bragg reflections (in radian) after correcting instrumental broadening, $K = 2\sin\theta/\lambda$, b is modulus of Burgers vector of dislocations, B is a constant (taken as 10 for a wide range of dislocation distributions [SHEN2005]), $C_{hkl} = C_{h00}\left(1 - qH^2\right)$ is dislocation contrast factor introduced to take care elastically anisotropic materials, where the residual strains affect some Bragg reflections more than the others, $H^2 = \left(h^2k^2 + k^2l^2 + l^2h^2\right)/\left(h^2 + k^2 + l^2\right)$ for a cubical system and q is a constant. In the MWHP formulation, Ungar et al [UNGA1991, UNGA1992] considered that dislocations/defect are the main contributors to the strain. The plots between $(\Delta K)^2$ and K^2C_{hkl} can be fitted using a straight line and the values of D and ρ could be calculated from intercept and slope of the fitted straight line, respectively. Note that the dislocation density is one of the major structural parameters [HULL2001] influencing the final nanocrystalline microstructure and correlated to the induced strain and reduced crystal size as

$$\eta = \frac{\rho D b}{2\sqrt{3}} \qquad (3.07)$$

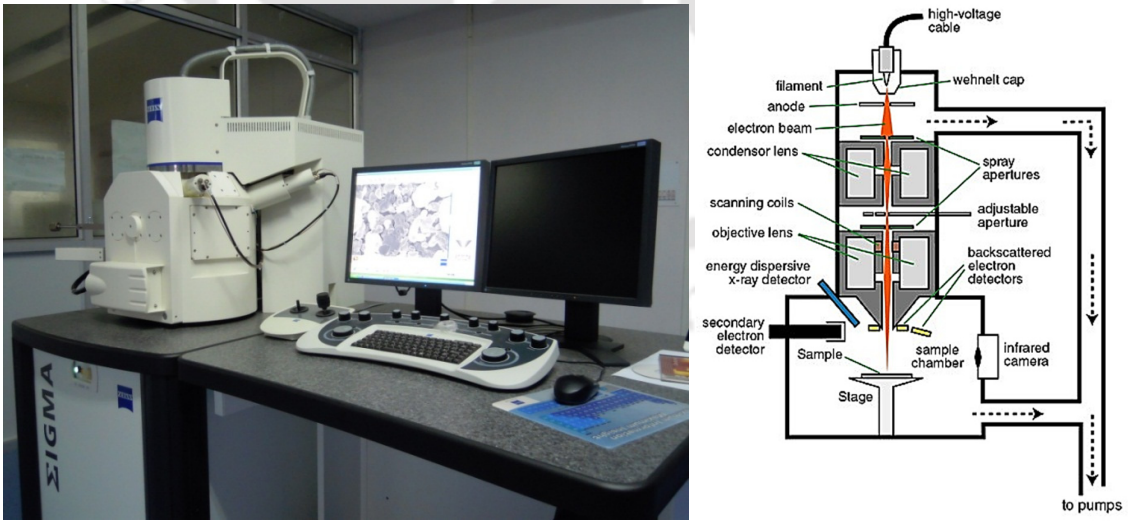

Figure 3.05: (left) Photographic view and (right) schematic view of field-emission scanning electron microscope.

3.3. Morphological and microstructural characterization

3.3.1. Scanning electron microscopy

Scanning electron microscope (SEM, Leo 1430VP) with energy dispersive spectroscopy (EDS) attachment (Oxford) and field emission scanning electron microscope (FE-SEM, Sigma Zeiss, Germany) were used to study the surface morphology and elemental compositions of the alloy powders. A photographic view of the FE-SEM used in the present study is shown in Figure 3.05. SEM is a microscopic technique that uses electrons to form an image of objects and to study surface morphology, fractured components, foreign particles and residues, polymers, electronic components, biological samples and countless others. The thermionically emitted electrons from a tungsten filament or field emission controlled electrons are drawn to an anode, focused by two successive condenser lenses into a beam with a narrow fine spot size (~ 50 Å). The shorter wavelength of electrons permits image magnifications of up to 100,000 times in SEM. Pair of scanning coils located at the objective lens deflects the beam either linearly or in raster fashion over a rectangular area of specimen surface.

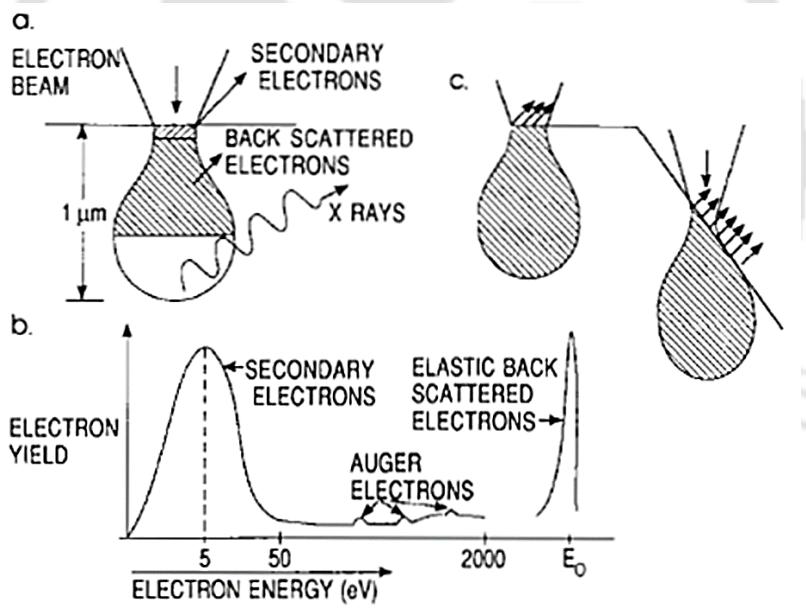

Figure 3.06: (a) Electron and photons signals emanating from tear-shaped interaction volume during electron beam impingement on specimen surface, (b) Energy spectrum of electrons emitted from the specimen surface and (c) Effect of surface topography on electron emission.

Figure 3.06 displays the interaction of electrons on the surface of the sample. Upon electron impingement on the surface, the interaction volume assumes a tear drop shape. These primary bombarding electrons on the surface of the specimen dislodge electrons called as

secondary electrons from the specimen. These dislodged secondary electrons are attracted and collected by a positively biased grid or detector, and then translated into a signal. These signals are then amplified, analyzed and translated into images of the topography being inspected. Finally, the image is shown on a cathode ray tube. The most common imaging mode relies on the detection of the very lowest portion of the emitted energy distribution. Their very lower energy means they are originated from a subsurface depth of no longer than several angstroms.

Apart from secondary electrons, the primary electron beam results in the emission of backscattered (or reflected) electrons (BSE) from the specimen. BSE possesses more energy than secondary electrons and have a definite direction. All emissions above 50 eV are considered to be backscattered electrons. It may be noted that the BSE imaging is useful in distinguishing one material from another, since the yield of the collected backscattered electrons increases monotonically with the specimen's atomic number Z ($\sim 0.05\ Z^{1/2}$). BSE imaging can distinguish elements with atomic number differences of at least 3, i.e., elements with atomic number differences of at least 3 would appear with good contrast on the image.

EDS analysis is quite useful in identifying materials and contaminants as well as estimating their relative concentrations on the surface of the specimen. During EDS analysis, the specimen is bombarded with an electron beam inside the SEM. The bombarding electrons colliding with the specimen knock off some of the electrons from the atoms. A position vacated by an ejected inner shell electron is eventually occupied by a higher-energy electron from an outer shell. To be able to do so, however, the transferring outer electron must give up some of its energy by emitting X-ray. The amount of energy released by the transferring electron depends on which shell it is transferring from, as well as which shell it is transferring to. Furthermore, the atom of every element releases X-ray with unique amounts of energy during the transferring process. Thus, by measuring the amounts of energy present in the X-ray being released by a specimen during electron beam bombardment, the identity of the atom from which the X-ray was emitted can be established. The output of an EDS analysis is an EDS spectrum, which is just a plot of how frequently an X-ray is received for each energy level. An EDS spectrum normally displays peaks corresponding to the energy levels for which the most X-ray had been received. Each of these peaks is unique to an atom, and therefore corresponds to a single element. The higher the peak in a spectrum, the more concentrated the element is in the specimen.

In the present work, a thin layer of the as-milled and annealed powders were spread on carbon coated tape and mounted on the FE-SEM stub. Gold coating, wherever necessary, was then applied over it to yield an electrically conducting surface for SEM observation.

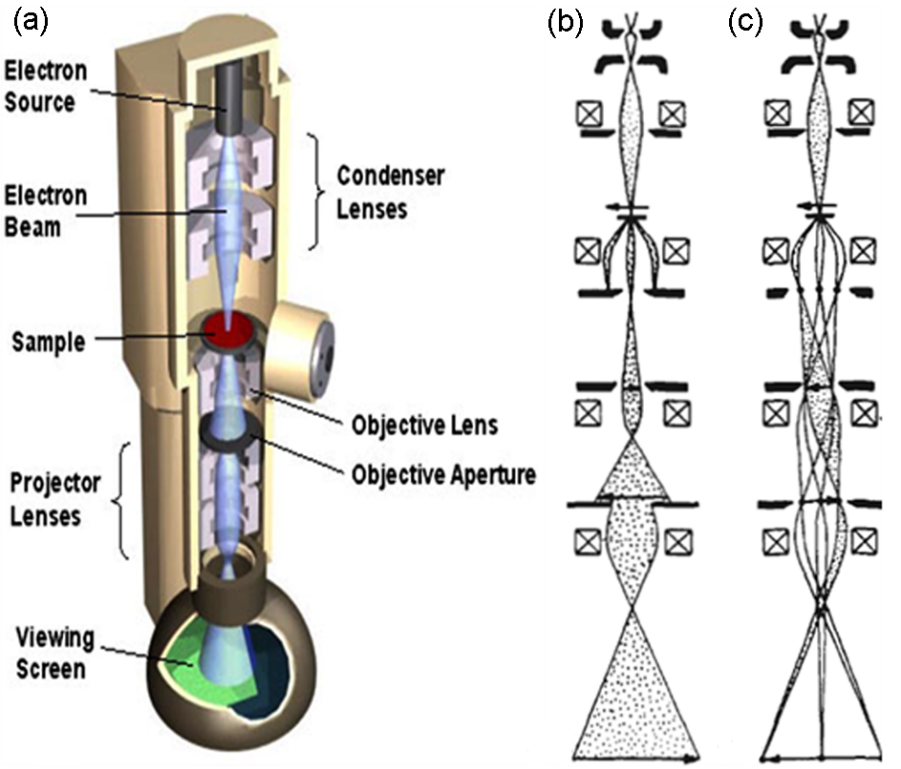

Figure 3.07: (a) Cut view of transmission electron microscope and (b) schematic ray diagrams of image mode and (c) diffraction mode.

3.3.2. Transmission electron microscopy

Transmission electron microscope (TEM, Jeol 2100, TECNAI G2 F30) has been used to study the microstructure of the powders. TEM is an optical analogue to the conventional light microscope. It is based on the fact that electrons can be ascribed a wavelength (of the order of 0.25 nm), but at the same time interact with magnetic fields as a point charge. A beam of electrons is applied instead of light and the glass lenses are replaced by magnetic lenses. The lateral resolution of the best microscopes is down to atomic resolution. A schematic diagram of a TEM is shown in Figure 3.07.

Electrons emitted from electron gun are accelerated to 100 - 300 keV and first projected on to the specimen by means of the electromagnetic lens systems. The scattering processes experienced by electrons during their passage through the specimen determine the kind of information obtained as shown in Figure 3.08. Elastic scattering involving no energy loss when electrons interact with the potential field of the ion cores gives rise to diffraction pattern. In-elastic scattering between beam and matrix electron at heterogeneities such as grain boundaries, dislocations, second-phase particles, defects, density variations cause complex absorption and

scattering effects. The generation of characteristic X-ray and Auger electrons also occurs, but these by-products are not usually collected in a typical TEM measurement. The emergent primary and diffracted electron beams are now made to pass through a series of post-specimen lenses. The objective lens produces the first image of the object. Depending on how the beams reaching the back focal plan of the objective lens, the beams are subsequently processed using different operation modes. Basically, either magnified images or diffraction patterns are obtained. The image can be studied directly by the operator or photographed with a camera.

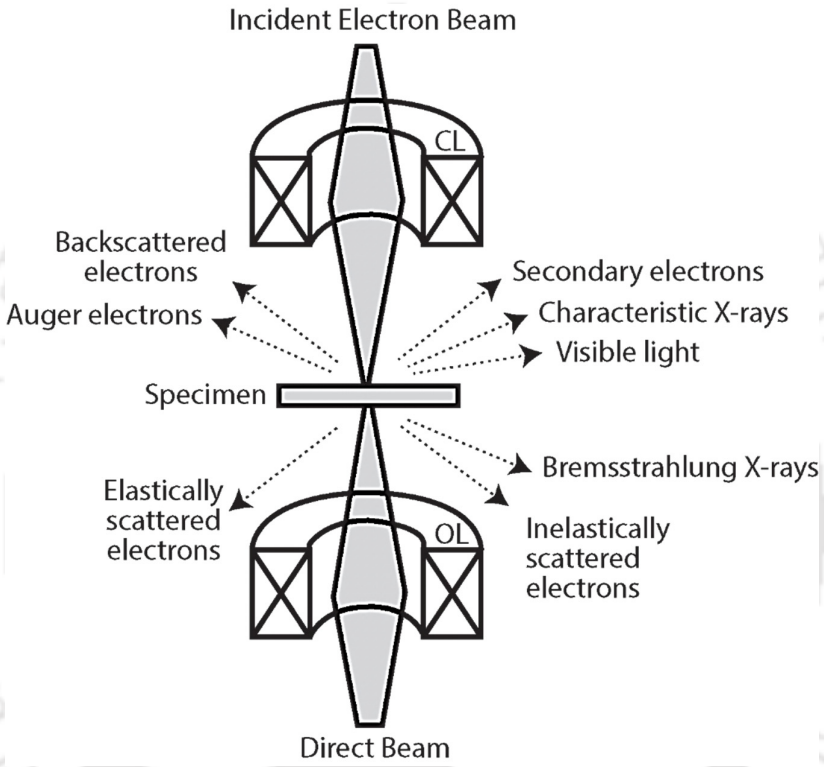

Figure 3.08: Various signals generated as a result of electron beam interaction with a thin solid specimen in TEM.

Images can be formed in different ways. The bright-field image is obtained by intentionally excluding all diffracted beams and only allowing the selected portion of the central beam passed through the specimen. This is done by placing suitably sized apertures in the back focal plane of the objective lens. Intermediate and projection lenses then magnify this central beam. Dark-field images are also formed by magnifying a single beam by choosing one of the diffracted beams by means of an aperture that blocks the central beam and the other diffracted beams. By selected area electron diffraction pattern, ring like structure is imaged, which corresponds to the particular plane of that element or compound. If only diffused rings appear then the system must have single amorphous phase. The high-resolution TEM image

obtained by allowing both the central beam passing through the specimen and one or more of the diffracted beams helps to evaluate the average grain size and dislocations more precisely.

For TEM observation, the sample in the form of powder was dispersed either in dimethyl formamide solvent or in isopropanol using an ultrasonicator. A drop of the colloidal solution was placed on a carbon coated TEM grid and allowed to dry in a clean environment. The grid with the dried powder particles was then used for the TEM observation.

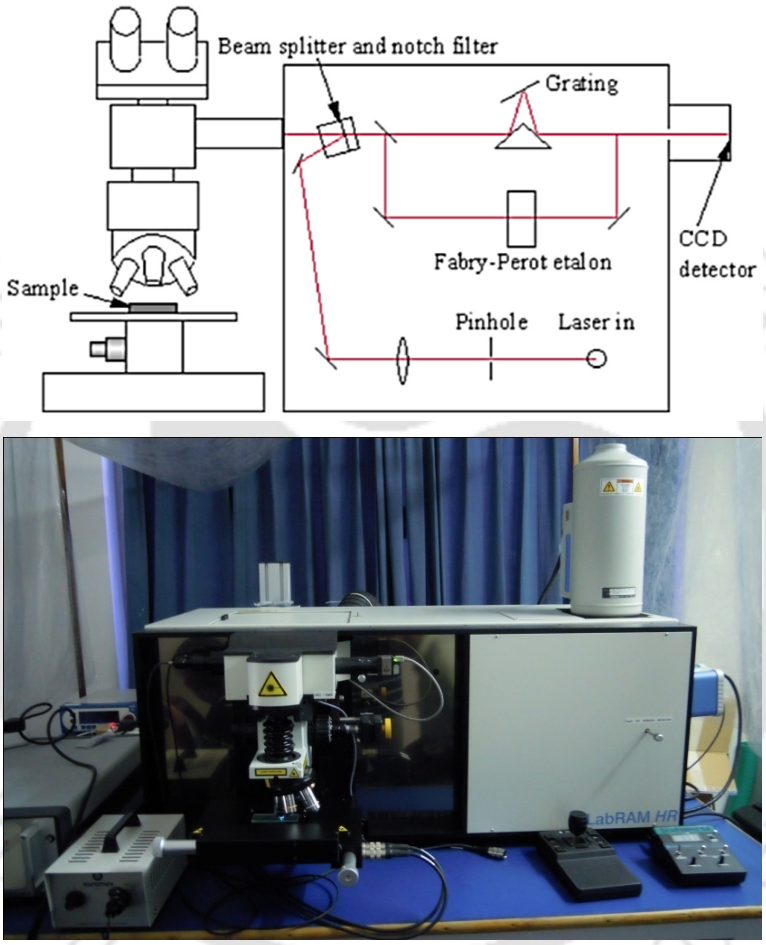

Figure 3.09: Schematic diagram (top) and photographic view (bottom) of Raman spectroscopy.

3.4. Spectroscopy characterization

3.4.1. Micro-Raman spectroscopy

Raman spectroscopy is a vibrational spectroscopic technique generally used to study properties such as crystalline phases, defects, strain, etc. in a material. It is basically a light scattering phenomenon based on the famous Raman effect corresponding to the photon-phonon interaction. Figure 3.09 depicts the schematic diagram and photographic view of Raman spectroscopy (LabRAM HR-800, Jobin Yvon, USA). In Raman spectroscopy, the sample is

illuminated with a monochromatic laser beam which interacts with the molecular vibration and are scattered. A fraction of the scattered beam has wavelength different from the incident wavelength and constitute the main features of Raman spectrum. If the scattered wavelength is shorter than the incident wavelength, the scattered lines are known as Stokes line, while if the scattered wavelength is longer, then they are known as anti-Stokes lines.

Raman spectrometer can be dispersive and non-dispersive. Dispersive spectrometer use grating or prism while non-dispersive spectrometer uses interferometer such as Michelson interferometer. Here, the intense laser beam is incident on the samples through a microscope with spot size of a few microns. The microscope is coupled confocally to an 800 mm focal length spectrograph equipped with two switchable gratings. The excitation photon can be supplied by using two sources namely He-Ne laser (wavelength 632.8 nm) or Ar laser (488 and 514 nm). The laser beam is totally reflected by the beam splitter, which splits the beam into two parts having equal wavelengths. The beam was allowed to fall on the sample where both Rayleigh and Raman scatterings occur. The notch filter allowing only the Raman scattered wavelength blocks the incident wavelength. The inelastic scattered light was allowed to pass through the grating and etalon, which in-turn resolves the weak inelastic scattered wavelength coming from the sample more efficiently. Further, the beam was allowed to enter into a charge couple device where it detects the change in polarizability of the sample from the change in wavelength and converts into the intensity. We could see intensity versus wave number graph in the computer screen.

A high resolution micro-Raman (LabRAM HR-800, Jobin Yvon, USA) spectroscopy instrument with liquid nitrogen cooled CCD detector is used for the characterization of the pure un-milled and milled powders.

3.4.2. Photoluminescence spectroscopy

Photoluminescence (PL) is the spontaneous emission of light from a material under optical excitation. Light is directed onto a sample, where it is absorbed and imparts excess energy into the material in a process called photo−excitation. One of the ways to dissipate this excess energy by the sample is through the emission of light or luminescence, as shown in Figure 3.10. In the case of photo−excitation, this luminescence is called photoluminescence. This light can be collected and analyzed spectrally, spatially and also temporally. The intensity and spectral content of this photoluminescence is a direct measure of various important material properties. PL spectroscopy is a contactless, versatile, non-destructive, powerful optical method of probing the electronic structure of materials.

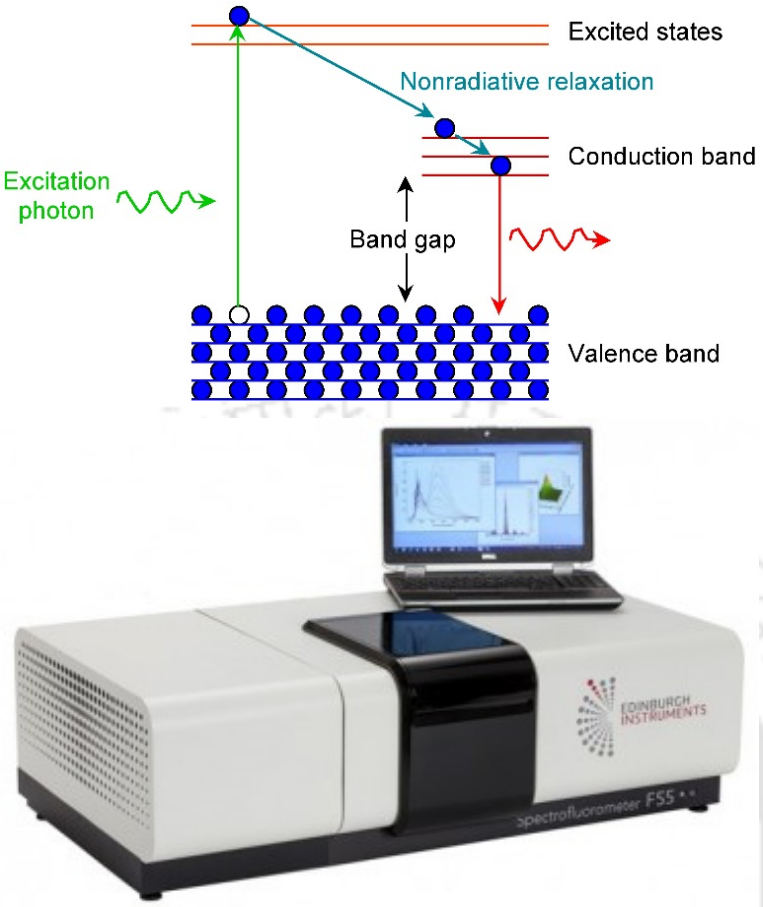

Figure 3.10: Principle (top) and photographic view (bottom) of photoluminescence spectroscopy.

Photo-excitation causes electrons to move into permissible excited states. When these electrons return to their equilibrium states, the excess energy is released and may include the emission of light (a radiative process) or may not (a non-radiative process). The energy of the emitted light relates to the difference in energy levels between the excited state and the equilibrium state, while the quantity of the emitted light is related to the relative contribution of the radiative process. PL spectroscopy gives information only on the low lying energy levels of the investigated system. In semiconductor systems, the most common radiative transition is between states in the conduction and valence bands, with the energy difference being known as the bandgap. During a PL spectroscopy experiment, excitation is provided by laser light with an energy much larger than the optical band gap. The photo excited carriers consist of electrons and holes, which relax toward their respective band edges and recombine by emitting light at the energy of the band gap. Radiative transitions in semiconductors may also involve localized defects or impurity levels and, therefore, the analysis of the PL spectrum leads to the

identification of specific defects or impurities, and the magnitude of the PL signal allows determining their concentration.

Hence, PL is a process of photon excitation followed by photon emission and important for determining band gap, purity, crystalline quality and impurity defect levels of a semiconducting material. It also helps to understand the underlying physics of the recombination mechanism. PL spectroscopy is quite different from the absorption spectroscopy, as the first one deals with the transitions from the excited state to the ground state, while the second one measures the transitions from the ground state to excited state. A high resolution PL spectrometer (Edinburg Instruments FSP920, UK) instrument is used for the characterization of the pure un-milled and milled powders.

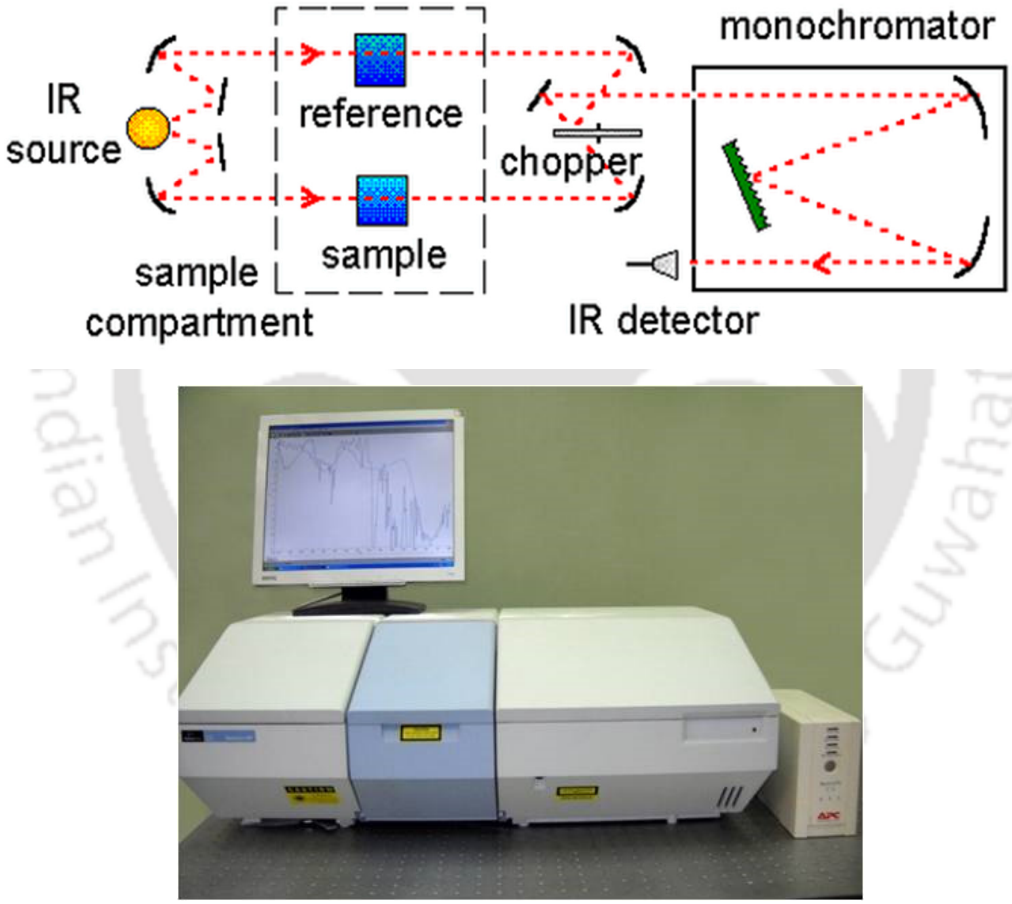

Figure 3.11: Principle (top) and photographic view (bottom) of Fourier-transform infrared spectroscopy.

3.4.3. Fourier transform infrared spectroscopy

Infrared spectroscopy (IRS) is an important technique to study the presence of various functional groups and to identify the pure compounds or the presence of specific impurities.

The analysis of IRS is based on the fact that the molecules have specific frequencies of internal vibration ranging between 4000 cm^{-1} and 200 cm^{-1}. When a sample is placed in a beam of IR radiation, the sample will absorb radiation at frequencies corresponding to molecular vibrational frequencies. The frequencies of radiation absorbed are measured by an IRS and the resulting plot of absorbed energy versus frequency is called IR spectrum. As different materials have different vibrations and yield different infrared spectra, the identification of the materials is quite easy. From the frequencies of the absorption, it is possible to determine whether various chemical groups are present or not in a chemical structure. In addition to the characteristic nature of the absorption, the magnitude of the absorption due to a given species is related to the concentration of that species.

Fourier-transform infrared spectroscopy (FTIR) is a technique used to obtain an infrared spectrum of absorption or emission of a solid, liquid or gas. FTIR is based on the phenomena "Michelson interference" combined with Fourier transformation of the source spectrum. [BRUN1992]. An FTIR spectrometer simultaneously collects high-spectral-resolution data over a wide spectral range and overcomes the limitations encountered with dispersive instruments. This provides a unique type of signal which has all of the infrared frequencies "encoded" into it. The signal can be measured very quickly, usually on the order of one second or so. Thus, the time element per sample is reduced to a matter of a few seconds rather than several minutes. Most interferometers employ a beam splitter which takes the incoming infrared beam and divides it into two optical beams (Figure 3.11). One beam reflects off of a flat mirror which is fixed in place. The other beam reflects off of a flat mirror which is on a mechanism which allows this mirror to move a very short distance (typically a few millimeters) away from the beam splitter. The two beams reflect off of their respective mirrors and are recombined when they meet back at the beam splitter. Because the path that one beam travels is a fixed length and the other is constantly changing as its mirror moves, the signal which exits the interferometer is the result of these two beams "interfering" with each other. The resulting signal is called an interferogram which has the unique property that every data point (a function of the moving mirror position) which makes up the signal has information about every infrared frequency which comes from the source. This means that as the interferogram is measured, all frequencies are being measured simultaneously. The measured interferogram signal cannot be interpreted directly and "decoding" the individual frequencies is required. This can be accomplished via a well-known mathematical technique called the Fourier transformation. This transformation is performed by the computer which then presents the user with the desired spectral information for analysis.

In this study, we used a commercial FTIR spectrometer (Perkin Elmer, Spectrum BX, Figure 3.11) to obtain the transmission spectrum of the pure and milled powders at room temperature in the range between 400 cm^{-1} and 4000 cm^{-1}. All the spectra were taken after background corrections. For the sample preparation, the pure un-milled and milled powders of very small quantity is mixed with KBr and ground in ceramic mortar and then prepared pellets using KBr press and die.

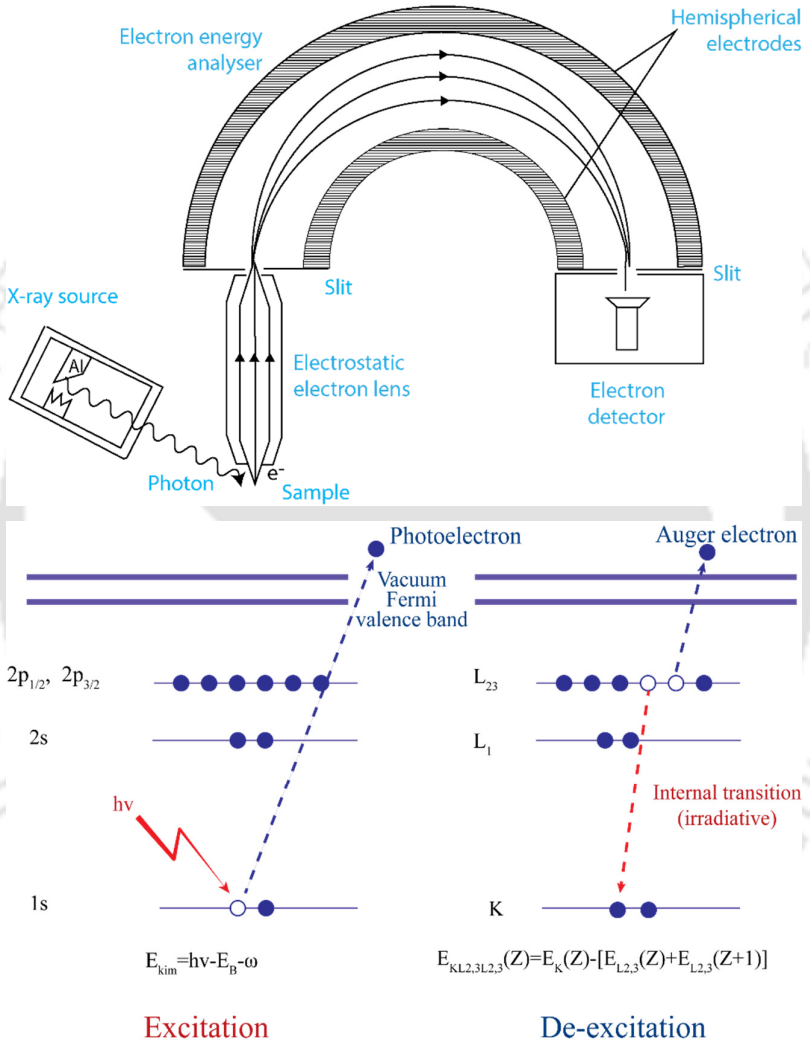

Figure 3.12: Schematic of XPS spectrometer (top) and excitation and de-excitation processes (bottom).

3.4.4. X-ray photoelectron spectroscopy

X-ray photoelectron spectroscopy (XPS) is a surface-sensitive quantitative spectroscopic technique. This measures the elemental composition at the parts per thousand range, empirical

formula, chemical state and electronic state of the elements that exist within a material. The principle of XPS is based on the photoelectric effect outlined by Einstein in 1905 and developed by Siegbahn and his research group [SIEG1967], where the concept of the photon was used to describe the ejection of electrons from a sample surface when photons impinge upon it. XPS requires high vacuum (~ 10^{-5} Pa) or ultra-high vacuum (UHV with pressure better than 10^{-5} Pa) conditions. XPS spectra are obtained by irradiating surface of the given material with a beam of X-ray as shown in Figure 3.12 and simultaneously measuring the kinetic energy and number of electrons that escape from the top sub-surface (~0 to 10 nm) of the material. This process can be expressed by the following equation:

$$BE = h\upsilon - KE - \Phi \tag{3.08}$$

where, BE is the binding energy of the electron in the atom, $h\nu$ is the photon energy of X-ray source, KE is the kinetic energy of the emitted electron that is measured in the XPS spectrometer and Φ is the spectrometer work function. The XPS principle for ejecting an electron from the atom as photoelectron during excitation and release of Auger electrons during the de-excitation process is shown in Figure 3.12. After the release of photoelectron, the atom turns into an excited state. To revert back to ground state, the electron from an outer shell occupies inner shell by releasing either X-ray or Auger electron. For XPS, Al-K_α (1486.6 eV) or Mg-K_α (1253.6 eV) is generally used as the source of X-ray. The photon is absorbed by an atom of the sample, leading to emission of a core (inner shell) electron. The energy of the photoelectrons leaving the sample is determined using an appropriate electron energy analyzer and this gives a spectrum with a series of photoelectron peaks. For each and every element, there will be a characteristic binding energy associated with each core atomic orbital, i.e., each element will give rise to a characteristic set of peaks in the photoelectron spectrum at kinetic energies determined by the photon energy and respective binding energies. The peak intensities measure how much of a material is at the surface, while the peak positions indicate the elemental and chemical composition. Other values, such as the full width at half maximum (FWHM) are useful indicators of chemical state changes and physical influences.

In this study, XPS measurements were carried out in standard ultrahigh vacuum surface science chamber consisting of PSP Vacuum Technology electron energy analyzer (angle integrating ±10°) and a dual anode X-ray source with (ULVAC-PHI, Inc.) using Mg-K_α X-ray beam (1253.6 eV) at a base pressure of 2×10^{-7} Pa and energy resolution at full width at half maximum is about 0.8 eV. The spectrometer was calibrated using Au $4f_{7/2}$ at 83.9 eV and used for the calibration of the XPS spectra recorded for various milled samples.

3.4.5. Electron spin resonance spectroscopy

Electron spin resonance (ESR) or Electron paramagnetic resonance (EPR) spectroscopy is a very powerful, sensitive, informative and nondestructive technique for the characterization of the electronic structures of materials with unpaired electrons. ESR is based on Zeeman effect that explains the splitting of energy level of a particle having spin ½ in a magnetic field. The energy difference between the two levels is given by

$$\Delta E = g\mu_B B \tag{3.09}$$

where, g is the Landé g-factor, μ_B is Bohr magneton and B is the amplitude of applied magnetic field.

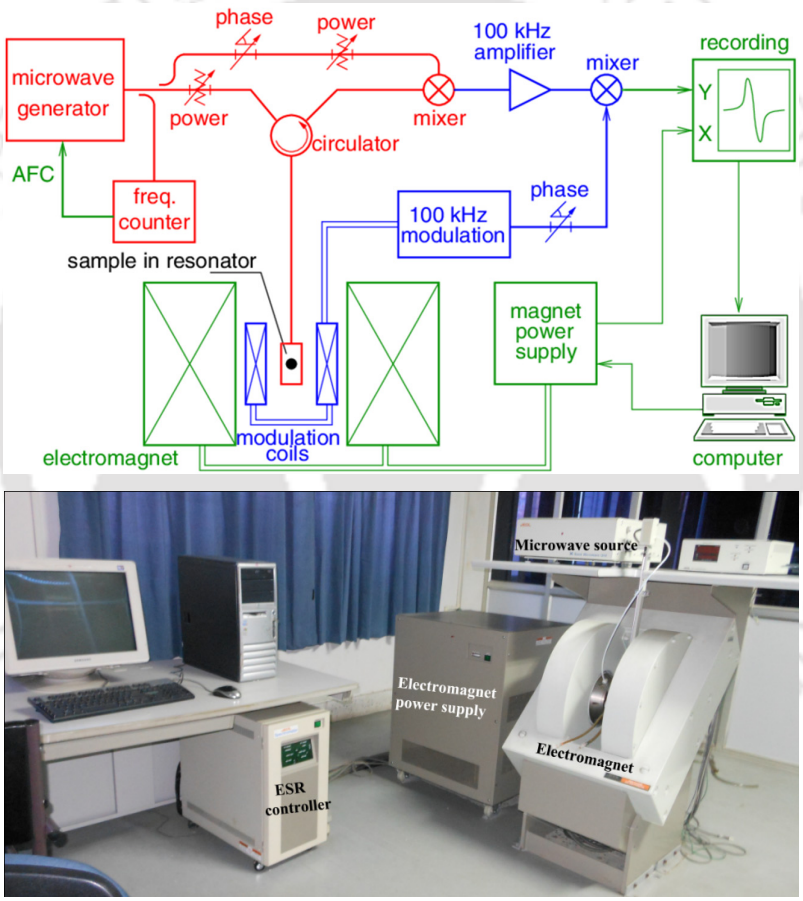

Figure 3.13: Block diagram (top) and photographic view of ESR spectrometer (bottom).

Since the energy difference between the two states depends on the magnetic field, electrons at the lower energy state can jump to the excited state at a particular value of the magnetic field. Alternatively, one can fix the magnitude of the applied field and vary its frequency. At certain value of frequency, the electrons can jump to the higher state giving rise absorption peak in the spectra. At resonance,

$$h\upsilon = g\mu_B B \tag{3.10}$$

where, υ is the frequency of the magnetic field, h is Planck's constant. Neither the field nor the frequency for resonance is a unique fingerprint for a system because spectra can be obtained at different value of B or frequency satisfying the eqn. (3.10). It is therefore the g-factor is the most useful parameter for the characterization of ESR spectra.

The basic building blocks of ESR are shown in Figure 3.13. The microwave generator generates and supplies microwave at controlled frequency and power, which are transmitted to the sample cavity through a waveguide. The sample cavity is mounted in the midst of the electromagnet pole pieces perpendicular to the magnetic field, B which can be varied in a controlled way. In addition to the main magnetic field, another magnetic field which is weaker comparative to the main field is generated and superimposed on the cavity by Zeeman modulation coils. Thus, the signal response from the cavity is modulated at the Zeeman modulation frequency. The ideal way for EPR spectra is to fix the magnitude of the magnetic field and continuously vary its frequency. However, microwave generators are tunable only to a limited range of frequency. Hence, the microwave frequency is fixed and magnitude of the magnetic field is varied. The magnetic field is swept until the sample absorbs the microwave frequency and jumps to the higher energy level, i.e., ESR absorption occurs.

Commercial ESR spectrometer works in the frequency range from several MHz to several GHz: 1-2 GHz (L-band) and 2-4 GHz (S-band), 8-10 GHZ (X-Band), 35 GHz (Q-band) and 95 GHz (W-band). In the present investigation, we have carried out the ESR measurement in powder form using JEOL Spectrometer (JES-FA200) operating at X-band frequency (ν = 9.4 GHz) with 100 kHz magnetic field modulation.

3.5. Magnetic property characterization

Magnetic properties of the materials can be characterized by using various experimental techniques such as magnetic property measurement system (MPMS) equipped with superconducting quantum interference device (SQUID) magnetometer, vibrating sample magnetometer (VSM), ac susceptometer, etc. In this section, a brief outline of the principle involved in VSM and SQUID magnetometers used in the present work is given.

3.5.1. Vibrating sample magnetometer

VSM (Lakeshore Model 7410, USA) was used to characterize room temperature and temperature dependent magnetic properties in the temperature range 20 K – 300 K and 300 K

– 1100 K. VSM measures net dipole moment when material is exposed to magnetic field [JANS2004, HORS2006].

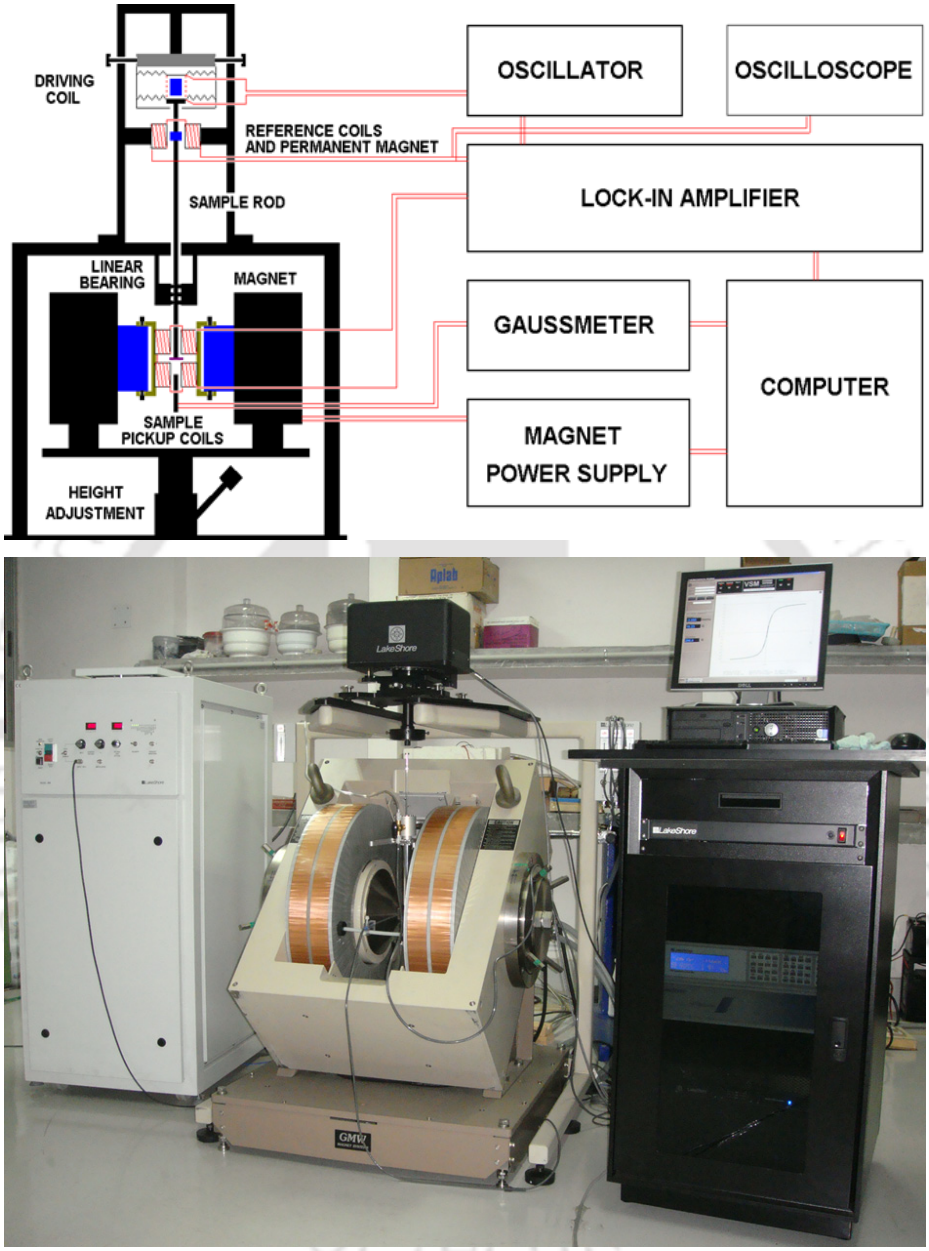

Figure 3.14: Schematic diagram (top) and photographic view (bottom) of a vibrating sample magnetometer.

The magnetic moment of the material can be obtained either as a function of field called magnetic hysteresis (*M-H*) loop to investigate the evolution of magnetic properties with field or as a function of temperature (*M-T*) to understand the magnetic phase transition of the

material. Figures 3.14 displays schematic diagram and photographic view of VSM used in the present study.

Figure 3.15: Photographic view of a SQUID magnetometer in MPMS (MPMS XL 7 system).

When a sample is placed in a uniform magnetic field, a dipole moment proportional to the product of the sample susceptibility and the applied field induced in the sample. If the sample is made to undergo sinusoidal motion, an electrical signal can be induced in suitably located stationary pickup coils (see figure.3.14). This signal has amplitude proportional to the magnetic moment of the sample, the vibrating amplitude and the vibration frequency. Through the use of lock-in-amplifier and feedback techniques, only that portion of the signal arising from the magnetic moment is picked up and is converted into direct read-out in the unit of magnetization (e.g. emu) on a digital panel meter. VSM consists of the following major parts: a) Vibration exciter and sample holder, b) water cooled electromagnet and power supply, c) Hall probe, d) pick-up coils, e) amplifier, f) control panel system, g) lock-in amplifier and h) computer interface. The sample was fixed at the lower end of the sample holder after

completing the calibration procedure using standard Ni sample. The measurement sequence is programmed as per the users choice using the software (IDEASVSM) provided with the instrument such that the program starts either from the maximum field or from the zero applied field. The sequence is made to collect more number of data, which helps to extract the magnetic parameters (saturation magnetization, remenance magnetization, coercivity, etc.) more accurately. The exciter is vibrated at a frequency of 72 Hz (Lakeshore model 7410) and the signal received from the hall probe and the pick-up coils is converted into the magnetic moment of the sample. The magnetic field is increased automatically in user-defined steps for measuring *M-H* loops. Similarly, for high temperature *M–T* measurements, a high temperature oven attachment capable of providing a controlled heating/cooling of the sample from room temperature to 1223 K was used. For *M–T* measurements, the nanocrystalline sample was loaded on a high temperature sustainable holder (ceramic holder or quartz rod) after the calibration using standard Ni sample. The oven was purged with nitrogen gas to avoid oxidization of the sample at high temperature. Magnetization was recorded at different temperatures at a constant in-plane applied magnetic field. The heating rate and *M–T* sequences were programmed using the IDEASVSM software.

3.5.2. Magnetic property measurement system

Magnetic property measurement system (MPMS), as displayed in Figure 3.15, equipped with SQUID magnetometer (MPMS XL 7, USA), was used to characterize magnetic properties in the temperature range of 2 K – 399 K. The fundamental property of superconducting rings is that they can enclose magnetic flux only in multiples of a universal constant called flux quantum, ϕ_0, i.e., an external magnetic field can penetrate a superconductive loop if and only if the magnetic field is an integer multiple of ϕ_0 [BARO1992]:

$$\phi_0 = \frac{h}{2e} = 2\times10^{-15}\ Wb \qquad (3.09)$$

where, h is the plank constant and e is the charge of electron. Since the flux quantum is the smallest quantity of the magnetic flux, SQUID has an extraordinarily sensitive magnetic detector. SQUIDs actually function as magnetic flux-to-voltage transducers by converting magnetic flux into corresponding voltage. SQUID mainly consists of two Josephson junctions, i.e., two superconducting metals separated by a thin insulating layer, which is typically a metal-oxide [BARO1992]. As a result, the tunneling super current across the junction has a phase which depends strongly on the magnetic field applied perpendicularly to junction. Furthermore,

each junction has a maximum value of the current that can flow without voltage drop across and above which normal electrons need to flow and a finite voltage drop appears. This finite voltage drop causes the supercurrent to cease. In particular, in a superconducting ring interrupted by two Josephson junctions, the application of a magnetic field normal to the ring causes an induced supercurrent to screen the magnetic field. When induced supercurrent exceeds the critical value, it allows the magnetic flux to enter the hollow portion of the ring, in multiples of one quantum unit as discussed earlier. The process repeats for an increasing external applied magnetic field and the flux increases each time by one quantum unit. A pick-up coil, located coaxially to the ring, enables the measurement of the magnetic field by counting the pulses of electromotive force induced each time of the magnetic flux changes.

In the present study, the sample was fixed in the suitable sample holder and temperature dependent magnetization measurements were carried out under zero-field-cooled (ZFC) and field-cooled (FC) conditions by setting the program. The sample was cooled down to 2 K without applying any field and the magnetization was measured during the warming process under a constant applied, known as ZFC process. Subsequently, the sample was cooled down to 2 K under the same constant field and the magnetization was measured during warming process, called as FC process. The temperature during measurements was controlled using suitable temperature controller (Quantum Design) from 2 K to 400 K.

Chapter 4

Properties of NiO powders prepared by ball milling process

4.1. Introduction

The study of fine nanocrystalline metal-oxide particles has become a subject of increasing interest and intense research in the myriad of different fields such as catalysis, magnetic resonance imaging contrast agents, targeted drug delivery, sensors, energy conversion, electrochromics, etc [LLAN2010, RUNG2010, HOSO2012]. These nanoparticles lie between clusters whose properties are strongly dependent on its size and submicron sized particles which have almost the properties same as bulk materials. In particular, the study of magnetism and magnetic interactions in various types of metal-oxide nanoparticles has generated much attention due to size and/or defect induced magnetic properties and their potential applications in biomedical, magnetoelectronic device, catalysis, spintronics, etc [DORM1997, FERN2004, ARIC2005, FIOR2005, DART2008, PANK2009, KITA2010, MORG20102, VEIS2010, HAAS2012, THAN2012]. Furthermore, the development of NiO based nanoparticles and thin films has been focused to obtain ferromagnetism (FM) above room temperature such that these oxides with cubic structure could facilitate integration of spintronic devices where both charge and spin are used to transport, store, and process information in novel ways [DORM1997, FIOR2005].

There have been a profusion of recent works on the magnetic properties of nanosized antiferromagnetic (AFM) particles and most of the reports demonstrate existence of FM moment on the nanoparticles [KHAD2003, BHOW2004]. This was mainly instigated from Néel's suggestion that fine nanoparticles of AFM nature should exhibit either a weak FM or superparamagnetism (SPM) [NEEL1962]. Richardson et al [RICH1956] reported the first investigation on size dependent properties of NiO system. Subsequently, the effect of size dependent magnetic properties [KODA1997, THOT2007] and the competition between finite size versus surface effects [MAND2011] on the room temperature magnetic crossover of NiO were reported. Some theoretical calculation and experimental data have shown that NiO nanoparticles ranging from 1 to 50 nm can have both AFM and FM couplings [YIJB2007]. It may be noted that most of the reported investigations on NiO based systems are bottom to top approach on selected size of the particles without any systematic investigations. Hence the comparison of the resulting magnetic properties in NiO is quite complex due to the interplay between finite size, surface effects and interface effects, etc. On the other hand, the approach of the top to bottom method for studying the magnetic properties of pure NiO particles without any impurity phases is significantly missing. Therefore, we report here an alternative and inexpensive technique called ball milling process using a high-energy planetary ball mill to prepare nanoscale NiO powders with the subsequent observations of (i) evolution of nanoscale

NiO powder with milling time, (ii) the effects of size reduction and stress induced during milling on the structural, vibrational, electronic, magnetic, resonance and optical properties of NiO powders, (iii) the effect of annealing of milled NiO powders at different temperatures to understand the origin of room temperature FM and (iii) correlation between the crystal structure, microstructure, vibrational, electronic, magnetic, resonance and optical properties of these ball milled powders and to explore the possibility to enhance their physical properties.

4.2. Experimental details

Weighed quantities of high purity NiO (> 99.9%, Sigma Aldrich, USA) powders, displaying pale green color, were taken in high energy planetary ball mill filled with high purity argon gas. The milling process of NiO powders was carried out for different milling periods (t_m) from 0.25 to 60 hrs using the mill operated at 500 rpm with a ball-to-powder weight ratio of 10:1. The optimization of the milling speed and ball-to-powder weight ratio was done mainly by analyzing the variation in the structural and magnetic properties of the NiO powders. In order to avoid any local heating during milling and its influence on the resulting properties, the milling process was programmed to halt for 15 minutes after every 15 minutes of operation. In addition, the milled powders were collected at regular intervals and characterized to monitor the evolution of nanostructure in NiO powders. These powders collected at random intervals were also subsequently annealed at air atmosphere for 3 hrs at different annealing temperatures (T_A).

The phase evolution and crystal structure of NiO powders were analyzed through X-ray diffraction (XRD) patterns obtained using high-power (18 kW) X-Ray diffractometer (Rigaku TTRAX III, Japan). XRD data were collected at a slow scan rate of 0.005°/s for analyzing the structural parameters as a function of t_m. The changes in the surface morphology of the powders were observed using field emission scanning electron microscope (FE-SEM) and overall composition of the pure un-milled and milled powders was determined using energy dispersive spectroscopy (EDS, Oxford) attached to SEM unit. The microstructural properties of the pure un-milled and milled NiO powders were analyzed using transmission electron microscopy (TEM, JEOL 2100 and TECNAI G^2 F30) technique. Raman spectra were obtained using micro-Raman spectroscopy (LabRam HR800, Jobin Yvon) using excitation wavelength of 614 nm at room temperature. X-ray photoelectron spectroscopy (XPS) analysis was carried out in a standard ultrahigh vacuum surface science chamber consisting of a PSP vacuum technology electron energy analyzer (angle integrating ±10°) and a dual anode X-ray source with an Mg-

K_α source (1253.6 eV) at a base pressure of 2×10^{-10} mbar and energy resolution at full width at half maximum (FWHM) is about 0.8 eV. The spectrometer was calibrated using Au $4f_{7/2}$ at 83.9 eV [ZHAN20121]. Mössbauer spectra were recorded at room temperature using a standard constant acceleration Mössbauer spectrometer in the transmission geometry. Magnetic properties of the pure un-milled and milled powders were characterized using vibrating sample magnetometer (VSM, LakeShore Model 7410) by performing (i) magnetic hysteresis (*M-H*) loops at different temperatures under zero-field-cooled (ZFC) and field-cooled (FC) conditions and (ii) high-temperature thermomagnetization (*M-T*) under constant applied magnetic fields over a wide range of temperatures from 300 K to 1100 K. Similarly, *M-T* measurements were also performed under ZFC and FC conditions in the temperature range between 2 K and 400 K at different constant applied fields using magnetic property measurement system with superconducting quantum interference device (SQUID, Quantum Design MPMS XL7) magnetometer. Room temperature electron paramagnetic resonance (EPR) measurements were carried out on a JEOL Spectrometer (JES-FA200) operating at X-band frequency (ν =9.4 GHz) with 100 kHz magnetic field modulation in powder form. Steady state photoluminescence (PL) spectra were recorded by using a 312 nm Xenon lamp excitation (AB2, Thermo spectronic).

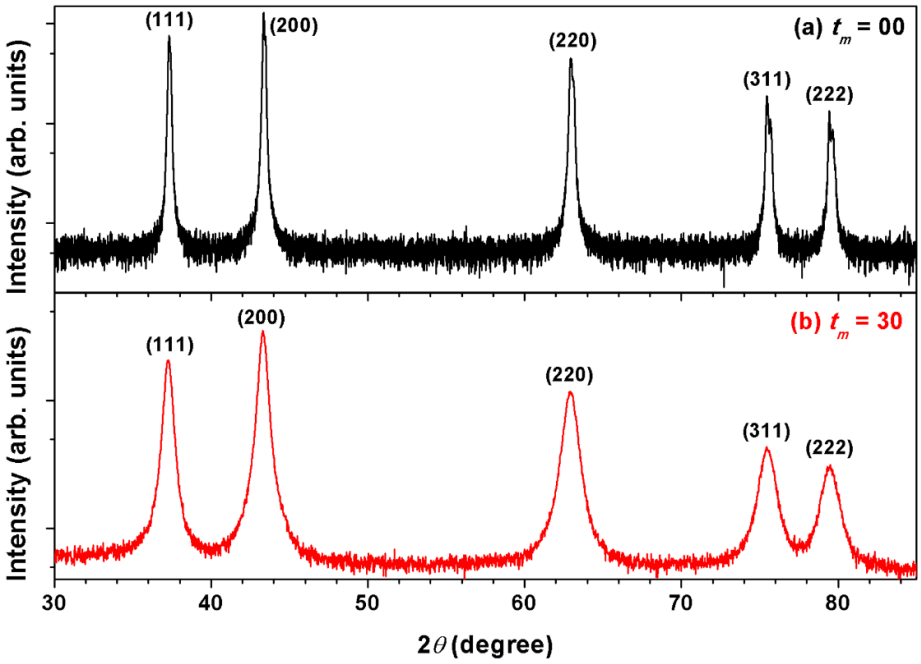

Figure 4.01: Room temperature XRD patterns of (a) pure un-milled NiO powder and (b) milled NiO powder for 30 hrs.

4.3. Results and discussion

4.3.1. Structural properties

Figure 4.01 depicts typical room temperature XRD patterns of pure un-milled NiO and 30 hrs milled NiO powders. The un-milled NiO powder shows Bragg reflections corresponding to face centered cubic (*fcc*) structure. Similarly, the milled NiO powder also exhibits *fcc* structure without any impurity phase within the detection limit of X-ray diffractometer. A careful observation of the XRD peaks reveals that the sharp Bragg reflections observed in pure NiO powders broadens significantly along with a considerable shift in peak position towards a lower diffraction angle. While the first one indicates the formation of highly refined and strained NiO powders, the latter one suggests a considerable change in the lattice parameter during the milling process.

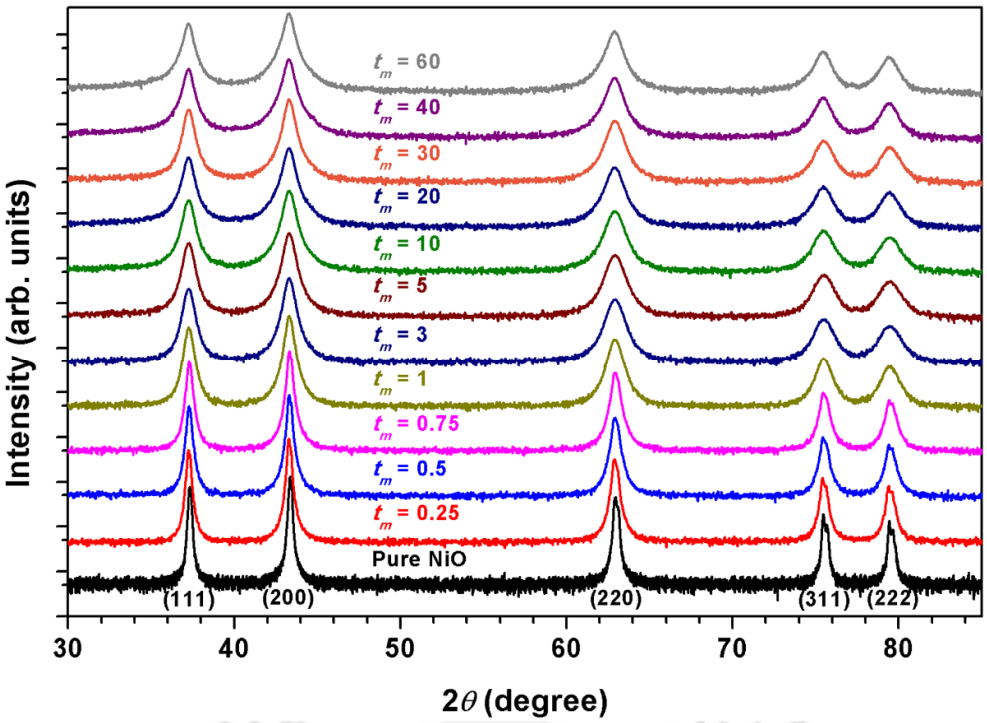

Figure 4.02: Room temperature XRD patterns of pure un-milled and milled NiO powders at different t_m.

In order to understand the evolution of nanocrystalline microstructure systematically, we have obtained XRD patterns of milled NiO powders collected at different t_m between 0.25 and 60 hrs. Figure 4.02 displays the XRD patterns of NiO powders milled at different t_m. All samples exhibit *fcc* structure without any other impurity phases. With increasing t_m, the peak broadening increases along with the shift in peak position to lower angles. It is well-known that

broadening of XRD peaks occurs due to the refinement of average crystallite size (D), instrumental broadening and strain (η) caused by the density of dislocations (ρ) induced during ball milling process [DING2001, SURY2001]. To separate the individual contribution from D and η, XRD patterns were analyzed using Williamson-Hall Plot (WHP) method [WILL1953] described by the formula given in eqn.(4.01)

$$\Delta\theta\cos\theta = \frac{k\lambda}{D_{WHP}} + 4\eta\sin\theta \qquad (4.01)$$

where $\Delta\theta$ is full width at half maximum (FWHM) of Bragg reflections (in radians) after eliminating the instrumental broadening contribution, θ is the peak position, λ (= 1.5406 Å) is the wavelength of the X-ray, D_{WHP} is average crystal size, k is constant taken as 0.9 by assuming spherical nature of particles and η is the effective lattice strain. In order to validate the WHP fit to XRD data, the eqn.(4.01) is modified to

$$\Delta K = \frac{k}{D_{WHP}} + K\eta \qquad (4.02)$$

where ΔK [= ($\Delta\theta$ cosθ)/λ] and K = 4sinθ/λ. Figure 4.03 depicts the plot of ΔK versus K for 30 hrs milled NiO powders and the typical linear fit to the data using eqn.(4.02). It is observed that the data do not fall into straight line and hence not entirely obey the linear fit to WHP formulation. The deviation observed in the data can be correlated to the existence of anisotropic variation in the residual strain. Hence, certain Bragg reflections may exhibit large strain component than others.

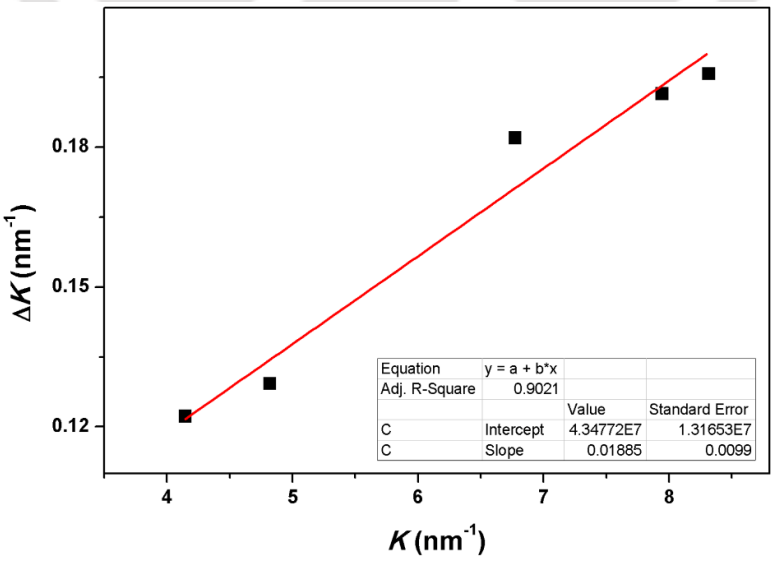

Figure 4.03: The plot of ΔK versus K for 30 hrs milled NiO powder. The straight line is the linear fit to eqn.(4.02).

Ungar et al [UNGA1991, UNGA1992] suggested a modification to WHP method by including dislocation contrast factor in order to consider the anisotropic distribution of dislocation effects on different Bragg peaks. Hence, to separate the size and strain effects effectively for the presently investigated samples, the XRD patterns were analyzed using Modified Williamson-Hall Plot (MWHP) method. According to this method, individual contribution to the broadening of reflections can be expressed as

$$(\Delta K)^2 = \left(\frac{0.9}{D}\right)^2 + \left(\frac{\pi b^2 \rho}{2B}\right) K^2 C \qquad (4.03)$$

where ΔK [$= (2\cos\theta\Delta\theta)/\lambda$], $K = 2\sin\theta/\lambda$, D is average crystal size, b is modulus of the Burgers vector of dislocations taken as $b = \left(\sqrt{3}/2\right)a$ [SHEN2005], ρ is average dislocation density and B is a constant (taken as 10 for a wide range of dislocation distributions [REVE1996] and C $\left(= C_{hkl} = C_{h00}\left(1 - qH^2\right)\right)$ is dislocation contrast factor introduced to take care the elastically anisotropic materials [UNGA1992, SHEN2005, KALI2008, MHAD2010], where the residual strains affect some Bragg reflections more than the others, q is a constant and $H^2 = \left(h^2k^2 + k^2l^2 + l^2h^2\right)/\left(h^2 + k^2 + l^2\right)$ for cubic system.

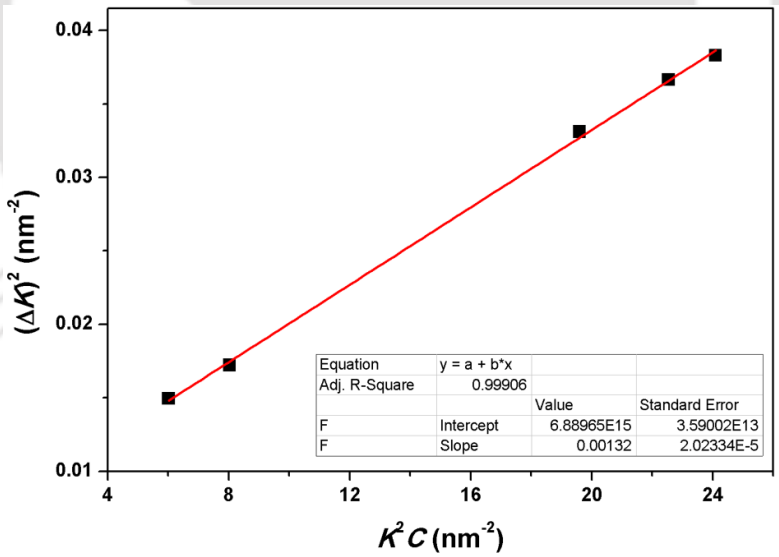

Figure 4.04: The plot of $(\Delta K)^2$ versus K^2C for 30 hrs milled NiO powder. The straight line is the best linear fit to eqn.(4.03).

Figure 4.04 depicts the typical plot of $(\Delta K)^2$ versus K^2C and the linear fit using eqn.(4.03). It is clear from the figure that all the XRD data almost fall into straight line and hence fitted using a straight line. The values of D and ρ were calculated from intercept and slope of the

fitted straight line, respectively. Note that the dislocation density is one of the major structural parameters [HULL2001] influencing the final nanocrystalline microstructure and correlated to the induced strain and reduced crystal size as $\eta = \frac{\rho D b}{2\sqrt{3}}$. The determined values of D and η for milled NiO powders are plotted as a function t_m in Figure 4.05.

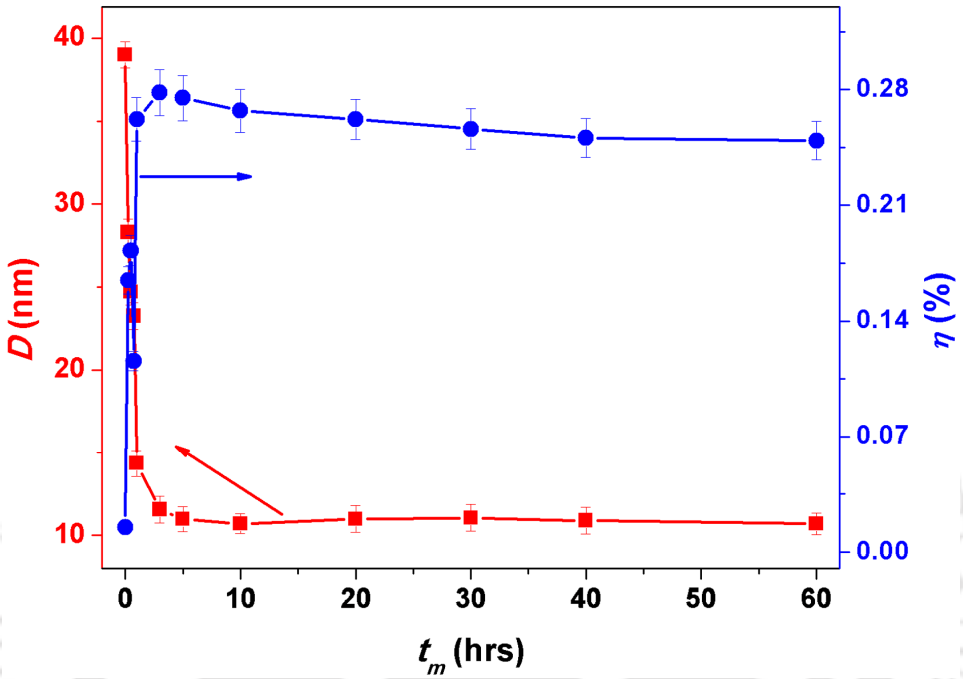

Figure 4.05: The variations of average crystal size (D) and effective strain (η) as a function of milling time (t_m) for milled NiO powders.

With increasing t_m, D decreases largely up to t_m = 10 hrs and then remains almost constant upon subsequent milling. NiO powders milled more than 10 hrs exhibit fine nanosized crystals with the size of around 11 nm. On the other hand, the strain increases drastically for t_m up to 10 hrs and then decreases slightly for higher t_m. The amount of strain in the milled powders is relatively high as compared to pure NiO powders or NiO powders prepared by chemical process [PROE2011, TAJI2015]. These results clearly indicate that the formation of dislocations caused by the high-energy ball mill is majorly influencing on the development of nanocrystalline microstructure. When the crystal size reaches the saturation value, further milling does not produce more dislocations due to the difficulty in generating additional dislocations in smaller crystals. On the other hand, the existing dislocations will be rearranged at this stage and some dislocations may be annihilated due to prolong milling. This results in a slight decrease in the strain values as observed in for the powders milled for 60 hrs.

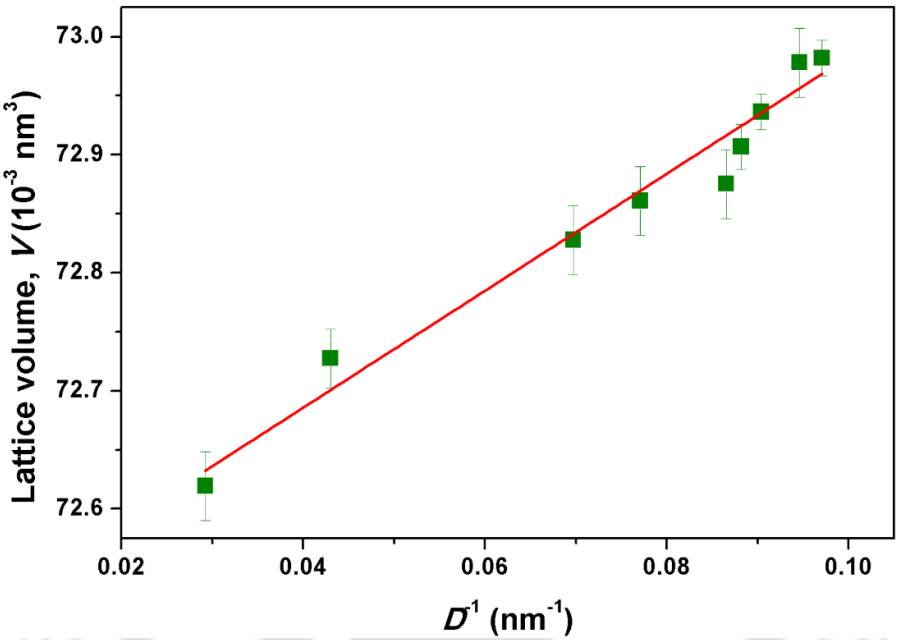

Figure 4.06: The plot of lattice volume (V) as a function of D^{-1}. The straight line is the best linear fit to the experimental data using eqn.(4.04).

To study the effect of structural refinement on the lattice parameters, the lattice constant was calculated from XRD patterns. Figure 4.06 displays the variation of volumetric change in the milled NiO powders as a function of inverse of average crystal size (D^{-1}). Interestingly, we observed almost a linear variation of volumetric change with D^{-1} and the data was fitted to a linear equation, as described in eqn.(4.04).

$$V(D) = V_B + AD^{-1} \qquad (4.04)$$

where V_B represents the volume of the bulk NiO and A is a constant. The linear fit to the data yields the values of V_B and A as 72.49 Å^3 and 49.56 Å^4, respectively. The obtained value of V_B is in close agreement with the bulk NiO value of 72.51 Å^3 [DUOL2010]. A similar variation of lattice change has been reported in other metal-oxide systems and correlated to (i) unpaired electron orbitals at outer surface [AYYU1995], (ii) the valence reduction [TSUN2000] and (iii) strong repulsive interactions of parallel surface defect dipole [LIL2006]. In contrast, Eto et al [ETOT2000] reported a continuous decrease in the lattice constant of NiO exhibiting a rhombohedral distorted $B1$ structure with increasing pressure up to 141 GPa. Therefore, the observed linear lattice expansion in the presently investigated samples can be related to negative interface pressure activated by the strain, which distorts the local structure without affecting overall crystal structure. This promotes a condition of non-stoichiometric in NiO and

therefore changes the color of NiO powder from pale green for pure un-milled NiO to dark green with increasing t_m [AHMA2006].

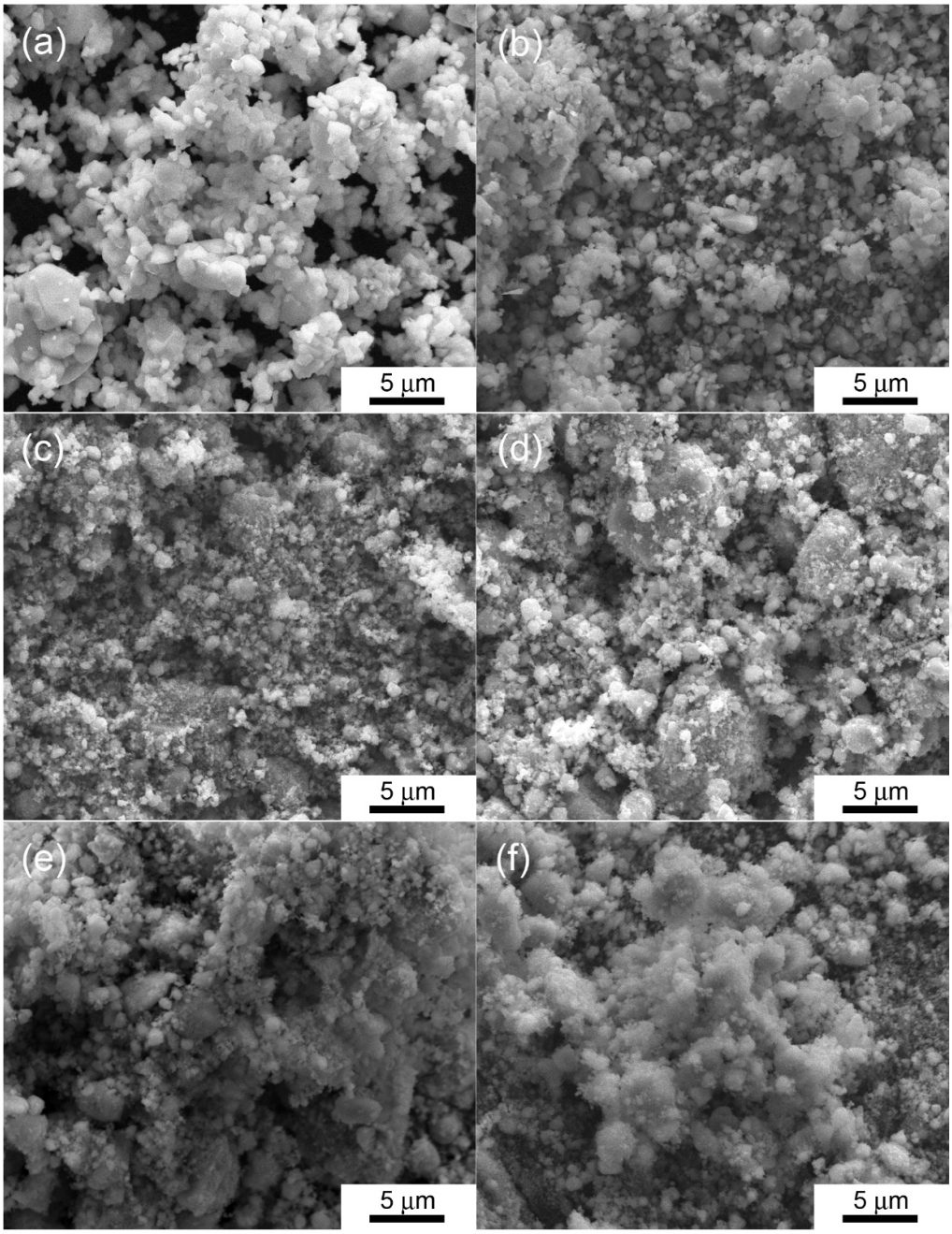

Figure 4.07: FE-SEM images of (a) pure un-milled and milled NiO powders at t_m = (b) 1, (c) 10, (d) 20, (e) 40 and (f) 60 hrs.

In order to understand the change in the surface morphology and evolution of nanocrystalline microstructures, the pure un-milled NiO and milled NiO powders were characterized using FE-SEM and TEM techniques. Figure 4.07 shows the typical FE-SEM

images of pure un-milled and milled NiO powders at different t_m. A clear particle morphology with the average particle size of 1 to 3 μm is observed in pure un-milled NiO powders.

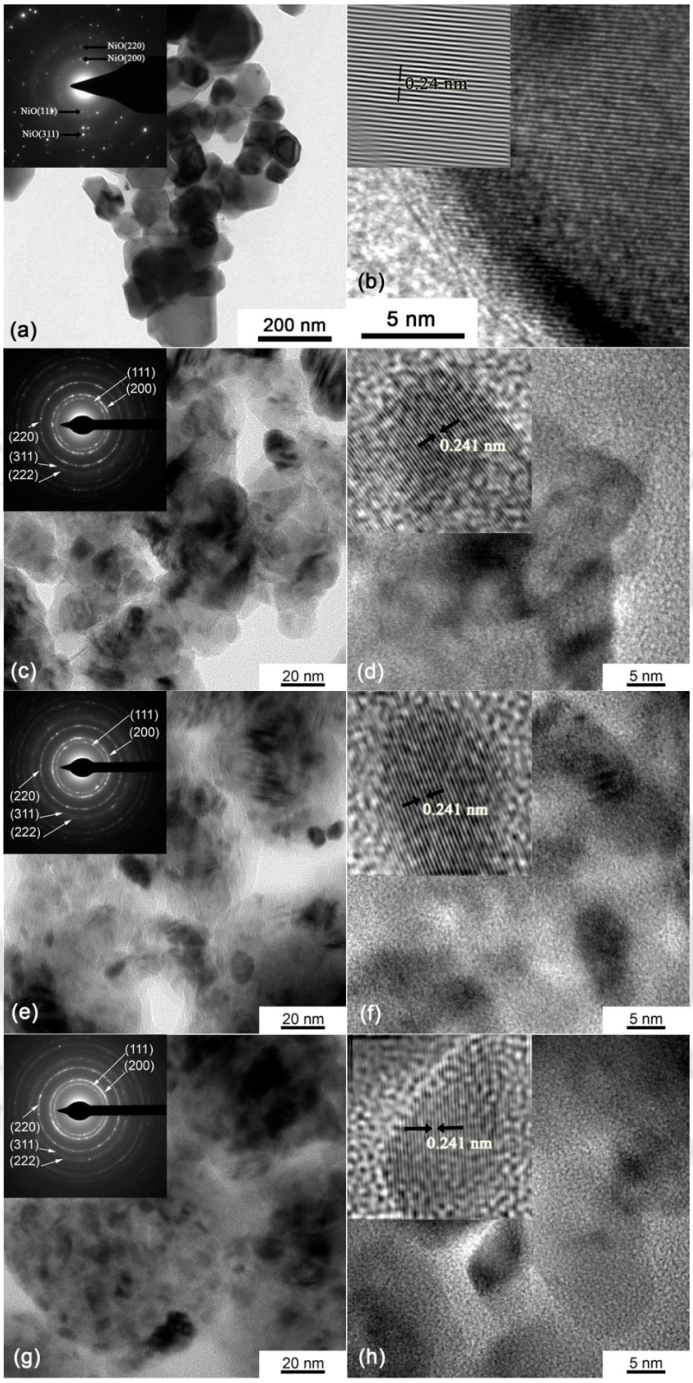

Figure 4.08: Bright-field TEM images, selected area electron diffraction patterns, high-resolution TEM images and inverse-fast Fourier transform images of selected areas of high-resolution TEM of (a,b) pure un-milled NiO and milled NiO powders at t_m = (c,d) 3 hrs, (e,f) 10 hrs and (g,h) 30 hrs, respectively.

With increasing t_m, the average particle size of the milled powders decreases considerably below 300 nm. At the same time, the agglomeration of the fine particles increases to form aggregated particles and the number of such particles increases with increasing t_m. Note that these aggregates are typical of ball-milled powders and result in from the repeated cold welding and fracture of powder during milling. Figure 4.08 shows typical plane-view bright-field TEM (BF-TEM) images, selected area electron diffraction (SAED) patterns, high-resolution TEM (HR-TEM) images and inverse-fast Fourier transform (i-FFT) images of selected areas of HR-TEM images of pure un-milled and milled NiO powders at 03, 10 and 30 hrs. BF-TEM image of the pure NiO powder reveals a clear particle morphology with size varying between 40 and 70 nm. The polycrystalline nature is evident from NiO diffraction rings in the SAED pattern. On the other hand, BF-TEM images of milled NiO powders confirm the presence of fine nanocrystalline microstructure with irregular morphology. In addition, the SAED patterns show diffraction rings, which could be indexed to *fcc* structure only and confirm the polycrystalline nature of the NiO particles. The average size of the crystals estimated from BF-TEM and HR-TEM images at random locations decreases from 40-70 nm for the pure un-milled NiO to about 14 nm and 11 nm after milling for 3 hrs and 30 hrs, respectively. The variations of TEM crystallite size of NiO exhibit almost a similar trend with that of XRD results. Nevertheless, the nanoscale powders exhibit irregular shapes with broad size distribution. In order to analyze the lattice parameter carefully, we have resolved the HR-TEM images by i-FFT method using a GATAN digital micrograph and shown as inset of all HR-TEM images. The i-FFT images help to resolve the lattice fringes with the subsequent determination of inter-planar spacing of about 0.24 nm corresponding to the NiO(111) lattice plane. Thus, the analyses of both TEM and XRD observations are in good agreement with each other and these structural modifications in NiO powders are expected to yield considerable changes in their physical properties.

4.3.2. Vibrational properties

As Raman scattering is considered to be one of the most effective tools for studying crystallinity and defects structure associated with the materials, Raman spectra were obtained for pure un-milled and milled NiO powders and depicted in Figure 4.09. Raman spectra were analyzed by curve fitting method with different band combinations to obtain the peak position, peak width and area under curves. The fitted curves are also shown in Figure 4.09. The commercially available NiO powder exhibits several bands above 300 cm^{-1}. While the bands observed at 380-410 cm^{-1}, 540-560 cm^{-1}, 700-730 cm^{-1}, 900 cm^{-1} and 1050-1110 cm^{-1} could be

correlated to one-phonon (1P) transverse optical (TO), 1P longitudinal optical (LO), two-phonon (2P) TO, 2P LO+TO and 2P LO of vibrational origin, respectively, the band around 1450 cm^{-1} is due to two-magnon (2M) scattering associated with Ni^{2+}-O^{2-}-Ni^{2+} super-exchange interaction.

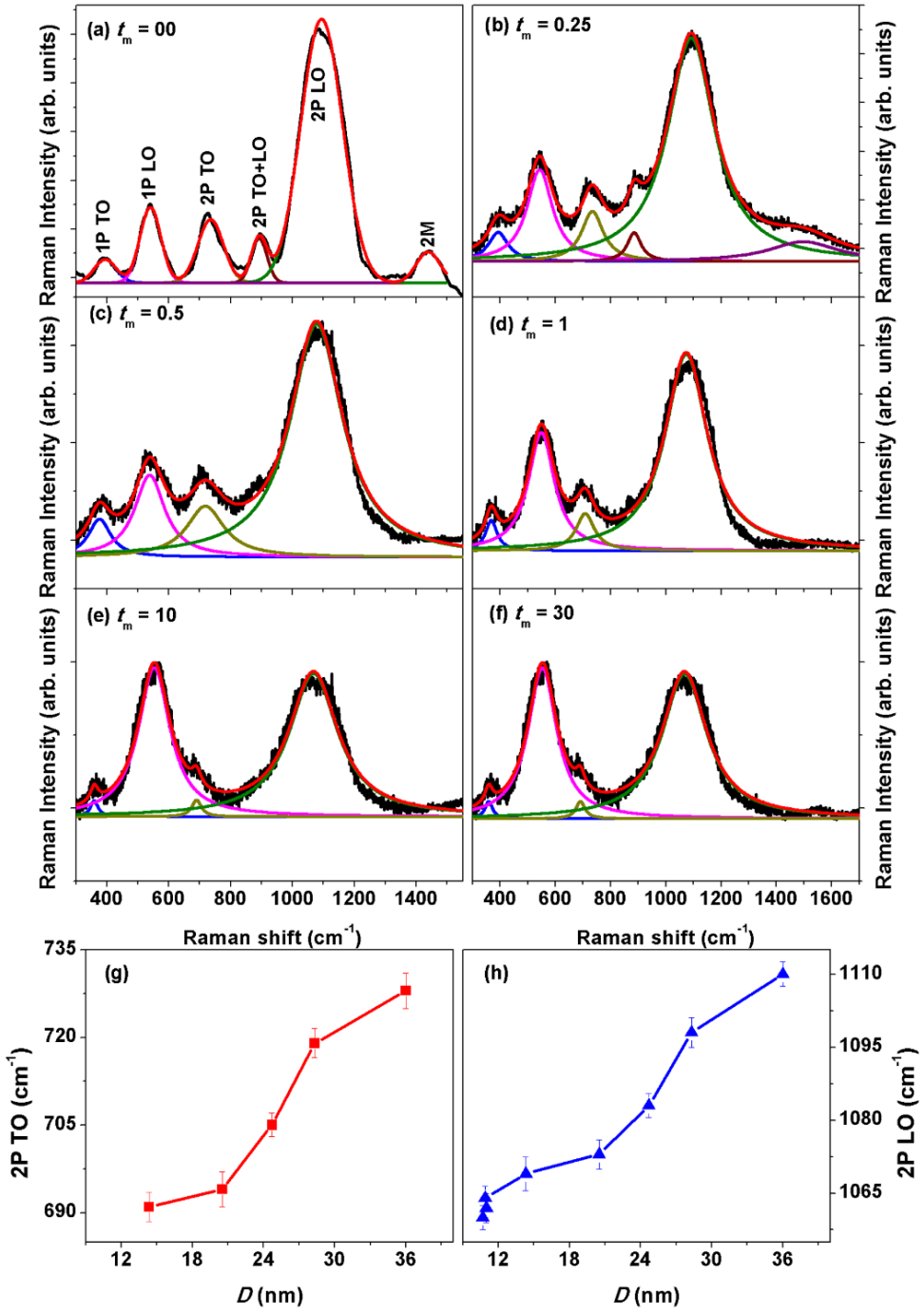

Figure 4.09: (a-f) Room temperature Raman spectra of pure un-milled and milled NiO powders at different t_m. All the modes are marked in (a). The variations of 2P TO (g) and 2P LO (h) modes with average crystal size (D) for NiO powders.

Although the perfect cubic and rhombohedral structured NiO should not show 1P LO band, which is generally attributed to the disordered induced defects, surface effects, imperfectness of the particles size and shapes [ULMA2007], the existence of a weak 1P LO band was observed in NiO by many groups [WANG2002, LUML2011] including for single crystal like particles [ULMA2007]. Therefore, the observation a weak 1P LO band in pure NiO is assumed to be typically good quality NiO crystals. In addition, the presence of 2M band confirms that the pure un-milled NiO power exhibits AFM state at room temperature. On the other hand, with increasing t_m, the 2M band decreases dramatically for $t_m = 0.25$ and disappears within the detection limit of the system even for the powders milled for 0.5 hrs. This may be attributed to breaking of Ni^{2+}-O^{2-}-Ni^{2+} super-exchange interaction due to either defects or size reduction induced by the ball milling process. Cazzanelli et al [CAZZ2003] studied vibrational and magnetic excitations in $Ni_cMg_{1-c}O$ solid solutions and observed that a large decrease in 2M band intensity upon dilution with Ni ions. This lowers local symmetry at the Ni^{2+} sites and the dependence of the 2M band in solid solutions on the composition and temperature is consistent with their magnetic phase diagram.

Similarly, Ulmane et al [ULMA2007] and Gandhi et al [GAND2011] observed a large decrease in 2M band intensity with decreasing crystal size and attributed to the decrease of AFM spin correlations. This suggests that the decrease and disappearance of 2M band intensity in milled NiO powders is due to the decrease of Ni^{2+}-O^{2-}-Ni^{2+} spin correlation length both by defects and size reduction. At the same time, the 1P LO band becomes clearly pronounced and broadened with decreasing crystal size. This could be attributed to induced defects, surface effects and imperfectness of particle shape and sizes caused by the milling process as evident from Figures 4.07 and 4.08. On the other hand, the phonon bands of the Raman spectra exhibit the following features: (i) The 2P TO+LO band displays a large decrease in its intensity with increasing t_m up to 0.5 hrs and then disappears eventually for the rest of the milled NiO samples. (ii) The 2P TO and 2P LO bands exhibit more broadening and the peak positions shift to lower value significantly. To understand the size dependent Raman vibration, the variations of 2P TO and 2 P LO bands as a function of crystal size were plotted in Figures 4.09(g) and (h). With decreasing crystal size, the phonon vibration frequency decreases considerably, which can be ascribed to size-induced phonon confinement, presence of defects in fine nanocrystals and surface relaxation effects caused by the lattice expansion as observed in Figure 4.06 [YANG2008, PROE2011, DUAN2012].

4.3.3. Electronic properties

In order to understand the chemical composition of pure un-milled and as-milled NiO powders, XPS survey spectra and Ni 2p, O 1s and C 1s spectra were obtained for both pure un-milled and milled NiO powders and depicted in Figures 4.10 and 4.11. In the survey spectra, the presence of Ni, O and its satellite peaks and C is observed. Ni 2p spectrum of pure NiO powder [see Figure 4.10(b)] displays five fitted peaks in two regions: Ni-2p$_{3/2}$ (848-867 eV) and Ni-2p$_{1/2}$ (867-885 eV) spin-orbit levels. The Ni-2p$_{3/2}$ and Ni-2p$_{1/2}$ peaks are observed at 854.4 eV and 873 eV, respectively along with their satellite peaks at 861.6 eV and 879.8 eV.

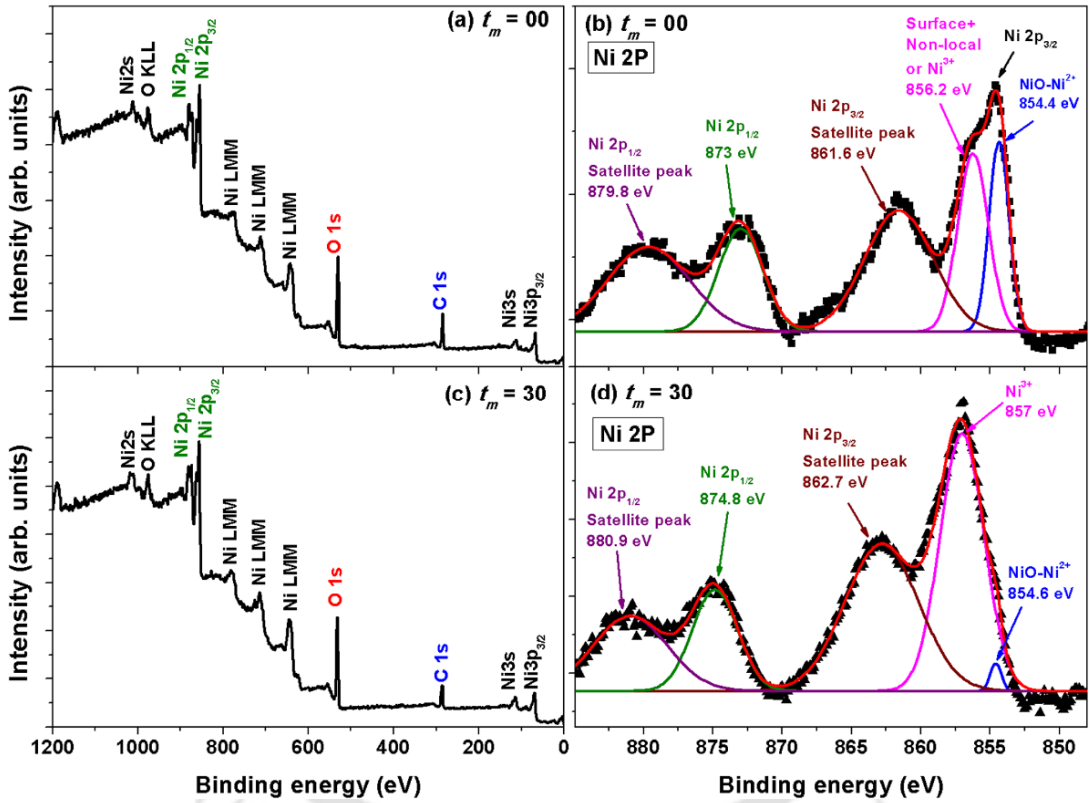

Figure 4.10: (a,c) Wide scan survey XPS spectra and (b,d) Ni 2p XPS spectra for pure un-milled and 30 hrs milled NiO powders.

The value of binding energy difference between Ni-2p$_{3/2}$ and Ni-2p$_{1/2}$ peaks is about 18.6 eV, which confirms the dominance of NiO [UHLE1992]. The NiO satellite peaks may arise due to various causes such as multi-electron excitations, multiple scattering or surface plasmon loss [SANZ1996]. In addition, Ni 2p spectrum exhibits a shoulder shifted by 1.8 eV toward higher binding energies from the main line, whose interpretation is still controversial [PRED2008]. Soriano et al [SORI2007] reported that the main line intensity comes from the Ni atoms octahedrally coordinated in the bulk, while the part of the intensity of the shoulder

labelled as surface + non-local comes from the pyramidally coordinated Ni atoms at the NiO surfaces. Peck et al [PECK2012] compared the XPS spectra of nanoscaled and bulk NiO and showed that the shoulder peak exists for bulk and nanoscale NiO down 5 nm. The shoulder peak has been reported to contain a partial contribution from surface states [GROS2006, MOSS2011]. On the other hand, Jing et al [JING2015] proposed the observation of such peak as one of the satellite peaks of Ni-$2p_{3/2}$. Recently, Rajagopal Reddy et al [RAJA2016] reported that the observation of peak at 856.2 eV is due to Ni^{3+}, as Ni^{2+} ions oxidize to Ni^{3+} ions to maintain neutral charge [JIAN2002]. To understand the origin of the shoulder in details, the detailed O 1s and C 1s spectra of the bulk NiO are recorded between 522 eV and 540 eV, and between 275 eV and 300 eV, respectively and shown in Figure 4.11. We observed two distinct peaks at 530.1 and 531.8 eV specifically related to the typical Ni-O bonds from Ni^{2+} and Ni^{3+}, respectively [ZHAO2009, RAJA2016, YOON2016, ADHI2017]. The signal from the former Ni-O is stronger than the latter, which suggests that Ni^{2+} is the dominant species [LIUC2016]. The C 1s spectrum reveals three peaks at 284.8, 286.4 and 288.6 eV, which are due to adventitious carbon species corresponding to the C-C, C-O and OH-C=O bonds, respectively.

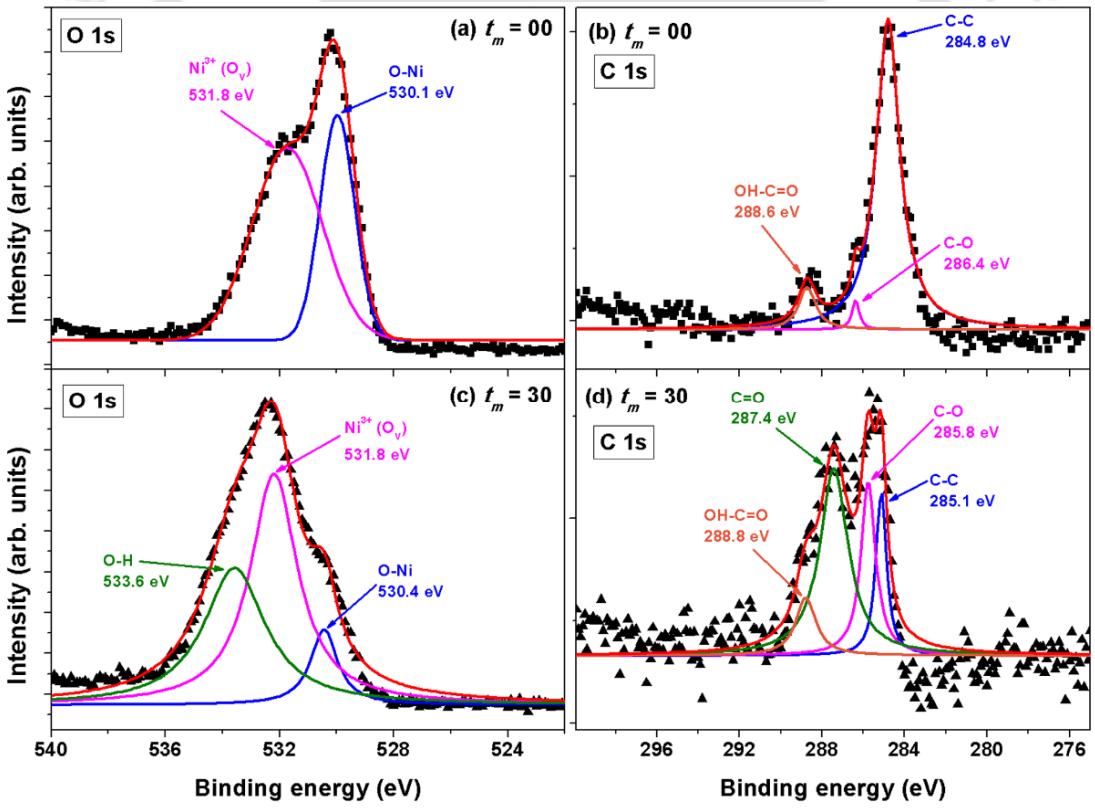

Figure 4.11: (a,c) O 1s XPS spectra and (b,d) C 1s XPS spectra for pure un-milled and 30 hrs milled NiO powders.

On the other hand, the milled NiO powders exhibit significantly different features in Ni 2p, O 1s and C 1s spectra, despite having similar survey spectrum. For instance, the binding energy difference between Ni-$2p_{3/2}$ and Ni-$2p_{1/2}$ peaks increases slightly to 20.2 eV and the peaks of Ni 2p are broadened. Importantly, the signal from Ni^{3+} peak at 857 eV enhances largely at the expense of Ni^{2+} peak intensity at 854.6 eV. This clearly supports the presence of non-stoichiometry in the milled samples due to decrease in Ni^{2+}-O^{2-}-Ni^{2+} spin correlation length caused by defects and size reduction. This is further supported from O 1s spectrum, where the signal from O-Ni bond of Ni^{2+} decreases and Ni^{3+} increases largely after the milling process. In addition, we observed additional peak at 533.6 eV, which can be ascribed to adsorbed water on the surface. The C 1s spectrum of milled NiO powders shows four peaks at 285.1, 285.8, 287.4 and 288.8 eV that are due to C-C, formation of C-O, C=O and OH-C=O bonds, respectively. The relative intensities of the peaks strongly depends on the milling conditions. These results are in very good agreement with vibrational properties.

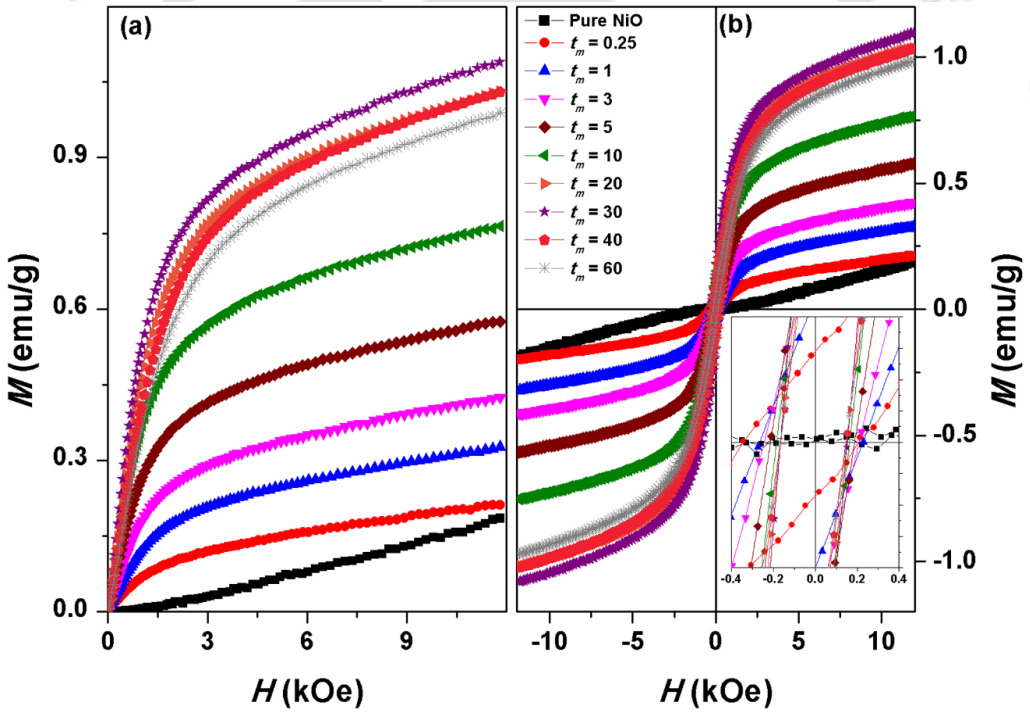

Figure 4.12: Room temperature (a) initial magnetization curves and (b) *M-H* loops of pure un-milled and milled NiO powders at different t_m. Inset shows the expanded view of *M-H* loops close to origin.

4.3.4. Magnetic properties

Figure 4.12 depicts room temperature initial magnetization (*IM*) curves and magnetic hysteresis (*M-H*) loops and expanded version of *M-H* loops close to origin (inset) for pure un-

milled and milled NiO powders at different t_m. It is observed that (i) pure un-milled NiO powder exhibits a weak response to applied field due to its AFM nature and *M-H* loop passes through the origin. (ii) On the other hand, the milled NiO powder exhibits different nature of response to the applied field, i.e., the magnetization increases moderately at lower applied fields and then shows a gradual increase at higher applied fields. The rate of increase in the magnetization at lower field increases progressively with increasing t_m up to 30 hrs and then decreases slightly with increasing t_m > 30 hrs. (iii) *M-H* loops are shifted slightly to negative axes (see inset of Figure 4.12(b)), but the amount of shift decreases with increasing t_m.

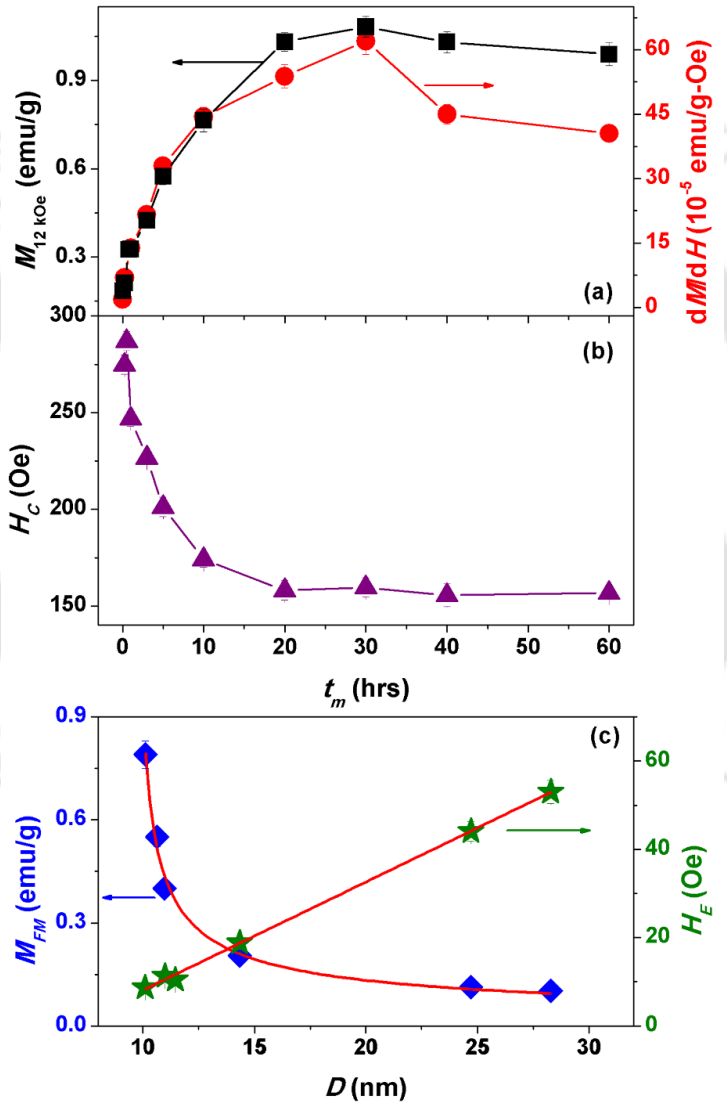

Figure 4.13: The variations of (a) magnetization obtained at 12 kOe (M_{12kOe}) and maximum change in *dM/dH* and (b) coercivity (H_C) as a function of t_m. (c) The variations of M_{FM} derived from eqn.(4.05) and H_E as a function of average crystal size (D). The solid lines passing through the data are the best fit to eqns.(4.06) and (4.07).

These results reveal that there are two possible magnetic components associated with the magnetization reversal process. As the bulk NiO powder exhibits a clear AFM nature and the milling of NiO powders produces defects and size reduction with the lattice expansion, the two-component nature can be ascribed to an easily magnetizing component at low-field regions and a non-saturating component responsible for a linear variation in the high-field region. These components can be extracted by fitting *IM* curves by eqn.(4.05)

$$M(H) = M_{FM}(H) + \chi_{AFM} H \tag{4.05}$$

where $M(H)$ is the magnetization variation as a function of applied field (H), M_{FM} is the magnetization due to easily magnetizing component, χ_{AFM} is AFM susceptibility. Figure 4.13 depicts the extracted values of magnetization at 12 kOe (M_{12kOe}), the maximum change in the magnetization with applied field in low-field region (dM/dH), coercivity (H_C) as a function of t_m, and the determined value of M_{FM} from the eqn.(4.05) and the calculated values of exchange bias, H_E [= $(|H_{C+}|-|H_{C-}|)/2$] plotted as a function of average crystal size. M_{12kOe} increases regularly with increasing t_m up to 30 hrs and then decreases slightly for t_m > 30 hrs, resulting in a maximum in the curve at around 30 hrs of milling. Similarly, the value of dM/dH also increases with increasing t_m up to 30 hrs and then decreases above 30 hrs of milling. On the other hand, H_C of pure NiO, observed as zero due to its AFM nature, has increased significantly (~ 290 Oe) after milling. With increasing t_m, H_C decreases from 290 Oe to about 160 Oe after milling for 20 hrs and then remains almost constant for t_m > 20 hrs. In order to understand any correlation between structural and magnetic parameters, the determined values of M_{FM} from eqn.(4.05) and H_E are plotted as a function of NiO crystal size in Figure 4.13(c). Interestingly, M_{FM} increases gradually with decreasing crystal size up to 15 nm and then exhibits a large increase below 15 nm. The relationship between M_{FM} and the crystal size has been closely approximated by using three-parameter empirical model [SEBE2003] as given in eqn.(4.06).

$$M_{FM}(D) = (x + y.D)^{-1/z} \tag{4.06}$$

where $M_{FM}(D)$ is the crystal size dependence of induced FM component, x, y and z are constants. The fitting of the experimental data yields the values of x, y and z as -31, 3.1 and 1.7, respectively. On the other hand, H_E decreases almost linearly with decreasing crystal size. This suggests that NiO transforms into induced FM at the expense of parent AFM behavior. To obtain the effect of crystal size, the variation of H_E with crystal size was fitted to eqn.(4.07).

$$H_E(D) = H_E(0) + m.D \tag{4.07}$$

where $H_E(D)$ is size dependent exchange bias, $H_E(0)$ is size independent exchange bias component and m is a constant. The fitting of the experimental data provides $H_E(0)$ = -18.94 Oe and m = 2.66 Oe/nm.

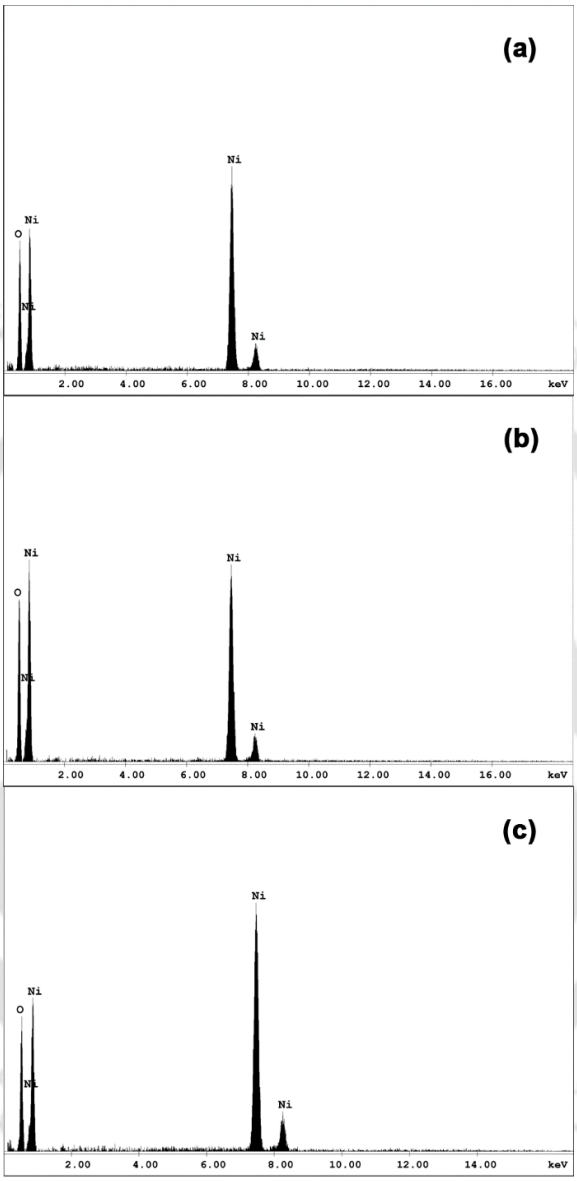

Figure 4.14: Energy dispersive X-ray spectrum for (a) pure un-milled and milled NiO powders at (b) t_m = 5 hrs and (c) t_m = 30 hrs.

To understand the origin of the observed FM in the milled NiO powders, we correlate both the structural and magnetic properties. In pure un-milled NiO (pale green colored) powder, spins within AFM coupled (111) planes are compensated as shown in Figure 2.01(b) and hence do not contribute to net magnetic moment [KODA1997, THOT2007, ULMA2007,

WINK2008]. Therefore, the *M-H* loop of un-milled NiO powder exhibits a weak response to the applied magnetic field and passes through origin. It is well-known that ball milling process promotes large size reduction and massive defects including the creation of vacancies in NiO. Structural analysis confirmed that the values of D decrease and, η and V increase with increasing t_m. In addition, pale green color of the pure un-milled NiO changed into dark green with milling, which can be related to the development of non-stoichiometric in NiO powders induced by the defects, size reduction and oxidization of Ni^{2+} into Ni^{3+} [AHMA2006]. This influences a change in the magnetic properties as follows: With increasing t_m, the Ni^{2+}-O^{2-}-Ni^{2+} super-exchange interaction diminishes due to defects and size reduction as evidenced from Raman and XPS spectra results and the number of uncompensated spins on the surfaces with respect to particle core increases [PECK2011]. This leads to an alignment of particles' net moment in a relatively low magnetic field. Under this circumstance, the exchange coupling between the induced FM at the surface and the spins of AFM core instigates the exchange bias effect. In addition, the formation of structural disorder due to the formation of defects (oxygen vacancies) also induces the net magnetization. Therefore, the magnetization of nanostructured NiO increases as expressed in eqn.(4.06) and the exchange bias effect decreases with decreasing crystal size as seen through eqn.(4.07). Furthermore, the lattice expansion in presence of defects and broken bonds, and possible surface anisotropy play a crucial role in controlling the Ni^{2+}-O^{2-}-Ni^{2+} super-exchange interaction and magnetic exchange interaction between uncompensated surfaces spins and particle core spins. These results confirm a good correlation between structural, vibrational, electronic and magnetic properties of NiO powders.

To further confirm the origin of the induced FM and to rule out any expected impurities contribution, magnetic structure, chemical bonding state and chemical compositions were analyzed using ^{57}Fe Mössbauer spectroscopy, XPS and EDS, respectively. In addition, the as-milled NiO powders at different t_m were annealed systematically at high temperatures under air atmosphere. The presence of impurities could not be detected in the magnetic structure using ^{57}Fe Mössbauer spectroscopy, chemical bonding using XPS (see Figures 4.10 and 4.11) and composition analysis using EDS (see Figure 4.14) at least to the detection limit of these techniques. As shown in Figures 4.10 and 4.11, XPS spectra of milled NiO powders reveal the existence of a mixed valency state of Ni supporting the presence of non-stoichiometry in the milled NiO powders [JIAN2002, GROS2006, MOSS2011, RAJA2016]. Figure 4.15 depicts *M-H* loops of pure NiO, milled NiO powders at different t_m and annealed NiO powders at different temperatures (T_A). *M-H* loops of pure un-milled and annealed NiO powders exhibit

almost a similar nature, i.e., a weak response to applied field due to its AFM nature and *M-H* loop passes through the origin. On the other hand, with increasing T_A for the as-milled powders, the magnetic moment reduces largely.

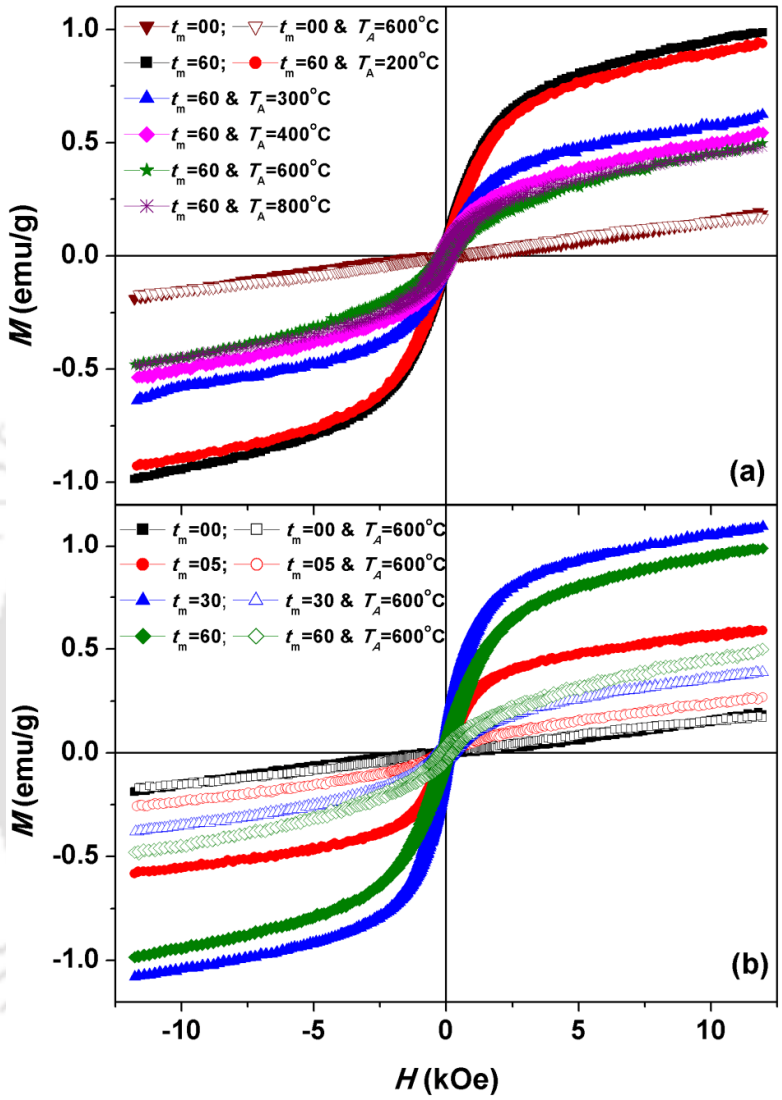

Figure 4.15: Room temperature *M-H* loops of (a) pure un-milled NiO powder and NiO powders milled at 60 hrs and annealed at different T_A for 3 hrs and (b) pure un-milled NiO powder and milled NiO powders at different t_m and annealed at 600 °C for 3 hrs.

To understand the effect of milling condition systematically, we have annealed the NiO powders milled at different t_m and displayed in Figure 4.15(b). The extracted values of M_{12kOe} for milled and annealed NiO powders are shown as a function of T_A in Figure 4.16. It is clear from the Figure 4.16 that the value of M_{12kOe} decreases from 0.59, 1.08 and 0.99 emu/g to 0.25, 0.39 and 0.5 emu/g for 5, 30 and 60 hrs milled NiO powders, respectively after annealing at

600 °C. The rate of decrease in magnetization with T_A strongly depends on the milling conditions, which can be related to the release of accumulated strain (defects), reduction of Ni^{3+} into Ni^{2+} [TADI2014] and increase in average value of D with annealing.

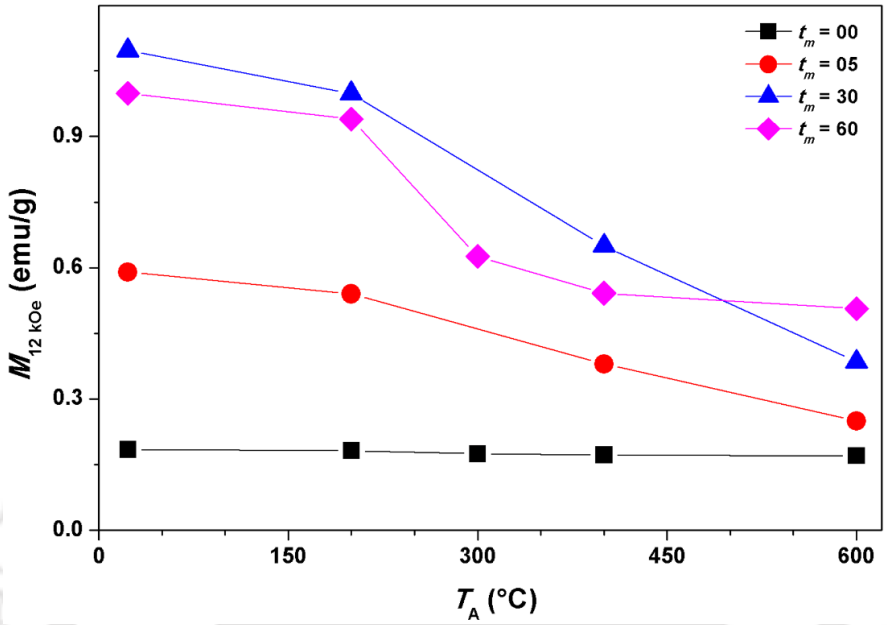

Figure 4.16: The variations of M_{12kOe} as a function of annealing temperature (T_A) for pure un-milled and milled NiO powders annealed at different T_A.

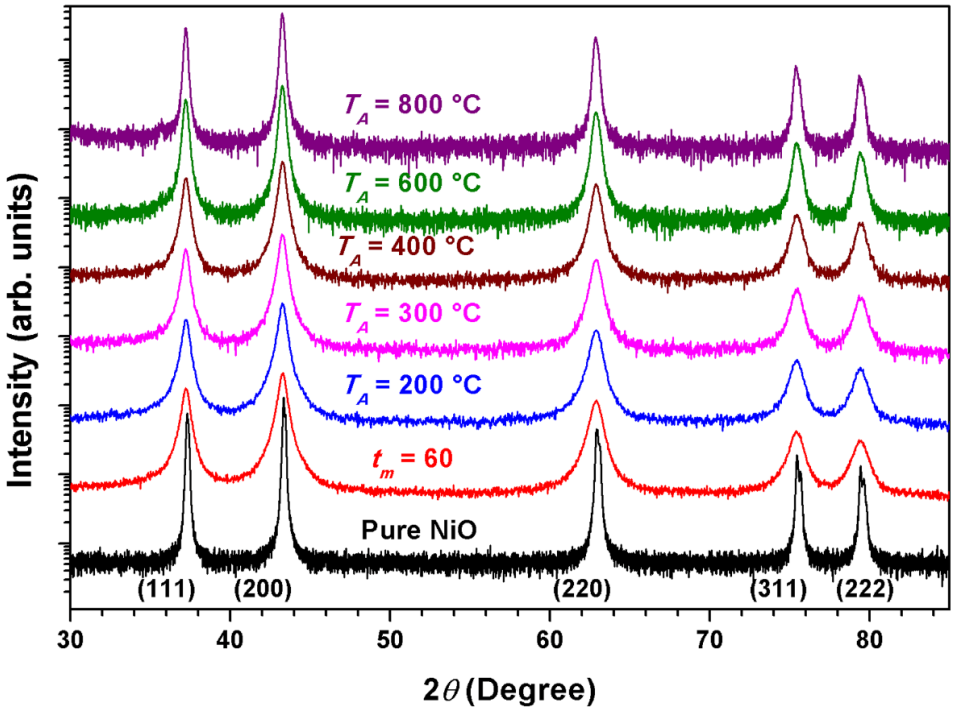

Figure 4.17: Room temperature XRD patterns of pure un-milled NiO powder and NiO powders milled at 60 hrs and annealed at different temperatures (T_A) for 3 hrs.

To study the effect of annealing on the structural properties of annealed powders, we have obtained XRD patterns for the annealed NiO powders and shown in Figure 4.17. It is observed that the peak width in the XRD patterns of the annealed powders reduces progressively up to 300 °C, but decreases considerably with increasing T_A > 300 °C. The decrease in the peak width with increasing T_A in the annealed powders can be correlated to the growth of the NiO crystals and the relaxation of strain accumulated in the as-milled powders. In order to evaluate the structural refinement carefully, XRD patterns were analyzed using MWHP and the determined values of D and η are plotted as a function of T_A in Figure 4.18.

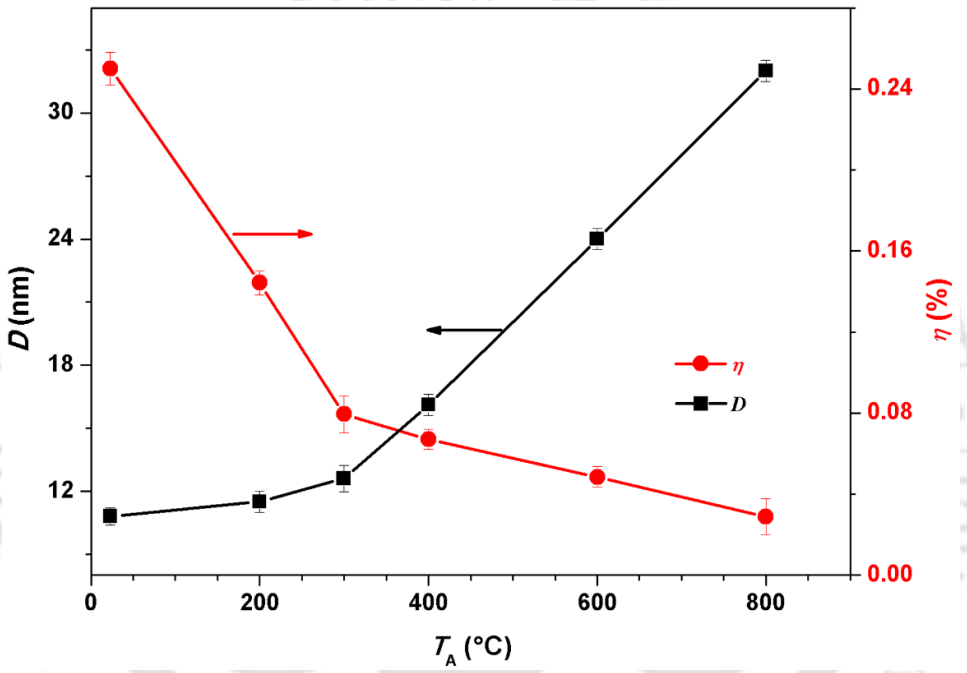

Figure 4.18: Variations of average crystallite size (D) and effective strain (η) with T_A for milled and annealed NiO powders.

The values of D increase gradually from 10.8 nm to 12.6 nm with increasing T_A up to 300 °C and then exhibit a large increase at a rate of 0.039 nm/°C above 300 °C. On the contrary, the variation of η with T_A displays two different regimes: (1) the values of η decrease largely from 0.25 % to 0.079 % up to 300 °C and then (2) decreases gradually from 0.079 % to 0.029 % with increasing T_A from 300 °C to 800 °C. These results confirm that the annealing process not only reduces the strain revealing that the dislocations/defects in the annealed powder decreases with increasing T_A, but increases D significantly with increasing T_A. NiO powder annealed at 800 °C exhibits the average crystallite size of about 31 nm. These results confirm that the observed FM properties in NiO powders are intrinsic one, i.e., the magnetization of the

as-milled powder decreases largely due to the release of strain (defects), reduction of Ni^{3+} to Ni^{2+} [HONG2006, TADI2014] and increase in the value of *D* with annealing. These processes eventually transform the induced FM into AFM nature in the annealed NiO powder with increasing D. This is in good agreement with the earlier reports by Thota et al [THOT2007] that magnetism of the NiO particles at room temperature changes from FM to AFM nature with increasing particle size. Nevertheless, the relative reduction in magnetization of annealed powders strongly depends on the milling conditions and the release of strain accumulated in the milled powders.

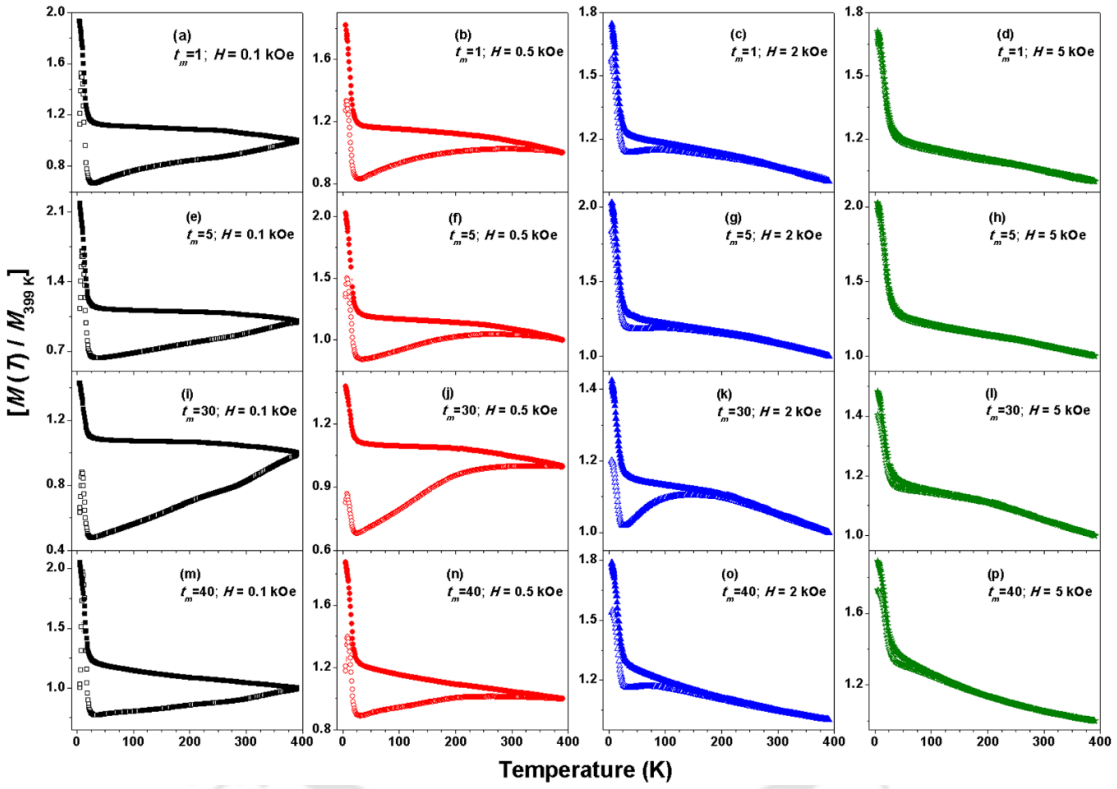

Figure 4.19: Low temperature *M-T* data of milled NiO powders at different t_m and measured under different applied magnetic fields.

To understand the effect of temperature and magnetic field on the magnetic properties of NiO powders milled at different t_m, low temperature *M-T* measurements at different constant applied fields under ZFC and FC conditions were performed in the temperature range between 2 K and 400 K. In these measurements, the sample was initially cooled down to 2 K under zero applied magnetic field. Then a probing constant DC magnetic field was applied to measure the magnetization as a function of temperature during warming process up to 400 K (ZFC process). Subsequently, the sample was cooled in the same constant applied field down to 2 K and then

the magnetization was recorded as the sample was heated to 400 K (FC process). Figure 4.19 displays normalized magnetization [$M(T)/M_{399K}$] as a function of temperature for the NiO powders milled at 1, 5, 30 and 40 hrs measured under ZFC (M_{ZFC}) and FC (M_{FC}) conditions at different applied magnetic field of 0.1, 0.5, 2 and 5 kOe. A bifurcation (T_{bifur}) between the M_{ZFC} and M_{FC} was observed at around 390 K for all the samples measured at low applied magnetic fields. Interestingly, the value of T_{bifur} shifts to low temperature with increasing applied field. It is generally accepted that the existence of T_{bifur} indicates a broader magnetic moment distribution, which originates from the broad size distribution of the crystals [ZYSL2000, DEBI2002, WINK2005, DELB2008]. In addition, M_{ZFC} curve presents two peaks: (i) a broad peak centered at a temperature below the T_{bifur} and (ii) another sharp peak at very low temperature below 10 K. These two peaks in the M_{ZFC} curve corresponds to two types of blocking processes, i.e., the peak (T_{broad}) below T_{bifur} can be attributed to the thermal relaxation of uncompensated spins, while the sharp peak at low temperature (T_{fz}) represents the freezing of disordered surface spins. A careful review of the literature revealed that T_{fz} depends on the size of the particles. Peck et al [PECK2011] reported only the observation of paramagnetic tail without any sharp T_{fz} at low temperature for the NiO nanoparticles of size around 18 nm. Duan et al [DUAN2012] reported that the values of T_{fz} as 10.4 K for 12.4 nm sized NiO. Meneses et al [MENE2010] obtained a T_{fz} of 11 K for NiO nanoparticles with the size of 5.8 nm. Similarly, Winkler et al [WINK2008] also observed a slightly higher T_{fz} of 17 K for 3 nm NiO powder. On the other hand, Meneses et al [MENE2010] and Tadic et al [TADI2011] reported a lower value of T_{fz} of 9 K and 6.5 K for 5.8 nm NiO nanoparticles dispersed in polyvinyl pyrrolidone and 3 nm NiO nanoparticles embedded in Silica matrix, respectively. The value of T_{fz} in Figure 4.19 are found to be 8.4 K, 9.7 K, 10.2 K and 11.1 K for the NiO powders milled at 14.4 nm, 11.5 nm, 11 nm and 10.8 nm, respectively. This is in close agreement with the results reported in literature indicating that the size dependent surface states of the fine NiO powders have significant effects on the freezing of the surface spins, i.e., the fraction of atoms lying on the surface of the powders increases with decreasing crystallite size. This leads to an increase in surface disorder with decreasing crystal size and accounts for increased value of T_{fz} with decreasing size. On the other hand, M_{FC} data are observed to increase gradually with decreasing temperature down to about 35 K for all the samples measured at different applied fields and then exhibit rapid increases in magnetization down to 4.2 K, which could be attributed to the surface spin freezing. Interestingly, none of the samples show any peak in M_{FC} curves under FC process, which is again in good agreement with the earlier reports [GHOS2006, MENE2010, PECK2011, TADI2011, ULMA2011]. With increasing the magnitude of applied

field, the difference between M_{ZFC} and M_{FC} data decreases up to 2 kOe. On further increasing the field to 5 kOe, both M_{ZFC} and M_{FC} data follow almost a similar variation with decreasing temperature.

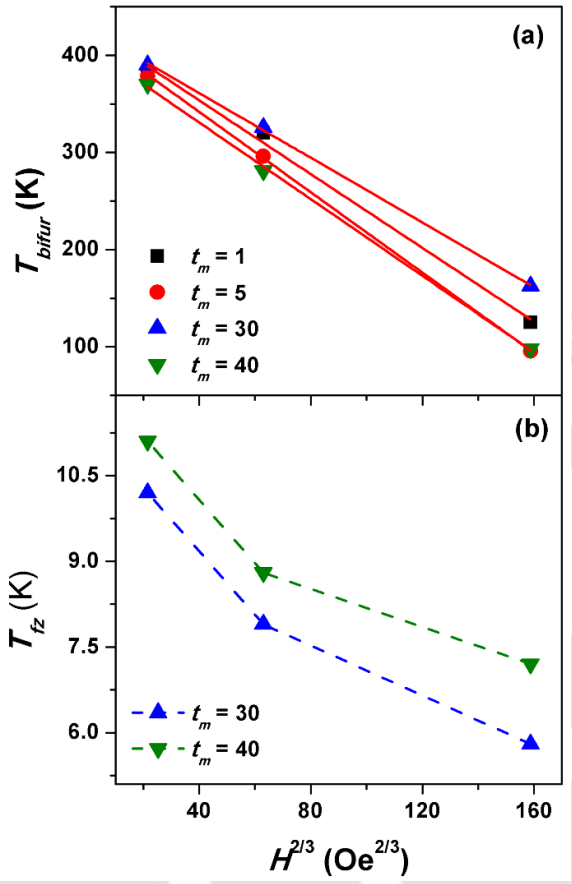

Figure 4.20: Plots of (a) T_{bifur} versus $H^{2/3}$ and (b) T_{fz} versus $H^{2/3}$ for the milled NiO powders at different t_m. The solid lines (in (a)) show linear fits to the data using eqn.(4.08) with R^2 of 0.995, 0.9986, 0.9991, 0.9982 for t_m = 1, 5, 30 and 40 hrs, respectively.

To elucidate the nature of magnetism and reason for the freezing of particle magnetic moments, the field dependent values of T_{bifur} and T_{fz} were plotted as a function of field in Figure 4.20 with de Almedia-Thouless (AT) line [ALME1978, YIJJ2008] described by eqn.(4.08).

$$H_{AT}(T) \propto \left(1 - T_{bifur} / T_{sg}\right)^{1.5} \qquad (4.08)$$

It is clearly seen that T_{bifur} decreases with increasing applied field and compliance with the AT line. This is considered to be a supportive evidence for the existence of spin glass like phase in the presently investigated samples. This could be described as follows: As evident from the Raman spectra (Figure 4.09), the exchange interaction between two neighboring Ni^{2+} ions in bulk NiO is mediated by an oxygen ion, which results in 2M scattering associated with Ni^{2+}-

O^{2-}-Ni^{2+} super-exchange interaction. With increasing t_m, the 2M band disappears due to either size reduction or defects, which create vacancies. For instance, if an oxygen ion misses from the surface, the exchange bond would be broken and the exchange interaction energy would be reduced. Furthermore, the average coordination number of Ni^{2+} ions at the surface changes than that in the bulk, which results in a distribution of exchange energies for the surface spins and color change of the powder due to non-stoichiometric in NiO [AHMA2006]. This gives rise to surface spin disorder and frustration leading to a spin glass phase in the presently investigated samples [KODA1997, MART1998, PECK2011]. In contrast, the variation of T_{fz} with the applied field does not follow AT line. This could be attributed to the different rate of change of T_{fz} with field upon decreasing the size of the NiO crystals [TIWA2005, THOT2007] with increasing t_m.

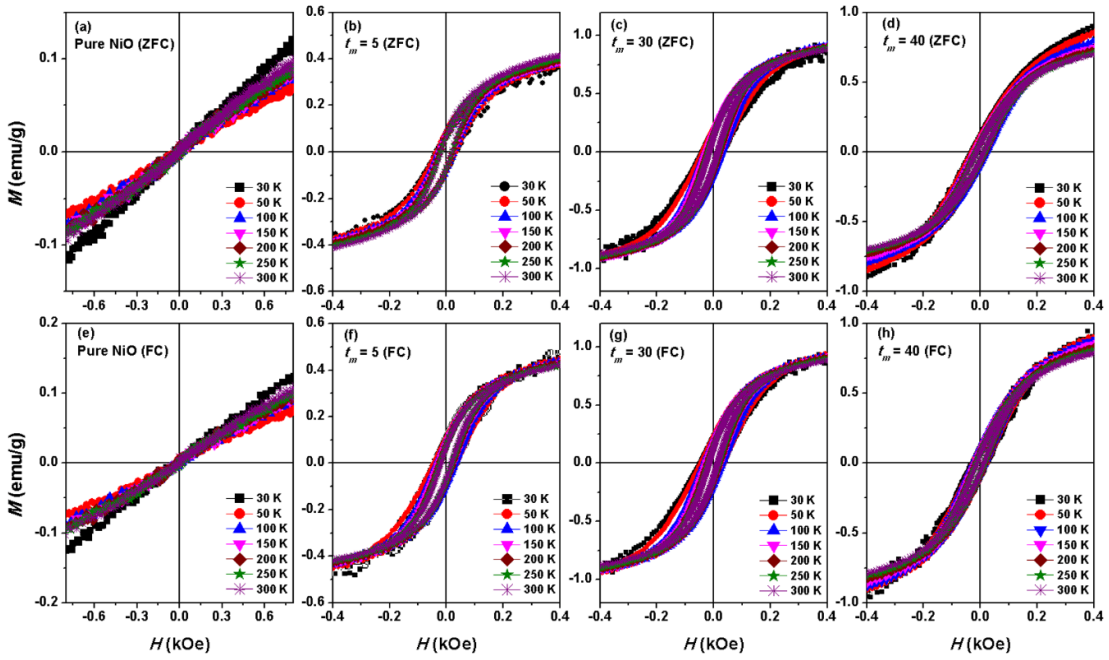

Figure 4.21: Temperature dependent *M-H* loops of pure un-milled NiO and milled NiO powders at different t_m measured under ZFC and FC conditions.

To study the effects of structural refinement on the magnetic properties, *M–H* loops were measured at different temperatures between 30 K and 300 K under ZFC and FC (cooled under 500 Oe applied field) conditions. Figure 4.21 shows expanded view of typical *M-H* loops measured under ZFC and FC conditions for pure un-milled NiO and milled NiO powders milled at 5, 30 and 40 hrs. It is observed that pure NiO powder exhibits a weak response to applied field due to its AFM nature and the shape of the loops measured under ZFC and FC

conditions does not change with temperature. Similarly, while the loop shape of the milled powders does not change with temperature, the applied field of 14 kOe is not enough to saturate the loops. However, the variation of H_C and area under the loop increases considerably with decreasing temperature. A careful observation of the loop nature suggests that NiO powders exhibit more shift towards negative axis with decreasing temperature under FC condition.

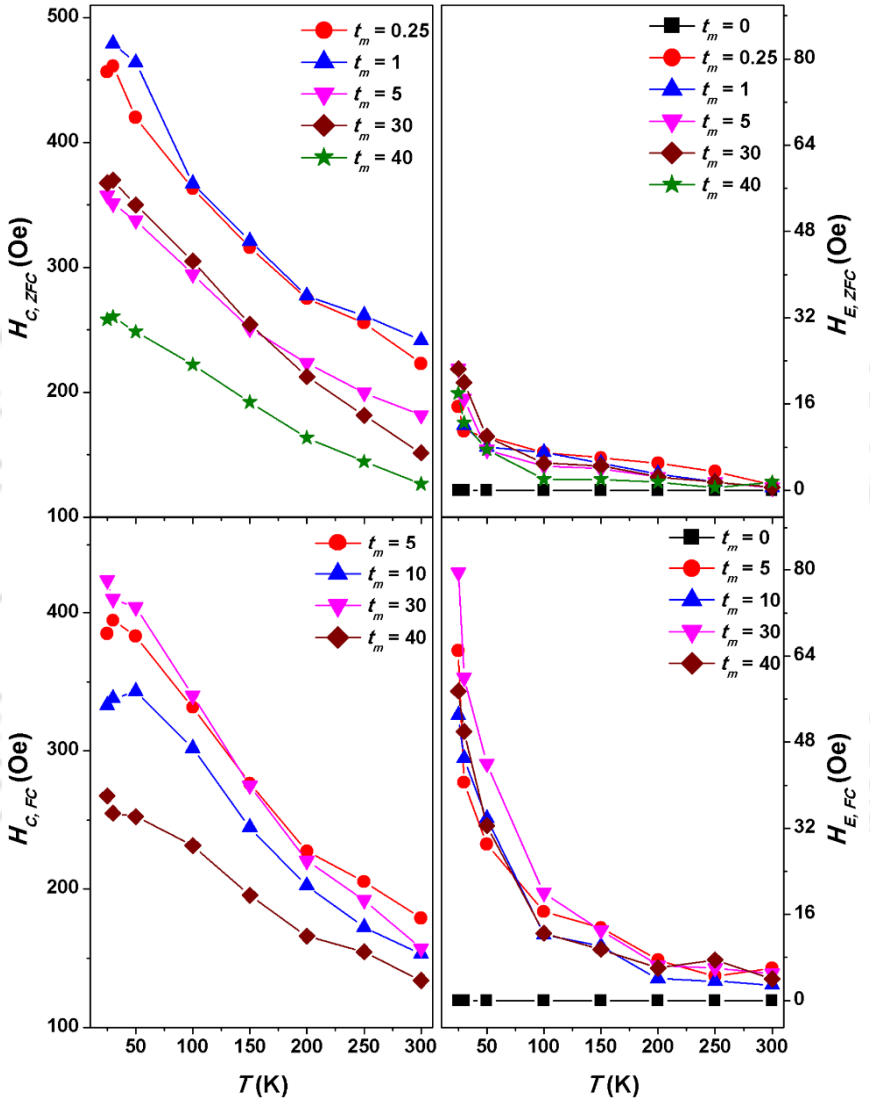

Figure 4.22: The variations of H_C and H_E as a function of temperature for pure un-milled and milled NiO powders under ZFC and FC conditions.

In order to understand the effect of temperature and FC on various magnetic parameters, the values of H_C and H_E are extracted from Figure 4.21 and plotted as a function of temperature in Figure 4.22. $H_C(T)$ of the milled NiO powders increases with decreasing temperature and the amount of increase in H_C strongly depends on the size of the NiO crystal and measurement

conditions. On the other hand, the variations of $H_E(T)$ obtained under ZFC conditions exhibit weak dependence on temperature, i.e., H_E increases gradually with decreasing temperature and exhibits a maximum of about 24 Oe at 30 K. In contrast, the FC conditions show larger variations with decreasing temperature particularly at low temperatures below 200 K, where the spin glass like behavior was observed for these powders. NiO powder milled at 30 hrs displays a maximum H_E of about 80 Oe at 30 K. This could be related to the fact that FC condition promotes additional anisotropy between freezing surface spins and compensated spins at the core due to the existence of spin glass phase. These results are in good agreement with the results of low temperature *M-T* data.

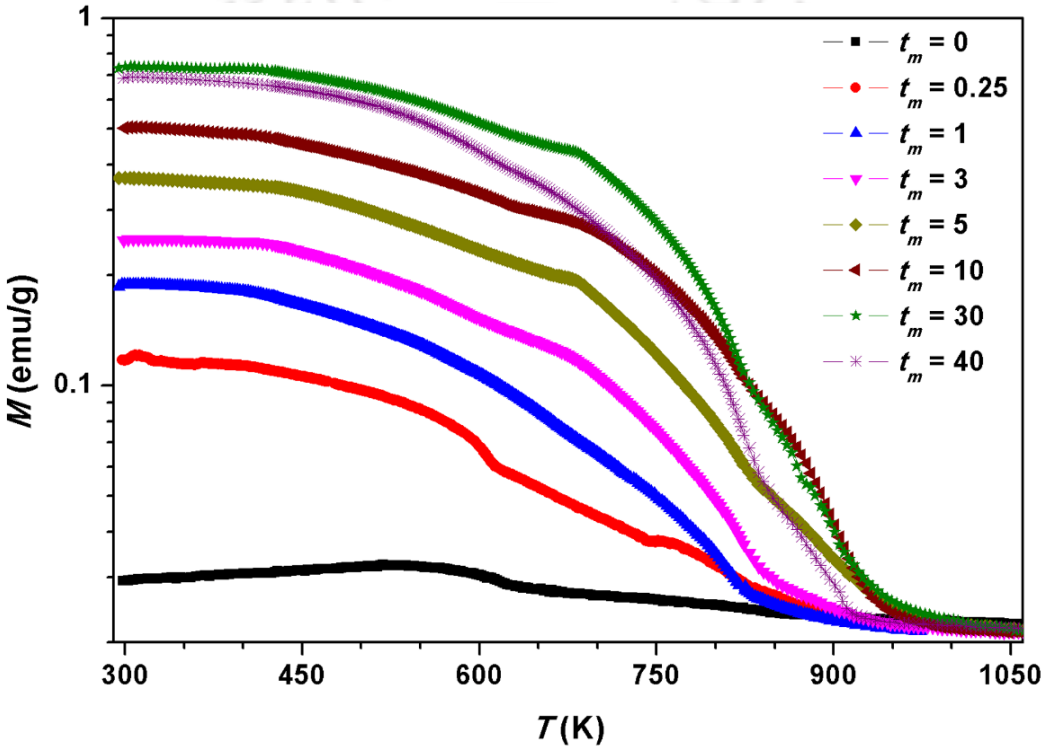

Figure 4.23: High temperature *M-T* data of pure un-milled and milled NiO powders at different t_m and measured under the applied magnetic field of 2 kOe.

To study the stability of induced FM behavior due to size and defects, high temperature *M-T* curves were measured at 2 kOe applied field with a heating rate of 4 °C/min from 300 K to 1100 K and depicted in Figure 4.23. For pure un-milled NiO powder, magnetization increases gradually with increasing temperature up to 525 K and then decreases above 525 K. Since, the pure NiO powder exhibits AFM nature at room temperature, the Néel temperature (T_N) is determined from the peak in *M-T* curve and found to be about 525 K. This is in good agreement with the earlier reports [THOT2013, MONT2016]. On the other hand, NiO powders

milled for different t_m exhibit enhanced magnetic moment, which is nearly constant close to room temperature regime and then decreases with increasing temperature. While the powder milled at 0.25 hr display a broad hump around 530 K, the NiO powders milled for more than 1 hr exhibit a continuous decrease in magnetization with increasing temperature. The temperature at which the magnetization becomes zero shifts to higher temperature with increasing t_m up to 30 hrs and then decreases slightly for t_m > 30 hrs. The thermal derivative of *M-T* data exhibits two minima: one close to T_N and another broad minimum around 780 K. This clearly supports the existence of two magnetic phases in milled NiO powders. Although the high temperature phase transition (T_C) should be associated with the Ni due to the formation of uncompensated surface spin, the value of T_C is considerably large as compared to its bulk counterpart (~ 630 K) [DAVI2000, LEGE2011]. This could be correlated to the stress induced during the ball milling process [LEGE1972, GORR2009] or strains due to the Ni and NiO lattice-constant mismatch arising at the interface and competing exchange interaction between the induced FM and AFM core. The presence of stress is evident from non-smooth decrease of magnetization in *M-T* curves, which acts more like hydrostatic one and hence increases T_C [LEGE1972]. Interestingly, such high T_C (~ 750 K) has also been reported in Ni/NiO system [FEYG2010] and Ni doped TiO_2 system (~ 820 K) [BAHA2012].

4.3.5. Resonance properties

EPR spectroscopy is a suitable technique for studying the materials with defects and states with unpaired electrons. As the presently investigated samples exhibit high defects due to ball milling process and to understand the effect of nanostructure, EPR measurement was carried out on all samples and displayed in Figure 4.24. It is seen that pure un-milled NiO and milled NiO powders exhibit different nature of spectra. While the pure NiO displays spectrum with large broadening and reduced intensity due to AFM nature [YIJB2007, SHIM2008, LYUK2010, ZHAN2016] associated with Ni^{2+}-O^{2-}-Ni^{2+} super-exchange interaction at larger *D*, the milled NiO powders exhibit resonant peaks at low fields. To understand the peak shift more in details, the extracted value of peak position is plotted as a function of *D* in the inset of Figure 4.24. As *D* decreases from 39 nm to 25 nm, the resonant peak position decreases dramatically. With a further decrease in *D*, the resonant peak position varies sluggishly. The large decrease in resonant peak position indicates possible FM signature in the materials [SRIN2011, ZHAN2016]. It may be noted that EPR signal of most bulk AFM materials disappears due to the effect of very strong exchange fields, which require resonance frequency higher than EPR GHz region.

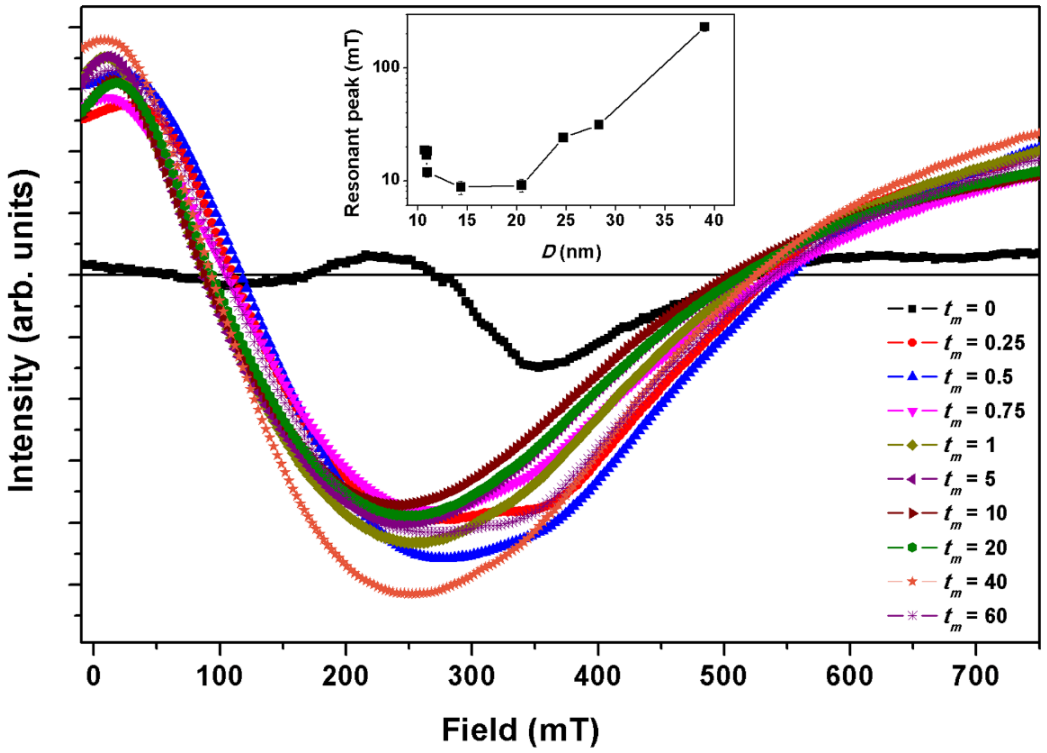

Figure 4.24: EPR spectra of pure un-milled and milled NiO powders at different t_m. Inset: The plot of resonant peak as a function of crystal size (D).

Therefore, the appearance of EPR signal in the presently investigated samples can be correlated to one or more of the following mechanisms: (i) formation of uncompensated spins on the surface of the crystal due to size reduction and defects [WINK2008, PROE2011] (ii) creation of a spin glass like shell on the crystal surface [KENN1987, TIWA2005], (iii) size effect which substantially changes Néel point [NEEL1962, RINA2014] and number of uncompensated spins on the surface [KODA1997, DELB2008, MAKH2008], (iv) the formation of a weak magnetic moment caused by the canting of the magnetic sublattices [ZYSL1994, KODA1997] and (v) extraneous ferromagnetic impurities in the sample. A comparison between EPR signal, vibrational and temperature dependent magnetic measurements suggests that the formation of EPR signal could be attributed to the existence of uncompensated spin on the surface of NiO crystals due to defects and size reduction, which provides supportable explanation for both temperature and field dependent magnetic properties. Therefore, it has been established that EPR signals are found to be affected by the milling process, which modifies the surface nature of the powders due to defects and size effects.

4.3.6. Optical properties

To extend the effect of size reduction on optical properties, room temperature photoluminescence spectra were recorded and depicted in Figure 4.25(a). Two major peaks (363 and 396 nm) at UV-blue band were observed for pure un-milled NiO powder. While the first peak located at 363 nm (E_g~3.42 eV) is corresponding to near band emission due to recombination of excitons, the peak observed at 396 nm can be ascribed to band transition of Ni^{2+} from ^3A_2g to $^3T_1g(G)$ [VOLK2001]. In addition, there exists a blue-shift for 363 nm peak with decreasing D. This could be correlated to possible quantum size effect. To study the effect of crystal size on the bandgap (E_g), E_g values are determined from the photoluminescence spectra and plotted against D in Figure 4.25(b). E_g increases gradually with decreasing crystal size from 39 nm to 20 nm and then exhibits a larger increase at lower crystal size.

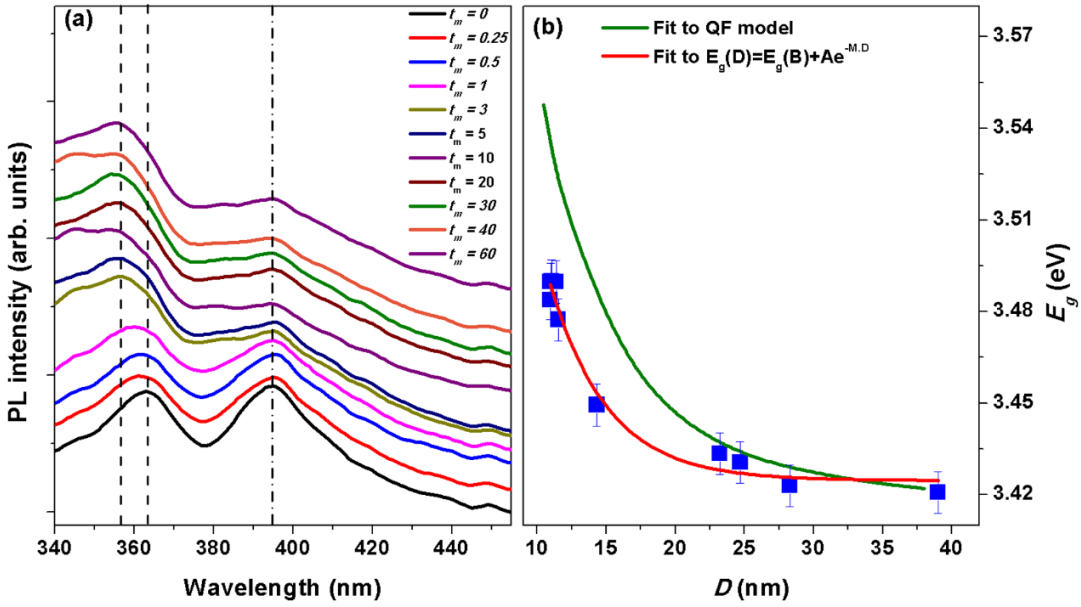

Figure 4.25: Room temperature (a) Photoluminescence spectra and (b) variation of band gap energy with average particle size (D) for pure un-milled and milled NiO powders.

The variation of E_g as a function of D is fitted to a model proposed by Kayanuma [KAYA1988]. Although the variation of E_g follows a similar trend with Kayanuma model, E_g values are considerably smaller than those predicted by Kayanuma. The dependence of E_g on D is varying as

$$E_g(D) = 3.425(9) + 0.94(3)e^{-0.245(4)D} \qquad (4.09)$$

in whole range, where the value of 3.425(9) eV denotes the E_g of bulk NiO powder [IRWI2008] and the values quoted within parenthesis represent error in determining the parameters.

The above results suggest that the NiO powders prepared by ball milling process having cubic structure, induced ferromagnetism at room temperature, high T_C and tunable optical properties could facilitate integration of spintronic devices.

4.4. Summary

A systematic study on the evolution of structural, vibrational, electronic, magnetic, resonance and optical properties of pure and milled NiO powders prepared by ball mill process in a planetary ball mill under dry mill conditions and at argon atmosphere has been carried out as a function of different t_m. The salient features of the NiO powders from the current investigations are as follows:

- The ball mill process produces single phase face centered cubic nanocrystalline NiO powders with the average crystallite size of nanometer range (around 11 nm). The lattice volume increases almost linearly with inverse of crystallite size. Microstructural studies reveal that the agglomeration of fine particles increases with increasing t_m and the nanocrystalline powders exhibit irregular shapes with broad size distribution. The analyses of both TEM and XRD observations are in good agreement with each other.
- Raman spectra reveal that two-magnon band associated with Ni^{2+}-O^{2-}-Ni^{2+} super-exchange interaction and observed in pure NiO powder disappears dramatically in milled NiO due to defects and/or size reduction. In addition, with increasing t_m, 1P LO band broadens due to defects, 2P TO+LO band disappears, 2P TO and 2P LO bands broaden and shift to lower value of Raman shift due to size-induced phonon confinement. This changes the color of the powder from the pale green for pure NiO into dark green for milled NiO powders.
- Electronic properties using XPS spectra confirm the existence of non-stoichiometry in the milled NiO powders, caused by the defects, size reduction, oxidization of Ni^{2+} to Ni^{3+} due to breaking of Ni^{2+}-O^{2-}-Ni^{2+} super-exchange interaction.
- Magnetic study reveals that pure NiO powder exhibits AFM nature, which transforms into FM gradually upon milling due to defects and size reduction. A maximum magnetization of 1.08 emu/g at 12 kOe applied field and a coercivity of about 160 Oe are obtained at room temperature for 30 hrs milled NiO powder. The exchange bias observed between the induced FM and AFM core decreases with decreasing NiO crystal size.
- Low temperature magnetization in the temperature range between 4 K and 300 K exhibits two peaks corresponding to freezing of surface spin and spin glass like phase.

The presence of spin glass like phase verified through de Almedia-Thouless (AT) line plot provides additional anisotropy and enhances exchange bias under field-cooling condition.

- High temperature magnetization in the temperature range between 300 K and 1000 K shows the presence of mixed magnetic phases for the initial period of milling and on-set of ferromagnetic behavior with a well-defined magnetic phase transition at around 780 K.
- Resonance study discloses a close correlation between the EPR results and magnetic properties.
- Optical studies reveal two major peaks at UV-blue band and blue-shift of peak (around 363 nm) with decreasing the crystal size. The variation of bandgap of milled NiO powders almost follows the model proposed by Kayanuma.
- Annealing of as-milled NiO powders results in a large reduction in magnetization, but the rate of reduction in magnetization strongly depends on the milling conditions. Furthermore, the annealing studies confirm the origin of FM as intrinsic one.

Chapter 5

Properties of ZnO powders prepared by ball milling process

5.1. Introduction

Wide band gap diluted magnetic semiconductors (DMS) have gained enormous attention recently as a promising route to realize semiconductor based spintronics. A successful fabrication of ferromagnetic (FM) DMS with Curie temperature (T_C) above room temperature is considered to be one of the key approaches for the development of multifunctional spintronic devices in future [OHNO1998]. Sharma et al [SHAR2003] reported the first experimental evidence of showing room temperature FM in Mn doped ZnO. The recent studies on ZnO system revealed realization of room temperature FM in either pure nanostructured ZnO without transition metal doping or ZnO doped with non-magnetic ions such as C and K [HONG2007, AKBA2011, GHOS2011]. However, a careful review of the literature reveals contradictory results on the development of room temperature FM in pure ZnO system. Bartolomé et al [BART2007] showed that the preparation of ZnO based particles using ball milling technique resulted in a drastic reduction in the average size of the crystals without any induction of FM properties. Sanyal et al [SANY2008] reported that the ball mill processed ZnO did not show induced FM properties despite the creation of Zn vacancy during the ball milling process. On the other hand, Potzger et al [POTZ2008] reported an easy mechanical way to create FM defective ZnO and correlated to flake like structures in planar compressed pieces of the powder. Xing et al [XING2010] suggested that the oxygen vacancies induce characteristic photoluminescence and boost the room temperature FM in ZnO nanowires synthesized using a vapor transport method. Furthermore, Podila et al [PODI2010] reported the formation of room temperature FM in ZnO films depending on the sample preparation and annealing conditions. This was also supported by *ab-initio* calculations exploring the role of surface defects on the magnetic behavior of nanoscale ZnO. Banerjee et al [BANE2007] reported the enhancement of FM in pure ZnO powder upon thermal annealing due to the formation of clusters of oxygen vacancy. Very recently, Phan et al [PHAN2013] and Ghose et al [GHOS2013] proposed that mechanical milling can be used to produce induced defect-related FM in ZnO nanoparticles from initial diamagnetic ZnO powders. These studies revealed that the development of FM in un-doped ZnO was attributed to the defect density of either oxygen or zinc. However, there are no detailed reports summarizing the stability of FM above room temperature in ZnO powders at nanoscale and the size effect on the development of room temperature FM in correlation with structural, vibrational, electronic and resonance properties. Also, the report on magnetic materials demonstrated that T_C can be enhanced moderately by introducing stress through ball milling process [GORR2009]. Furthermore, ZnO is an optically transparent II-VI semiconductor, electro-optical and well known piezoelectric material with

hexagonal wurtzite structure and exhibiting wide band gap (3.27 – 3.42 eV). Hence, it is expected to show possible size dependent properties. Therefore, in this chapter, we report (i) evolution of nanoscale ZnO powder with milling time, (ii) the effects of size reduction and defects induced during milling on the structural, vibrational, electronic, magnetic, resonance and optical properties of ZnO powders, (iii) the effect of annealing of milled ZnO powders at different temperatures to understand the origin of room temperature FM and (iii) correlation between the crystal structure, microstructure, vibrational, electronic, magnetic, resonance and optical properties of these ball milled powders and to explore the possibility to enhance their magnetic properties.

5.2. Experimental details

Weighed quantities of high purity ZnO (> 99.9%, Merck) powders, exhibiting hexagonal wurtzite structure and paramagnetism (PM) at room temperature, were taken in high energy planetary ball mill filled with high purity argon gas. The milling process of ZnO powders was carried out for different milling periods (t_m) from 0.25 to 60 hrs using the mill operated at 500 rpm with a ball-to-powder weight ratio of 10:1. The optimization of the milling speed and ball-to-powder weight ratio was done mainly by analyzing the variation in the structural and magnetic properties of the ZnO powders. In order to avoid any local heating during milling and its influence on the resulting properties, the milling process was programmed to halt for 15 minutes after every 15 minutes of operation. In addition, the milled powders were collected at regular intervals and characterized to monitor the evolution of nanostructure in ZnO powders. These powders collected at random intervals were also subsequently annealed at air atmosphere for 3 hrs at different annealing temperatures (T_A).

The phase evolution and crystal structure of ZnO powders were analyzed through X-ray diffraction (XRD) patterns obtained using high-power (18 kW) X-Ray diffractometer (Rigaku TTRAX III, Japan). XRD data were collected at a slow scan rate of 0.005°/s for analyzing the structural parameters as a function of t_m. The changes in the surface morphology of the powders were observed using field emission scanning electron microscope (FE-SEM) and overall composition of the pure un-milled and milled powders was determined using energy dispersive spectroscopy (EDS, Oxford) attached to SEM unit. The microstructural properties of the pure un-milled and milled ZnO powders were analyzed using transmission electron microscopy (TEM, JEOL 2100 and TECNAI G^2 F30) technique. Raman spectra were obtained using micro-Raman spectroscopy (LabRam HR800, Jobin Yvon) using excitation wavelength of 614 nm at

room temperature. X-ray photoelectron spectroscopy (XPS) analysis was carried out in a standard ultrahigh vacuum surface science chamber consisting of a PSP vacuum technology electron energy analyzer (angle integrating ±10°) and a dual anode X-ray source with an Mg-K_α source (1253.6 eV) at a base pressure of 2×10^{-10} mbar and energy resolution at full width at half maximum (FWHM) is about 0.8 eV. The spectrometer was calibrated using Au $4f_{7/2}$ at 83.9 eV [ZHAN20121]. Magnetic properties of the pure un-milled and milled powders were characterized using vibrating sample magnetometer (VSM, LakeShore Model 7410) by performing (i) magnetic hysteresis (*M-H*) loops at different temperatures under zero-field-cooled (ZFC) and field-cooled (FC) conditions and (ii) high-temperature thermomagnetization (*M-T*) under constant applied magnetic fields over a wide range of temperatures from 300 K to 1100 K. Similarly, *M-T* measurements were also performed under ZFC and FC conditions in the temperature range between 2 K and 400 K at different constant applied fields using magnetic property measurement system with superconducting quantum interference device (SQUID, Quantum Design MPMS XL7) magnetometer. Room temperature electron paramagnetic resonance (EPR) measurements were carried out on a JEOL Spectrometer (JES-FA200) operating at X-band frequency (ν =9.4 GHz) with 100 kHz magnetic field modulation in powder form. Steady state photoluminescence (PL) spectra were recorded by using a 312 nm Xenon lamp excitation (AB2, Thermo spectronic).

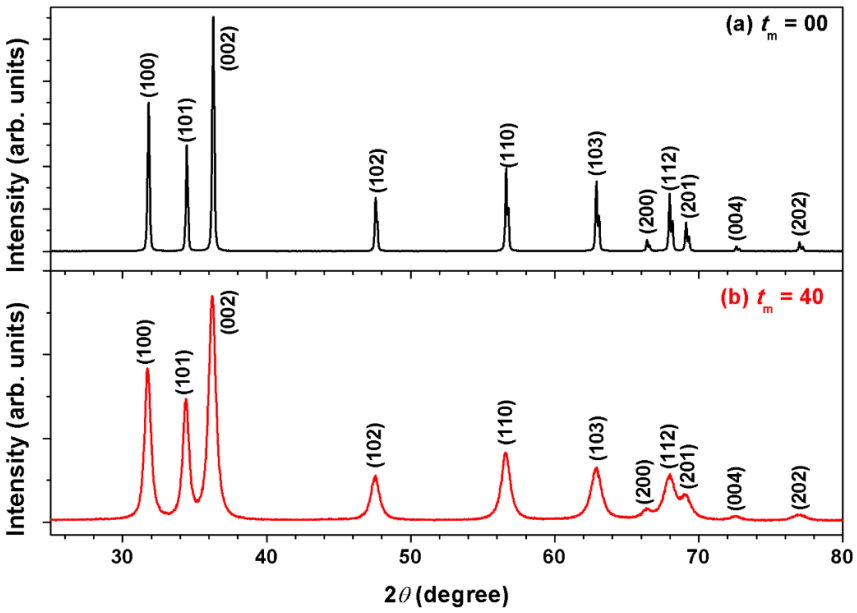

Figure 5.01: Room temperature XRD patterns of (a) pure un-milled ZnO powder and (b) milled ZnO powder for 40 hrs.

5.3. Results and discussion

5.3.1. Structural properties

Figure 5.01 displays typical room temperature XRD patterns of pure un-milled ZnO and 40 hrs milled ZnO powders. The pure un-milled ZnO powder exhibits Bragg reflections corresponding to hexagonal wurtzite structure. Similarly, the milled ZnO powder also exhibits hexagonal wurtzite structure without any impurity phases within the detection limit of X-ray diffractometer. A careful observation of the XRD peaks confirms that the sharp Bragg reflections observed in pure un-milled ZnO powders broadens along with a considerable shift in peak position towards a lower diffraction angle. While the first one suggests the formation of highly refined and strained ZnO powders, the latter one suggests a considerable change in the lattice parameter during the milling process.

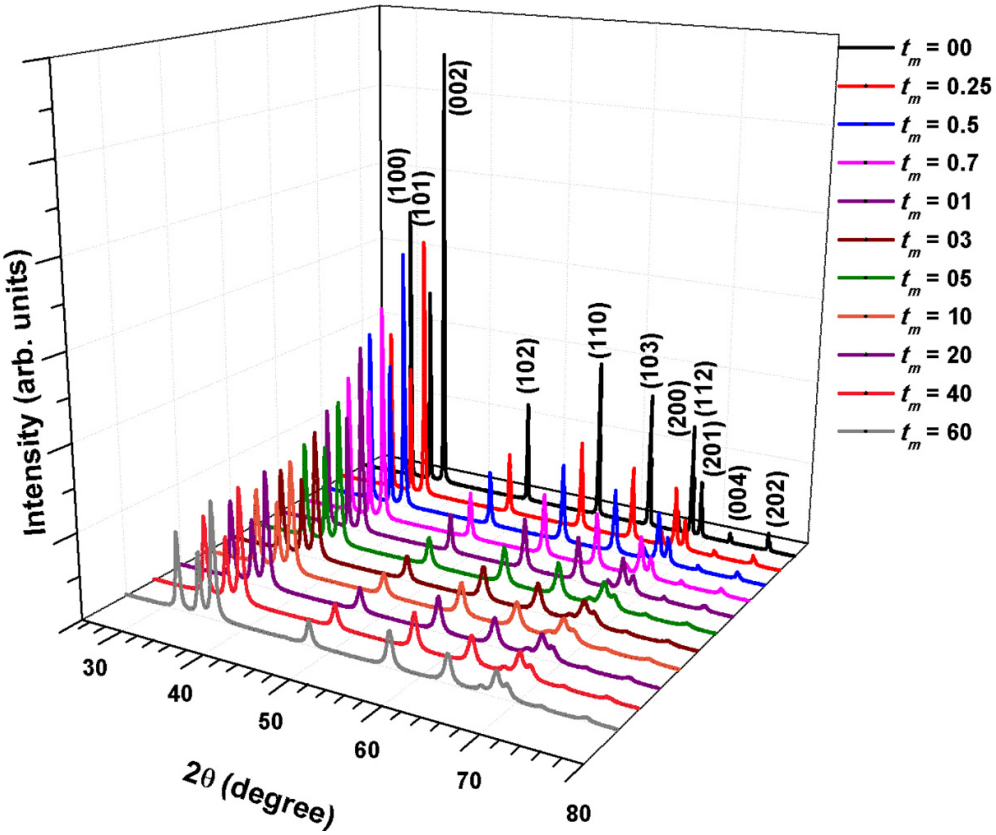

Figure 5.02: Room temperature XRD patterns of pure un-milled and milled ZnO powders at different t_m.

To understand the evolution of nanocrystalline microstructure systematically, we have obtained XRD patterns of milled ZnO powders collected at different t_m between 0.25 and 60 hrs. Figure 5.02 depicts the XRD patterns of ZnO powders milled at different t_m. All samples

exhibit hexagonal wurtzite structure without any other impurity phases. With increasing t_m, the peak broadening increases progressively along with the shift in peak position to lower angles. This can be attributed to the refinement of average crystallite size (D), instrumental broadening and strain (η) caused by the defects (ρ) induced during ball milling process [DING2001, SURY2001].

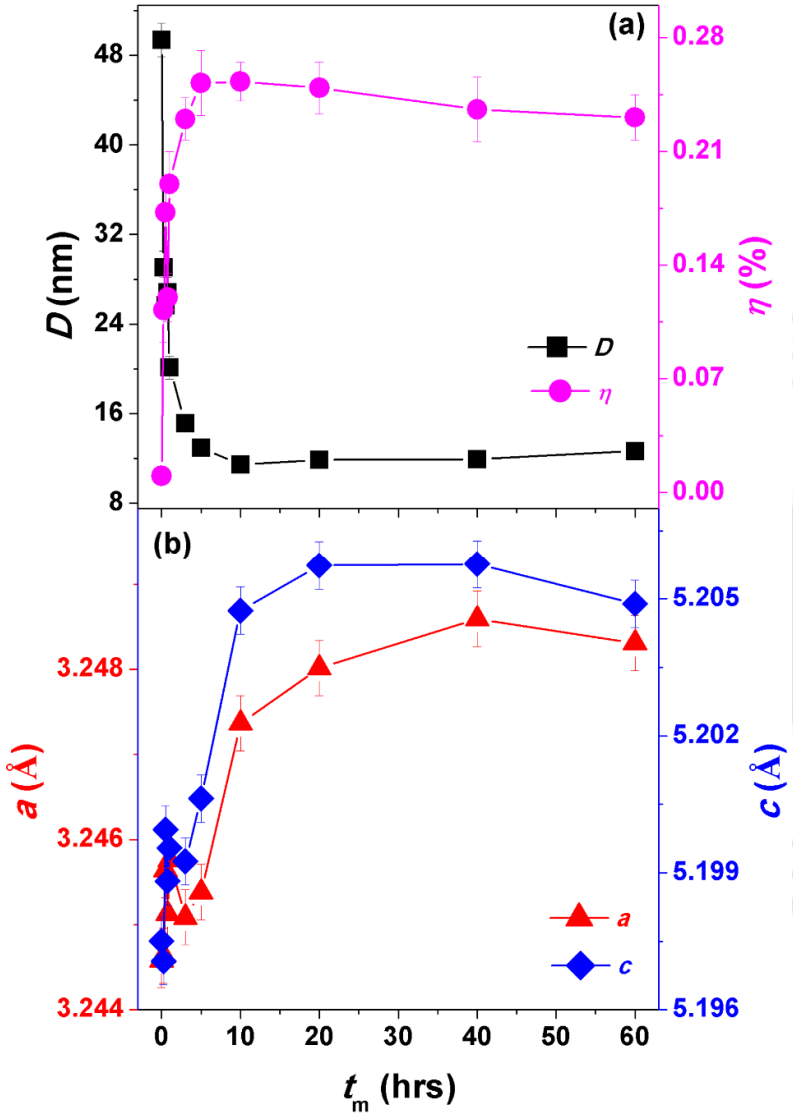

Figure 5.03: The variations of (a) average crystal size (D), strain (η) and (b) lattice constant (a and c) as a function of milling time (t_m) for milled ZnO powders.

To separate the individual contribution from D and η, XRD patterns were analyzed using modified Williamson-Hall Plot (MWHP) [UNGA1991, UNGA1992] as described in Chapter

04. Similarly, to study the effect of structural refinement on the lattice parameters, the lattice constant was calculated from XRD patterns using eqn.(5.01).

$$\sin^2\theta = \frac{\lambda^2}{4}\left[\frac{4}{3}\left(\frac{h^2+hk+k^2}{a^2}\right)\frac{l^2}{c^2}\right] \qquad (5.01)$$

where θ is the peak position, λ (= 1.5406 Å) is the wavelength of the X-ray, h, k and l are Miller indices, a and c are lattice constants. The determined values of D, η, a and c for milled ZnO powders are plotted as a function t_m in Figure 5.03.

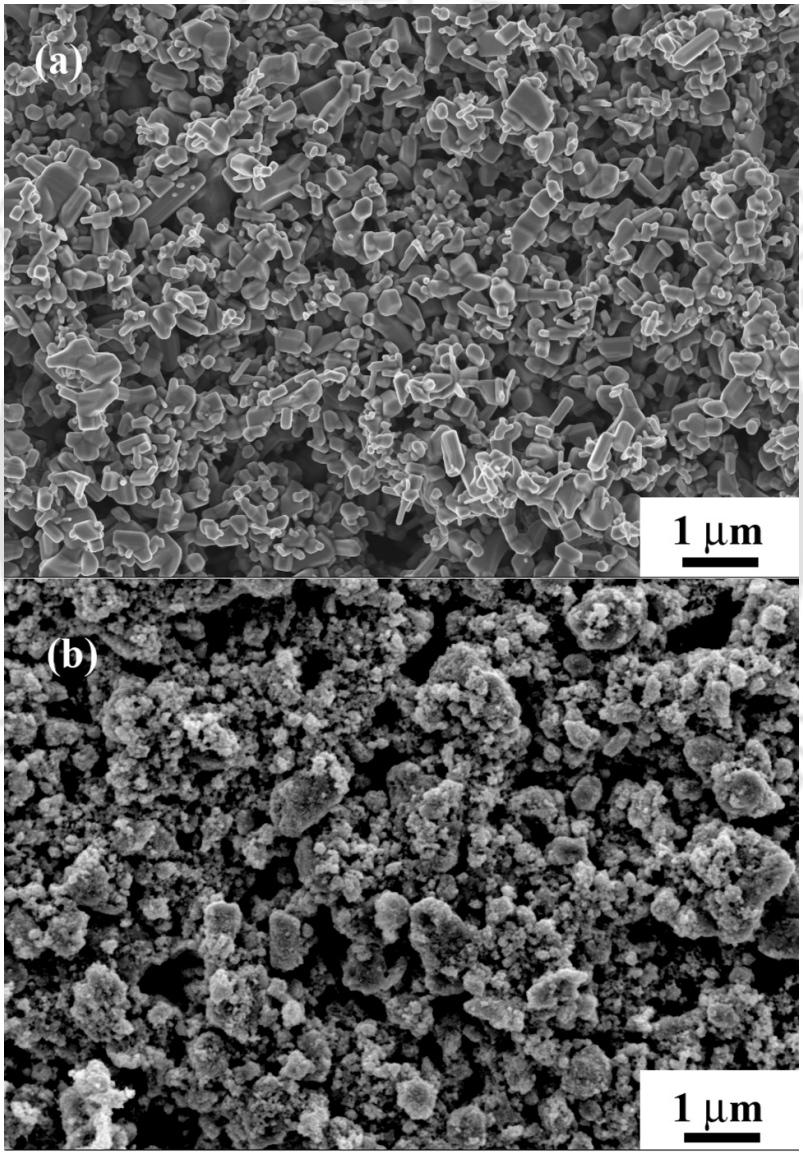

Figure 5.04: FE-SEM images of (a) pure un-milled ZnO and (b) milled ZnO powder at 40 hrs.

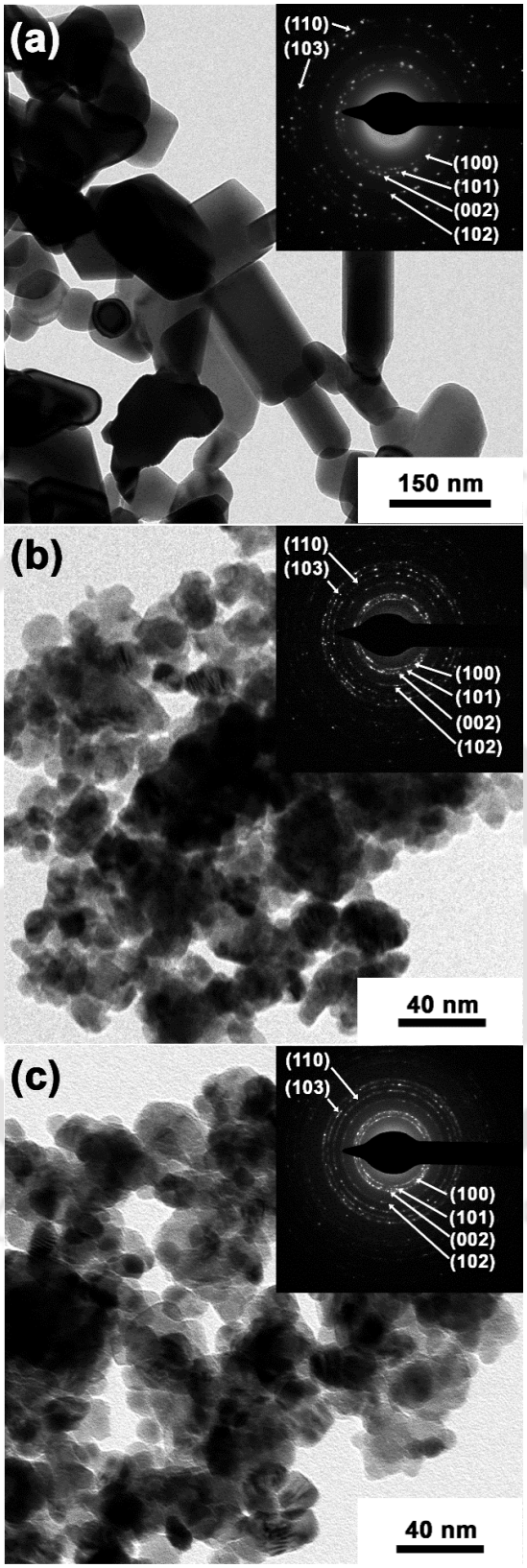

Figure 5.05: Bright-field TEM images and selected area electron diffraction patterns of (a) pure un-milled ZnO and milled ZnO powders at t_m = (b) 5 hrs and (c) 40 hrs.

It is clearly observed that with increasing t_m, D decreases largely up to t_m = 10 and then tends to remain constant upon subsequent milling. ZnO powders milled more than 10 hrs exhibit fine nanosized crystals with the size of around 12 nm. On the other hand, the strain increases drastically for t_m up to 10 hrs and remains nearly constant up to 20 hrs. On further increasing t_m, a slight decrease in strain was observed. This indicates that the formation of nanocrystalline microstructure with milling in pure ZnO powders. On the other hand, the lattice constant calculated from XRD peaks shows a slow increase up to 1 hr of milling and then decreases slightly for 3 hrs of milling. On further increasing t_m, lattice constant increases largely up to 20 hrs and then exhibits weak dependence above 20 hrs of milling. This could be attributed to the formation of defect density along with size reduction with increasing milling periods. A slight increase in crystallite size and decrease in strain was observed for powders milled for 60 hrs, which can be correlated to the prolong milling.

In order to understand the change in the surface morphology, the pure un-milled ZnO and milled ZnO powders were characterized using FE-SEM technique. Figure 5.04 displays the typical FE-SEM images of pure un-milled ZnO and milled ZnO powders at 40 hrs. A clear particle morphology with the average particle size of 0.1 to 1 μm is observed in pure un-milled ZnO powders. In addition, the shape of the particles is found to be quite random in nature. With increasing t_m, the average particle size of the milled powders decreases considerably below 100 nm. At the same time, the agglomeration of the fine particles increases to form aggregated particles, which are typical of ball-milled powders [SREC2008, ELIL2012]. This arises mainly from the repeated cold welding and fracture of powder during milling. Figure 5.05 shows typical plane-view bright-field TEM (BF-TEM) images and selected area electron diffraction (SAED) patterns for pure un-milled ZnO powder and milled ZnO powders at 5 and 40 hrs. BF-TEM image of the pure ZnO powder exhibits a clear particle morphology with different size of the crystals ranging between 50 and 100 nm. The size and shape of the crystals are observed to be quite random, but the polycrystalline nature is evident from ZnO diffraction rings in the SAED pattern. Similarly, BF-TEM images of milled ZnO powders confirm the presence of fine nanocrystalline microstructure with irregular morphology. In addition, the SAED patterns show diffraction rings, which could be indexed to hexagonal wurtzite structure only and confirm the polycrystalline nature of the ZnO particles. The average size of the crystals estimated from BF-TEM images at random locations decreases from 50-100 nm for the pure un-milled ZnO to about 13 nm and 11.5 nm after milling for 5 hrs and 40 hrs, respectively. The variations of ZnO crystallite size observed using TEM show almost a similar trend with that of

XRD results. Nevertheless, the nanoscale powders exhibit irregular shapes with broad size distribution. Thus, the analyses of both TEM and XRD observations are in good agreement with each other and these structural modifications in ZnO powders are expected to modify physical properties.

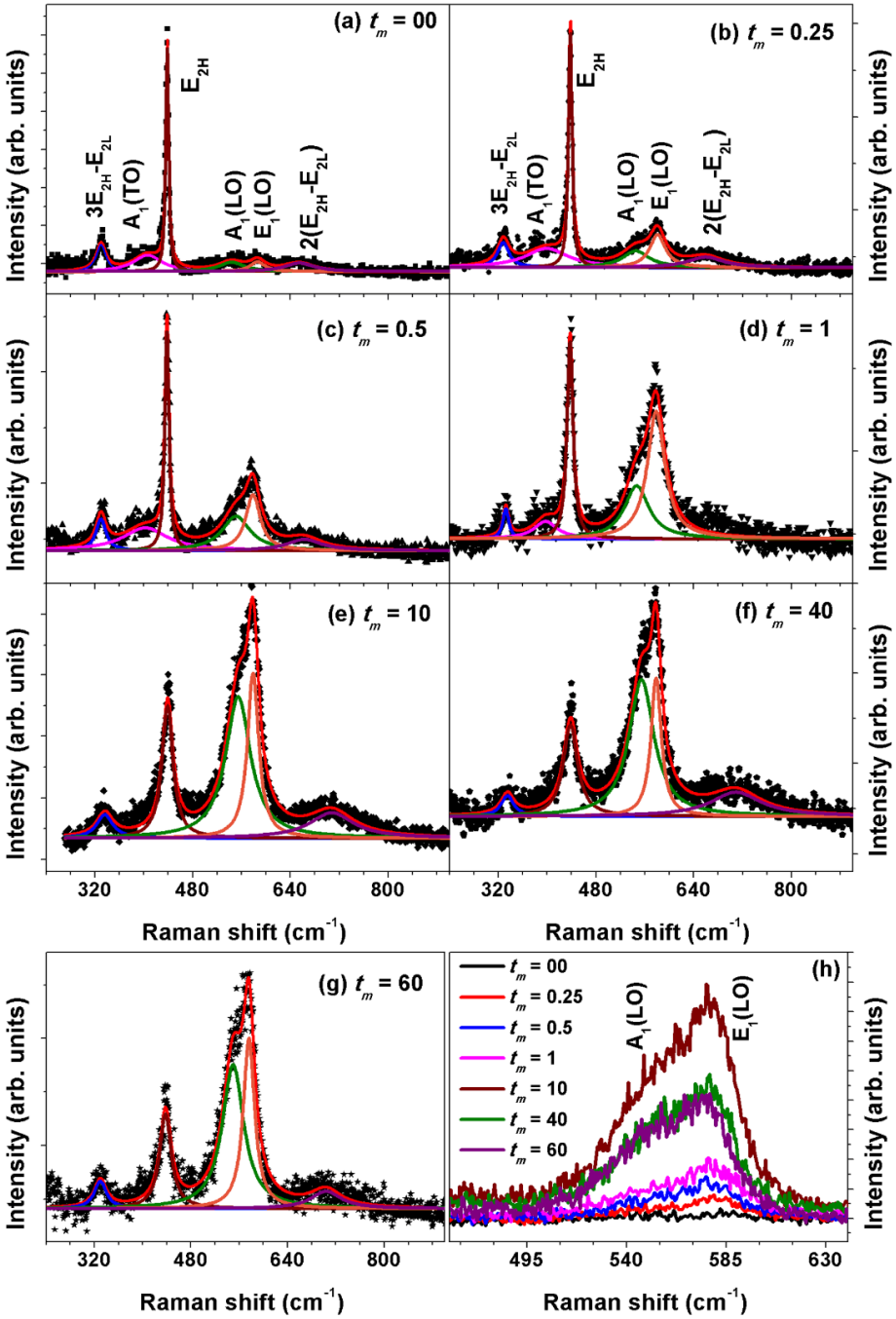

Figure 5.06: (a-f) Room temperature Raman spectra of pure un-milled (a) and milled ZnO powders (b-g) at different t_m. All the modes are marked in (a and b). (h) The development of A_1(LO) and E_1(LO) modes is shown distinctly for the ZnO powders.

5.3.2. Vibrational properties

To study crystallinity and defects structure associated with the milled powders [WANG20061, SING2010], Raman spectra were obtained for pure un-milled and milled ZnO powders and shown in Figure 5.06. Raman spectra were analyzed by curve fitting method with different band combinations to obtain the peak position, peak width and area under curves. The fitted curves are also shown in Figure 5.06. As well-documented in literature [CALL1977, OZGU2005, CUSC2007, WANG2007, TAPI2010], wurtzite ZnO belongs to the space group C_{6v}^4 with 2 formula units in the primitive cell and the zone-center optical phonons can be classified according to the irreducible representations: $\Gamma_{opt} = A_1 + 2E_2 + E_1 + 2B_1$. The B_1 modes are silent modes. The A_1 and E_1 modes are polar modes, both Raman and infrared active, and each split into transverse-optical (TO) and longitudinal-optical (LO) components with different frequencies. The nonpolar E_2 modes have two frequencies: E_2 (high) and E_2 (low) associated with the motion of oxygen (O) atoms and vibration of the zinc (Zn) sublattice, respectively [MEAD1997, CUSC2007, TAPI2010].

As shown in Figure 5.06(a) for pure un-milled ZnO, a major peak was observed at 438 cm^{-1}, which is assigned to the E_2 (high) (E_{2H}) mode. Smaller peaks were also observed at around 330, 381, 543, 581 and 660 cm^{-1}, which could be assignable to the E_{2H}-E_{2L}, A_1(TO), A_1(LO), E_1(LO) and 2(E_{2H}-E_{2L}) modes, respectively [OZGU2005, SAMA2006, CUSC2007, TAPI2010, KHAN2014, KURI2014, BECH2015, MELO2016]. With increasing t_m, the E_{2H} mode at 438 cm^{-1} decreases drastically and broadens asymmetrically. On the other hand, the weak existence of A_1(LO) and E_1(LO) modes in pure ZnO powders becomes more prominent for the milled ZnO powders. This could be attributed to the existence of various defects (surface and bulk defects) caused by the oxygen vacancies, Zn interstitial defect states, size effects, lower crystallinity, etc [ALAR2006, VOJI2008, PHAN2010, PARA2012, CHOI2015, MELO2016]. In addition, A_1(LO) and E_1(LO) modes shifts appreciably towards lower frequencies as t_m increases. This is in good agreement with the XRD results, which revealed that the *c*-axis length increases in ball milled ZnO powders. The expansion of the unit cell implies elongation of respective bonds along *c*-axis, leading to weakened force constant and thus softened mode of the phonons with lower vibration frequency. These results clearly support that the ball milling process induces defects and size reduction in ZnO powders with increasing t_m.

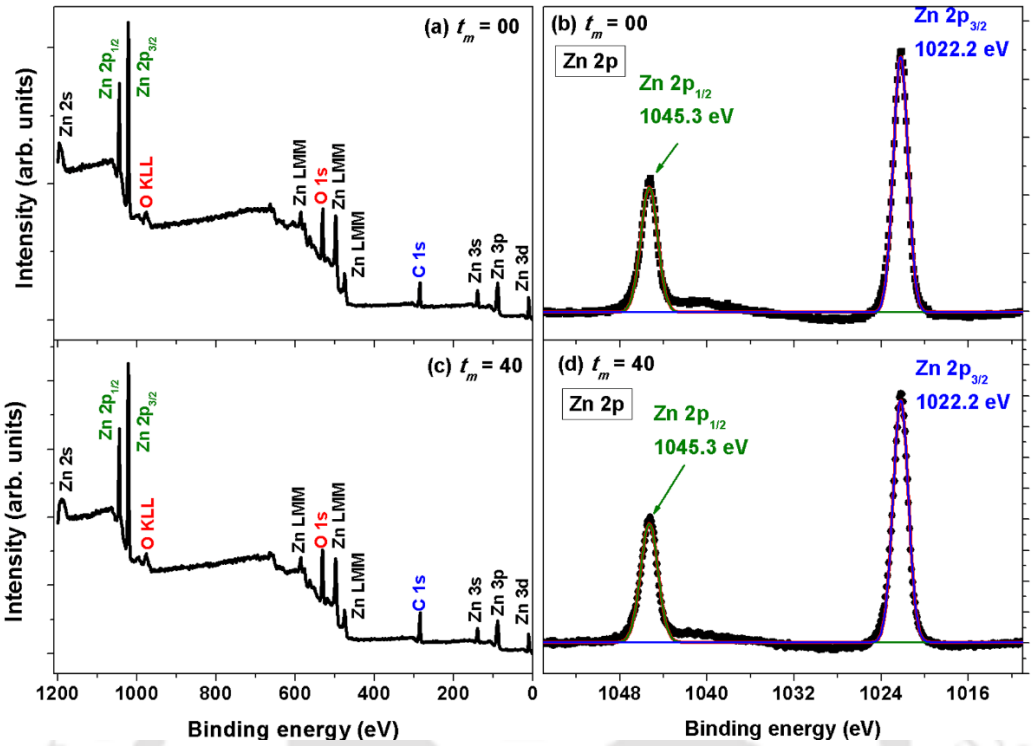

Figure 5.07: (a,c) Wide scan survey XPS spectra and (b,d) Zn 2p XPS spectra for pure un-milled and 40 hrs milled ZnO powders.

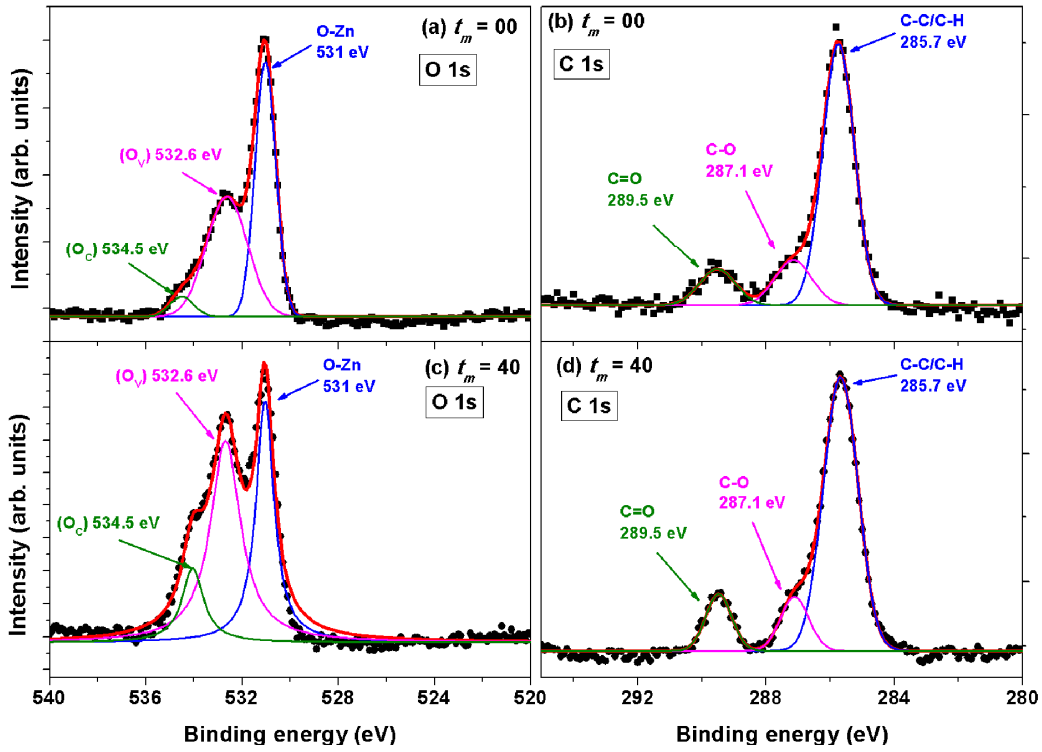

Figure 5.08: (a,c) O 1s XPS spectra and (b,d) C 1s XPS spectra for pure un-milled and 40 hrs milled ZnO powders.

5.3.3. Electronic properties

In order to understand the chemical composition of pure un-milled and milled ZnO powders, XPS survey spectra, Zn 2p, O 1s and C 1s spectra were obtained for both pure un-milled and milled ZnO powders. Figures 5.07 and 5.08 display wide scan survey spectra and Zn 2p spectra and O 1s and C 1s spectra for pure and milled ZnO powders, respectively. From the survey spectra obtained over a wide energy scan range, we have observed the presence of Zn, O and C. Zn 2p spectrum of pure ZnO powder (see Figure 5.07(b)) reveals two fitted almost symmetrical peaks: Zn-$2p_{3/2}$ (1022.2 eV) and Zn-$2p_{1/2}$ (1045.3 eV) spin-orbit levels. The value of binding energy difference between Zn-$2p_{3/2}$ and Zn-$2p_{1/2}$ peaks is about 23.1 eV, which confirms the dominance of ZnO [MOUL1995, ITAN2012, HUJ2015]. The zinc Auger peak of Zn LMM is further taken for chemical assessment of the zinc compounds with the main peak binding energy of 498 eV, corresponding to ZnO. These results suggest that there are only one valance state of Zn is present. We have almost observed similar behaviors for ZnO milled powder as well. However, the O 1s photoelectron peak is asymmetrical and shows visible shoulders. The O 1s peak can be de-convoluted into three component peaks centered at 531 eV (O-Zn), 532.6 eV (O_V) and 534.5 eV (O_C) by fitting the XPS spectra (see Figure 5.08(a)) [ESCU2011]. It is understood that the O-Zn component of the O 1s spectrum is attributed to the O^{2-} ions in the ZnO lattice [ROSA2007], while the O_V component is associated with the O^{2-} ions in oxygen-deficient regions within the ZnO matrix. The O_C component is usually attributed to the chemisorbed and dissociated oxygen species or OH [REMA2008, GAOD2009, MAEN2009, GOGU2014, HUJ2015]. Interestingly, with increasing t_m, the percentage of O_V increases largely and O_C component increases slightly at the expense of the O-Zn component [SZOR1995]. This clearly supports that the milling process in ZnO introduces considerable oxygen vacancies providing oxygen-deficient regions within the ZnO matrix. This is in very good agreement with the results of Raman studies for the presently investigated samples. The increase in O_C component with milling suggests the enhanced sensitivity of the gas sensing performance for the as-milled ZnO powders [ZHAN20122]. To further understand the distribution of C element, the C 1s spectra were obtained and shown in Figure 5.08(b) and (d). According to the analysis result, the binding energy of C 1s at 285.7 eV, 287.1eV and 289.5 eV is the chemisorbed carbon species in the form of C–C/C–H, C–O and C=O, respectively. The relative intensities of the peaks strongly depend on the milling conditions. These results are in very good agreement with the vibration properties of the presently investigated samples.

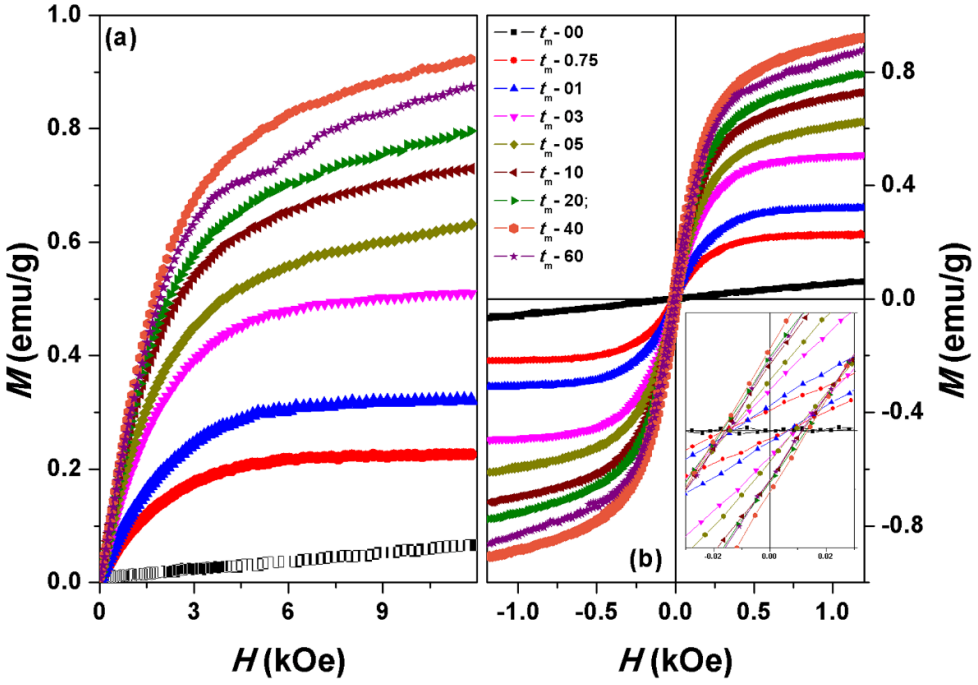

Figure 5.09: Room temperature (a) initial magnetization curves and (b) *M-H* loops of pure un-milled and milled ZnO powders at different t_m. Inset shows the expanded view of *M-H* loops close to origin.

5.3.4. Magnetic properties

To study the effects of nanocrystalline microstructure and defects on the magnetic properties of ZnO powders, we have measured (i) initial magnetization curves (*IM*), (ii) *M-H* loops at room temperature and at low temperatures and (iii) thermomagnetization (*M-T*) measurements over a wide range of temperature from 20 K to 1000 K for the pure un-milled and milled ZnO powders. Figure 5.09 depicts room temperature *IM* curves and *M-H* loops and expanded version of *M-H* loops close to origin (inset) for pure un-milled ZnO and milled ZnO powders at different t_m. It is observed that (i) pure un-milled ZnO powder exhibits a weak response to applied field due to its PM nature and *M-H* loop passes through the origin (see inset). (ii) On the other hand, the milled ZnO powder exhibits different nature of response to the applied field, i.e., the magnetization increases moderately at lower applied fields and then shows a gradual increase at higher applied fields. The rate of increase in the magnetization at lower field increases progressively with increasing t_m up to 40 hrs and then decreases significantly with increasing t_m > 40 hrs. (iii) the expanded version of the *M-H* loops reveals that the loops are shifted slightly to negative axes [see inset of Figure 5.08(b)], but the amount of shift decreases with increasing t_m.

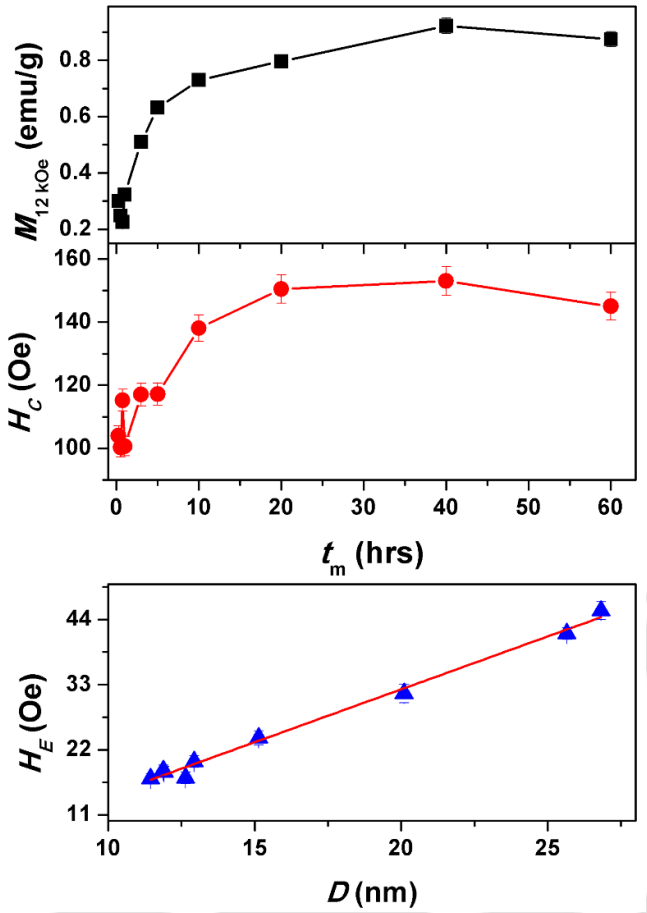

Figure 5.10: The variations of (a) magnetization obtained at 12 kOe (M_{12kOe}), (b) coercivity (H_C) as a function of t_m. (c) The variations of H_E as a function of average crystal size (D). The solid line passing through the data is the best fit to eqn.(4.07).

Figure 5.10 displays the extracted values of magnetization at 12 kOe (M_{12kOe}), coercivity (H_C) as a function of t_m, and the calculated values of exchange bias, H_E [= ($|H_{C+}|$-$|H_{C-}|$)/2] plotted as a function of average crystal size. M_{12kOe} increases at a faster rate for t_m up to 10 hrs and then the rate of increase in M_{12kOe} decreases slowly with increasing t_m up to 40 hrs. On further increasing t_m, a slight decrease in M_{12kOe} is observed. This results in a maximum in the curve at around 40 hrs of milling. On the other hand, H_C of pure ZnO, observed as zero due to its PM nature, has increased significantly (~ 100 Oe) after initial milling. With increasing t_m, H_C increases from about 100 Oe to about 150 Oe after milling for 40 hrs and then decreases slightly for t_m=60 hrs. To understand any correlation between structural and magnetic parameters, the determined values of H_E are plotted as a function of crystal size of ZnO in Figure 5.09(c). Noticeably, H_E decreases almost linearly with decreasing average crystal size, which reveals that PM ZnO transforms into induced FM. To obtain the effect of crystal size,

the variation of H_E with crystal size was fitted to eqn.(4.07). The fitting of the experimental data provides $H_E(0)$ = -3.54 Oe and m = 1.79 Oe/nm. The exchange bias properties are reported in literature for doped ZnO systems [ZHEN2004, LIUH2008]. However, earlier reports suggest that the exchange bias is observable only when the FM semiconductors are capped by the additional AFM layers [LIUH2005, SEEH2007]. Zheng et al also suggested that to generate exchange bias, at least one fixed magnetic phase that does not reverse during hysteresis loop measurements should exist [ZHEN2004]. Hence, a detailed further research might need to be done to clarify the observed exchange in milled ZnO powder.

To understand the origin of the observed FM in the milled ZnO powders, we correlate the structural, vibrational, electronic and magnetic properties. The pure un-milled ZnO exhibits a weak response to the applied magnetic field and the *M-H* loop passes through origin. This is mainly due to the PM nature. It is well understood that the ball milling process, involving repeated cold-welding and fracturing to form nanostructured materials, introduces massively defects to a starting materials. As a result, the size reduction and creation of vacancies occurs in milled ZnO powders, as observed in the presently case. This is in good agreement with the earlier results on similar materials [MISH2004, POTZ2008, XING2010, PHAN2013, GHOS2013]. If the ball milling process increases the defect density with increasing t_m, then the FM ordering is also expected to increase with defect density. This is clearly evidenced from Raman and XPS spectra results as shown in Figures 5.06 and 5.08. However, the increase of t_m above 40 hrs results in a slight reduction in magnetization due to the small increase in average crystal size due to prolong milling. These results suggest that the origin of FM in the presently investigated ZnO is due to the finite sized ZnO in the nanometer range with oxygen vacancies and/or Zn interstitials created during the milling process. These results confirm a good correlation between structural, vibrational, electronic and magnetic properties of ZnO powders.

To rule out any impurities contribution and understand the origin of the induced FM, chemical compositions and chemical bonding state were analyzed using EDS and XPS, respectively. In addition, the as-milled ZnO powders at different t_m were annealed at high temperatures (600 °C) under air atmosphere. The presence of impurities in the milled ZnO could not be detected in the composition analysis using EDS (see Figure 5.11) at least to the detection limit of this technique. As demonstrated in Figures 5.07 and 5.08, XPS spectra of milled ZnO powders reveal the presence of Zn, O and C and remarkably, with increasing t_m, the percentage of O_V increases largely and O_C component increases slightly at the expense of

the O-Zn component. This confirmed that the milling process in ZnO introduces considerable oxygen vacancies providing oxygen-deficient regions within the ZnO matrix.

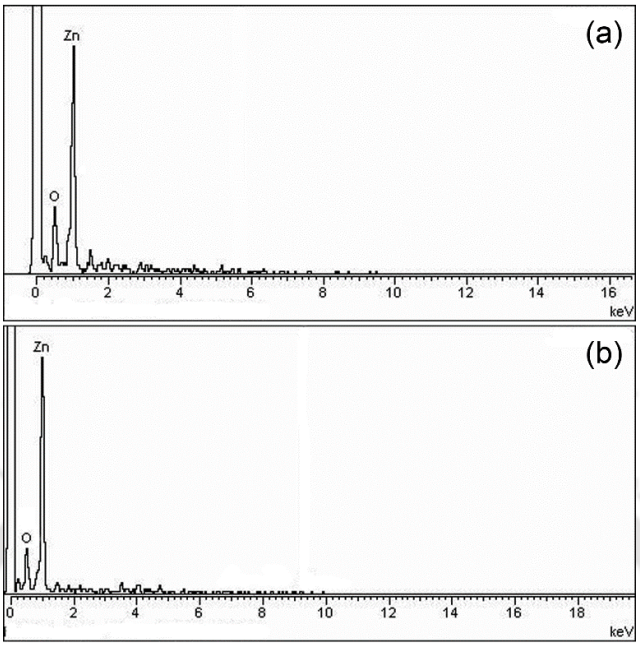

Figure 5.11: Energy dispersive X-ray spectra for milled ZnO powders at (a) t_m = 10 hrs and (b) t_m = 40 hrs.

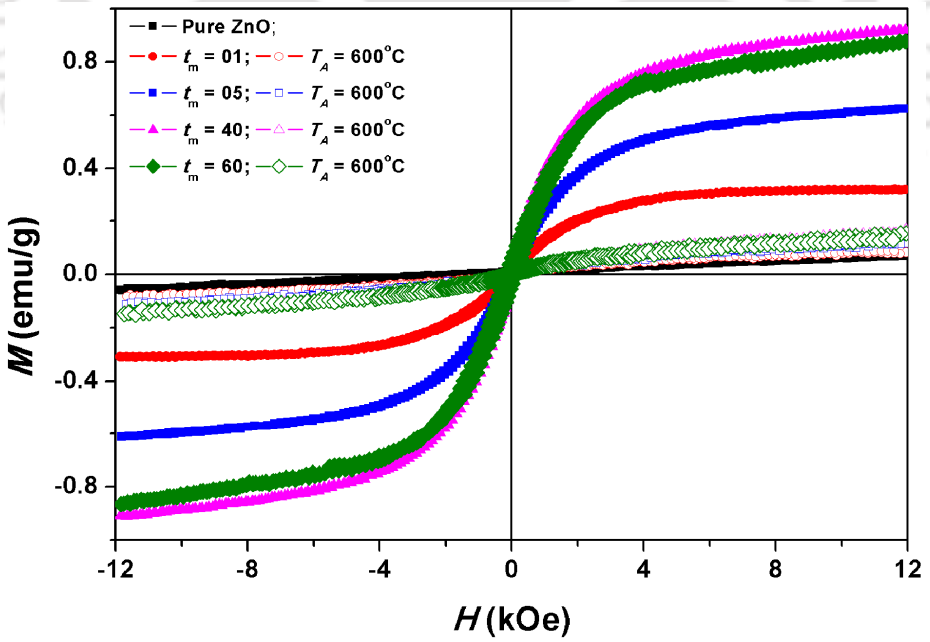

Figure 5.12: Room temperature *M-H* loops of pure un-milled ZnO powder and ZnO powders milled at different t_m followed by the annealing at 600 °C for 3 hrs.

Figure 5.12 depicts room temperature *M-H* loops of pure ZnO, milled ZnO powders at different t_m and annealed ZnO powders at T_A = 600 °C. The extracted values of M_{12kOe} for the as-milled and annealed powders are summarized in Figure 5.13. It is clear from the figures that the annealing process changes the nature of the *M-H* loops of the as-milled powders drastically and reduces the magnetization largely. However, the rate of decrease in magnetization strongly depends on the milling conditions, i.e., M_{12kOe} of 1 hr, 40 hrs and 60 hrs milled ZnO powders decreases from 0.32, 0.92 and 0.88 emu/g to 0.075, 0.156 and 0.158 emu/g, respectively after annealing at 600 °C for 3 hrs. This may be attributed to the effective release of accumulated strain (defects), reduction of oxygen vacancies and increase in average particle size with annealing. These results clearly confirm that the induced FM behavior in ZnO nanocrystalline powders is mainly originated from the intrinsic properties due to size reduction and defects.

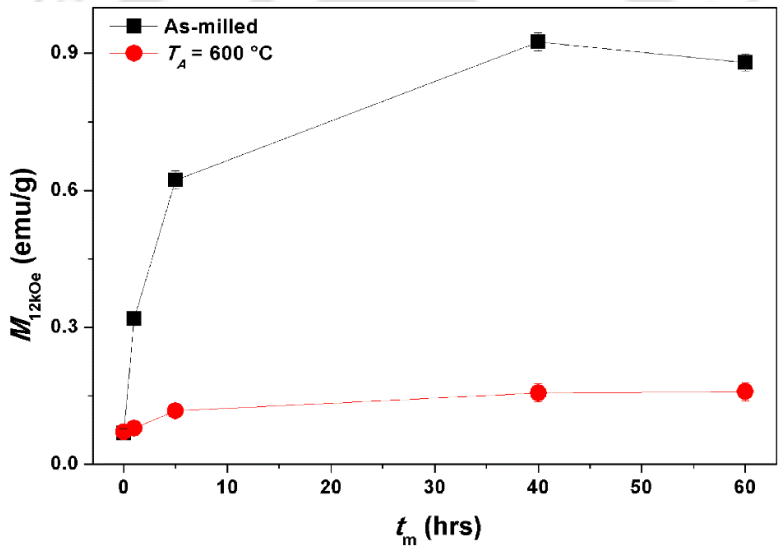

Figure 5.13: The extracted values of M_{12kOe} for the milled and annealed powders at 600 °C for different t_m.

To study the effect of temperature and magnetic field on the magnetic properties of ZnO powders milled at different t_m, low temperature *M-T* measurements at different constant applied fields under ZFC and FC conditions were performed in the temperature range between 2 K and 400 K. In these measurements, the sample was initially cooled down to 2 K under zero applied magnetic field. Then a probing constant DC magnetic field was applied to measure the magnetization as a function of temperature during warming process up to 400 K (ZFC process). Subsequently, the sample was cooled in the same constant applied field down to 2 K and then the magnetization was recorded as the sample was heated to 399 K (FC process). Figure 5.14 displays normalized magnetization [$M(T)/M_{399K}$] as a function of temperature for the ZnO

powders milled at 1 and 40 hrs measured under ZFC (M_{ZFC}) and FC (M_{FC}) conditions at different applied magnetic field of 100, 500 and 5000 Oe. It is clear from the figure that the magnetization data obtained under ZFC and FC conditions are quite different for all the samples measured under low applied magnetic fields of below 500 Oe. As a result, the bifurcation between M_{ZFC} and M_{FC} was observed at around 399 K for all the samples.

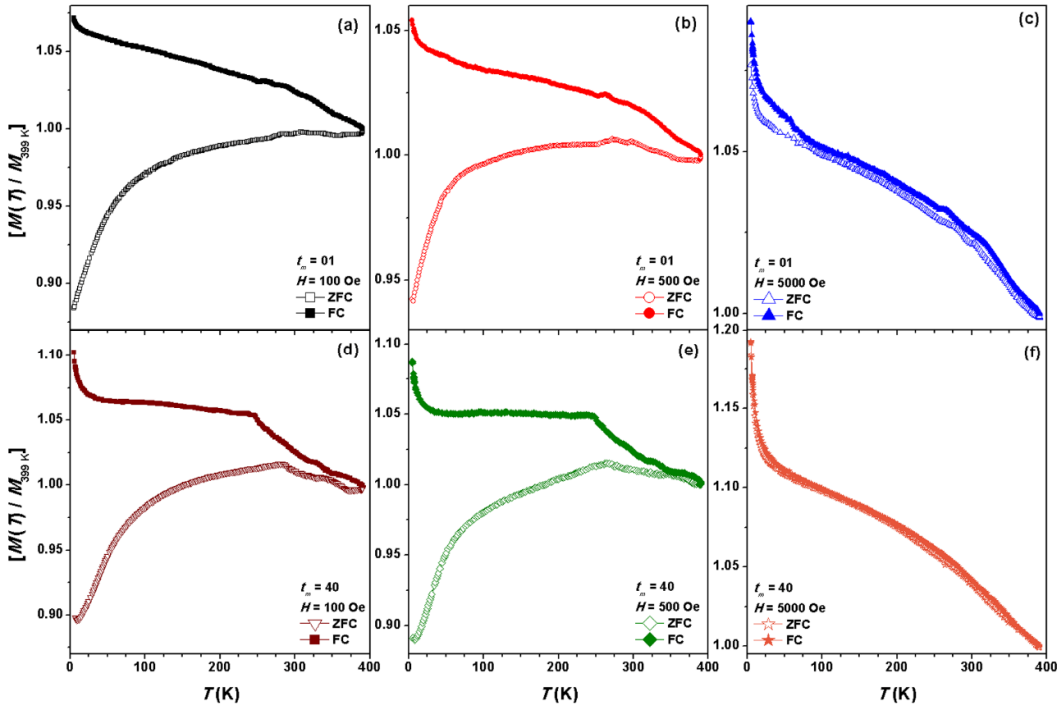

Figure 5.14: Low temperature *M-T* data of milled ZnO powders at different t_m and measured under different applied magnetic fields.

M_{ZFC} decreases largely with decreasing temperature below 300 K, while M_{FC} increases gradually with decreasing temperature down to 20 K followed by a sudden increase at low temperatures below 20 K. The amount of increase in M_{FC} below 20 K increases considerably with increasing t_m. This could be due to the field and temperature dependent magnetic properties of fine ZnO nanocrystals with large defects inducing magnetic moment in milled ZnO powders. Furthermore, the existence of bifurcation between M_{ZFC} and M_{FC} indicates a broader magnetic moment distribution, which originates from the broad size distribution of the crystals as evidenced in Figure 5.05. Interestingly the bifurcation point disappears for the samples measured under 5000 Oe. Such behaviors have also been reported earlier on ZnO NPs, nanowires, nanoflowers and thin films [BANE2007, BIEX2010, XING2010, XING2011]. Interestingly, we have not observed any peaks in M_{ZFC} curve at lower temperature as observed

in NiO due to freezing of disordered surface spins. In addition, we have not observed any systematic variation of bifurcation point with applied magnetic field. These results suggest that the temperature dependent magnetic properties in milled ZnO powder is quite different from the one observed for NiO system.

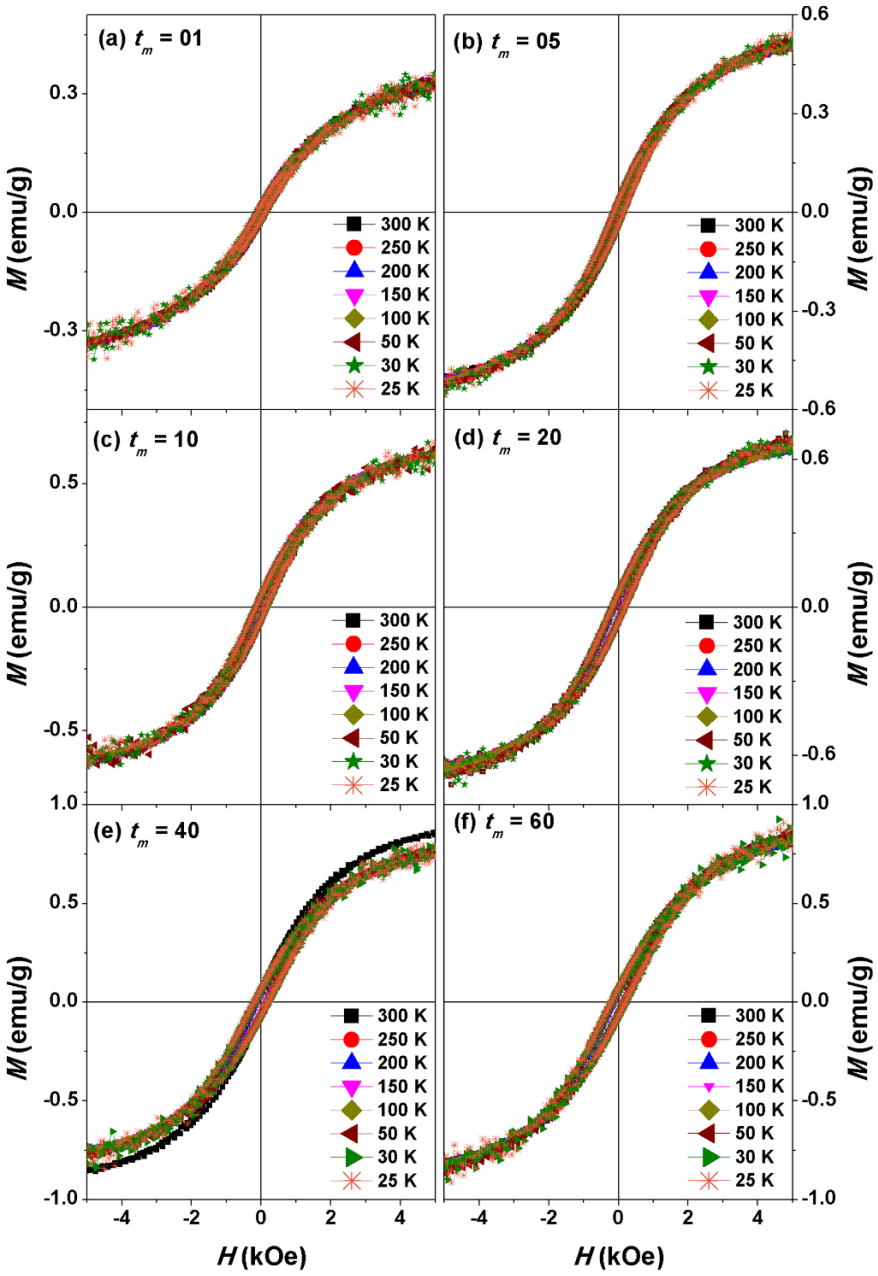

Figure 5.15: Temperature dependent *M-H* loops of milled ZnO powders at different t_m measured under ZFC condition.

To study the effects of structural refinement on the magnetic properties, *M–H* loops were measured at different temperatures between 30 K and 300 K under ZFC condition. Figure 5.15

shows typical *M-H* loops measured under ZFC condition at different temperatures for milled ZnO powders at 1, 5, 10, 20, 40 and 60 hrs. It is observed that the loop shape of the milled powders does not change with temperature, but the variations of H_C and area under the loop increase considerably with decreasing temperature. It is observed that (i) pure ZnO powder exhibits a weak response to applied field due to its PM nature (not shown) and nature of the loops does not change with temperature. (ii) Similarly, the nature of the loops for milled powders also does not change with measurement temperature. (iii) However, the area under the loops increases considerably with decreasing temperature for all the milled powders. In order to understand the effect of temperature on various magnetic parameters, the values of H_C are extracted from Figure 5.15 and plotted as a function of temperature in Figure 5.16.

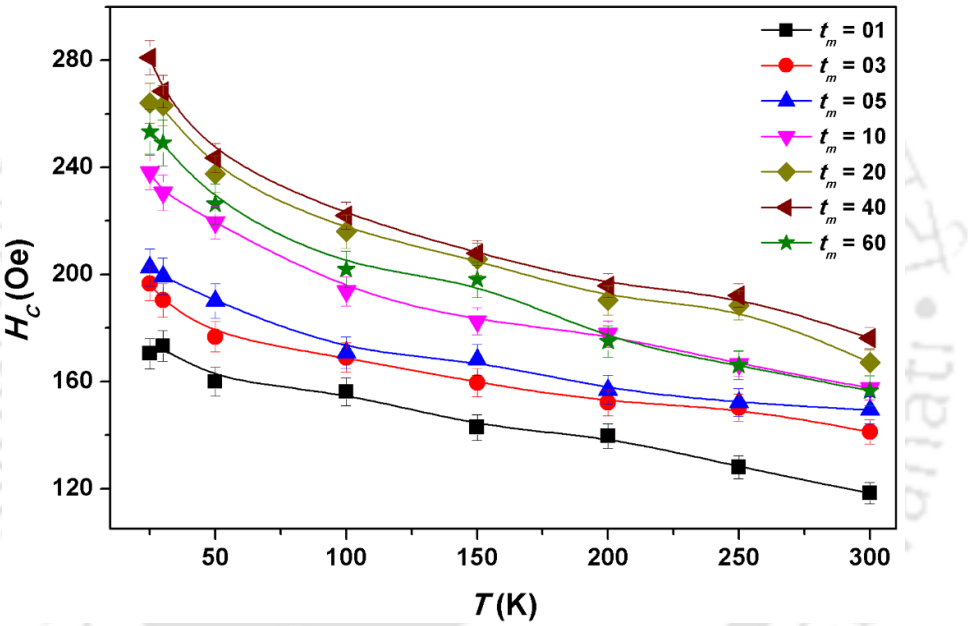

Figure 5.16: The variations of H_C as a function of temperature for milled ZnO powders at different t_m.

$H_C(T)$ of the milled ZnO powders increases with decreasing temperature, but the amount of increase in H_C strongly depends on t_m and size of the ZnO crystals. $H_C(T)$ varies almost linearly for the ZnO powders milled at 1 hr. With increasing t_m, the linear variation of $H_C(T)$ changes into non-linear form particularly at lower temperatures. This could be correlated to different field and temperature dependent magnetic properties of fine ZnO nanocrystals with milling time dependent defects. Nevertheless, we have not observed any systematic variations of $H_E(T)$ for ZnO milled at different t_m.

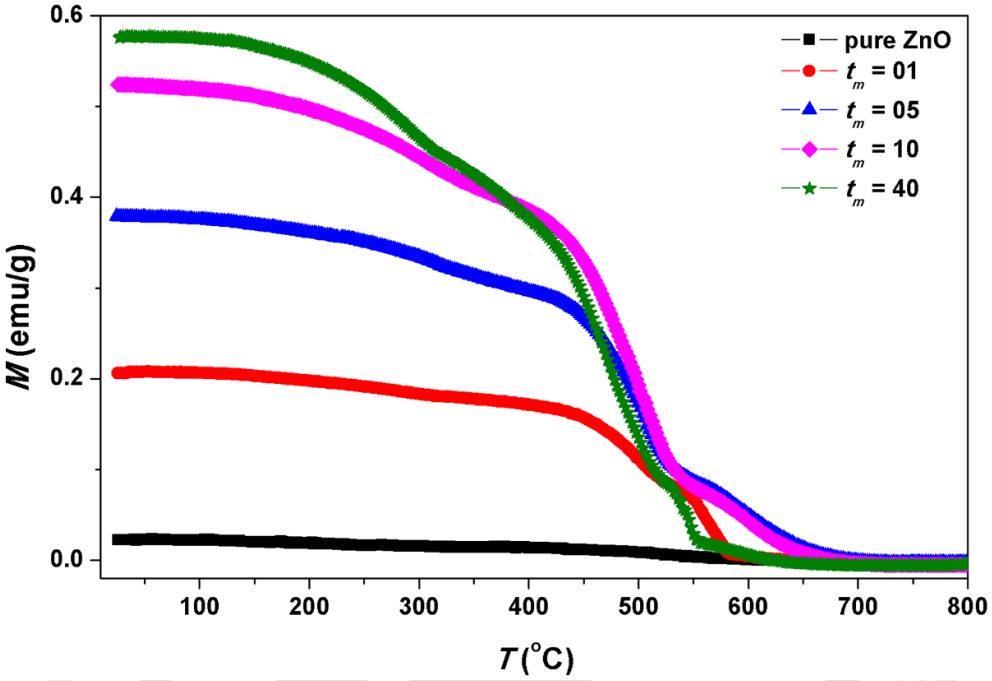

Figure 5.17: High temperature *M-T* data of pure un-milled and milled ZnO powders at different t_m and measured under the applied magnetic field of 2 kOe.

To understand the stability of induced FM above room temperature, high temperature *M-T* curves were obtained at 2 kOe applied field in the temperature range 25 to 800 °C with a heating rate of 4 °C/min for the un-milled and milled ZnO powders and depicted in Figure 5.17. For pure ZnO powder, magnetization varies almost independent of temperature due to its PM nature. On the other hand, the ZnO powder milled for 1 hr exhibits increased moment at room temperature and remains almost constant up to 450 °C and then decreases to zero magnetization above 600 °C. This can be attributed to the presence of induced FM phases in ZnO powder. Conversely, the ZnO powders milled for more than 5 hrs exhibit a continuous decrease in magnetization with temperature and the temperature at which the magnetization becomes nearly zero shifts to higher temperature with increasing t_m up to 20 and decreases for $t_m \geq 40$. Curie temperature (T_C) is obtained from the thermal derivative of *M-T* data and found that it shifts from 500 °C to 525 °C with increasing t_m from 1 to 20 hrs and decreases to 502 °C for $t_m \geq 20$ hrs. Nevertheless, T_C of ZnO is quite high as compared to Co doped ZnO system (430 °C) [NAGA2010]. Such high T_C observed in the ball milled ZnO powders can be attributed to stress (defect density) induced during MA process [GORR2009]. The presence of stress is also evident from the non-smooth decrease of magnetization in *M–T* curves.

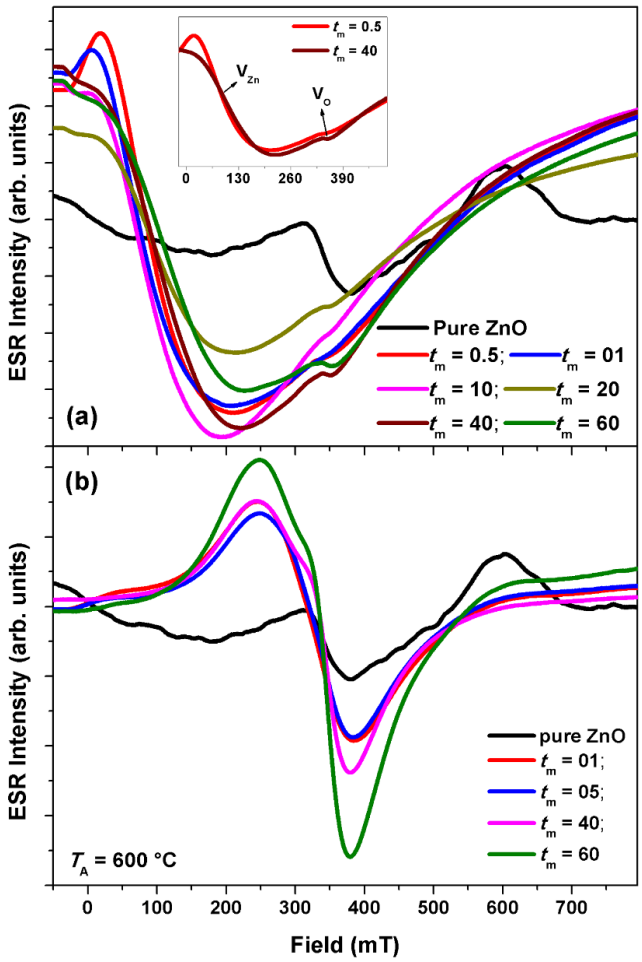

Figure 5.18: EPR spectra of (a) pure un-milled ZnO and milled ZnO powders at different t_m and (b) milled ZnO powders annealed at 600 °C for 3 hrs. Inset: EPR spectra for selected samples for comparison.

5.3.5. Resonance properties

Electron paramagnetic resonance (EPR) spectroscopy is a suitable technique for studying the materials with defects states with unpaired electrons. As the presently investigated samples exhibit high defects due to ball milling process, EPR measurement was carried out on all the pure and milled ZnO powders and the results are depicted in Figure 5.18(a). It is observed that the pure ZnO powders exhibit a single weak resonance signal at a *g* value of 1.95 revealing the PM nature of the pure ZnO powder [SANC1972, GARC2002, HUY2008, LEES2010]. On the other hand, the milled ZnO powders exhibit different spectra, i.e., with increasing t_m the position of the resonance field shifts far away from 336 mT indicating a clear FM signature in the milled powders. The existence of Zn (V_{zn}) and O (V_O) vacancies at lower and higher resonance fields are clearly observed (as depicted in inset), which are in good agreement with

the earlier reports [KAKA1997, ISCH2005, XIAZ2011]. This supports that the milled ZnO powders exhibit obvious defect induced FM.

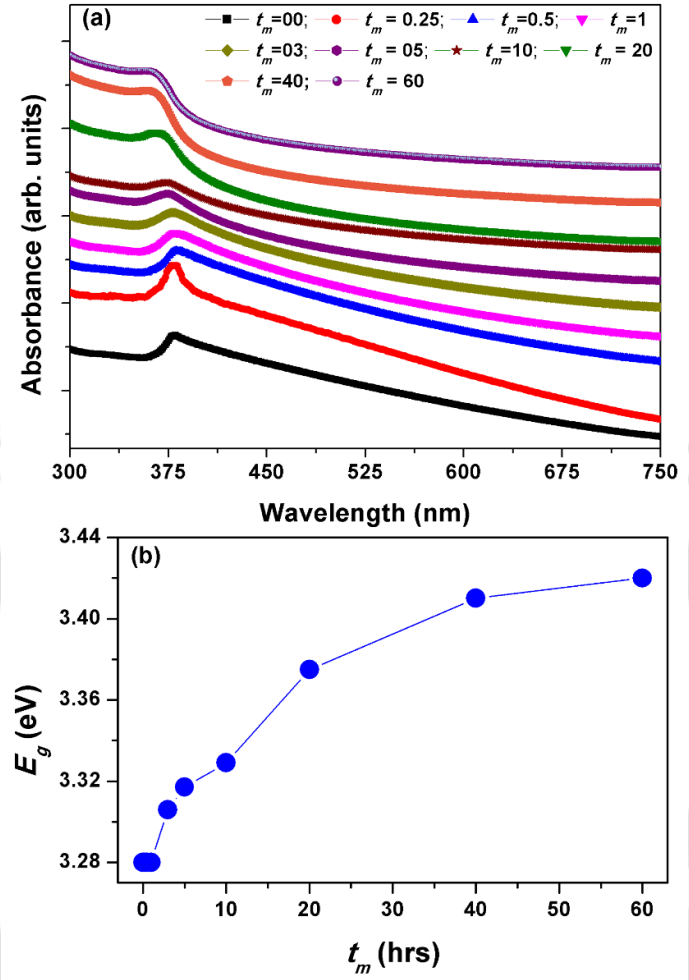

Figure 5.19: Room temperature (a) UV-Vis spectra of pure un-milled and milled ZnO powders and (b) the variation of band gap (E_g) in ZnO powders as a function of t_m.

To understand the effect of annealing on the milled ZnO powders, we have also obtained EPR spectra for the different t_m milled powders and annealed at 600 °C for 3 hrs. Figure 5.18(b) displays the EPR spectra of the ZnO annealed powders and compared with pure ZnO powders. As compared to milled ZnO powders, the annealed ZnO powders display different EPR spectra with different strength of the signals, but similar to the one obtained for pure ZnO powders. In addition, the existence of vacancies is clearly disappeared after annealing at 600 °C. However, the presence of small shoulder at around 296 mT was observed for the ZnO powders milled at higher t_m and annealed. This could attributed to the milling time dependent defects releasement upon annealing. Such observations are in close agreement with the *M-H* measurements shown

in Figure 5.12. In the presently investigated samples, the formation of EPR signal in comparison with magnetic properties could be attributed to the existence of defects in the milled ZnO powders, which provide supportable explanation to the observed room temperature magnetic properties. In the case of ZnO thin films, the magnetic properties of the films are controlled by tuning the density of defects using film thickness [HONG2007, KAPI2009, XING2011]. These results are in good agreement with the results obtained from the calculations on nanostructured ZnO materials [WANG2008, ZUOX2009, PENG2012].

5.3.6. Optical properties

To extend the effect of size reduction on the optical properties, room temperature UV-Vis spectra were recorded for pure un-milled and milled ZnO powders and depicted in Figure 5.19(a). Excitonic absorption peak observed at 379 nm for pure un-milled ZnO powder shifts to 364 nm for 60 hrs milled ZnO powder. A clear blue-shift in the absorption peak is observed with reducing the average crystal size of ZnO powder. This is indicative of the increase in band gap with size reduction. However, the observed properties cannot be fully attributed to quantum size effect in ZnO as the crystal size lies in the range much higher than excitonic–Bohr diameter in ZnO (6.48 nm). The enhanced absorption in nanoparticles can be attributed to a large surface to volume ratio and increased oscillator strength with size reduction. The determined value of band gap for the milled ZnO powder, plotted against t_m [see Figure 5.19(b)] increases with increasing t_m. Since the excitonic absorption is substantially increased in the milled ZnO nanoparticles, the presently investigated ZnO nanoparticles have great potential for the use as efficient UV light absorber [YADA2006].

The above results suggest that the ZnO powders prepared by ball mill process exhibit significantly induced FM at room temperature due to defects, high T_C and tunable optical properties could facilitate integration of spintronic devices.

5.4. Summary

A systematic investigation on the evolution of structural, vibrational, electronic, magnetic, resonance and optical properties of pure and milled ZnO powders prepared by ball mill process in a planetary ball mill under dry mill conditions and at argon atmosphere has been carried out as a function of different t_m. The salient features of the ZnO powders from the current investigations are as follows:

- The ball mill process produces single phase hexagonal wurtzite structured nanocrystalline ZnO powders with the average crystallite size of nanometer range

(around 12 nm). The lattice volume increases with increasing t_m up to 20 hrs and then exhibits weak dependence above 20 hrs of milling. Microstructural investigations show that the agglomeration of fine particles increases with t_m and the nanocrystalline powders exhibit irregular shapes with broad size distribution.

- Vibrational properties using Raman spectra show that pure ZnO powders exhibit six Raman modes. With increasing t_m, E_{2H} mode decreases drastically and broadens asymmetrically. In addition, the modes of A_1(LO) and E_1(LO) become more prominent and shift to lower frequencies in milled ZnO powders due to defects and lattice expansion.
- Electronic properties using O 1s XPS spectra of milled ZnO powders confirm the existence of oxygen deficient regions within the matrix of ZnO and the percentage of oxygen deficient region increases at the expense of the O-Zn component. These results are in good agreement with the results obtained from Raman spectra.
- Paramagnetic nature observed in un-milled ZnO gradually unveils room temperature ferromagnetism with modest magnetization and coercivity. A maximum magnetization of 0.92 emu/g at 12 kOe applied field and a coercivity of 172 Oe were obtained for 40 hrs milled ZnO powder.
- Low temperature magnetization in the temperature range between 4 K and 400 K shows applied field dependent bifurcation between ZFC and FC curves. High temperature *M-T* data disclose a clear magnetic phase transition from FM to PM state around 500 °C, which shifts slightly towards higher temperature with increasing t_m up to 20 hrs and then decreases for $t_m \geq 40$.
- Resonance study reveals that FM order increases with increasing milling time due to the increase in oxygen and zinc vacancies. A close correlation between EPR results and magnetic properties has been observed.
- The optical studies reveal a blue-shifting of excitonic absorption peak at UV-blue band with crystal size reduction. This results in an increase in band gap with size reduction in milled ZnO powders.
- Annealing of milled ZnO powders results in a large reduction in magnetization and confirms the origin of ferromagnetism in milled ZnO powders as intrinsic one.

Chapter 6

Properties of TiO_2 powders prepared by ball milling process

6.1. Introduction

Diluted magnetic semiconductor (DMS) based on metal-oxide (in particular Titanium oxide (TiO_2), an important wide band gap semiconductor) has been studied extensively in the past decades due to its wide range of applications like photo catalysis, solar cells, photovoltaic, etc [SOWW2001, PAUL2006, LID2010, CHEN2017]. Another important aspect of TiO_2 is the exhibition of ferromagnetism (FM) above room temperature by the addition of magnetic impurities [MATS2001, WANG20061, CHOU2011]. The discovery of room temperature FM in Co doped TiO_2 thin film was first reported by Matsumoto et al [MATS2001]. Subsequently, extensive studies have been carried out for the development of FM TiO_2 semiconductor to produce multifunctional spin based electronic devices where both charge and spin degrees of freedom can be manipulated in a single given material [FURD1988, ZUTI2004]. However, the origin of FM and reproducibility of FM semiconductors remain a challenge [SHIN2004, TIAN2008].

Furthermore, a careful review of the literature reveals contradictory results on the development of FM in TiO_2 system. For example, Hong et al [HONG2006] and Yoon et al [YOON2006] reported that FM in TiO_2 thin films is likely to be caused by oxygen vacancies. Kim et al [KIMD2009] shown that oxygen vacancy induced lattice distortion in TiO_2 makes it FM. Zhou et al [ZHOU2009] revealed that Ti^{3+} ions formed due to oxygen ion irradiation provide local 3*d* moments and induce FM in defective TiO_2 single crystals. In contrast, Pandey et al [PAND2011] argued that an oxygen vacancy leads to electron doping in TiO_2 system, but does not induce appreciable magnetic moment using *ab-initio* electronic structure calculation. Recently, Hoa et al [HOAN2012] reported enhanced FM in un-doped TiO_2 nanowire as compared to Ni doped TiO_2 nanowire. On the other hand, Sundaresan et al [SUND2009] suggested that existence of FM in nanostructured metal-oxide is universal feature [SUND2009]. However, the determination of nature of defects and phase change responsible for the observed FM remains a challenge. Theoretical studies indicated that cation vacancy and di-vacancy are ferromagnetically coupled [PENG2009]. Furthermore, the theoretical and experimental evidences show that the magnetic ordering of un-doped TiO_2 is strongly related to oxygen vacancy [RUMA2007, KIMD2009]. These controversial results among different research groups suggest that the magnetic properties of oxide materials are critically dependent on fabrication, growth conditions and doping agents. As compared to various fabrication methods, high energy ball mill method is a very simple and low cost process, where one can easily tune the surface defects and phase changes by controlling milling intensity. It may be noted that the particle size and crystal morphology play an important role in magnetic,

magneto-optic, photocatalytic and thermal properties of TiO_2 [CHEN2007, TONG2013, LIX2014, WUS2014, WANG2015].

Therefore, in this chapter, we report (i) evolution of nanoscale TiO_2 powder with increasing milling time (t_m), (ii) the effects of size reduction and defects induced during milling on the structural, vibrational, electronic, magnetic, resonance and optical properties of TiO_2 powders and (iii) the correlation between the crystal structure, microstructure, vibrational, electronic, magnetic, resonance and optical properties of these ball milled powders.

6.2. Experimental details

Weighed quantities of TiO_2 powders (white color) were taken in high energy planetary ball mill filled with high purity argon gas. The milling process of TiO_2 powders was carried out for different milling periods (t_m) from 0.25 to 60 hrs using the mill operated at 500 rpm with a ball-to-powder weight ratio of 10:1. The optimization of the milling speed and ball-to-powder weight ratio was done mainly by analyzing the variation in the structural and magnetic properties of the TiO_2 powders. In order to avoid any local heating during milling and its influence on the resulting properties, the milling process was programmed to halt for 15 minutes after every 15 minutes of operation. In addition, the milled powders were collected at regular intervals and characterized to monitor the evolution of nanostructure in TiO_2 powders.

The phase evolution and crystal structure of TiO_2 powders were analyzed through X-ray diffraction (XRD) patterns obtained using high-power (18 kW) X-Ray diffractometer (Rigaku TTRAX III, Japan). XRD data were collected at a slow scan rate of 0.005°/s for analyzing the structural parameters as a function of t_m. The changes in the surface morphology of the powders were observed using field emission scanning electron microscope (FE-SEM) and overall composition of the pure un-milled and milled powders was determined using energy dispersive spectroscopy (EDS, Oxford) attached to SEM unit. The microstructural properties of the pure un-milled and milled TiO_2 powders were analyzed using transmission electron microscopy (TEM, JEOL 2100 and TECNAI G^2 F30) technique. Raman spectra were obtained using micro-Raman spectroscopy (LabRam HR800, Jobin Yvon) using excitation wavelength of 488 nm at room temperature. X-ray photoelectron spectroscopy (XPS) analysis was carried out in a standard ultrahigh vacuum surface science chamber consisting of a PSP vacuum technology electron energy analyzer (angle integrating ±10°) and a dual anode X-ray source with an Mg-K_α source (1253.6 eV) at a base pressure of 2×10^{-10} mbar and energy resolution at full width at half maximum (FWHM) is about 0.8 eV. The spectrometer was calibrated using Au $4f_{7/2}$ at

83.9 eV [ZHAN20121]. Room temperature magnetic properties of the pure un-milled and milled TiO_2 powders were characterized using vibrating sample magnetometer (VSM, LakeShore Model 7410). Room temperature electron paramagnetic resonance (EPR) measurements were carried out on a JEOL Spectrometer (JES-FA200) operating at X-band frequency (ν =9.4 GHz) with 100 kHz magnetic field modulation in powder form. Steady state photoluminescence (PL) spectra were recorded by using a 312 nm Xenon lamp excitation (AB2, Thermo spectronic). Fourier transform infrared (FTIR) spectra were measured in the range 400 - 4000 cm^{-1} with FTIR spectrometer (Perkin Elmer, Spectrum BX).

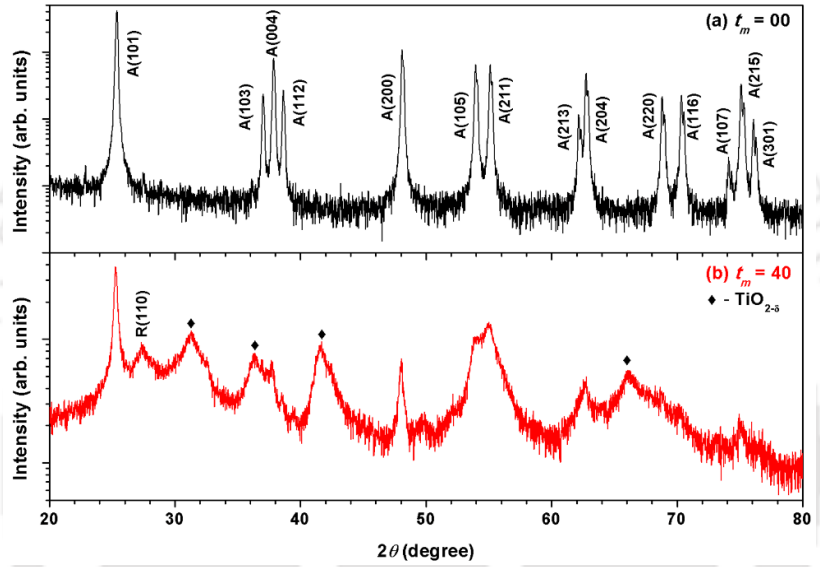

Figure 6.01: Room temperature XRD patterns of (a) pure un-milled TiO_2 powder and (b) milled TiO_2 powder for 40 hrs.

6.3. Results and Discussion

6.3.1. Structural properties

Figure 6.01 depicts typical room temperature XRD patterns of pure un-milled TiO_2 powder and TiO_2 powder milled at t_m = 40. The un-milled TiO_2 powder shows Bragg reflections corresponding to anatase phase structure [YANJ2013]. Similarly, the milled TiO_2 powder for 40 hrs also exhibits majorly anatase phase of TiO_2 without any impurity phases within the detection limit of X-ray diffractometer. However, we have observed new peaks at 2θ= 27.39°, 31.34°, 36.33°, 41.64° and 66.17° for the milled powders. In comparison with standard JCPDS data, these new peaks may be assigned to rutile phase of TiO_2 (2θ = 27.39°) and oxygen deficient TiO_2 phase ($TiO_{2-\delta}$). In addition, a careful observation of the XRD peaks reveals that

the sharp Bragg reflections observed in pure TiO_2 powders broadens significantly along with a considerable shift in peak position towards a lower diffraction angle.

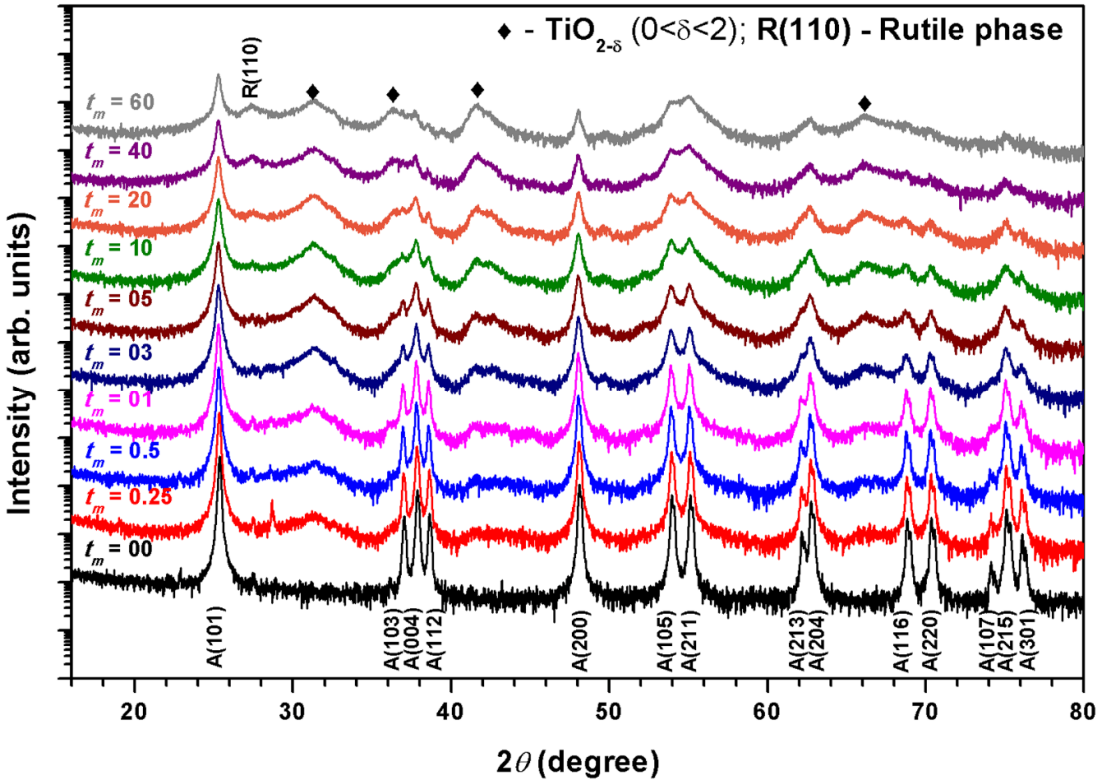

Figure 6.02: Room temperature XRD patterns of pure un-milled and milled TiO_2 powders at different t_m.

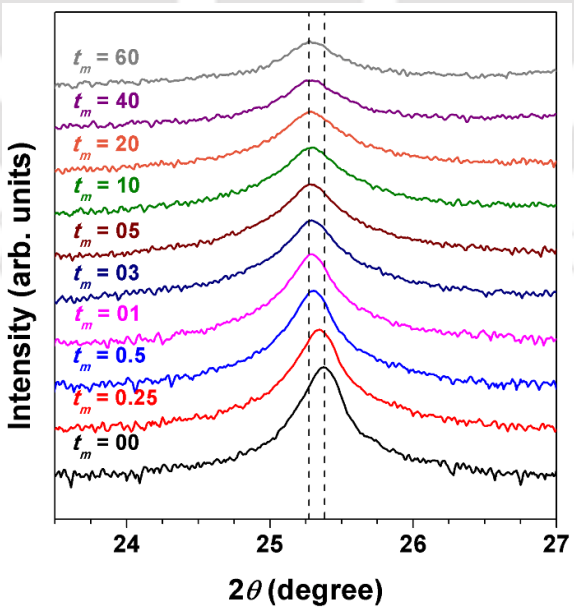

Figure 6.03: Expanded version of XRD patterns close to A(101) peak at $2\theta = 25.3°$ for pure un-milled and milled TiO_2 powders at different t_m.

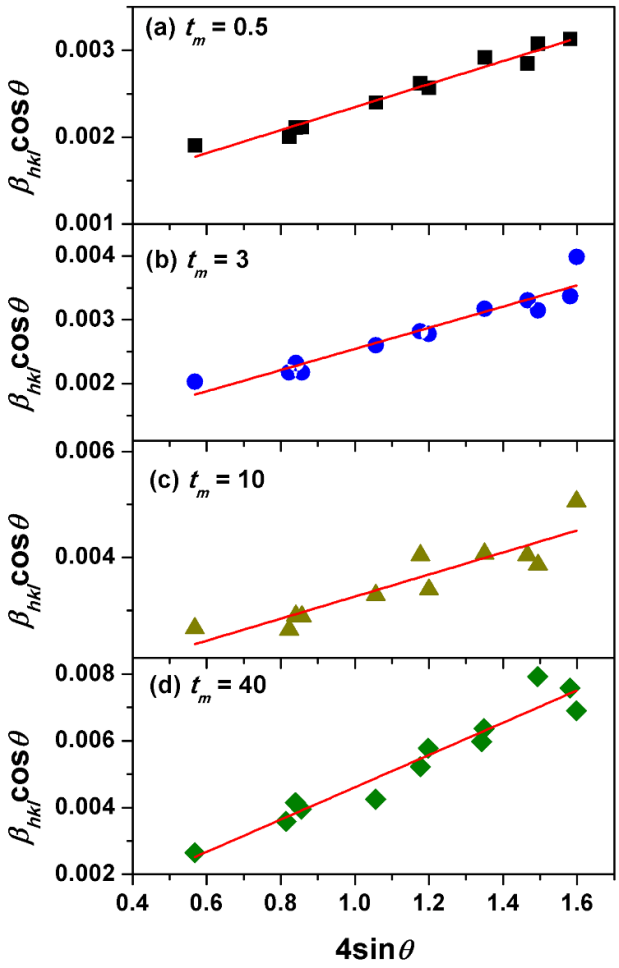

Figure 6.04: WHP fit for the milled TiO_2 powders at different t_m.

In order to understand the effect of milling systematically, room temperature XRD patterns of milled TiO_2 powders at different t_m were taken systematically and shown in Figure 6.02. It is observed that (i) With increasing t_m, the anatase phase of the peaks gets broadened, which results in a merging of the peaks and the peak position shifts gradually to lower diffraction angle as shown in Figure 6.03. While the peak broadening indicates the formation of highly refined and strained TiO_2 powders, the peak shifts suggest a considerable change in the lattice parameter during the milling process. (ii) The development of additional peaks corresponding to the oxygen deficient TiO_2 phase is observed even for 0.25 hrs milled TiO_2 powders and the peak intensity increases with increasing t_m. (iii) Upon increasing t_m above 10 hrs, a new peak corresponding to rutile phase of TiO_2 is observed. These results clearly confirm that with increasing t_m, the ball milling induces defects and phase changes in anatase phase of TiO_2 besides its size reduction. This is consistent with the recent report on similar system [SEPE2012]. In order to calculate the average crystal size and strain, XRD patterns were

analyzed using uniform deformation model as defined by Williamson-Hall Plot (WHP) method using eqn.(6.01).

$$\beta_{hkl}\cos\theta = \frac{k\lambda}{D} + 4\eta\sin\theta \qquad (6.01)$$

where D is the average crystal size, k is a constant taken as 0.9 for spherical particles, λ is the wavelength of the X-ray, η is strain, β_{hkl} is the full width at half maximum (FWHM) of the peaks in radian and θ is the peak center.

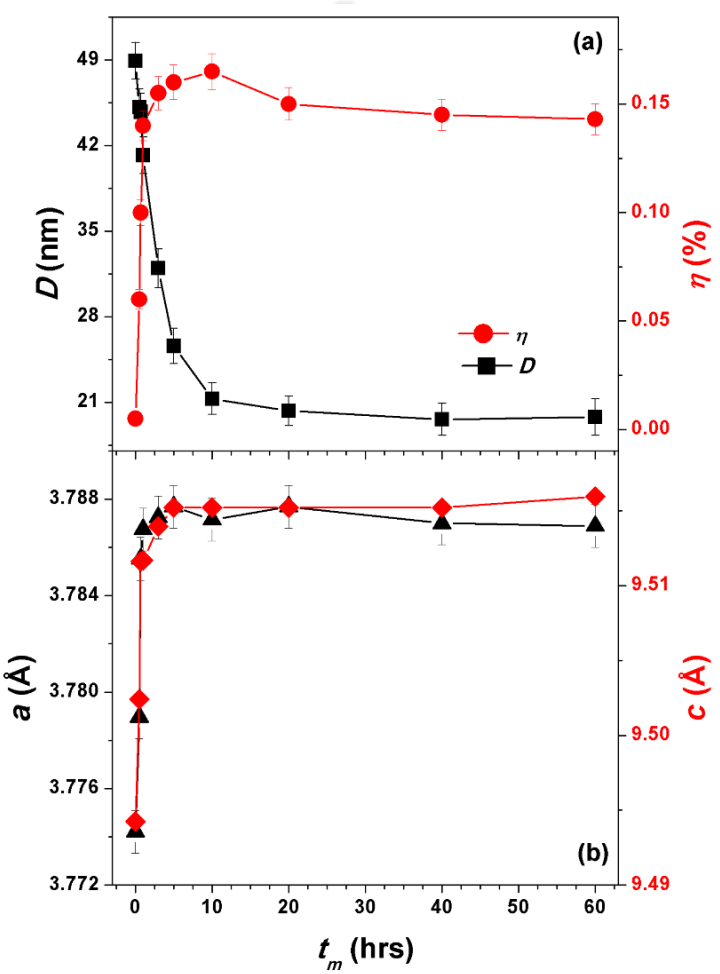

Figure 6.05: The variations of (a) D, η and (b) a and c for pure un-milled and milled TiO_2 powders at different t_m.

Figure 6.04 shows the typical plot of WHP method for the milled TiO_2 powders. Average crystal size (D) and strain (η) were calculated from intercept and slope, respectively by plotting $\beta_{hkl}cos\theta$ versus $4\sin\theta$ and fitting the data using linear fit. Figure 6.05(a) depicts the variations of D and η as a function of milling time. D decreases almost largely up to 10 hrs of milling and

then tends to saturate for higher milling time. The minimum crystal size reachable by this milling process is about 19 nm for 40 hrs milled TiO_2 powders. On the other hand, strain increases considerably at initial milling period and then slightly decreases for higher milling period above 10 hrs. As compared to NiO and ZnO milled powders, the strain value is observed to be low and hence the minimum crystal size achievable is limited only to about 19 nm. From the shift in the XRD peak positions, the values of lattice constant *a* and *c* were calculated using eqn.(6.02) for pure and milled TiO_2 and depicted in Figure 6.05(b).

$$\frac{1}{d^2} = \frac{h^2 + k^2}{a^2} + \frac{l^2}{c^2} \tag{6.02}$$

where, *d* is interplanar spacing; *h, k, l* are Miller indices and *a*, *c* are lattice constants. The determined values of lattice constants increase with increasing t_m up to 10 hrs and then remains almost constant on further increasing t_m. This could be correlated to the milling process that the formation of dislocations (defects) caused by the high-energy ball mill to develop nanocrystalline microstructure increases initially and then reaches the saturation when the crystal size attains minimum value. As a result, the lattice constant increases by the negative interface pressure activated by the strain, which distorts the local structure without affecting overall crystal structure. The further milling does not produce more dislocations due to the difficulty in generating additional dislocations in smaller crystals and limits the change in the lattice constants. This results in a saturation in the variation of lattice constant as observed in the presently investigated samples.

To monitor the change in surface morphology and evolution of nanocrystalline microstructure of the milled TiO_2 powders, the pure un-milled TiO_2 and milled TiO_2 powders were characterized using FE-SEM and TEM techniques. Figure 6.06 depicts the typical FE-SEM images of pure un-milled TiO_2 and milled TiO_2 powders at different t_m. A clear particle morphology displaying spherical shaped particles with the average particle size of 150 to 350 nm is observed in pure un-milled TiO_2 powders. With increasing t_m to 0.25 hrs, we have observed almost the same particle morphology without any significant changes in the average particle size of the milled powders. On further increasing t_m to 5 hrs, the particle size decreases considerably below 100 nm along with the formation of significant agglomerated particles. Upon increasing t_m above 5 hrs, the agglomeration of the fine particles increases to form aggregated particles and the number of such particles increases with increasing t_m. Note that these aggregates are typical of ball-milled powders, which occurs from the repeated cold welding and fracture of powder during milling. Figure 6.07 displays typical plane-view bright-

field TEM (BF-TEM) images and selected area electron diffraction (SAED) patterns for pure un-milled TiO_2 and milled TiO_2 powders at 05 hrs and 40 hrs.

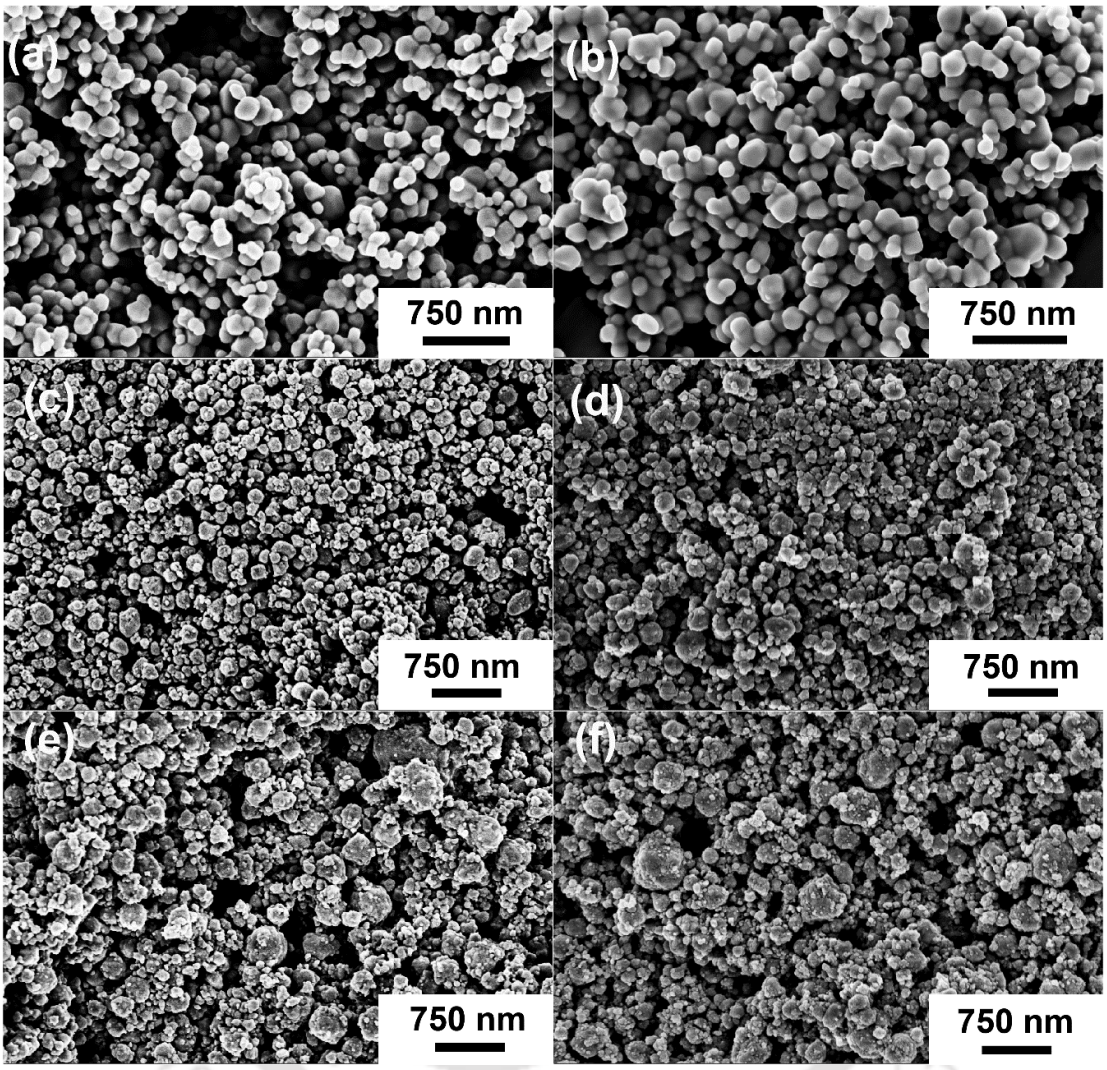

Figure 6.06: FE-SEM images of (a) pure un-milled TiO_2 powder, and milled TiO_2 powders at different t_m: (b) t_m = 0.25, (c) t_m = 5 hrs, (d) t_m = 20 hrs, (e) t_m = 40 hrs and (f) t_m = 60 hrs.

BF-TEM image of the pure TiO_2 powder reveals a clear particle morphology with size varying between 50 and 120 nm. The polycrystalline nature and the anatase phase are evident from TiO_2 diffraction rings in the SAED pattern. On the other hand, BF-TEM images of milled TiO_2 powders confirm the presence of fine nanocrystalline microstructure with irregular morphology. The SAED pattern of 5 hrs milled TiO_2 shows diffraction rings, which could be indexed to anatase phase only and confirm the polycrystalline nature of the TiO_2 particles. The average size of the crystals estimated from BF-TEM images at random locations decreases from 60-140 nm for the pure un-milled TiO_2 to about 26 nm after milling for 3 hrs.

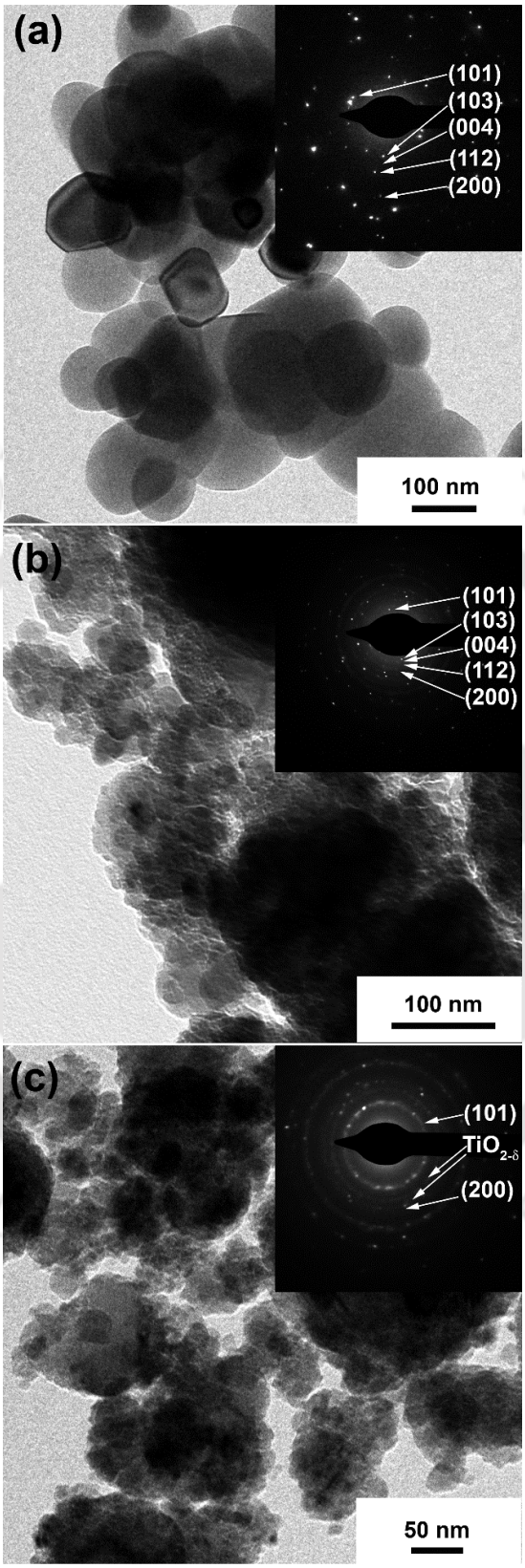

Figure 6.07: Bright-field TEM images and selected area electron diffraction patterns of (a) pure un-milled TiO_2 powder, and milled TiO_2 powders at different t_m: (b) t_m = 5 and (c) t_m = 40 hrs.

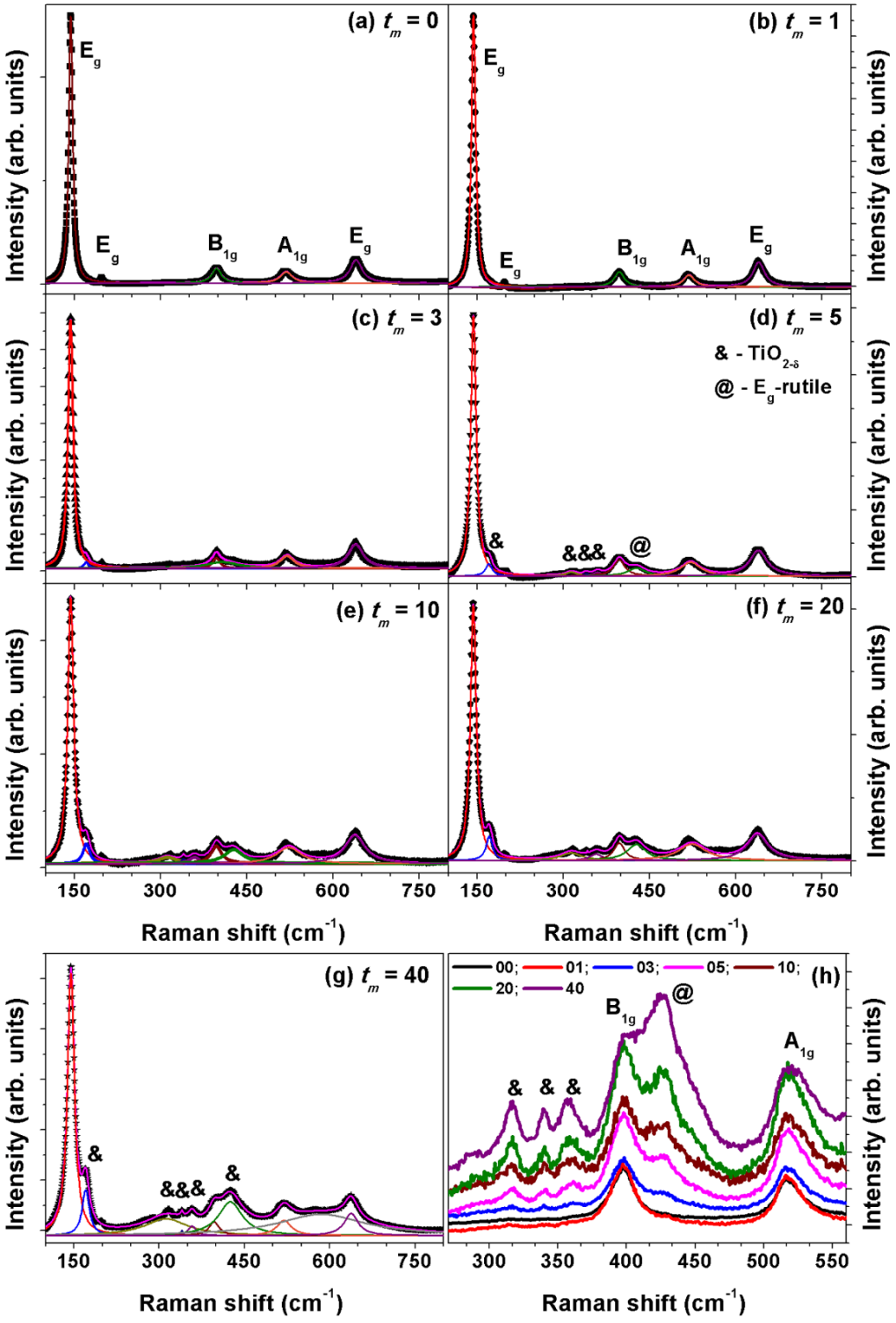

Figure 6.08: Room temperature Raman spectra of pure un-milled (a) and milled TiO_2 powders at different milling periods (b-g). (h) The expanded view of Raman spectra in the range between 270 and 570 cm^{-1}.

On further increasing t_m to 40 hrs, the nanocrystalline microstructure is further refined with the average crystal size of about 19 nm. The SAED pattern reveals not only the existence of polycrystalline TiO_2 with the anatase phase, but also diffraction rings corresponding to oxygen deficient TiO_2. These observations are in good agreement with the XRD results and the variations of TEM crystallite size of TiO_2 exhibit almost a similar trend with that of XRD results. Nevertheless, the nanoscale powders exhibit irregular shapes with broad size distribution.

6.3.2. Vibrational properties

Figure 6.08 depicts room temperature Raman spectra for pure un-milled and milled TiO_2 powders at different t_m. The expanded version of Raman spectra in the range between 270 and 570 cm^{-1} is shown separately in Figure 6.08(h) for comparison. According to factor group analysis, anatase phase of TiO_2 has six Raman active modes (A_{1g}+ $2B_{1g}$+$3E_g$) [OHSA1980]. All the observed Raman modes in the pure TiO_2 samples can be assigned to the Raman spectrum of the anatase phase of TiO_2: ~ 144 cm^{-1} (E_g), 197 cm^{-1} (E_g), 399 cm^{-1} (B_{1g}), 513 cm^{-1} (A_{1g}) and 639 cm^{-1} (E_g). These peaks are not only consistent with the literature results [OHSA1978, KELL1997, ZHAN2000, SEEP2006, TIAN2012], but consistent with the XRD results as shown in Figure 6.01. It has been known that E_g peak is mainly caused by symmetric stretching vibration of O-Ti-O in TiO_2, the B_{1g} peak is caused by symmetric bending vibration of O-Ti-O, and A_{1g} peak is caused by the antisymmetric bending vibration of O-Ti-O. With increasing t_m up to 1 hr, we have not observed any additional peaks, except the observation of considerable broadening, peak shifting in the peaks to lower wavenumber, and reduction in peak intensity. On further increasing t_m above 1 hr, we have noticed the development of additional peaks at 171 cm^{-1}, 315 cm^{-1}, 340 cm^{-1}, 357 cm^{-1} and 426 cm^{-1} and the intensity of these peaks increases gradually with increasing t_m. While the peaks at 171 cm^{-1}, 315 cm^{-1}, 340 cm^{-1} and 357 cm^{-1} can be correlated to the development of oxygen deficient TiO_2 phase ($TiO_{2-\delta}$) [WUY2012, OULD2014], the peak at 426 cm^{-1} is related to the E_g of rutile phase [SAMS2015]. These observations are in close agreement with the XRD results. The broadening (full width at half maximum) of the Raman peak at 144 cm^{-1} increases from about 8 for pure un-milled TiO_2 powder to 14.56 for 40 hrs milled TiO_2 powder and in addition, the intensity of the peak also decreases largely. This can be majorly correlated to the decrease in the average crystal size. On the other hand, the shift in Raman wavelength of E_g band to higher values confirms the tensile strain in as-milled powders [MEUL2004, ZARD2009, CHEN2010]. As

the observed crystal size using structural analysis is about 19 nm, the observation of phonon confinement is not expected in the presently investigated samples [BERS1998, LIBA2005, SAHO2009, GEOR2012].

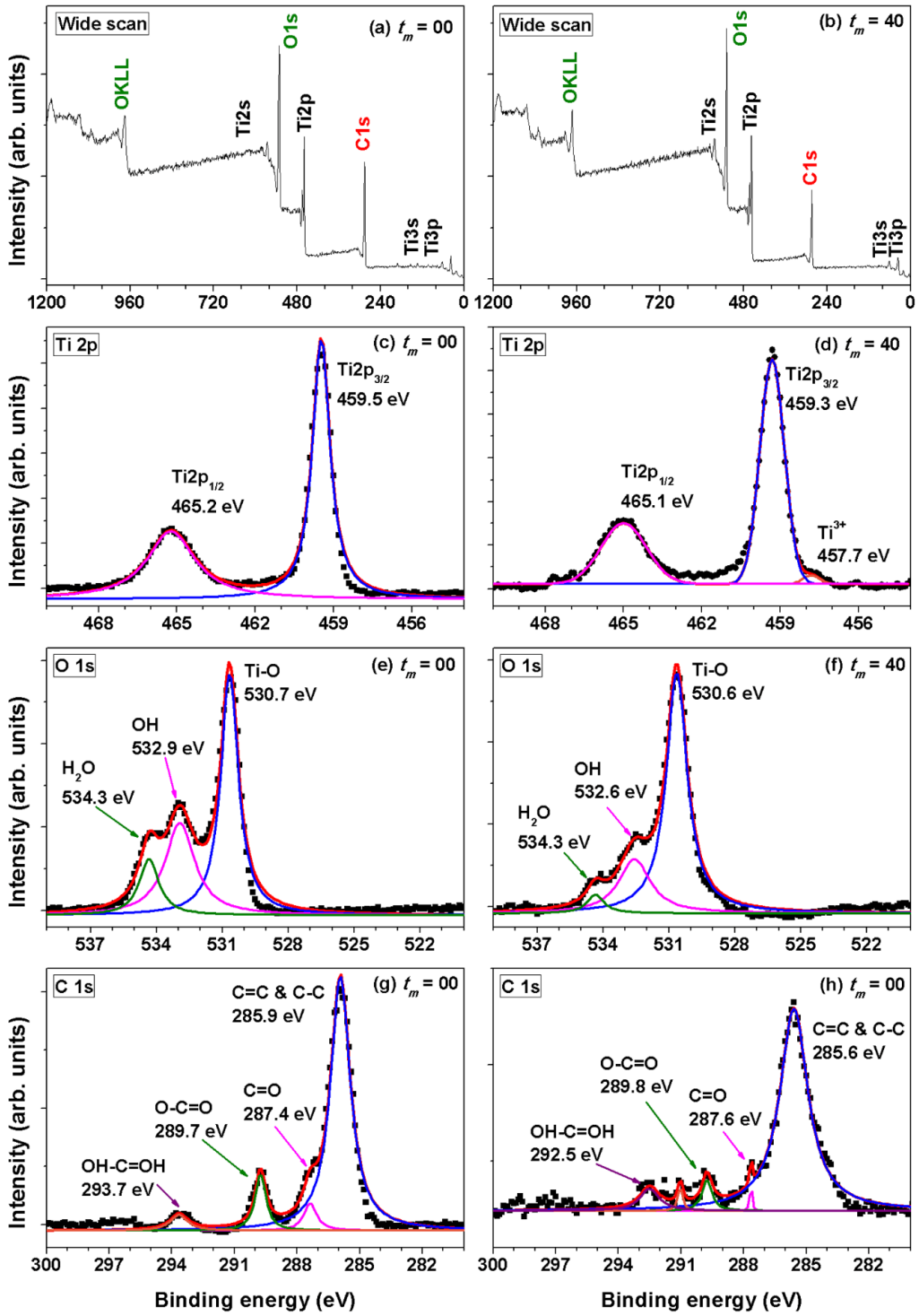

Figure 6.09: XPS spectra of wide scan, Ti 2p, O 1s and C 1s for (a,c,e,g) pure un-milled TiO_2 and (b,d,f,h) 40 hrs milled TiO_2 powders.

6.3.3. Electronic properties

To understand the chemical composition of pure un-milled and milled TiO_2 powders, XPS survey spectra, high resolution Ti 2p, O 1s and C 1s spectra were obtained for both pure un-milled and milled TiO_2 powders and depicted in Figure 6.09. In the survey spectra, the presence of Ti, O and C is observed. Ti 2p spectrum of pure un-milled TiO_2 powder displays Ti $2p_{1/2}$ and Ti $2p_{3/2}$ spin-orbit splitting photoelectrons located at binding energies of 459.5 eV and 465.2 eV, respectively. The peak separation of 5.7 eV between Ti $2p_{1/2}$ and Ti $2p_{3/2}$ signals is in good agreement with the reported literature values [DIEB1996, MCCA1998, SCAN2013] confirming Ti^{4+} in TiO_2 and identical chemical state of Ti atoms in pure TiO_2. The O 1s signal of pure TiO_2 shows a peak at 530.7 eV and a shoulder located toward the side of higher binding energies. The curve-resolved O 1s signal of the pure TiO_2 results in a two peaks located at 532.9 eV and 534.3 eV, which are assigned to hydroxyl (OH) and water molecule (H_2O), respectively [PATR2014]. Similarly, the C 1s spectrum shows the peaks at 285.9 eV, 287.4 eV, 289.7 eV, 293.7 eV corresponding to C=C/C-C, C=O, O-C=O, and OC-C=OH species in the pure TiO_2 sample. The binding energy difference of 71.3 eV between the observed peak positions of Ti $2p_{3/2}$ and O 1s (oxide) is also in excellent agreement with reported literature values of 72.9 – 71. 2 eV. On the other hand, the milled TiO_2 powder for 40 hrs shows almost the similar features except considerable peak broadening and additional peaks in Ti 2p spectrum. The additional peak observed at 457.7 eV is mainly due to the formation of oxygen deficient TiO_2 and/or Ti^{3+} [RATH2009, BARM2015, BHAR2016]. In addition, the relative intensities of the peaks in O 1s spectrum of the milled TiO_2 powder vary significantly from the pure TiO_2 powder, mainly due to the oxygen vacancies created in the milled TiO_2 powder. These results are in good agreement with the results of XRD and Raman spectra as demonstrated in Figure 6.02 and 6.08, respectively.

6.3.4. Magnetic properties

Figure 6.10 depicts room temperature initial magnetization (*IM*) curves and magnetic hysteresis (*M-H*) loops and expanded version of *M-H* loops close to origin (inset) for pure un-milled and milled TiO_2 powders at different t_m. It is observed that (i) pure un-milled TiO_2 powder exhibits a weak response to applied field due to its paramagnetic (PM) nature and hence *M-H* loop passes through the origin [SUND2006]. (ii) On the other hand, the milled TiO_2 powder exhibits different nature of response to the applied field, i.e., the magnetization increases moderately at lower applied fields and then exhibits a gradual increase at higher

applied fields. The rate of increase in the magnetization at lower field increases progressively with increasing t_m up to 3 hrs and then decreases slightly for t_m = 5 hrs.

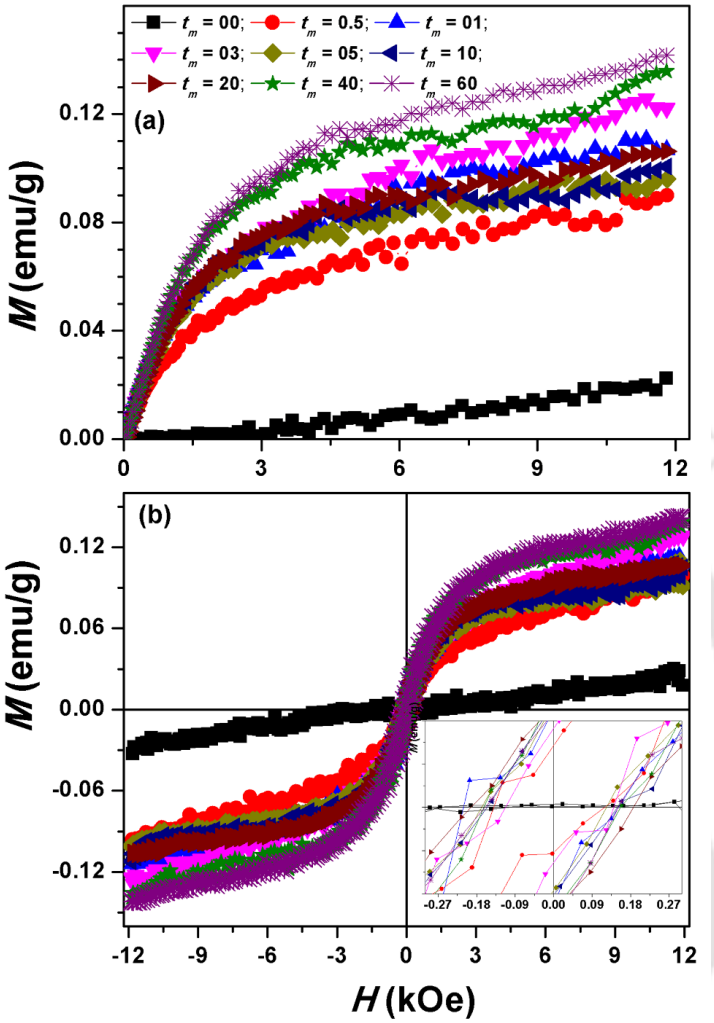

Figure 6.10: Room temperature (a) initial magnetization curves and (b) *M-H* loops of pure un-milled and milled TiO_2 powders at different t_m. Inset shows the expanded view of *M-H* loops close to origin.

On further increasing t_m, the rate of increase in the magnetization at lower field increases gradually up to 60 hrs. To understand the effect of milling on the magnetic parameters of TiO_2 powders, the extracted values of coercivity (H_C) and magnetization at 12 kOe (M_{12kOe}) are plotted as a function of t_m in Figure 6.11. M_{12kOe} increases at a faster rate for t_m up to 3 hrs and then decreases slightly for 5 hrs of milling. On further increasing t_m, M_{12kOe} is observed to increase and tend to saturate at 60 hrs of milling. The maximum value of M_{12kOe} is observed to be 0.15 emu/g for the powders milled at 60 hrs. As compared to NiO and ZnO milled powders,

this is noticeably small value. Nevertheless, M_{12kOe} at room temperature in the presently investigated samples is significantly larger than that reported for Fe doped TiO_2 [WANG20122] and other reported literatures [PATE2011, PATE2013]. On the other hand, H_C of pure un-milled TiO_2, observed as zero due to its PM nature, has increased significantly (~ 142 Oe) after milling for 0.25 hrs. With increasing t_m, H_C exhibits oscillatory behavior up to 3 hrs. On further increasing t_m, H_C increases up to 20 hrs of milling and then decreases slightly for 40 hrs and 60 hrs milling powders. This results in a maximum H_C of 176 Oe for 20 hrs milling powders.

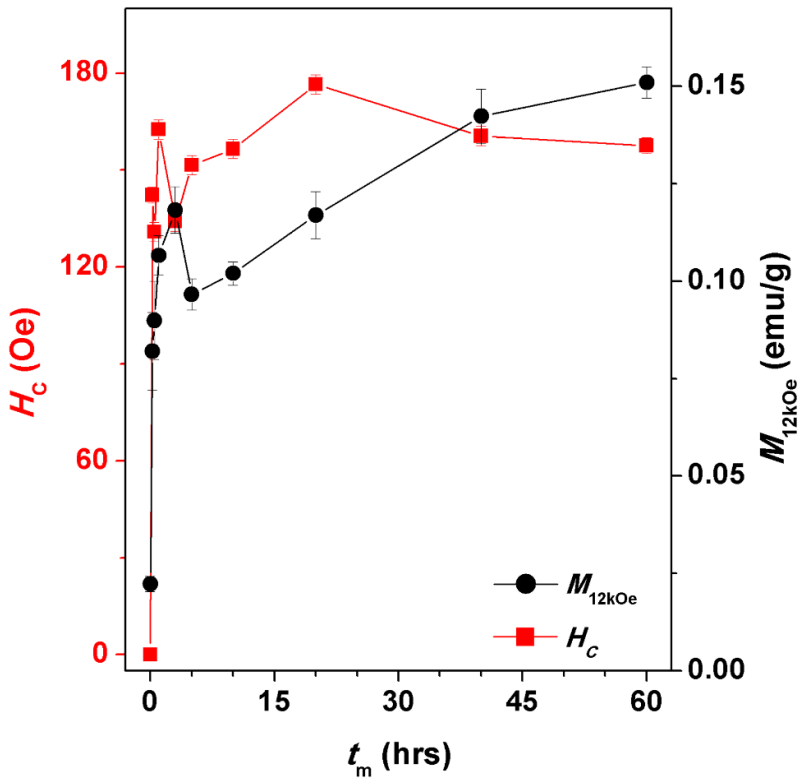

Figure 6.11: The variations of coercivity (H_C) and magnetization at 12 kOe (M_{12kOe}) are plotted as a function of t_m for pure un-milled and milled TiO_2 powders.

To understand the origin of the FM in the milled TiO_2 powders, we correlate the structural, vibrational, electronic and magnetic properties. The pure un-milled TiO_2 exhibits a weak response to the applied magnetic field and the *M-H* loop passes through origin. This is mainly due to PM nature of bulk TiO_2 powder. As the ball milling process induces large number of defects to a starting materials due to repeated cold-welding and fracturing, the milling process results in a considerable size reduction, creation of vacancies and formation of new (rutile) phases in milled TiO_2 powders [HIRA2003, THAK2012]. If the ball milling process

increases the defect density with increasing t_m, then the induced FM due to defects is also expected to increase with defect density. This is clearly evidenced from Raman and XPS spectra results as shown in Figures 6.08 and 6.09. However, the decrease of magnetization for 5 hrs milled TiO_2 powders can be correlated to the formation of rutile phase, as evidenced from XRD patterns and Raman spectra. It has been reported that oxygen vacancy induces lattice distortion in rutile TiO_2 and induces FM in un-doped TiO_2 films due to charge redistribution [KIMD2009]. Therefore, the observed results suggest that the origin of FM in the presently investigated TiO_2 powder is due to finite sized TiO_2 in nanometer range with significant oxygen vacancies created during the milling process. Furthermore, we observed a good correlation between structural, vibrational, electronic and magnetic properties of TiO_2 powders.

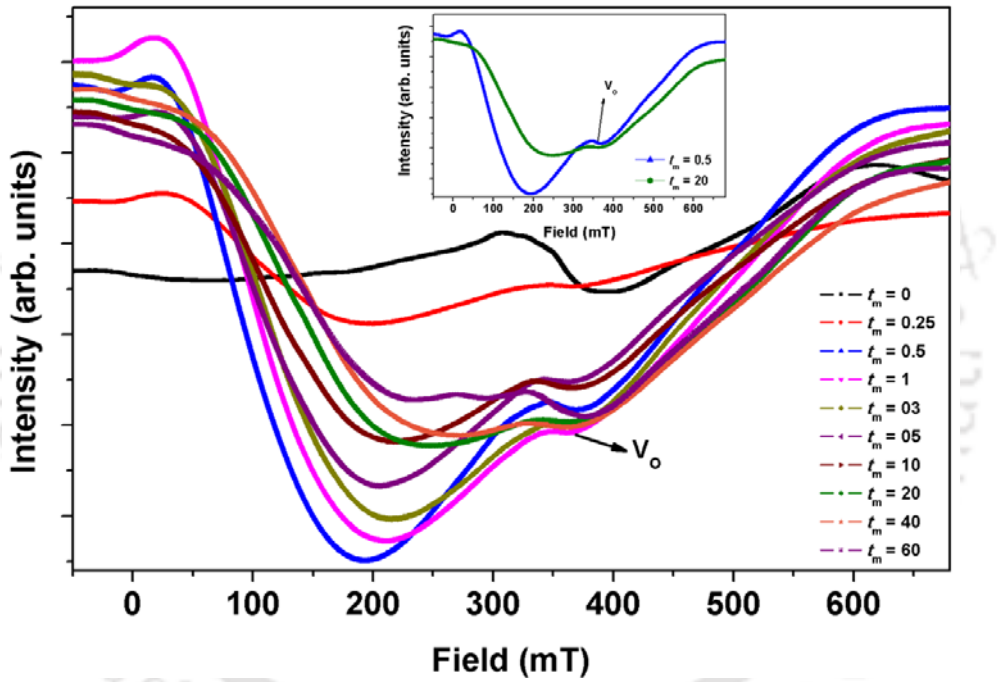

Figure 6.12: Room temperature electron paramagnetic resonance curves for pure and milled TiO_2 powders at different t_m. Inset: EPR spectra for selected powders for comparison.

6.3.5. Resonance properties

EPR spectroscopy is a suitable technique for studying the materials with defects and states with unpaired electrons. As the presently investigated samples exhibit high defects due to ball milling process, room temperature EPR measurement was carried out on pure un-milled and milled TiO_2 powders and the results are depicted in Figure 6.12. Pure un-milled TiO_2 show only a very weak signal due to PM nature. Rhydderch et al correlated such weak signal is due

to the residual Ti^{3+} ions in the titania [RHYD2015]. Gao et al [GAOD2011] have also reported that the weak EPR signal in other oxide system is mainly due to its PM nature.

On the other hand, the milled TiO_2 powders have obviously magnetic resonance signals, which are far away from the 350 mT (center magnetic field of the free electron) [LEES2010] and the relative position of the magnetic resonance signals depends on t_m. This result indicates that the milled TiO_2 powders have obvious FM and hence the observed resonance signal are the FM resonance signals. The observed results are also in good agreement with the magnetization measurements. With increasing t_m to 0.25 hrs, the development of small resonance signal at around 345 mT is observed. On further increasing t_m, the signal at 345 mT becomes more prominent. This can be related to the formation of oxygen vacancy (V_O) due to the transformation of Ti ions from 4+ to 3+ state upon milling [SING2011] caused by the milling process. This is in close agreement with the Raman and XPS results. Such vacancies are also reported in other oxide system [LAGU2005]. Therefore, the observation of EPR signal in milled TiO_2 powders is majorly related to the size reduction along with the formation of defect states, which provides supportable explanation to the observed room temperature magnetic properties [SING2011].

6.3.6. Optical properties

To study the effect of milling, size reduction and defects induced optical properties in milled TiO_2 powders, photoluminescence (PL) spectra were recorded at room temperature and depicted in Figure 6.13. The pure un-milled TiO_2 powder majorly displays two major peaks around 395 nm and 470 nm, which could be attributed to the band-to-band direct transitions (band gap transitions) [SOFI2014, GRAB2017] and charge-transfer transition from Ti^{3+} to oxygen anion in the TiO_6 octahedra [PUGA2013]. On the other hand, milled TiO_2 powders show the following features: (i) the peak at 395 nm shifts very progressively to higher wavelength, (ii) development of additional peaks at around 450 nm and 480 nm with increasing t_m. The shift of bad gap transition peak to higher wavelength indicates a considerable reduction in band gap (E_g) due to milling process. This is in close agreement with the earlier results on similar system using mechanical alloying process [SAVI2012]. On the other hand, the development of additional peaks at 450 and 480 nm can be attributed to surface recombination [YUJC2002] and oxygen vacancies and surface defects of the milled samples, respectively. The development of oxygen vacancies are also clearly supported from XRD, Raman and XPS results. Yin et al [YINW2010] reported that the bandgap of anatase TiO_2 can be tuned efficiently by applying stress along soft direction perpendicular to the layer plane, as it has a

layered structure. This suggests that the band gap modification in the present investigation is due to the combined effect of lattice strain and lattice defects induced by the ball milling. Since, the achieved band gap of 3.133 eV in the milled TiO_2 falls in the border of UV-visible region, they would be suitable for UV-visible light emitter and photocatalysis.

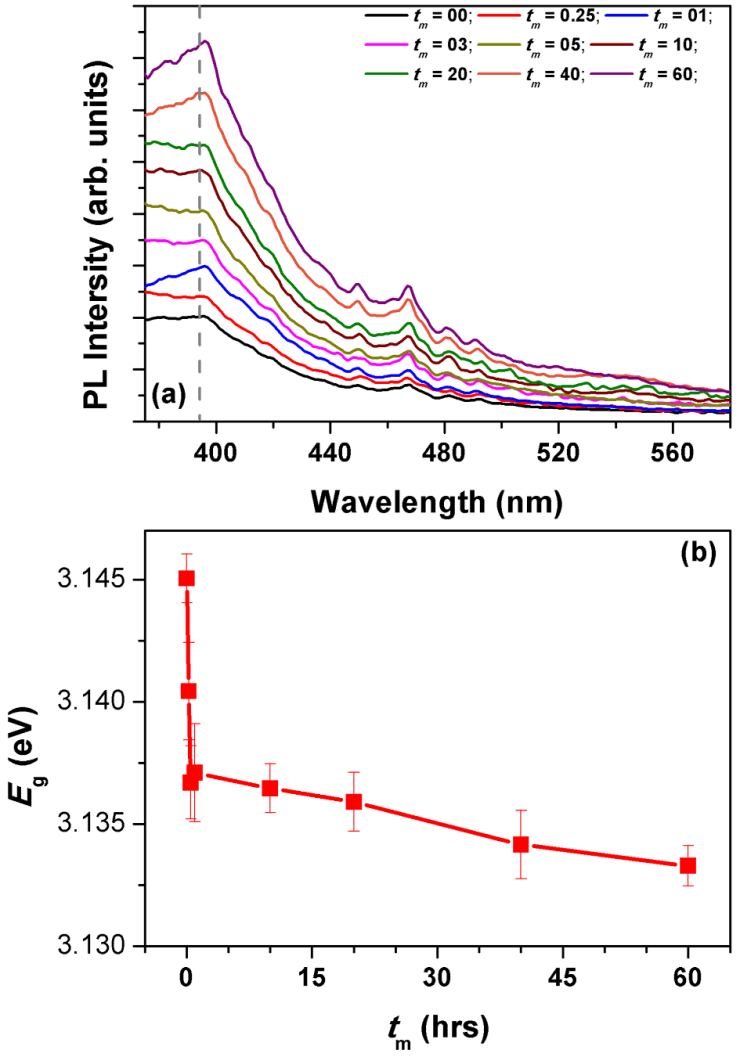

Figure 6.13: (a) Room temperature photoluminescence spectra and (b) the variation of bandgap (E_g) for pure un-milled and milled TiO_2 powders at different t_m.

6.3.7. Infrared spectroscopy

Fourier transform infrared spectroscopy (FTIR) spectroscopy has been employed to investigate the effect of oxygen vacancies in the vibration bands of the pure and milled TiO_2 powders. All spectra were obtained in the range of 400 – 4000 cm^{-1}. Figure 6.14 displays the FTIR spectra for pure un-milled and milled TiO_2 powders. A broad band at 3445/cm in the TiO_2 powders is assignable to OH stretching of structural hydroxyl groups and water presents in the powders.

Similarly, a sharp band observed at 1630/cm is due to asymmetric stretch of water (deformation mode).

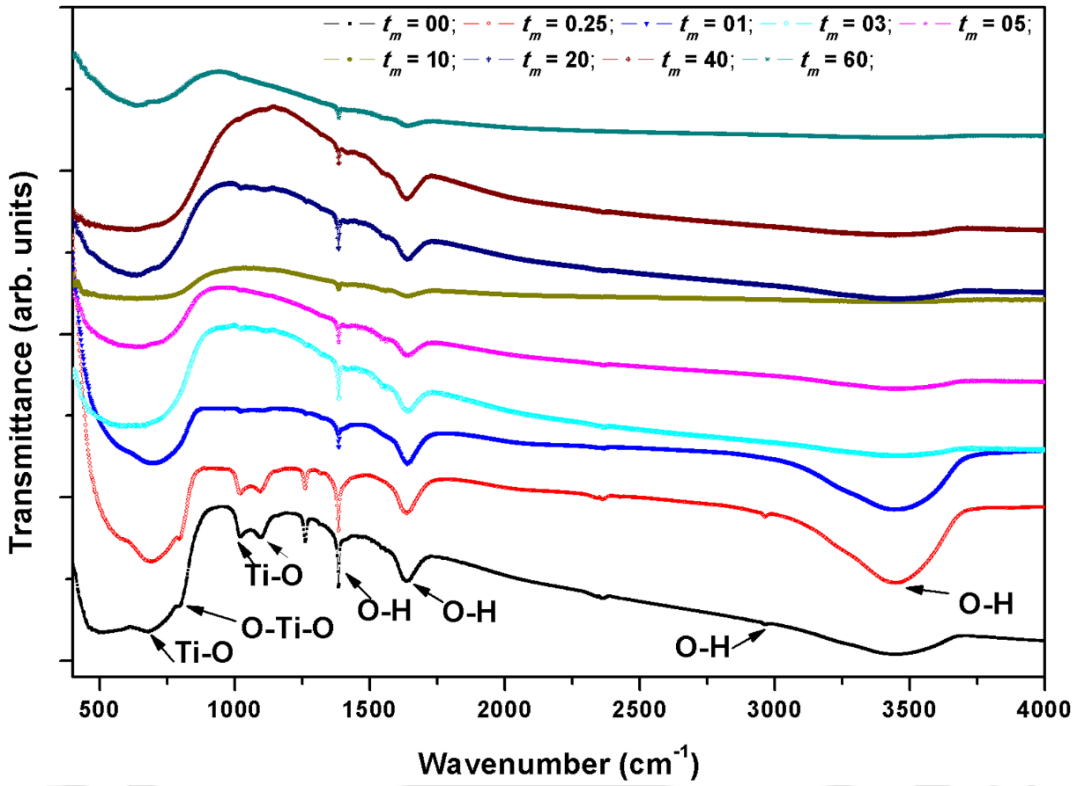

Figure 6.14: Room temperature FTIR spectra for pure un-milled and milled TiO_2 powders at different t_m.

The bands observed at 1380/cm and 2965/cm may also due to OH stretch of water [COST1999, WANG20123]. The vibration modes observed at 687, 1020, and 1100 cm^{-1} are assignable to anatase TiO_2. A close observation of vibration bands shows (i) an obvious blue-shift of vibration bands at 687 cm^{-1} to 680 cm^{-1} after milling, which could be attributed to the higher concentration of oxygen vacancies induced. (ii) Disappearance of vibration bands at 1020 and 1100/cm with increasing t_m. Such behaviors are also reported in Co doped TiO_2 system and correlated due to the oxygen vacancy [DASK2009]. The other vibration bands observed at 687 and 1015 cm^{-1} are due to the O-Ti-O bending and band at 1094 cm^{-1} is due to Ti-O stretching vibrations [OTHM2012].

6.4. Summary

The evolution of structural, vibrational, electronic, magnetic, resonance and optical properties of pure and milled TiO_2 powders prepared by ball mill process in a planetary ball mill under

dry mill conditions and at argon atmosphere has been systematically carried out as a function of different t_m. The salient features of the TiO_2 powders from the current investigations are as follows:

- The ball milling produces nanocrystalline TiO_2 powders with the average crystallite size of nanometer range (around 19 nm). While the majority of the phase is anatase in nature, with increasing t_m, the development of oxygen deficient TiO_2 and rutile phase of TiO_2 is observed. The lattice volume increases for the initial period of milling and then remain constant above 10 hrs of milling. Microstructural studies reveal that the agglomeration of fine particles increases with increasing t_m and the nanocrystalline powders exhibit irregular shapes with broad size distribution.
- Raman spectra show Raman modes for anatase phase, but the peak width gets broadened, peak position shifts to lower wavenumber and reduction in peak intensity. For $t_m > 1$ hrs, additional peaks corresponding to the oxygen deficient TiO_2 and rutile phase of TiO_2 are observed. These observations show close correlation with the XRD results.
- XPS spectra confirm the formation of oxygen deficient TiO_2 and/or Ti^{3+} in the milled TiO_2 powders, caused by the defects and size reduction. The observed results are in good agreement with the results of XRD patterns and Raman spectra.
- Magnetic properties reveal that the paramagnetic nature of the pure un-milled TiO_2 powder transforms into FM progressively upon milling due to defects and size reduction. A maximum magnetization of 0.15 emu/g at 12 kOe applied field and a coercivity of about 155 Oe are obtained at room temperature for 60 hrs milled TiO_2 powder.
- Resonance study displays that pure un-milled TiO_2 powders exhibit only weak signal due to paramagnetic nature, while the milled TiO_2 powders show magnetic resonance signals due to ferromagnetic nature. The EPR signal in milled TiO_2 powders is majorly related to the size reduction along with the formation of defect states, which provides supportable explanation to the observed room temperature magnetic properties.
- Optical studies reveal two major peaks around 395 nm and 470 nm due to band-to-band direct transitions in pure TiO_2 powders. Upon milling, additional peaks are observed due to surface recombination, oxygen vacancies and surface defects. The lattice strain and lattice defects reduce the bandgap slightly.

- The results of infrared spectroscopy study support the formation of oxygen vacancies in milled TiO_2 powders and in close agreement with the results obtained from XRD patterns, Raman and XPS spectra.

Chapter 7

Properties of NiO nanoparticles prepared by sol-gel technique

7.1. Introduction

Nanostructure materials such as nanoparticles, nanoflakes, nanorods, nanowires and nanotubes display novel properties, which are considerably different from those observed in bulk materials. In particular, the study of magnetism and magnetic interaction in various types of fine magnetic nanosized particles has generated increasing interest due to their unique magnetic properties such as enhanced magnetization, exchange coupling and magnetization reversal by quantum tunneling, and their potential technological applications in electrical, optical and magnetic properties [JOHN2010, HOSO2012, PARR2013]. The detailed investigation on various types of metal-oxides in the earlier chapters revealed that the development of induced ferromagnetism (FM) in oxide based materials is quite possible by size reduction and defects persuaded during the ball milling process. However, the magnitude of induced FM strongly depends on the materials. For example, NiO powders milled up to 30 hrs exhibit the maximum magnetization of 1.08 emu/g without changing its crystal structure from face centered cubic, while the ZnO powder shows the maximum magnetization of about 0.92 emu/g after 40 hrs of milling. On the other hand, the milling of TiO_2 not only reveals size reduction including defects with increasing milling time, but also exhibits oxygen deficient TiO_2 and rutile phase and hence the induced magnetization in the nanoscale TiO_2 was not observed to be the values close to ZnO and NiO. Since NiO powders at nanoscale exhibit moderate magnetization without changing its crystal structure from face centered cubic, the development of NiO based nanoparticles using different preparation method is also attempted to obtain FM above room temperature such that these oxides with cubic structure could facilitate integration to spintronics devices [FIOR2005]. Furthermore, the nanostructured NiO is especially attractive for catalysis [GONG2014], energy conversion, storage device [ARIC2005], battery cathodes, gas sensors [SOLE2013] and electrochromic films [BODU2014].

As the synthesis of nanomaterials is controlled by various processing parameters such as concentration of reactant, calcinations time, calcination temperature and pH value, it is worth analyzing the physical properties of NiO nanoparticles prepared with different molar concentrations and different particle size after exposing to different annealing temperatures (T_A). Hence, in this chapter, we have synthesized NiO nanoparticles using a sol-gel method with different molar concentrations (0.1 M, 0.2 M, 0.3 M and 0.5 M). The as-prepared nanoparticles exhibiting nickel hydroxide structure were annealed at different temperatures (T_A = 350 °C and 500 °C) to form pure NiO with variable sizes. Subsequently, the structural,

vibrational, optical, magnetic and resonance properties of annealed NiO nanoparticles were investigated as a function of molar concentration and annealing temperatures.

7.2. Experimental details

Nickel acetate tetrahydrate ($(CH_3COO)_2Ni.4H_2O$)) received from Merck was dissolved first in doubly distilled deionized water with different molar concentrations of 0.1, 0.2, 0.3 and 0.5 under constant stirring for 2 hrs at moderate temperatures of 40 to 50 °C to obtain a light greenish sol. Subsequently, 2 to 3 ml of ethylene glycol (from Merck) was added slowly to the warm sol to obtain a greenish thick gel. A clear gel of 0.1 M, 0.2 M, 0.3 M and 0.5 M solution was achieved. The gel product was eventually dried at 120 °C for 12 hrs. These as-made particles exhibit nickel hydroxide structure. In order to improve crystallinity and to remove the hydroxide phases, the dried powders were subjected to air annealing at different temperatures (350 ^oC and 500 ^oC) for 3 hrs [RAUT2011]. This annealing process produces fine black powders of NiO. NiO powders of different molar concentrations of 0.1, 0.2, 0.3 and 0.5 annealed at 350 ^oC were designated as S1, S2, S3 and S4, while the powders annealed at 500 ^oC were represented as S5, S6, S7 and S8, respectively.

Crystal structure and phase purity of NiO nanoparticles was analyzed using X-ray diffraction (XRD) obtained using high-power X-Ray diffractometer (XRD, Rigaku TTRAX III 18 kW) with Cu-K_α radiation (λ = 1.54036 Å). In order to analyze the structural parameters carefully by using Williamson-Hall plot (WHP) method [WILL1953], the XRD data were collected at a slow scan rate of 0.005 °/s. The microstructural properties were analyzed using transmission electron microscopy (TEM, JEOL 2100) technique. Raman spectra at room temperature were obtained using micro-Raman spectroscopy (LabRam HR800, Jobin Yvon) with excitation wavelength of 614 nm. Composition of the annealed powders was analysed using energy dispersive spectroscopy (EDS, Oxford) attached to scanning electron microscope (SEM, Leo 1430vp). The steady state Photoluminescence (PL) spectrum was recorded at room temperature by using a 312 nm Xenon lamp excitation (AB2, Thermo spectronic). Magnetic properties at different temperatures (20 – 900 K) were characterized using vibrating sample magnetometer (VSM, LakeShore Model 7410) by performing (i) magnetic hysteresis (*M-H*) loops at different temperatures, (ii) low temperature thermomagnetization (*M-T*) measurements under zero-field-cooled (ZFC) and field-cooled (FC) conditions in the temperature range of 20 K to 300 K at different applied fields, and (iii) high temperatures *M-T* measurements from 300 K to 900 K performed at 5 ^oC/min heating rate with applied field of 2 kOe. Room temperature

electron paramagnetic resonance (EPR) measurements were carried out on a JEOL Spectrometer (JES-FA200) operating at X-band frequency (ν =9.4 GHz) with 100 kHz magnetic field modulation in powder form.

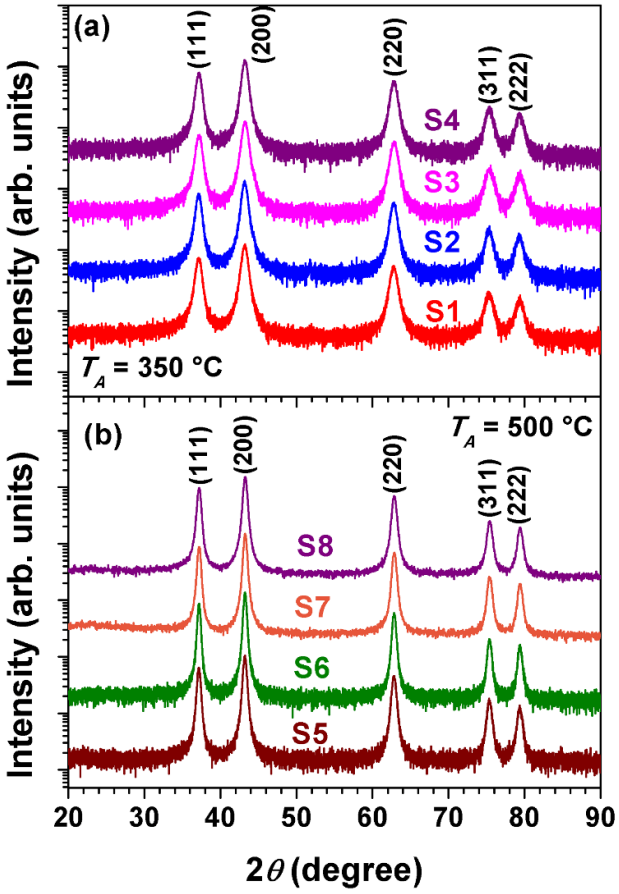

Figure 7.01: (a) Room temperature XRD patterns of S1-S4 samples annealed at 350 °C and (b) for S5-S8 samples annealed at 500 °C.

7.3. Results and discussion

7.3.1. Structural properties

Figure 7.01 shows room temperature XRD patterns of NiO nanoparticles with different molar concentrations annealed at different T_A. It is clearly observed that all the annealed powders exhibit nickel oxide phase and the Bragg reflections observed in XRD patterns are indexed to face centre cubic (*fcc*) structure. The absence of any impurity peaks in the annealed powders confirms the formation of high purity nickel oxide, which is further confirmed through the EDS analysis carried out on all samples annealed at different T_A. All the samples show the presence of Ni and O only without the observation of any other impurities within the detection limit of EDS system. A close observation of the Bragg reflections confirms that the peaks are relatively

broadened for samples annealed at 350 °C, but the broadening decreases along with considerable shift of the peak position to higher diffraction angles with increasing T_A. Figure 7.02 demonstrates the reduction of peak broadening and peak shift to higher angles for the samples annealed at different T_A. This can be attributed to the increase in average crystallite size and decrease in lattice constant with increasing T_A.

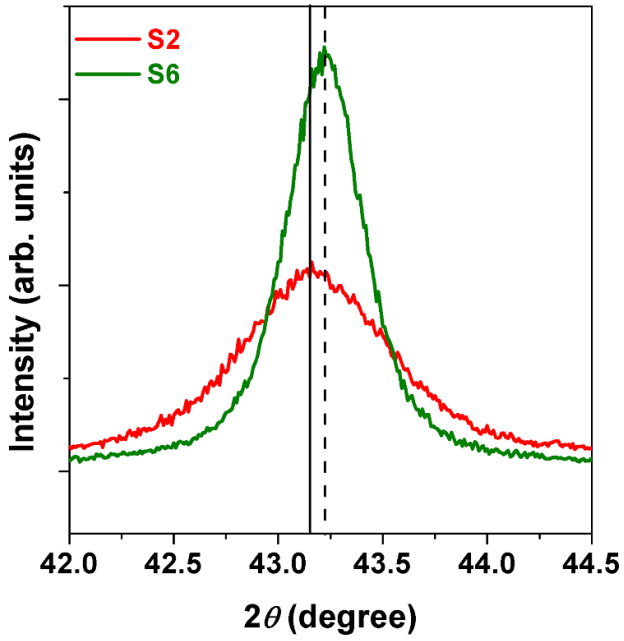

Figure 7.02: The representation of peak shift of (200) Bragg reflection with annealing temperature.

In order to quantify various structural parameters, the XRD data were analyzed using WHP method as expressed in eqn.(7.01),

$$\beta_{total}\, cos\theta = \frac{k\lambda}{D_{XRD}} + 4\eta\, sin\theta \qquad (7.01)$$

where β_{total} is full-width at half-maximum of the XRD peak (in radians), k is the Scherrer's constant taken as 0.9 for spherical nanoparticles, λ is the incident X-ray wavelength (=1.54056 Å), θ is diffraction angle, D_{XRD} is average crystallite size and η is microstrain parameter. According to eqn.(7.01), the plot between $\beta_{total} cos\theta$ and $4 sin\theta$ falls into a straight line and hence the values of D_{XRD} and η can be determined from the intercept and slope of the fit, respectively. In order to verify the applicability of WHP plot to XRD data, the plots of $\beta_{total} cos\theta$ and $4 sin\theta$ are displayed for all samples (S1-S8) in Figure 7.03. Considering the validity of data to merely

fall into straight lines nature, XRD data were fitted to eqn.(7.01) and determined the values of D_{XRD} and η from the intercept and slope of the fit, respectively.

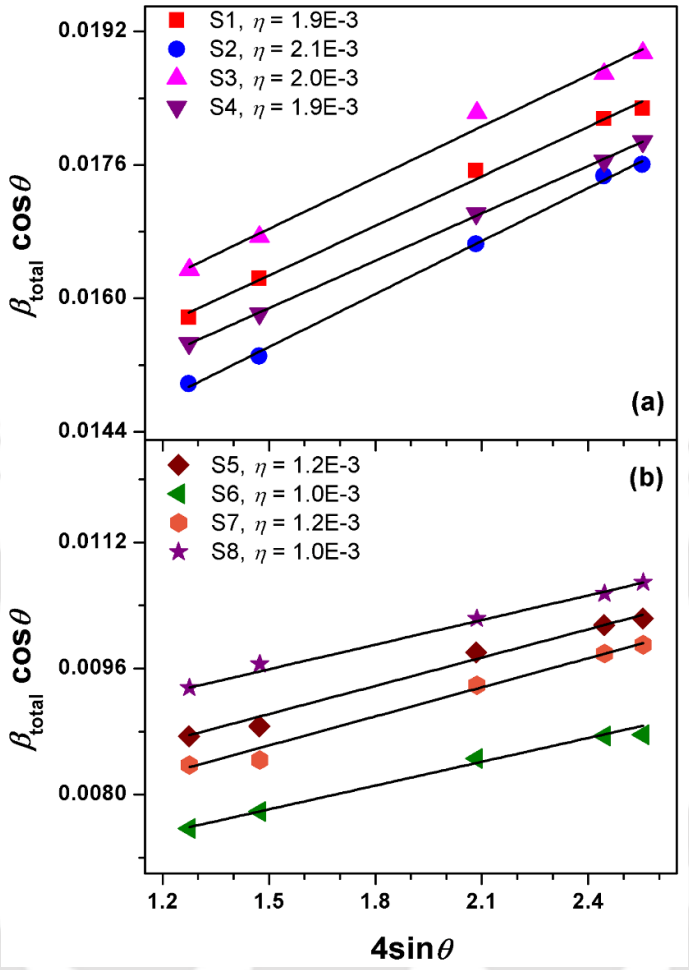

Figure 7.03: The plots of $\beta_{total}\cos\theta$ versus $4\sin\theta$ for NiO powders annealed at 350 °C (a) and 500 °C (b). The straight lines passing through the data points are the best fit obtained using eqn.(7.01).

Figure 7.04 depicts the variation of D_{XRD} and lattice constant, a_{XRD} as a function of molar concentration for annealed NiO powders. It is observed that the values of D_{XRD} increase from about 9 nm to about 17 nm with increasing T_A from 350 °C to 500 °C, respectively. However, the variation of D_{XRD} exhibits a weak dependent on molar concentrations. On the other hand, a_{XRD} is found to increase with decreasing size of the NiO crystals, i.e., the values of a_{XRD} are found to be larger for the NiO annealed at 350 °C than the NiO annealed at 500 °C. This confirms a considerable lattice expansion in NiO nanoparticles with decreasing the crystal size. Such lattice expansion in NiO nanoparticles is in good agreement with the earlier reports on

similar system [LIL2006]. With increasing molar concentration, (i) a_{XRD} for NiO annealed at 350 °C is observed to be nearly same up to 0.2 M and then decreases significantly up to 0.5 M and (ii) for NiO annealed at 500 °C, a_{XRD} decreases almost linearly up to 0.3 M and then remains constant up to 0.5 M. Nevertheless, the magnitude of the microstrain determined from the fitting procedure is found to be on the order of 10^{-3}, which is typically negligible as compared to the strain observed in ball milled NiO powders (Chapter 04). This is in close agreement with earlier reports on similar NiO nanoparticles [PROE2011]. Therefore, the presence of such small strain is not expected to play any major role on the physical properties of these nanomaterials.

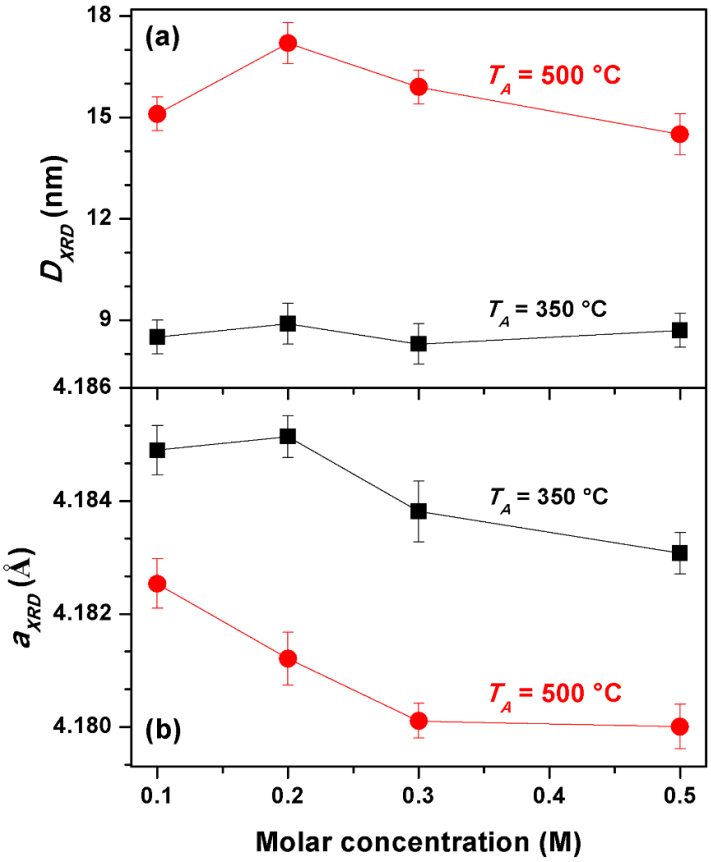

Figure 7.04: The variation of (a) average crystallite size (D_{XRD}) and (b) lattice constant (a) as a function of molar concentration for the samples annealed at different T_A.

To confirm the fine particle morphology in nanoscale, the microstructure of annealed NiO powders were characterized using TEM. Figure 7.05 displays typical bright-field TEM (BFTEM) images and selected area diffraction patterns (SAED) patterns for S3 and S7 samples. To obtain the average particle size and the variance, BFTEM images were fed into

imaging software Scion Image and manipulated by interplaying threshold intensity in the software to recognize each particle and to obtain the area data. These data were then converted into particle diameter data to achieve the average particle size and size distribution.

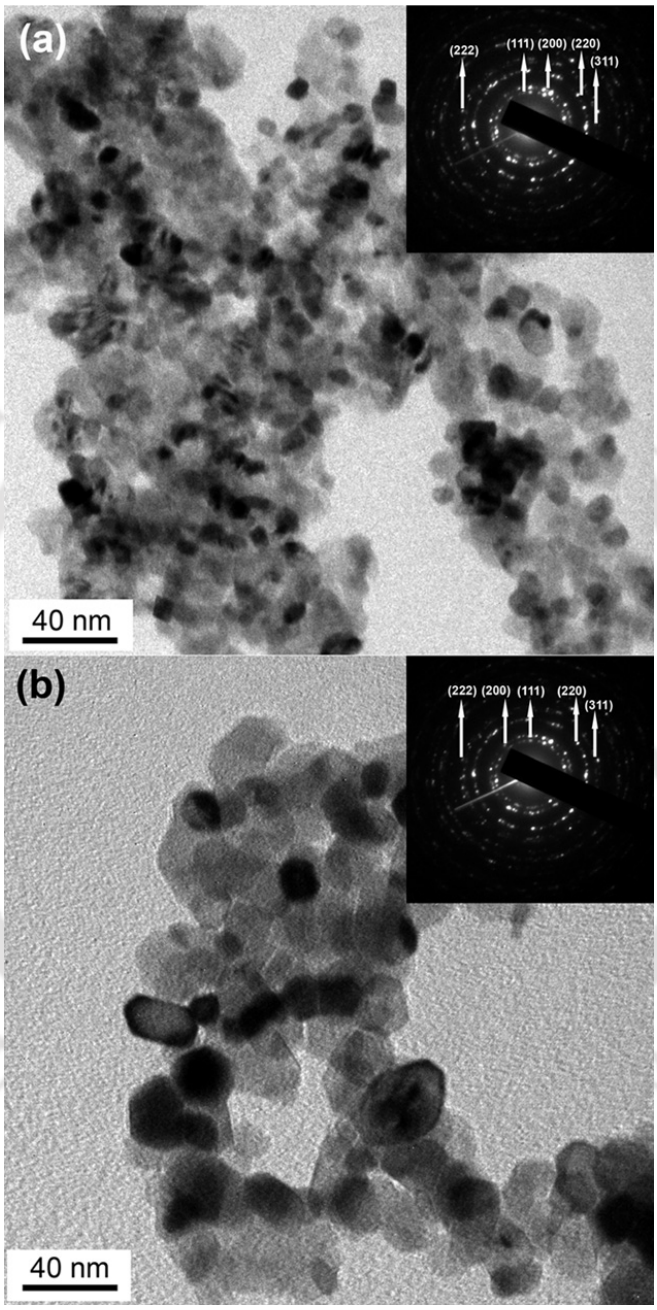

Figure 7.05: Bright-field TEM micrographs and selected area diffraction (SAED) patterns for (a) S3 sample annealed at 350 °C and (b) S7 sample annealed at 500 °C.

It is interesting to note that the sample S3 annealed at 350 °C depicts nearly spherical nature of particles with the average size of about 9 nm, while the sample S7 annealed at 500

°C deviates from spherical nature, i.e., the shape of most of the particles exhibits non-spherical in nature. The average size of the particles calculated with the assumption of near spherical nature is found to be about 18 nm. In addition, the SAED patterns display diffraction rings corresponding to the *fcc* structure and confirming the presence of polycrystalline nature in NiO particles. The lattice constant determined from SAED pattern for S3 and S7 samples is obtained to be 4.184 Å and 4.1798 Å, respectively. These results are in good agreement with the results obtained from XRD data.

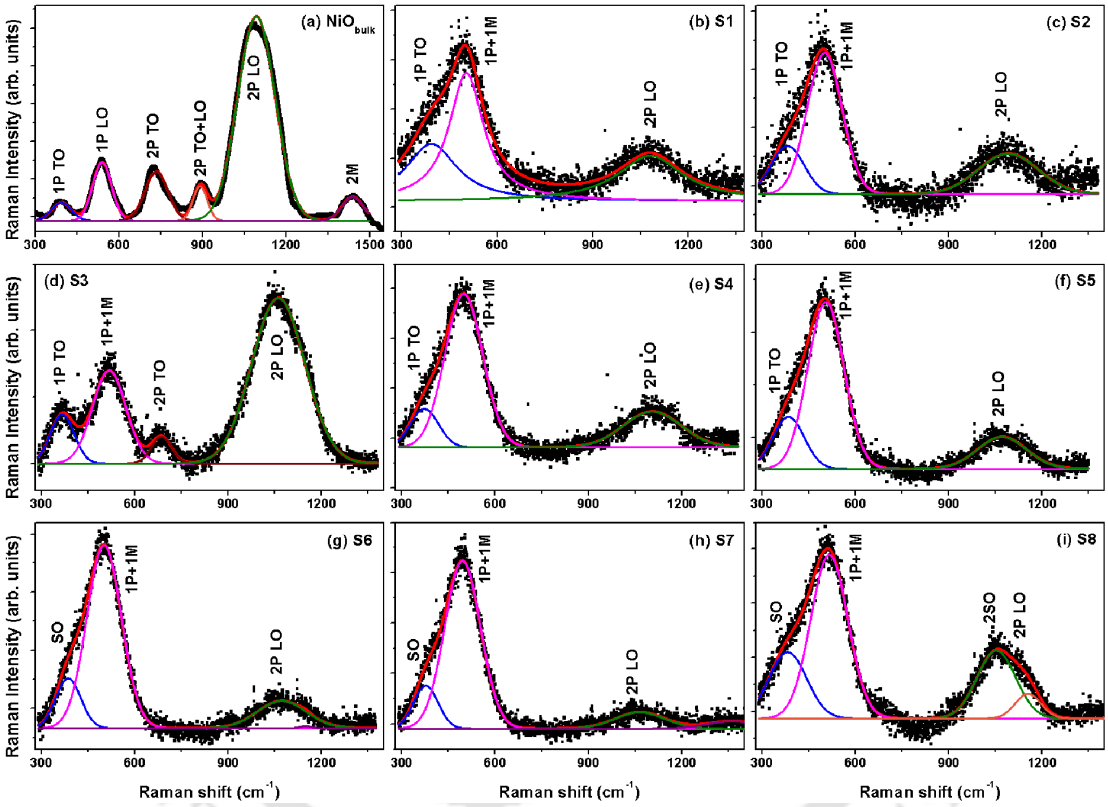

Figure 7.06: (a) Room temperature Raman spectra of commercially available NiO powder, NiO nanoparticles annealed at 350 °C (S1-S4) and NiO nanoparticles annealed at 500 °C (S5-S8).

7.3.2. Vibrational properties

Figure 7.06 shows room temperature Raman spectra of NiO nanoparticles with different molar concentrations annealed at 350 °C (a) and 500 °C (b) and NiO powders available commercially (Sigma Aldrich). The Raman spectra have been analyzed by curve fitting method with different band combinations to obtain peak intensities, peak widths and peak positions. A typical curve fitting is also shown in the figure to identify different band combinations. The commercially available NiO powder exhibits peaks at 540–560 cm^{-1}, 690 cm^{-1}, 900 cm^{-1}, 1040–1100 cm^{-1} and 1400–1500 cm^{-1} corresponding to one-phonon (1P) LO, two-phonon (2P) TO, 2P TO+LO

and 2P LO of vibrational origin and two-magnon (2M) band associated with Ni^{2+}-O^{2-}-Ni^{2+} super-exchange interaction, respectively [ULMA2007]. The presence of 2M band in bulk NiO powder supports the existence of antiferromagnetic state in commercial NiO at room temperature. Similarly, NiO particles annealed at 350 °C exhibit vibration modes at 350-400 cm^{-1}, 690 cm^{-1} and 1040-1100 cm^{-1} corresponding to 1P TO, 2P TO and 2P LO excitation of NiO, respectively. Interestingly, we have also observed a new Raman band around 500 cm^{-1} in the presently investigated nanoparticles. This could be attributed to 1P (~ 440 cm^{-1}) plus one-magnon (1M) (~ 40 cm^{-1}) excitation induced by strong phonon-magnon interaction at nanoparticle surfaces or some defects [ULMA2011, TADI2014]. Ulmane et al [ULMAARTI] showed that the sharp band of 1P+1M excitation exhibits (i) temperature dependence upon heating by laser and (ii) size dependence upon different annealing temperatures. The origin was attributed to the strong phonon-magnon interaction at nanoparticles surface or some defects, which compete with the magnetic ordering of the nanoparticles. Similarly, NiO powders annealed at 500 °C exhibit bands at 500 cm^{-1} and 1040-1100 cm^{-1} corresponding to 1P+1M and 2P LO modes. However, a close observation of spectra along with the curve fitting technique confirms that these samples (S5-S8) exhibit multiple peaks merged over each other and the probability of multiple peaks increases with increasing molar concentration above 0.1. This reveals the existence of possibly another type of excitation due to SO mode [PIGE1980, LEWI2001, DUAN2012]. The relative intensities of first and second order SO modes with respect to those of 1P+1M and 2LO modes increase with increasing molar concentration. It may be noted that the SO mode in Raman spectra appears when the particles size is about one size range smaller than the exciting laser wavelength, but forbidden in total spherical crystallites as SO modes do not couple to radial charge distribution [PIGE1980, LEWI2001]. Therefore, the appearance of SO modes in 500 °C annealed NiO nanoparticles suggests that NiO nanoparticles are imperfect from spherical nature and accounts for non-radial carrier distribution in the crystallite [PIGE1980]. This is in good agreement with the observation of non-spherical NiO nanoparticles from the microstructural analysis using TEM as shown in Figure 7.05(b). Nevertheless, the presence of 2M band was not observed in the presently investigated samples. Ulmane et al [ULMA2011] reported a dramatic reduction in 2M and TO+LO modes with decreasing NiO particle size and vanishes completely for crystallites below 100 nm. Such observation has been attributed to the decrease of antiferromagnetic spin correlations. Furthermore, the pronounced observation of 1P band with reducing the size of the crystallites has been attributed to the presence of defects and surface effects. The analysis of

1P+1M mode in Figure 7.06 reveals that vibration frequency of 1P+1M band increases significantly with increasing molar concentration from 0.1 M to 0.3 M (S1-S3) and decreases largely for 0.5 M (S4) sample annealed at 350 °C.

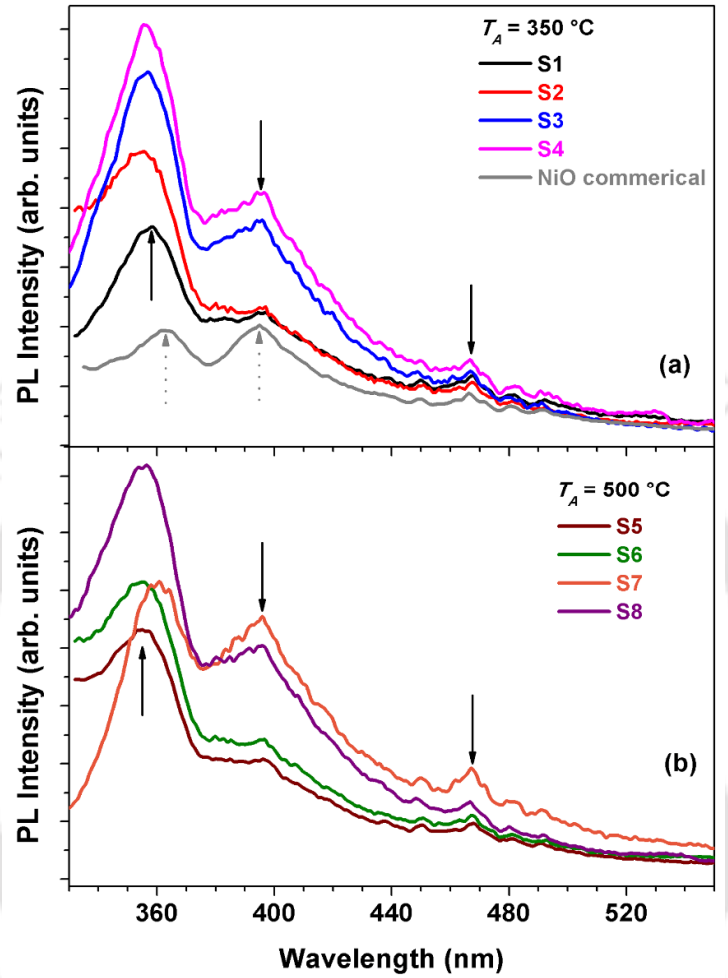

Figure 7.07: Room temperature PL emission spectra of NiO powder available commercially from Sigma Aldrich and NiO nanoparticles annealed at (a) 350 °C (S1-S4) and (b) 500 °C (S5-S8).

Although the existence of 1P+1M band in NiO was not reported in many literature, its appearance in the presently investigated samples can be attributed to the magnetic origin resulting from defects and surface effects, and scattering from the extended region other than the Brillouin zone centre due to the damage of transmission symmetry in nanostructures. The red-shift of 1P+1M Raman vibration is observed for the first time. The red-shift of Raman vibration with the particle size has been reported in many literatures and ascribed to the size-induced phonon confinement effect and surface relaxation. Defects and surface effects can also

induce red-shift of phonon vibrations [YANG2008]. On the other hand, Duan et al [DUAN2012] reported a blue-shift and intensity enhancement of 2LO mode after the nanoparticles are exposed to high power laser and interpreted that the defects observed in as-grown particles are annihilated by the laser beam heating. Therefore, the red-shift of 1P+1M mode Raman band can be ascribed to the enhancement of magnetic origin and surface relaxation effects.

7.3.3. Optical properties

It is well known that the size effect in nanoscale regime affects the optical property of fine nanoparticles. PL studies are very important to investigate the structural defects such as oxygen vacancies and quantum size effect. Figure 7.07 depicts the room temperature PL spectra of NiO nanoparticles with different molar concentrations annealed at different T_A. PL spectrum of pure NiO powder available commercially (sigma Aldrich) is also shown for comparison. Three emission peaks were observed around 355 nm, 395 nm and 467 nm corresponding to bandgap (E_g) of 3.51 eV, 3.16 eV and 2.67 eV, respectively. The first peak observed at 355 nm reveals a strong UV emission corresponding to a near band-edge emission due to direct recombination of excitons through an exciton-exciton scattering. This can be attributed to the intrinsic transition of excitons from conduction band to valance band, i.e., electronic transition of Ni^{2+} ions. This confirms that these NiO nanoparticles are also very good room temperature UV-blue emitters. Such strong UV emission was attributed to pure *fcc* NiO and hence the luminescence peak comes from the electronic transition of the cationic state, which can be exploited as a good emitter around 350 nm [ANAN2011].

Adler et al [ADLE1970] reported a series of absorption peaks below 4 *eV* correlating to pure intraionic $3d^8$-$3d^8$ transitions of Ni^{2+}. This was further supported from the studies of electron energy loss spectroscopy and spin polarized electron energy loss spectroscopy in NiO [GORS1994]. While Anandan et al [ANAN2011] and Gondal et al [GOND2012] reported the strong UV strong emission around 340 nm (3.62 eV) in NiO nanoparticles, Salavati-Nisasari et al [NIAS2012] and Qi et al [QIY2009] did not observe any such strong emission, but observed two other emission peaks at 390 nm and 467 nm. It was reported in bulk NiO that radiative recombination of carriers consists of two photoemission maxima: one at 390 nm (~ 3.2 eV) and another at 450 nm (~ 2.8 eV), which can be assigned to $^1T_{1g}(G) \rightarrow {}^3A_{2g}$ and $^1T_{2g}(D) \rightarrow {}^2A_{2g}$ transitions, respectively [DIAZ1997]. As the presently investigated nanoparticles are of typical transition metal elements, the optical property and carrier related phenomenon are governed by *d-d* transitions present within the band gap. Since the Ni^{2+} ions has the

configuration of $3s^2 3p^6 3d^8$, this transition metal ion has six O^{2-} surrounding ions to form an elementary octahedron with octahedral symmetry. Thus, the oxygen ions crystal field splits *d*-electron states into e_g and t_{3g} states [VOLK2001]. A comparison between the NiO bulk and nanoparticles reveals that PL of strong UV radiation around 350 nm exhibit blue-shift due to the size reduction. This is in good agreement with the earlier reports on similar system [KISA2013], but contradicts to the results reported by Qi et al [QIY2009] showing the red-shift in nanostructures due to wide particle size distributions and native defects in NiO nanostructures.

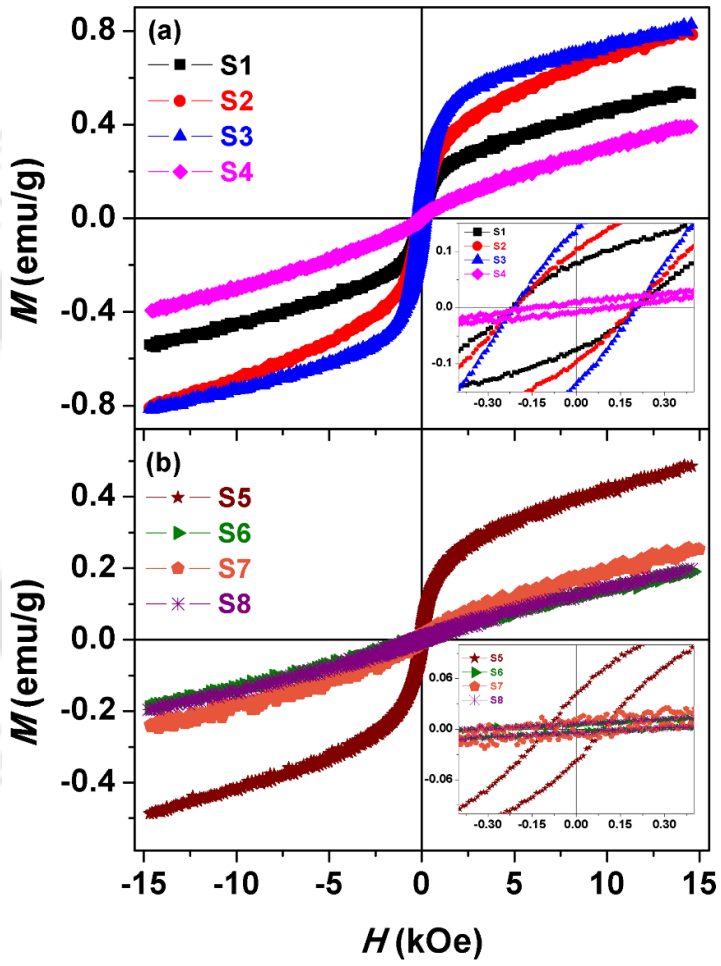

Figure 7.08: Room temperature *M-H* loops of (a) NiO particles annealed at 350 °C (S1-S4), (b) 500 °C (S5-S8). Insets show the expanded version of the *M-H* loops close to origin.

7.3.4. Magnetic properties

To understand effects of molar concentration and T_A on the magnetic properties of NiO particles, room temperature *M-H* loops and temperature dependent *M-H* loops and *M-T*

measurements magnetic properties under ZFC and FC conditions over a wide range of temperatures 20 K – 900 K were carried out. Figure 7.08 displays room temperature *M-H* loops for NiO particles annealed at different T_A. Insets depict the expanded of *M-H* loops close to origin. All the samples exhibit hysteresis behavior at room temperature.

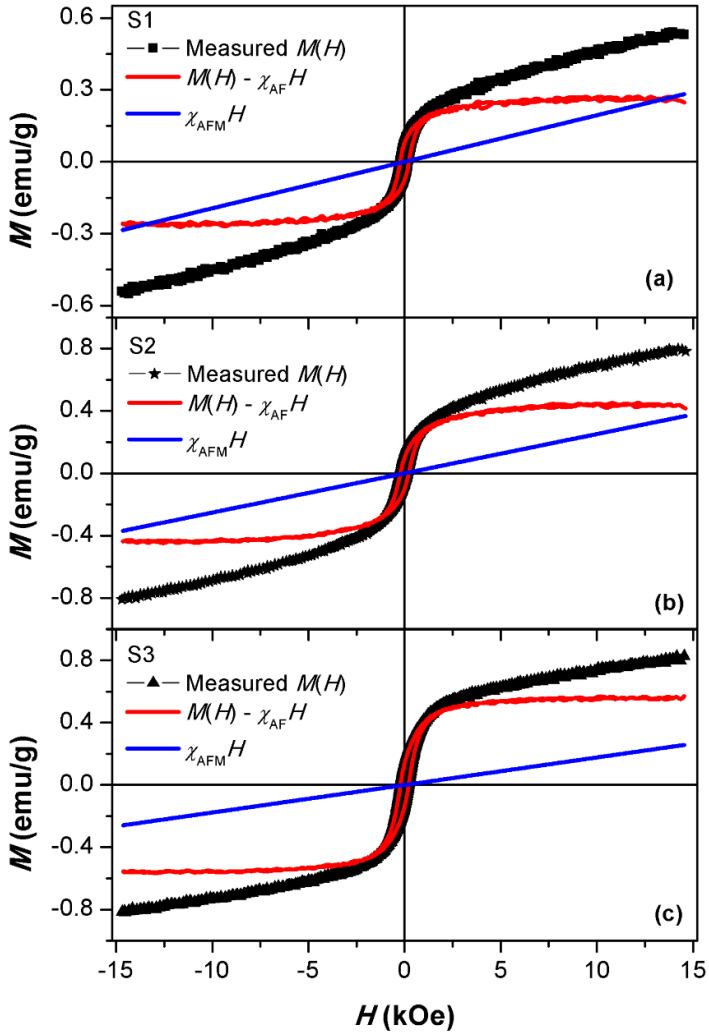

Figure 7.09: Room temperature *M-H* loops of S1, S2 and S3 samples before and after subtracting the antiferromagnetic and ferromagnetic components.

During the initial magnetization process, the magnetization increases significantly with increasing applied field in lower-field region. However the increase of magnetization slows down as we further increase the applied magnetic field. Finally the magnetization increases almost linearly with increasing the magnetic field up to 14 kOe and does not saturate. These results indicate that there are two possible components associated with the magnetization reversal process: (i) an easily magnetizing component at low-field region and (ii) a non-

saturating component responsible for almost linear variation in the high-field region. In order to separate these two components, the field dependent magnetization curves are fitted by by the eqn.(7.02),

$$M(H) = M_{FM} + \chi_{AFM} H \qquad (7.02)$$

where χ_{AFM} is antiferromagnetic susceptibility of the core and M_{FM} is ascribed to the magnetization due to uncompensated surface spins. χ_{AFM} was determined by fitting the linear portion of *M-H* curves at high-fields.

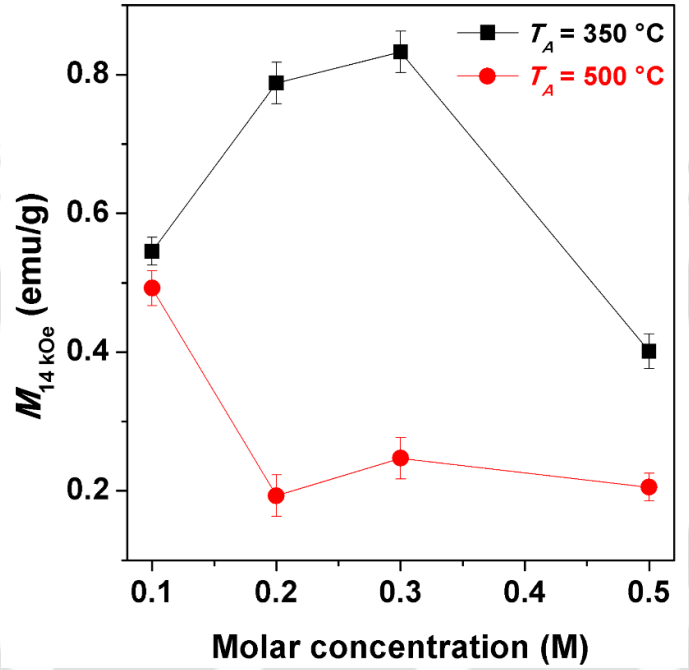

Figure 7.10: The variation of magnetization obtained at 14 kOe applied field (M_{14kOe}) as a function of molar concentration for NiO particles annealed at 350 °C and 500 °C.

Figure 7.09 depicts measured loops, loops after subtracting AFM component ($\chi_{AFM}H$) and variations of $\chi_{AFM}H$. It is clearly evident that the applied field required for saturating M_{FM} component in NiO particles annealed at 350 °C reduces with increasing molar concentration up to 0.3 M. Saturation fields of about 10 – 20 kOe have been reported by various investigators in similar systems [MAKH2002, PUNN2002]. In addition, χ_{AFM} decreases and M_{FM} increases with increasing molar concentration up to 0.3 for the samples annealed at 350 °C. This confirms that the number of uncompensated spins on the surface of NiO particles is increased and hence resulting in the enhancement of FM properties. This is also supported by Raman scattering results with the increase in 1P+1M mode. Such observations are in good agreement with the

variation of M and H reported earlier on NiO nanoparticles [TIWA2005, MENE2010, TADI2011]. The extracted values of magnetization obtained at 14 kOe applied field (M_{14kOe}) depicted in Figure 7.10 reveal that M_{14kOe} increases with increasing molar concentration up to 0.3 and then decreases largely for the 0.5 M sample annealed at 350 °C, while M_{14kOe} of the 500 °C annealed samples decreases largely with increasing molar concentration from 0.1 to 0.2 and remains almost constant for other samples. These results suggest that M_{14kOe} decreases with increasing T_A [THOT2007, KISA2013], but the actual reduction in magnetization is sensitive to concentration. The optimum magnetic properties having moderate magnetization of 0.85 emu/g were obtained for spherical shaped NiO particles with an average particle size of about 9 nm.

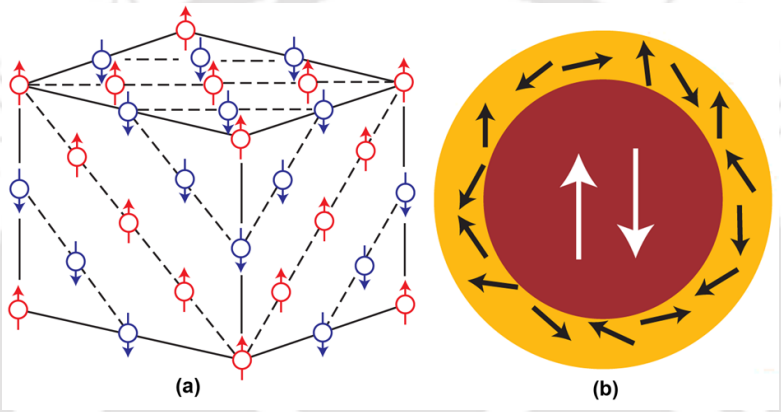

Figure 7.11: (a) Crystal and magnetic structures of bulk NiO and (b) schematic spin structure of NiO nanoparticles.

To understand the development of room temperature FM in these NiO nanoparticles, we correlate the magnetic properties with the structural and vibrational properties and illustrate magnetic structure schematically in Figure 7.11. It is understood that the bulk NiO exhibits AFM nature due to compensation of antiferromagnetically coupled (111) planes as shown in Figure 7.11(a). Therefore, bulk NiO exhibits a weak magnetic response to applied magnetic field [BAHA2012]. In this case, the exchange interaction between two neighboring Ni^{2+} ions is mediated by an oxygen ion through super-exchange interaction. This is evidenced by the presence of 2M band in Raman spectrum (see Figure 7.06). When the size of NiO is reduced into nanoscale, the exchange interaction between two neighbouring Ni atoms would be broken if an oxygen ion is missing from the surface and the exchange interaction energy would be reduced. As a result, the average coordination number for Ni^{2+} ions at the surface would be less than that in the bulk, which can result in a distribution of exchange energy barriers for the

surface spins [ROYA2014]. Furthermore, as the super-exchange interaction is sensitive to bond angles and bond lengths, they are likely to be modified at the surface as compared to that in the bulk. This is supported by the absence of 2M mode in Raman spectra for NiO nanoparticles. Therefore, the uncompensated spin at the surface of a particle turns out to be disordered [KODA1997, PECK2011] as depicted in Figure 7.11(b), which leads to an alignment of the particle's net moment in a relatively low-field region as reported in Figure 7.08(a). The formation of surface spins is further confirmed from the presence of magnetically originated 1P+1M band in Raman spectra. There is also a bulk like high-field contribution which originates from canting of sublattices. Kodama et al [KODA19991] proposed that multi-sublattice spin configuration directly follows from exchange interactions between magnetic ions and the low coordination at surface sites of nanostructures. The increased number of surface spins and magnetic multi-sublattice enhances net moments with reducing size of NiO [KISA2013]. Furthermore, the lattice expansion due to presence of broken bonds and defects as well as disorder distribution of uncompensated surface spins with size reduction gives rise to increase in bond length of Ni-O and weakening super-exchange interactions of magnetic ions in the multi-sublattice. The comparison between the Raman shift and magnetization as a function of molar concentration for 350 °C annealed NiO particles reveals that the red-shift of 1P+1M band with molar concentration could be attributed to the enhanced moment originating from uncompensated surface spins. On the other hand, the presence of SO modes in 500 °C annealed samples possibly reduces the magnetization due to the imperfection from spherical nature [PIGE1980]. A careful review on the literature in comparison with the present results shows that the development of FM in NiO particles strongly depends on both the preparation and annealing conditions, i.e., (i) Proenca et al [PROE2011] reported room temperature superparamagnetism in NiO nanoparticles of around 13 nm prepared by a sol-gel process. (ii) Similarly, Duan et al [DUAN2012] reported that NiO particles of size up to 12 nm prepared by thermal decomposition of nickel acetate show superparamagnetism at room temperature. (iii) Winkler et al [WINK2005] also reported superparamagnetism at room temperature for 3 nm NiO nanoparticles prepared by chemical precipitation technique. On the other hand, Tiwari et al [TIWA2005] and Ulmane et al [ULMA2011] shown that NiO particles exhibit room temperature FM. (iv) Thota et al [THOT2007] demonstrated that room temperature magnetism in NiO particles changes from FM to AFM nature with increasing the particle size from 4 nm to 13 nm.

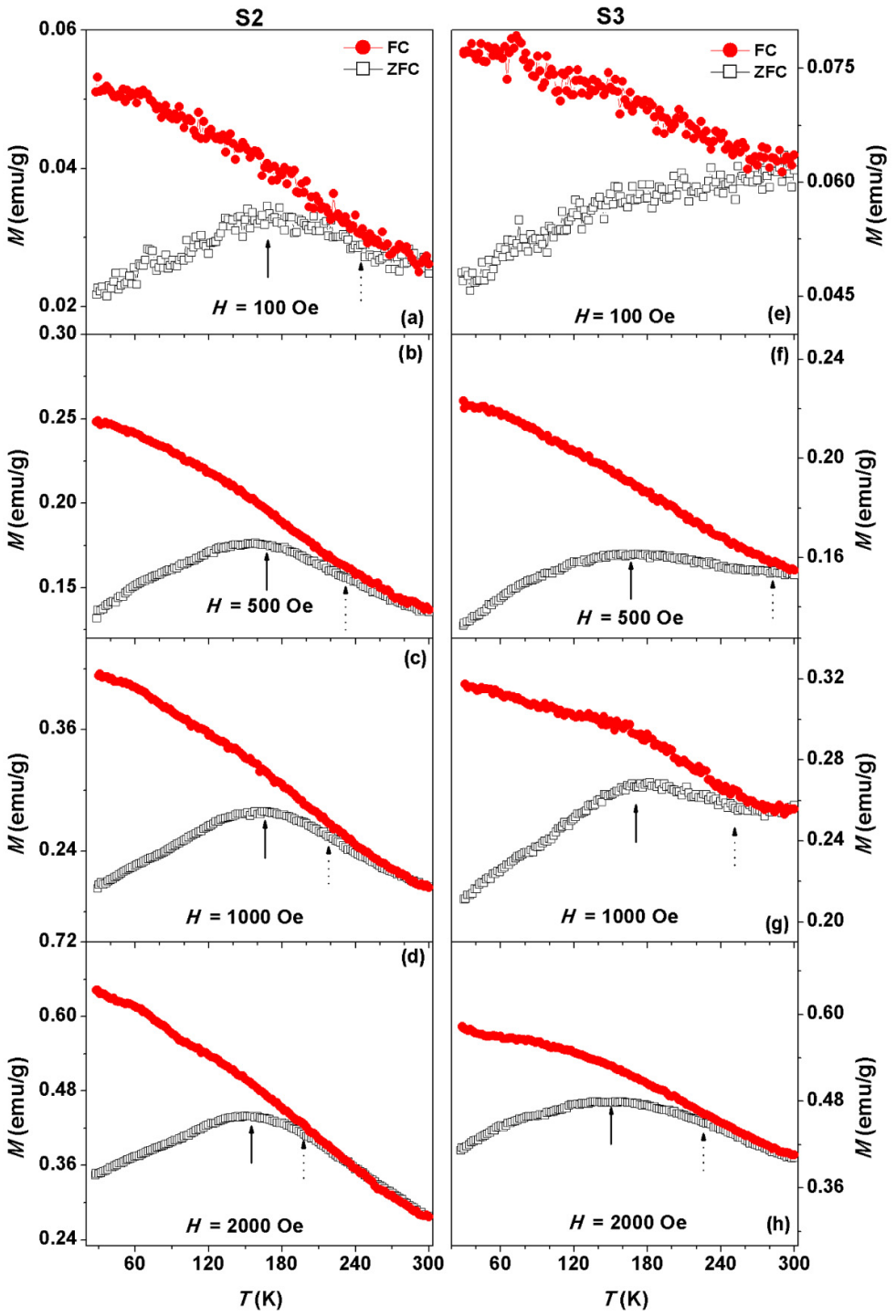

Figure 7.12: Low temperature *M-T* curves measured at different applied fields of 100, 500, 1000 and 2000 Oe under ZFC and FC conditions for S2 and S3 samples. The solid and dotted arrows indicate the positions of T_{peak} and T_{bifur}, respectively.

To understand the effect of temperature and magnetic field on the magnetic properties of NiO nanoparticles, *M-T* measurements at different constant applied fields under ZFC and FC conditions were performed in the temperature range 20 – 300 K. Figure 7.12 depicts *M-T* data obtained under different applied magnetic fields of 100, 500, 1000 and 2000 Oe for the samples S2 and S3. In these measurements, the sample was initially cooled to 20 K under zero-field condition. Magnetization was then recorded as the sample was heated to room temperature under a constant applied field (ZFC process). Subsequently, the sample was cooled in the same constant applied field to 20 K and then the magnetization was recorded as the sample was heated to room temperature (FC process). The magnetization data obtained under ZFC and FC conditions are quite different for the presently investigated samples. For S2 sample, ZFC magnetization data obtained at different applied fields increase initially with decreasing temperature from 300 K followed by a continuous decrease at low temperature. This results in a broad peak (T_{peak}) in the ZFC curve. On the other hand, FC data exhibit a continuous increase in magnetization with decreasing temperature and the rate of increase of magnetization is reduced with decreasing temperatures signifying the tendency towards saturation behavior at low temperatures. Thus, magnetization data obtained under ZFC and FC processes depict bifurcation point at a given temperature called T_{bifur}. Interestingly, the values of T_{peak} and T_{bifur} shift to low temperature with increasing applied magnetic fields as observed in many other metallic glasses and nanoparticles. In contrast, the sample S3 does not show T_{peak} in ZFC curves measured under 100 Oe, but exhibits at fields larger than 100 Oe. The shift of T_{peak} and T_{bifur} to low temperature with increasing applied fields was observed for this sample as well. The observation of peak in ZFC curves was generally reported both in superparamagnetism and spin glass materials. However, FC data become saturated below T_{peak} for spin glasses, but continue to increase below T_{peak} for superparamagnetism [BITO1995, TIWA2005, PROE2011].

Nevertheless, there are reports stating that the glassy behavior in magnetic nanoparticles exhibits a continuous increase in FC data with decreasing temperature below T_{peak} [LUOW1991]. In order to understand these results, the extracted values of T_{peak} and T_{bifur} are plotted as a function of applied field in Figure 7.13. In typical spin glasses, the observation of spin glass phase is very sensitive to applied magnetic field and vanishes under the application of a few hundred gauss field, i.e., T_{peak} shifts to low temperature and disappears eventually at higher applied field [NARL2005]. However, in the presently investigated samples, the presence of T_{peak} was observed up to 2 kOe field. Tiwari et al [TIWA2005] observed the existence of T_{peak} in ZFC curve up to 20 kOe field. In order to confirm the nature of the

magnetic phase at low temperature, T_{peak} and T_{bifur} were plotted as a function of field with de Almeida-Thouless (AT) line [ALME1978, YIJJ2008] described by eqn.(7.03),

$$H_{AT}(T) \propto \left(1 - T_{peak}/T_{sg}\right)^{1.5} \qquad (7.03)$$

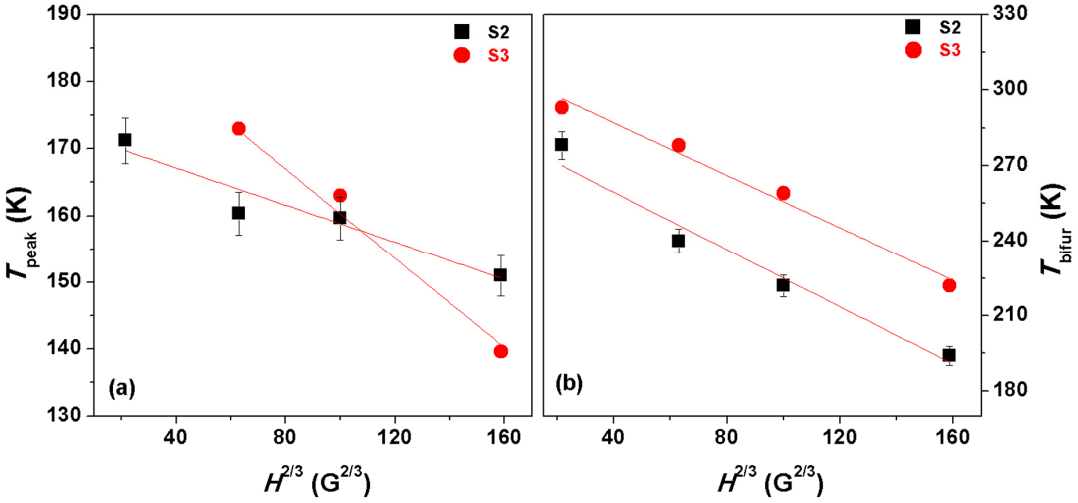

Figure 7.13: AT line plots for S2 and S3 samples. The solid lines passing through the data points are the best fits to eqn.(7.03).

The extrapolation of the AT line back to zero applied field provides the spin glass transition temperature T_{sg} which turns out to be 173 and 194 K for the samples S2 and S3, respectively. It is clearly seen that both T_{peak} and T_{bifur} decrease with increasing applied field and compliance with the *A-T* line. This is considered to be a strong evidence for the existence of spin glass phase in the presently investigated samples. Interestingly, T_{peak} decreases at a faster for S3 sample than S2 sample. The observed spin glass behavior and enhancement of magnetization in AFM nanoparticles have been explained in terms of enhanced surface disorder and interacting cationic vacancy [MAND2009]. Winkler et al [WINK2005] and Mandal et al [MAND2011] reported that the NiO nanoparticles in the size range of 30 nm do not show any peak down to 25 K in the ZFC curve. Some of the earlier reports claimed that the freezing of uncompensated surface spins can lead to a spin glass phase, which survives up to certain high-fields. Following the model described in Figure 7.11 and considering the finite number of surface spins on each particle, which vary with the particle's shape and size, the observation of broad peak in ZFC due to the distribution of freezing temperature can be understood. To study the effect of T_A or the particle size on the magnetic properties of NiO particles, we have also performed *M-T* measurements under ZFC and FC conditions for NiO samples with different molar concentrations annealed at 350 °C and 500 °C.

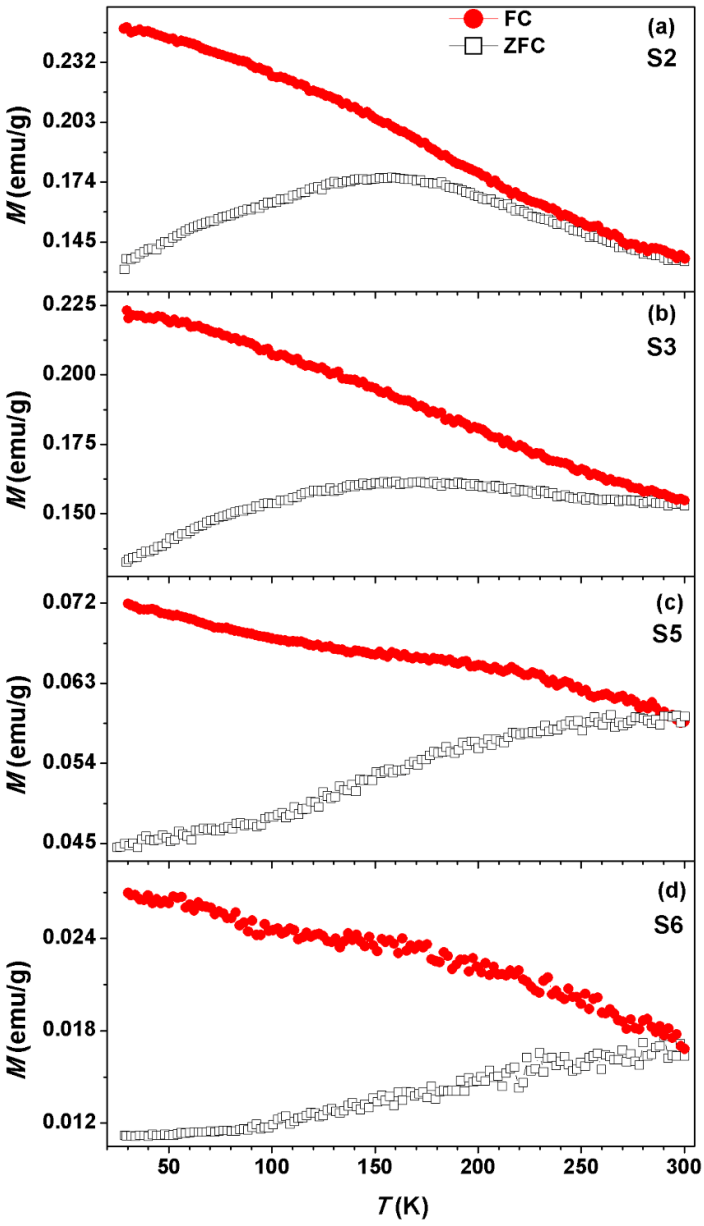

Figure 7.14: Low temperature *M-T* curves measured at 500 Oe applied field under ZFC and FC conditions for S2, S3, S5 and S6 samples.

Figure 7.14 depicts *M-T* data measured at 500 Oe applied field under ZFC and FC conditions for S2, S3, S5 and S6 samples. The salient features observed from the figure are as follows: (i) For samples S2 and S3, ZFC magnetization increases initially with decreasing temperature from 300 K followed by a continuous decrease at low temperature resulting a broad peak in the ZFC curves. (ii) For the samples S5 and S6, ZFC magnetization decreases continuously with decreasing temperatures and saturates at low temperature below 50 K for S6 sample. (iii) However, FC magnetization invariably depicts progressive increases in the

magnetization (though with varying rates in different temperature regimes) with decreasing temperature from 300 K. (iv) The value of magnetization at any temperature decreases with increasing T_A or average particle size. A similar nature of the *M-T* curves was reported in $Ni_{0.7}Zn_{0.3}O$ nanoparticles with increasing the average particle size [LUOW1991]. These results along with room temperature *M-H* curves as shown in Figure 7.08 reveal that the magnetic nature of NiO particles changes from FM to AFM with increasing the average particle size and hence resulting a different temperature dependent magnetic properties. This is in close agreement with the earlier reports by Thota et al [THOT2007] on similar systems.

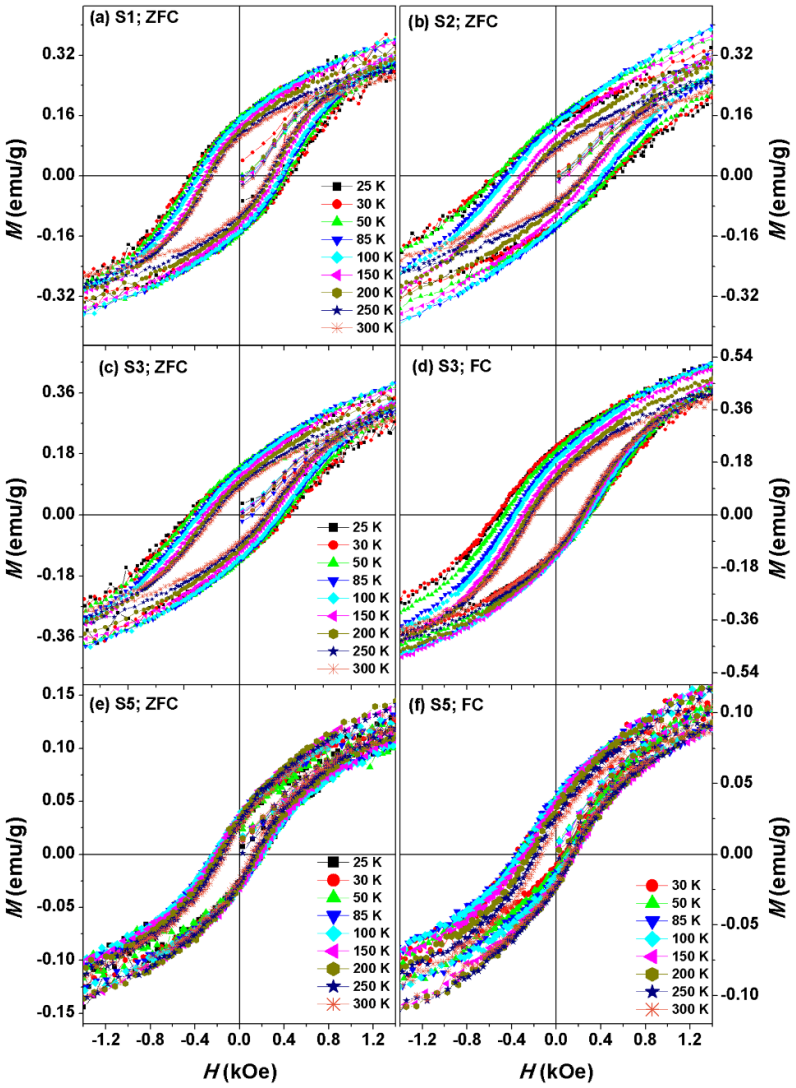

Figure 7.15: Low temperature *M-H* loops of S1, S2, S3 and S5 samples measured under ZFC conditions and FC condition for S3 and S5 samples.

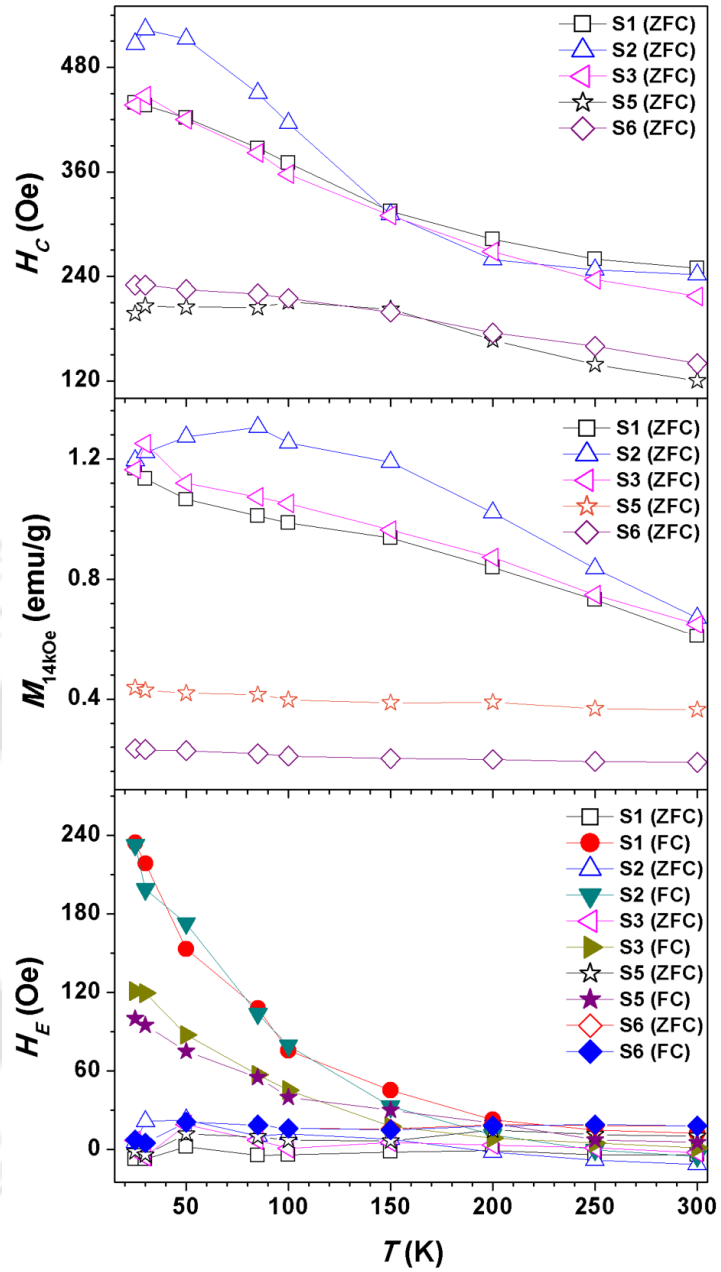

Figure 7.16: The variations of H_C, M_{14kOe} and H_E as a function of temperature for S1, S2, S3, S5 and S6 samples obtained from temperature dependent *M-H* loops measured under ZFC and FC conditions.

To study the effect of applied field on the magnetic nature at low temperature, *M–H* loops at different temperatures in the temperature range from 25 K to 300 K were measured under ZFC and FC conditions. Figure 7.15 depicts expanded view of typical *M-H* loops measured under ZFC conditions for S1 (a), S2 (b), S3 (c), S5 (e) samples and FC condition for S3 (d) and S5 (f) samples at different temperatures. While the nature of the loops does not change with

temperature, the applied field of 14 kOe is not enough to saturate the loops. A careful observation of the loops suggests that FC samples exhibit more shift towards negative axis with decreasing temperature. This can be explained based on the enhanced surface anisotropy between the compensated inner core and uncompensated surface spin on the nanoparticles. Figure 7.16 displays the extracted values of H_C, M_{14kOe} and calculated values of exchange bias ($H_E = (|H_{C-}|-|H_{C+}|)/2$) as a function of temperature for S1, S2, S3, S5 and S6 samples obtained under ZFC and FC conditions. While the values of H_C and M_{14kOe} increase considerably with decreasing temperature as expected for typical FM materials, the rate of increase of magnetization with decreasing temperature is significantly weak suggesting that number of surface spins on NiO nanoparticles is limited. On the other hand, the variations of $H_E(T)$ obtained under ZFC condition exhibit weak dependence on temperature, whereas the FC condition shows a larger variation with temperature particularly at lower temperatures below 150 K where the spin glass nature was observed for these samples. This can be attributed to the fact the FC condition promotes additional anisotropy between freezing surface spins and compensated spins at the core. A comparison of variation in $H_E(T)$ for the samples annealed at 350 °C and 500 °C reveals that (i) NiO samples annealed at 350 °C show large variation in the $H_E(T)$ under FC condition due to the existence of spin glass phase, which induce additional anisotropy between surface spins and compensated core spins. (ii) For the NiO samples annealed at 500 °C, the variation in $H_E(T)$ is small due to the change in the magnetic nature from FM to AFM with increasing particle size [THOT2007, PECK2011]. Since the enhanced H_C and loop shift are considered to be the key experiment manifestations of the multi-sublattice surface-spin ordering and the exchange bias effect, their presence in the nanoparticles are true nanoscale phenomena, originating from the large surface to volume ratio of the NiO nanoparticles.

To understand the stability of FM above room temperature, high temperature *M-T* curves were obtained at 2 kOe applied field with 4 °C/min heating rate from 300 K to 900 K for S1, S2 and S3 samples and depicted in Figure 7.17. *M-T* curve of commercially available NiO powder is also shown for comparison. For commercially available NiO powder, magnetization increases slowly up to 525 K and then decreases above 525 K. The Néel temperature determined from peak in *M–T* curve is found to be 525 K. On the other hand, the sample S1 exhibits a gradual decrease in magnetization with increasing temperature up to 560 K. On further increasing temperature, a large decrease in magnetization was observed and varies sluggishly at higher temperatures.

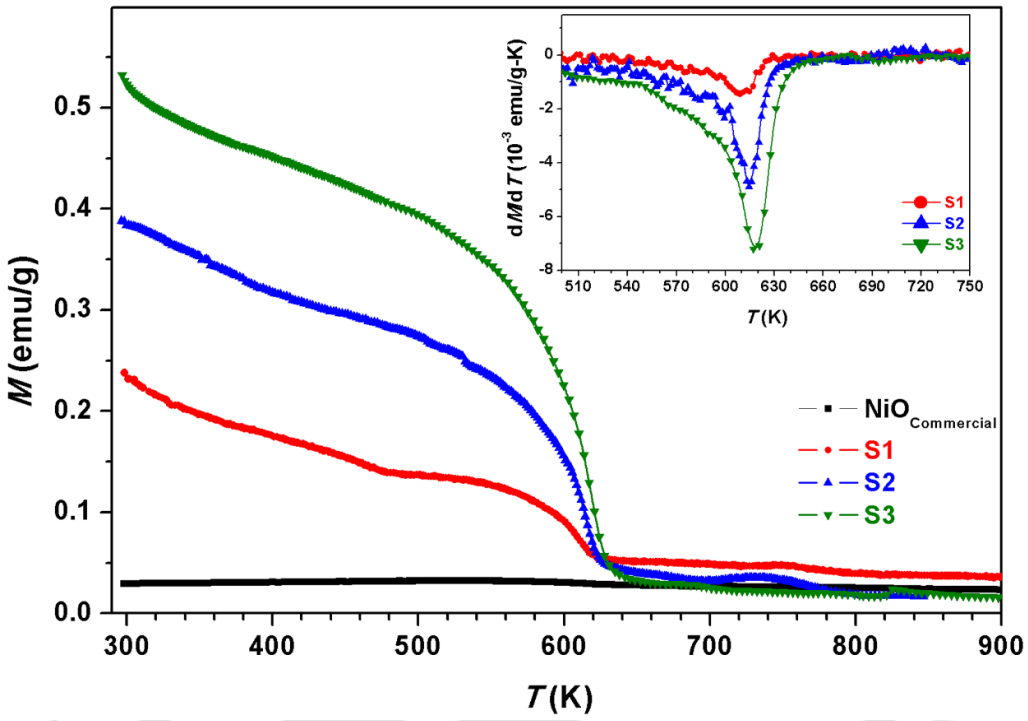

Figure 7.17: High temperature *M-T* curves of commercially available NiO powder, S1, S2 and S3 samples. Inset depicts the thermal derivative of magnetization data for S1, S2 and S3 samples close to transition.

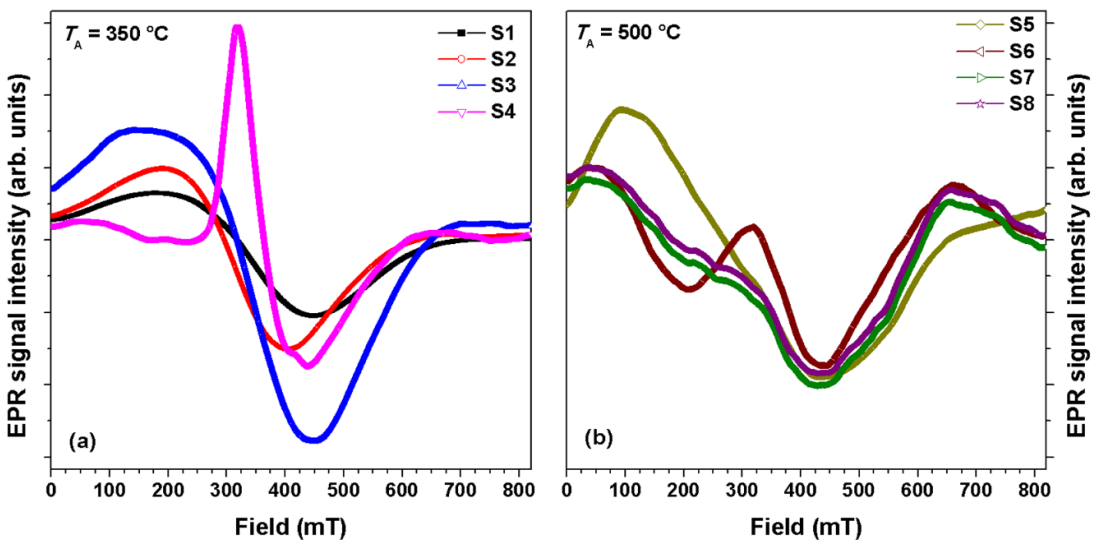

Figure 7.18: Room temperature EPR spectra of NiO nanoparticles annealed at (a) 350 °C (S1-S4) and (b) 500 °C (S5-S8).

A similar behavior has been observed for S2 and S3 samples, but the drop of magnetization around 600 K increases with increasing molar concentration up to 0.3. This

could be attributed to the induced FM phase in NiO particles resulting a clear magnetic phase transition from FM to PM state at high temperature. Curie temperature of the phase transition (T_C) was determined from the thermal derivation of *M-T* data as shown in inset of Figure 7.17. The minimum point in the *dM*/*dT* curve is very broad for S1 sample due to weak FM, which becomes much sharper for S2 and S3 samples. T_C was observed to be around 610 K, but found to increase slightly from 610 K to 618 K with increasing molar concentration from 0.1 to 0.3. Nevertheless, the obtained value of T_C is lower than the bulk Ni (~ 630 K) [MAND2009]. These results certainly support the existence of uncompensated surface spins inducing FM in size reduced NiO particles.

7.3.5. Resonance properties

EPR spectroscopy is a useful technique for studying the materials with unpaired electrons and defects. In order to understand the effects of nanostructures and molar concentration on the magnetic properties, EPR measurement was carried out on all samples and displayed in Figure 7.18. It is seen that all the spectra of NiO samples annealed at 350 °C are found to exhibit a broad resonant peak except for S4 sample. The value of *g* is approximately ranging between 2.2 - 2.4, which could be attributed to the Ni^{2+} ions. The relative intensity and line width of these absorption lines exhibit a strong dependence on molar concentration, i.e., with increasing molar concentration up to 0.3 the peak intensity increases significantly and the broad peak shifts towards lower fields indicating a clear FM signature of the materials [SRIN2011]. On further increasing molar concentration to 0.5, the width of the signal and *g* value were reduced, which can be attributed to the variation of magnetic nature in the sample resulting in a decrease in FM properties [NIBA2003]. Changes in line width, strong dipole-dipole and exchange interaction between nickel ions are reported for NiO nanoparticles annealed at 350 ºC [WINK2005]. On the other hand, the samples annealed at 500 ºC exhibit different nature of the spectra except for S5 sample. The EPR spectrum of S5 sample is almost similar to S2 sample, but with large broadening. It may be noted that S5 sample exhibits moderate room temperature FM.

In contrast, the samples S6-S8 show completely different spectra with large broadening as compared to samples annealed at 350 °C. The decreasing intensity of the EPR signal with increasing particle size can be correlated to the reduced surface Ni spins with increasing the particle size and changes the magnetic properties from FM to AFM nature [YIJB2007, SHIM2008]. It may be noted that EPR signal of most bulk AFM materials disappear below its

transition temperature due to the effect of very strong exchange fields, which require resonance frequency higher than EPR GHz region. On the other hand, the appearance of EPR signal in nanoparticles can be correlated to one or more of the following different mechanisms: (i) size effect which substantially lowers the Néel point [KENN1987], (ii) formation of uncompensated spins on the surface of the particle [NEEL1962] (iii) creation of a spin glass-like shell on the particle surface [TIWA2005], (iv) formation of a weak magnetic moment caused by the canting of the magnetic sublattices [ZYSL1994, KODA1997], and (v) extraneous FM impurities produced during sample fabrication. A comparison between EPR signal and magnetic measurements suggests that the formation of EPR signal could be attributed to the existence of uncompensated spin on the surface of NiO particles, which provides supportable explanation for temperature and field dependent magnetic properties. Therefore, it has been concluded that EPR signals are found to be affected by not only T_A but also by molar concentration, which modifies the surface nature of the nanoparticles.

These results also suggest that the preparation conditions strongly affect the physical properties of the nanoparticles. Nevertheless, the preparation of fine NiO nanoparticles with relatively large magnetization at room temperature for the optimum molar concentration in the present investigation is remarkable.

7.4. Summary

A systematic investigation of structural, vibrational, optical, magnetic and resonance properties of NiO nanoparticles prepared using sol-gel method with different molar concentrations and annealed at different temperatures has been carried out. The salient features of the NiO nanoparticles from the current investigations are as follows:

- Structural properties reveal that as-made particles exhibit nickel hydroxide structure, which transforms into single phase face centered cubic NiO with negligible strain after air annealing at different temperatures. The average crystallite size increases with increasing annealing temperature. Microstructural studies show that the shape of the particles changes from spherical into non-spherical nature with increasing different temperatures.
- Vibrational studies show a new Raman band at 500 cm^{-1} associated with magnetic origin induced by strong phonon-magnon interaction. This peak shows red-shift with increasing molar concentration for the samples annealed at 350 °C. The presence of 2M mode was not observed in the presently investigated samples. However, the

appearance of another type of excitation (SO modes) is observed for the non-spherical NiO nanoparticles.

- The optical properties exhibit a strong UV emission around 350 nm, which depicts blue-shift for NiO nanoparticles as compared to bulk.
- Magnetic study reveals that all samples exhibit magnetic hysteresis properties indicating the ferromagnetic nature. However, the ferromagnetic nature decreases with increasing annealing temperature, but the actual reduction in magnetization is sensitive to concentration. The optimum magnetic properties having moderate magnetization of 0.85 emu/g and coercivity of 210 Oe were obtained for spherical shaped NiO particles with an average particle size of about 9 nm.
- Low temperature magnetization shows a bifurcation between ZFC and FC curves and a peak in ZFC curves, which shift to lower temperature with increasing applied magnetic fields. The existence of spin glass like phase was verified through AT line plot. The presence of spin glass like phase provides additional anisotropy between the freezing surface spins and the compensated spins at the core under field cooling condition, which results in a larger exchange bias variation at lower temperatures.
- A well-defined magnetic phase transition due to induced ferromagnetic nature is observed at high temperature around 610 K, but the phase transition temperature increases slightly from 610 K to 618 K with increasing molar concentration up to 0.3 M.
- Electron paramagnetic resonance studies revealed a close correlation with the magnetic properties.

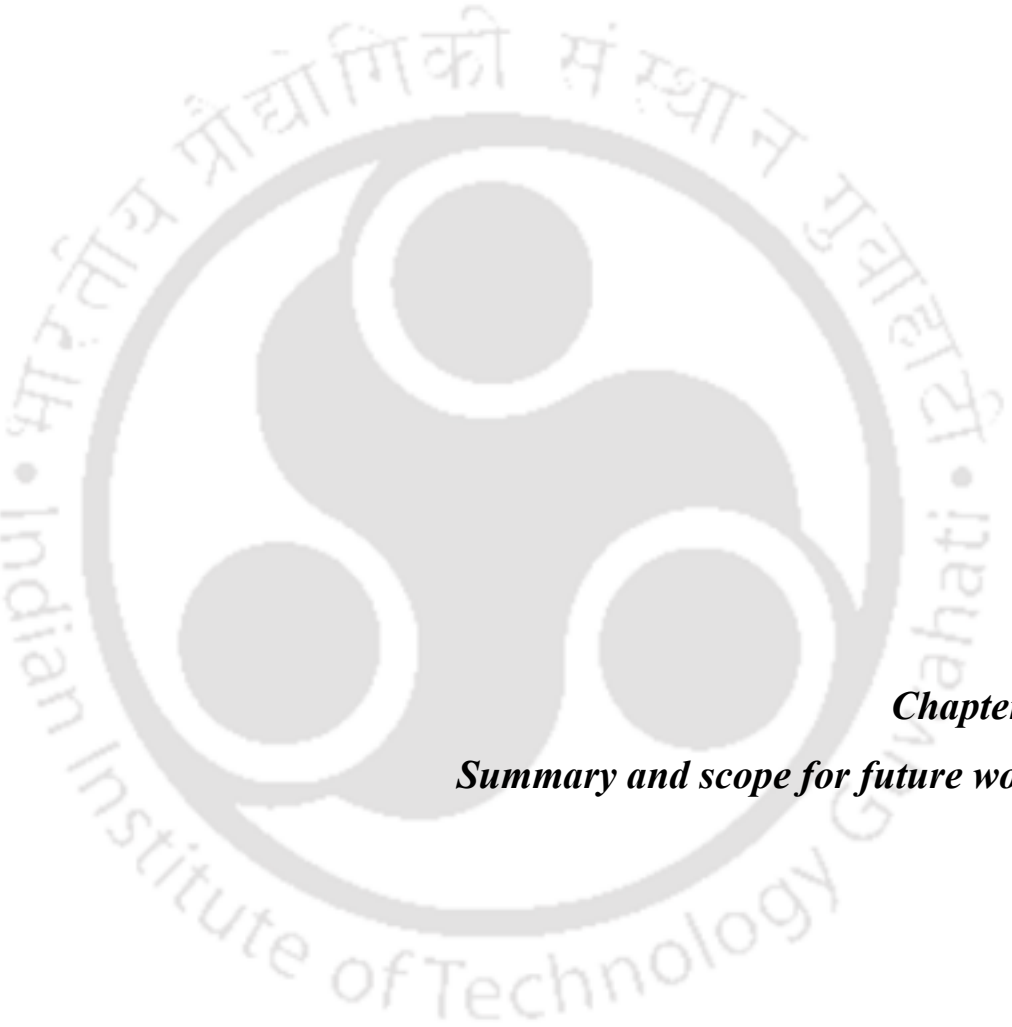

Chapter 8

Summary and scope for future work

The overall summary of the salient results obtained on the structural, vibrational, electronic, magnetic, resonance and optical properties of (a) NiO, (b) ZnO and (c) TiO_2 nanocrystalline powders prepared by ball mill process and (d) NiO nanoparticles prepared by sol-gel method is listed in this chapter. Highlights of the current investigations and the possibilities for future work are also summarized below:

8.1. Summary of the results

Nanocrystalline NiO, ZnO and TiO_2 powders were prepared by ball mill process under dry mill conditions in high energy planetary ball mill filled with high purity argon gas. Systematic studies of the evolution of nanocrystalline structure, vibrational, electronic, magnetic, resonance and optical properties of NiO, ZnO and TiO_2 powders were carried out to understand the effect of milling characteristics on tuning the properties of these metal-oxide powders. The milled powders were subsequently heat treated at elevated temperatures under air atmosphere in a furnace. The changes occurring in the structure and physical properties of the annealed powders were evaluated to understand the origin of various physical properties in the nanocrystalline powders. For comparative study, NiO nanoparticles were prepared by sol-gel method with different molar concentrations and annealed at different annealing temperatures, and characterized structural, vibrational, optical, magnetic and resonance properties.

Structural evolution during the course of milling was analyzed from the X-ray diffraction (XRD) using Williamson-Hall plot and Modified Williamson-Hall plot methods and microscopy techniques. During the milling process, the average crystallite size of the powders decreased and reached down to around 11, 12 and 19 nm for the NiO, ZnO and TiO_2 powders, respectively after milling for typically 30 to 40 hrs. On the other hand, the NiO nanoparticles prepared by sol-gel method exhibited nickel hydroxide structure, which transformed into single phase face centered cubic NiO with negligible strain after air annealing at different temperatures. The average crystallite size increased from about 9 nm to 15 nm with increasing annealing temperature from 350 °C to 500 °C.

For NiO powders, the ball milling produced single phase face centered cubic nanocrystalline NiO powders without any impurities within the detection limit of the techniques utilized. Lattice volume decreased almost linearly with decreasing inverse of crystal size (D^{-1}). Raman spectra showed the disappearance of two-magnon (2M) band immediately, broadening and enhancement of one-phonon (1P) longitudinal optical (LO) band and decrease of two-phonon (2P) LO and 2P TO vibration frequency with decreasing NiO crystal size. As a

result, the color of the NiO powders has changed from the pale green for pure NiO powder to dark green for milled NiO powder. This was attributed to the existence of non-stoichiometry in the milled NiO powders caused by the defects, size reduction, oxidization of Ni^{2+} to Ni^{3+} due to breaking of Ni^{2+}-O^{2-}-Ni^{2+} super-exchange interaction, as evidenced clearly from X-ray photoelectron spectroscopy (XPS) spectra. Photoluminescence (PL) study showed blue-shifting of band edge emission peak, which confirmed the finite size effect in milled NiO powders. The pure NiO powder exhibited antiferromagnetic (AFM) nature, which transformed into ferromagnetic (FM) gradually at room temperature. The magnitude of induced FM in milled NiO powders dependent on the milling period. A maximum magnetization of 1.08 emu/g at 12 kOe applied field and a coercivity of about 160 Oe were obtained at room temperature for 30 hrs milled NiO powder. As a result, the exchange bias decreased almost linearly with decreasing crystal size. Annealing of as-milled NiO powders (i) resulted in a large reduction in magnetization, but the rate of reduction strongly dependent on the milling conditions and (ii) confirmed the origin of FM as intrinsic one. Temperature dependent magnetization (*M*-*T*) measurements in the low temperature range exhibited two peaks corresponding to freezing of surface spin and spin glass like phase. The presence of spin glass like phase was verified through de Almedia-Thouless (AT) line plot. The spin glass phase provided additional anisotropy and enhanced exchange bias under field-cooling condition. High temperature *M*-*T* measurements showed the presence of mixed magnetic phases for the initial period of milling and on-set of ferromagnetic behavior with a well-defined magnetic phase transition (T_C) at around 780 K. Electron paramagnetic resonance (EPR) study disclosed a close correlation between the EPR results and magnetic properties.

Similarly, both pure un-milled and milled ZnO powders exhibited single phase hexagonal wurtzite structure without any detectable impurities. Bulk ZnO powder yielded six Raman-active modes including two B_1 silent modes. Upon milling, the development of E_1(LO) vibration mode attributed to defects due to oxygen vacancies and/or Zn interstitials in ZnO powders has been observed. XPS spectra of bulk ZnO powder exhibited two strong peaks centered around 1022 and 1045 eV, which were in agreement with the binding energies of Zn $2p_{3/2}$ and Zn $2p_{1/2}$, respectively, with a spin-orbital-splitting of 23 eV. This confirmed that Zn is present as Zn^{2+}. In addition, the O 1s spectrum exhibited a broad asymmetric feature indicating the presence of multi-component oxygen species: (i) low binding energy peak at 530.3 eV due to O^{2-} ions on the wurtzite structure of the hexagonal Zn^{2+} ion array, which are surrounded by zinc atoms with their full complement of nearest-neighbor O^{2-} ions, (ii) intermediate binding energy peak at 531.5 eV associated with O^{2-} ions that are in oxygen

deficient regions within the matrix of ZnO and higher binding energy peak at 532.7 eV due to absorbed H_2O or O_2 molecules on the surface. With increasing milling time, the peaks at 531.5 eV and 532.7 eV increased at the expense of the peak at 530.3 eV, indicating the increase in oxygen vacancies with milling. The optical studies revealed a blue-shifting of excitonic absorption peak with crystal size reduction. This resulted in an increase in band gap with size reduction in milled ZnO powders. Paramagnetic (PM) nature observed in un-milled ZnO gradually unveiled room temperature FM with modest magnetization and coercivity. A maximum magnetization of 0.92 emu/g at 12 kOe applied field and a coercivity of 172 Oe were obtained for 40 hrs milled ZnO powder. Annealing of the as-milled ZnO powders displayed a drastic reduction in room temperature magnetization signifying the observed FM properties as intrinsic one. High temperature *M-T* data disclosed a clear magnetic phase transition from FM to PM state around 500 °C, which shifted slightly towards higher temperature with increasing milling period up to 20 hrs. EPR study showed that FM order increased with increasing milling time due to the increase in oxygen and zinc vacancies. A close correlation between EPR results and magnetic properties was observed.

On the other hand, the milled TiO_2 powders exhibited peak broadening in XRD peaks along with the development of new phases corresponding to oxygen deficient $TiO_{2-\delta}$ and rutile phases. Vibrational studies confirmed the formation of news phases with increasing milling period. XPS spectra of pure TiO_2 powder showed that in Ti 2p spectra, two peaks centered around binding energy of 459 and 465 eV, assignable to $2p_{3/2}$ and $2p_{1/2}$, respectively, of Ti^{4+} in TiO_2. This suggested the identical chemical state of Ti atoms in pure TiO_2. However, with increasing milling period, a significant Ti^{3+} signals could be observed in Ti 2p spectra providing the evidence of oxygen vacancies in the milled powders. In addition, O 1s signal of milled powders depicted three contributions at 530.7, 532.9 and 534.3 eV after peak modeling. The main peak at 530.7 eV was ascribed to lattice oxygen in TiO_2, while the signal at 532.9 eV was related to surface hydroxyl groups. The calculated spectrum exhibited additional feature at 534.3 eV arising from the O atom of the water molecule. Paramagnetic nature observed in pure anatase phase of TiO_2 transformed into induced FM with crystal size reduction. A maximum magnetization of 0.15 emu/g at 12 kOe applied field and a coercivity of about 155 Oe were obtained for 60 hrs milled TiO_2 powder. EPR study showed that the nature of EPR signals changes with milling time due to the increase in oxygen and Ti vacancies and exhibited a good agreement with magnetic properties. Optical studies revealed two major peaks around 395 nm and 470 nm due to band-to-band direct transitions in pure TiO_2 powders. Upon milling, additional peaks were observed due to surface

recombination, oxygen vacancies and surface defects. The lattice strain and defects reduced the bandgap slightly.

The NiO nanoparticles prepared by sol-gel method with different molar concentrations and annealed at different temperatures showed single phase face centered cubic structure with negligible strain and without any detectable impurity phases. The shape of NiO particles changed from spherical to non-spherical with increasing annealing temperature. Raman spectra exhibited a new Raman band at 500 cm^{-1} associated with magnetic origin induced by strong phonon-magnon interaction. This peak showed red-shift with increasing molar concentration for the samples annealed at 350 °C. The presence of 2M mode was not observed in the presently investigated samples. The optical properties exhibited a strong UV emission around 350 nm, which depicted blue-shift for NiO nanoparticles as compared to bulk. Low temperature *M-T* curves in 350 °C annealed samples displayed peaks in zero-field-cooled curves, which shifted to lower temperature with increasing applied magnetic fields. The existence of spin glass like phase due to freezing of the uncompensated surface spins was verified through AT line plot. The presence of spin glass like phase provided additional anisotropy between the freezing surface spins and the compensated spins at the core under field cooling condition, which resulted in a larger exchange bias variation at lower temperatures. However, the samples annealed at 500 °C with molar concentration more than 0.1 M neither showed spin glass nor exhibited large exchange bias. A well-defined magnetic phase transition due to induced FM nature was observed at high temperature around 610 K, but the phase transition temperature increased slightly from 610 K to 618 K with increasing molar concentration up to 0.3 M. EPR studies showed good agreement with the observed magnetic properties.

The present studies have brought out several interesting results which contribute to the understanding of the evolution of magnetic properties in nanocrystalline metal-oxide powders under different preparation conditions. These studies have also revealed the strong correlation between structure, vibrational, electronic, magnetic, resonance and optical properties of metal-oxide powders prepared under optimum conditions.

8.2. Scope for future work

The present investigations on as-milled and annealed metal-oxide powders have revealed that there are several aspects of interest in these materials. A study of the local environment of metal and oxygen in these powders milled for various milling time periods would help in understanding (i) the development of defects such as vacancies of Ni, Zn, Ti and O and (ii) the manner in which

the super-exchange interaction fades away with decreasing the average crystal size and increasing defects. It has been observed that for NiO powders, the two-magnon band in Raman spectra disappears rapidly within the milling period of 30 minutes. However, the determined crystallite size for 30 minutes milled NiO powder is around 25 nm. This raises the question that whether the size reduction or defects dominates the breaking of super-exchange interaction in NiO powders. Hence, the milling of NiO under low milling intensity (low milling speed and reduced ball-to-powder weight ratio) would possibly provide the dominant contribution from defects and size reduction. X-ray magnetic circular dichroism studies on the pure and milled NiO powders would reveal the magnetic interactions in these nanocrystalline powders and might provide insights on enhancing the magnetic properties. The maximum magnetization of 1.08 emu/g, 0.92 emu/g, 0.15 emu/g and 0.85 emu/g was observed for nanocrystalline NiO, ZnO and TiO_2 powders prepared by ball milling and NiO nanoparticles prepared by sol-gel method, respectively. Although this is found to be one of the challenging results, the obtained behaviors suggest that the fine tuning of size in these metal-oxide powders may help in further enhancing the magnetic properties. Additionally, it is worthy to investigate green compacted and sintered targets of the above powders towards developing thin films suited for applications in spintronics.

References

[ABRA1969] Abrahams S. C, Bernstein J. L, Acta Crystallogr. B 25 (1969) 1233.

[ACHA2013] Acharyya D, Hazra A, Dutta K, Gupta R. K, Bhattacharyya P, Sem. Sci. Tech. 28 (2013) 125001.

[ADHI2017] Adhikari S, Madras G, Phys. Chem. Chem. Phys. 19 (2017) 13895.

[ADLE1970] Adler D, Feinleib J, Phys. Rev. B 2 (1970) 3112.

[AHMA2006] Ahmad T, Ramanujachary K. V, Lofland S. E, Ganguli A. K, Solid State Sci. 8 (2006) 425.

[AKBA2011] Akbar S, Hasanain S. K, Abbas M, Ozcan S, Ali B, Shah S. I, Solid State Commun. 151 (2011) 17.

[ALAR2006] Alaria J, Bieber H, Colis S, Schmerber G, Dinia A, Appl. Phys. Lett. 88 (2006) 112503.

[ALME1978] Almeida J R L de, Thouless D. J, J. Phys. A: Math. Gen. 11 (1978) 983.

[ALSE2014] Al-Sehemi A. G, Al-Shihri A. S, Kalam A, Du G, Ahmad T, J. Molecular Struc. 1058 (2014) 56.

[ANAN2011] Anandan K, Rajendran V, Mater. Sci. in Semiconductor Proc. 14 (2011) 43.

[ANDE1955] Anderson P. W, Hasegawa H, Phys. Rev. 100 (1955) 675.

[ANDE1958] Anderson P. W, Phys. Rev. 109 (1958) 1492.

[ARIC2005] Arico A. S, Bruce P, Scrosati B, Tarascon J. M, Schalkwijk W. V, Nature Mater. 4 (2005) 366.

[AYYU1995] Ayyub P, Palkar V. R, Chattopadhyay S, Multani M, Phys. Rev. B 51 (1995) 6135.

[BAAB2015] Ba-Abbad M. M, Chai P. V, Takriff M. S, Benamor A, Mohammad A. W, Mater. Design 86 (2015) 948.

[BAHA2012] Bahadur N, Pasricha R, Govind, Chand S, Kotnala R. K, Mat. Chem. Phys. 133 (2012) 471.

[BAHL2006] Bahl C. R. H, Hansen M. F, Pedersen T, Saadi S, Nielsen K. H, Lebech B, Morup S, J. Phys.:Condens. Matter 18 (2006) 4161.

[BAND2016] Bandyopadhyay S, Cahay M, Introduction to Spintronics, 2nd Edition, CRC Press, Taylor & Francis Group, London (2016).

[BANE2007] Banerjee S, Mandal M, Gayathri N, Sardar M, Appl. Phys. Lett. 91 (2007) 182501.

[BARA2016] Barakat M. A, Kumar R, Photocatalytic Activity Enhancement of Titanium Dioxide Nanoparticles: Degradation of pollutants in Wastewater, Springer, London (2016).

[BARD1954] Bardeen J, Blatt F. J, Hall L. H, in proceedings of the conference on photoconductivity, Atlantic city, Breckenridge R. G, Russell B. R, Hahn E. E, (Edt.), John Wiley, New York (1954) 146.

[BARM2015] Barman A, Saini C. P, Sarkar P, Satpati B, Bhattacharya S. R, Kabiraj D, Kanjilal D, Dhar S, Kanjilal A, J. Appl. Phys. 118 (2015) 224903.

[BARO1992] Barone A, Antonion B, Principles and Applications of Superconducting Quantum Interference Device, World Scientific, UK (1992).

[BART2007] Bartolome F, Blasco J, Garcia L. M, Garcia J, Jimenez S, Lozano A, J. Magn. Magn. Mater. 316 (2007) e195.

[BASO1964] Basolo F, Johnson R. C, Coordination Chemistry; the Chemistry of Metals Complexes, Benjamin W. A, New York (1964).

[BATL2002] Batlle X, Labarta A, J. Phys. D 35 (2002) R15.

[BECH2015] Bechambi O, Chalbi M, Najjar W, Sayadi S, Appl. Surf. Sci.347 (2015) 414.

[BERG2004] Bergqvist L, Eriksson O, Kudrnovsky J, Drchal V, Korzhavyi P, Turek I, Phys. Rev. Lett. 93 (2004) 137202.

[BERS1998] Bersani D, Lottici P. P, Ding X. Z, Appl. Phys. Lett. 72 (1998) 73.

[BHAR2016] Bharti B, Kumar S, Lee H. N, Kumar R, Scientific Reports 6 (2016) 32355.

[BHOW2004] Bhowmik R. N, Nagarajan R, Ranganathan R, Phys. Rev. B 69 (2004) 054430.

[BIAN2012] Bianchi A. E, Stewart S. J, Zysler R. D, Punte G, J. Appl. Phys. 112 (2012) 083904.

[BIEX2010] Bie X. F, Wang C. Z, Ehrenberg H, Wei Y. J, Chen G, Meng X, Zou G. T, Du F, Solid State Sci. 12 (2010) 1364.

[BIND1986] Binder K, Young A. P, Rev. Mod. Phys. 58 (1986) 801.

[BINN2002] Binns C, Baker S. H, Maher M. J, Louch S, Thornton S. C, Edmonds K. W, Dhesi S. S, Brookes N. B, Phys. Status Solidi A 189 (2002) 339.

[BITO1995] Bitoh T, Ohba K, Takamatsu M, Shirane T, Chikazawa S, J. Phys. Soc. Jpn. 64 (1995) 1305.

[BLIN1996] Blinowski J, Kacman P, Majewski J. A, Phys. Rev. B 53 (1996) 9524.

[BLUN2003] Blundell S, Magnetism in Condensed Matter, Oxford University Press, Chapter 3 (2003).

[BODK1994] Bødker F, Mørup S, Linderoth S, Phys. Rev. Lett. 72 (1994) 282.

[BODK2000] Bødker F, Hansen M. F, Bender Koch C, Morup S, J. Magn. Magn. Mater. 221 (2000) 32.

[BODU2014] Bodurov G, Stefchev P, Ivanova T, Gesheva K, Mater. Lett. 117 (2014) 270.

[BOUZ2003] Bouzerar G, Kudrnovsky J, Bergqvist L, Bruno P, Phys. Rev. B 68 (2003) 081203(R).

[BRUM2001] Brumage W. H, Dorman C. F, Quade C. R, Phys. Rev. B 63 (2001) 104411.

[BRUN1992] Brundle C. R, Charles J, Evans A, Wihon S, Encyclopedia of material Characterization: surface, interfaces, thin films (1992).

[CALL1977] Calleja J. M, Cardona M, Phys. Rev. B 16 (1977) 3753.

[CAZZ2003] Cazzanelli E, Kuzmin A, Mariotto G, Ulmane N. M, J. Phys. Condens. Matter. 15 (2003) 2045.

[CHAN2007] Chang Y. H, Park C. H, Sato K, Katayama-Yoshida H, Phys. Rev. B 76 (2007) 125211.

[CHEN1995] Chen Y. F, Chou W. C, Twardowski A, Solid state commun. 96 (1995) 865.

[CHEN2007] Chen X, Mao S. S, Chem. Rev. 107 (2007) 2891.

[CHEN2010] Chen J, Conache G, Pistol M. E, Gray S. M, Borgstrom M. T, Xu H, Xu H. Q, Samuelson L, Håkanson U, Nano Lett. 10 (2010) 1280.

[CHEN2013] Chen X, Liu L, Liu Z, Marcus M. A, Wang W. C, Oyler N. A, Grass M. E, Mao B, Glans P. A, Yu P. Y, Guo J, Mao S. S, Scientific Reports 3 (2013) 1510.

[CHEN2017] Chen X, Cui Y, Black TiO_2 Nanomaterials for Energy Applications, World Scientific Publishing Europe Ltd (2017).

[CHOI2015] Choi Y. I, Jung H. J, Shin W. G, Sohn Y, Appl. Surf. Sci. 356 (2015) 615.

[CHOU2011] Choudhury B, Choudhury A, Maidul Islam A. K. M, Alagarsamy P, Mukherjee M, J. Magn. Magn. Mater. 323 (2011) 440.

[COEY2004] Coey J. M. D, Douvails A. P, Fitzgerald C. B, Venkatesan M, Appl. Phys. Lett. 84 (2004) 1332.

[COEY2010] Coey J. M. D, Magnetism and Magnetic Materials, Cambridge university press, Cambridge (2010).

[COPP2013] Copper J. F. K, Lonescu A, Langford R. M, Ziebeck K. R. A, C. H. W. Barnes, Gruar R, Tighe C, Darr J. A, Thanh N. T. K, Ouladdiaf B, J. Appl. Phys. 114 (2013) 083906.

[COST1999] Costa T. M. H, Gallas M. R, Benvenutti E. V, Jornada J. A. H, J. Phys. Chem. B103 (1999) 4278.

[CULL2001] Cullity B. D, Stock S. R, Elements of X-ray diffraction, 3rd Ed., Pearson Education, Boston (2001).

[CUSC2007] Cuscó R, Alarcón-Lladó E, Ibáñez J, Artús L, Jiménez J, Wang B. G, Callahan M. J, Phys. Rev. B 75 (2007) 165202.

[DART2008] Darton N. J, Sederman A. J, Ionescu A, Ducati C, Darton R. C, Gladden L. F, Slater K. H, Nanotechnology 19 (2008) 395102.

[DASK2009] Das K, Sharma S. N, Kumar M, De S. K, J. Phys. Chem. C 113 (2009) 14783.

[DAUD1997] Daude N, Gout C, Jouanin C, Phy. Rev. B 15 (1997) 3229.

[DAVI2000] Davis J. R, Nickel, Cobalt and Their Alloys, ASM International, USA (2000).

[DEBI2002] De Biasi E, Ramos C. A, Zysler R. D, Romero H, Phys. Rev. B 65 (2002) 144416.

[DELB2008] del Bianco L, Boscherini F, Fiorini A. L, Tamisari M, Spizzo F, Antisari M. V, Piscopiello E, Phys. Rev. B 77 (2008) 094408.

[DIAZ1997] Diaz-Guerra C, Remon A, Garcia J. A, Piqueras J, Phys. Stat. Sol. (a) 163 (1997) 497.

[DIEB1996] Diebold U, Madey T. E, Surf. Sci. Spectra 4 (1996) 227.

[DIEP2004] Diep H. T, Frustrated spin system, Chapter1, World Scientific (2004).

[DIET1997] Dietl T, Haury A, d'Aubigne Y. M, Phys. Rev. B 55 (1997) R33447(R).

[DIET2000] Dietl T, Ohno H, Matsukura F, Cibert J, Ferrand D, Science 287 (2000) 1019.

[DING2001] Ding J, Li Y, Chen L. F, Deng C.R, Shi Y, Chow Y. S, Gang T. B, J. Alloys Compd. 314 (2001) 262.

[DING2014] Ding Y, Xiao B, Comp. Mat. Sci. 82 (2014) 202.

[DJUR2007] Djurisic A. B, Leung Y. H, Tam K. H, Hsu Y. F, Ding L, Ge W. K, Zhong Y. C, Wong K. S, Chan W. K, Tam H. L, Cheah K. W, Kwok W. M, Phillips D. L, Nanotechnology 18 (2007) 095702.

[DOBR2005] Dobrynin A. N, Levlev D. N, Temst K, Lievens P, Margueritat J, Gonzalo J, Afonso C. N, Zhou S. Q, Vantomme A, Piscopiello E, Van Tendeloo G, Appl. Phys. Lett. 87 (2005) 012501.

[DOOL1994] Dooley K. M, Chen S. Y, Ross J. R. H, J. Catalysis, 145 (1994) 402.

[DORM1997] Dormann J. L, Fiorani D, Tronc E, Adv. Chem. Phys. 98 (1997) 283.

[DUAN2012] Duan W. J, Lu S. H, Wu Z. L, Wang Y. S, J. Phys. Chem. C 116 (2012) 26043.

[DUOL2010] Duo L, Finazzi M, Ciccacci F, Magnetic Properties of Antiferromagnetic Oxide Materials: surfaces, interfaces and thin films, Wiley-VCH Verlag GmbH & Co, Weinheim (2010).

[DZYA1958] Dzyaloshinsky I, J. Phys. Chem. Solids 4 (1958) 241.

[EKUM2011] Ekuma C. E, Bagayoko D, Japn. J. Appl. Phys. 50 (2011) 101103.

[ELIL2012] Elilarassi R, Chadrasekaran G, Optoelect. Lett. 8 (2012) 0109.

[ESCU2011] Escudero R, Escamilla R, Solid State Comm. 151 (2011) 97.

[ETOT2000] Eto T, Endo S, Imai M, Katayama Y, Kikegawa T, Phys. Rev. B 61 (2000) 14984.

[FERN2004] Fernández-García M, Martínez-Arias A, Hanson J. C, Rodriguez J. A, Chem. Rev. 104 (2004) 4063.

[FEYG2010] Feygenson M, Kou A, Kreno L. E, Tiano A. L, Patete J. M, Zhang F, Kim M. S, Solovyov V, Wong S. S, Aronson M. C, Phys. Rev. B 81 (2010) 014420.

[FINA2009] Finazzi E, Valentin C. D, Pacchioni G, The J. Phys. Chemistry C 113 (2009) 3382.

[FIOR2005] Fiorani D, Surface effects in magnetic nanoparticles, New York, XIV USA: Springer (2005) 300.

[FURD1988] Furdyna J. K, J. Appl. Phys. 64 (1988) R29.

[GAND2011] Gandhi A. C, Huang C. Y, Yang C. C, Chan T. S, Cheng C. L, Ma Y. R, Wu S. Y, Nanoscale Res. Lett. 6 (2011) 485.

[GAOD2009] Gao D, Zhang Z, Fu J, Xu Y, Qi J, Xue D, J. Appl. Phys. 105 (2009) 113928.

[GAOD2011] Gao D, Yang Z, Zhang J, Yang G, Zhu Z, Qi J, Si M, Xue D, AIP Advances 1 (2011) 042168.

[GARC2002] Garces N. Y, Wang L, Bai L, Giles N. C, Halliburton L. E, Cantwell G, Appl. Phys. Lett. 81 (2002) 622.

[GEOR2012] Georgescu D, Baia L, Ersen O, Baia M, Simon S, J. Raman Spectrosc. 43 (2012) 876.

[GHOS2006] Ghosh M, Biswas K, Sundaresana A, Rao C. N. R, J. Mater. Chem. 16 (2006) 106.

[GHOS2011] Ghosh S, Khan G. G, Das B, Mandal K, J. Appl. Phys. 109 (2011) 123927.

[GHOS2013] Ghose S, Sarkar A, Chattopadhyay S, Chakrabarti M, Das D, Rakshit T, Ray S. K, Jana D, J. Appl. Phys. 114 (2013) 073516.

[GING1994] Gingras M. J. P, Magnetic system with competing interaction, H. T. Diep (Edts.), World scientific publishers, Singapore (1994) 238.

[GOGU2014] Gogurla N, Sinha A. K, Santra S, Manna S, Ray S. K, Sci. Rep. 4 (2014) 6483.

[GOND2012] Gondal M. A, Saleh T. A, Drmosh Q. A, Appl. Surf. Sci. 258 (2012) 6982.

[GONG2014] Gong J, Liu J, Chen X, Jiang Z, Wen X, Mijowska E, Tang T, RSC Adv. 4 (2014) 33806.

[GOOD1995] Goodenough J. B, Phys. Rev. 100 (1995) 564.

[GOPI2008] Gopinadhan K, Kashyap S.C, Pandya D. K, Chaudhary S, J. Phys.: Condens. Matter 20 (2008) 125208.

[GORR2009] Gorria P, Martínez-Blanco D, Pérez M. J, Blanco J. A, Hernando A, Laguna-Marco M. A, Haskel D, Souza-Neto N, Ronald I. Smith, William G. Marshall, Garbarino G, Mezouar M, Fernández-Martínez A, Chaboy J, Fernandez Barquín L, Rodriguez Castrillón J. A, Moldovan M, García Alonso J I, Zhang J, Llobet A, Jiang J. S, Phys. Rev. B 80 (2009) 064421.

[GORS1994] Gorschluter A, Merz H, Phys. Rev. B 49 (1994) 17293.

[GRAB2017] Grabowskaa E, Diak M, Klimczuk T, Lisowski W, Medynska A. Z, Mol. Cat. 434 (2017) 154.

[GRIF2008] Griffin R. K, Varela M, Rashkeev S, Pantelides S. T, Pennycook S. J, Krishnan K. M, Phys. Rev. B 78 (2008) 014409.

[GROS2006] Grosvenor A. P, Biesinger M. C, Smart R. C. St, McIntyre N. S, Surf. Sci. 600 (2006) 1771.

[GRUY2009] Gruyters M, Phys. Rev. B 79 (2009) 134415.

[GUIM1998] Guimaraes A. P, Magnetism and Magnetic Resonance in Solids, Oliveira I. S, John Wiley and Sons, New York (1998).

[HAAS2012] Haase C, Nowak U, Phys. Rev. B 85 (2012) 045435.

[HEIS1928] Heisenberg V.W, für. Z. Phys. 49 (1928) 619.

[HEJ2005] He J, Xu S, Yoo Y. K, Xue Q, Lee H. C, Cheng S, Xiang X. D, Dionne G. F, Takeuchi I, Appl. Phys. Lett. 86 (2005) 052503.

[HEJH2008] He J. H, Yuan S. L, Tian Z. M, Yin Y. S, Li P, Wang Y. Q, Liu K. L,Yuan S. J, Wang X. L, Liu L, J. Magn. Magn. Mater. 320 (2008) 3293.

[HERN2009] Herng T. S, Lau S. P, Wei C. S, Wang L, Zhao B. C, Tanemura M, Akaike Y, Appl. Phys. Lett. 95 (2009) 133103.

[HIRA2003] Hirano M, Nakahara N, Ota K, Tanaike O, Inagaki N, J. Solid State Chem 170 (2003) 39.

[HOAN2013] Hoa N. T. Q, Huyen D. N, J. Mat. Sci: Mats Elect. 24 (2013) 793.

[HOCH2006] Ho C. H, Lai C. H, IEEE Trans. Magn. 42 (2006) 3069.

[HONG2004] Hong N. H, Sakai J, Prellier W, J. Magn. Magn. Mater. 281 (2004) 347.

[HONG2006] Hong N. H, Sakai J, Poirot N, Brize V, Phys. Rev. B 73 (2006) 132404.

[HONG2007] Hong N. H, Sakai J, Brize V, J. Phys.: Condens. Matter 19 (2007) 036219.

[HORS2006] Horst C, Saito T, Smith L, Handbook of materials measurements methods, Springer, Berlin (2006).

[HOSO2012] Hosokawa M, Naito M, Nogi K, Yokoyama T, Nanoparticle Technology Handbook, 2nd Edition, Elsevier, UK (2012).

[HOTO2000] Hotový I, Huran J, Spiess L, Čapkovic R, Š. Haščík, Vacuum 58 (2000) 300.

[HOWA1991] Howard C. J, Sabine T. M, Dickson F, Acta Cryst. B 47 (1991) 462.

[HUAN1985] Huang C. Y, J. Magn. Magn. Mater. 51 (1985) 1.

[HUJ2015] Hu J, Zhong Z, Zhang F, Xing W, Low Z. X, Fan Y, Ceramics Inter. 41 (2015) 7080.

[HULL2001] Hull D, Bacon D. J, Introduction to Dislocations, 4th Ed., Pergamon Press, Oxford (2001).

[HUY2008] Hu Y, Chen H. J, J. Nanopart. Res. 10 (2008) 401.

[ICHI2003] Ichiyanagi Y, Wakabayashi N, Yamazaki J, Yamada S, Kimishima Y, Komatsu E, Tajima H, Physica B 329-333 (2003) 862.

[IRWI2008] Irwin M. D, Buchholz D. B, Hains A.W, Chang R. P. H, Marks T. J, Proc Natl Acad. Sci. USA 105 (2008) 2783.

[ISCH2005] Ischenko V, Polarz S, Grote D, Stavarache V, Fink K, Driiess M, Adv. Funct. Mater. 15 (2005) 1945.

[ITAN2012] Itani H, Duchoslav J, Arndt M, Steck T, Gerdenitsch J, Faderl J, Preis K, Winkler W, Stifter D, Anal. Bioanal. Chem. 403 (2012) 663.

[JAGO2009] Jagodic M, Jaglicic Z, Jelen A, Lee J. B, Kim Y. M, Kim H. J, Dolinsek J, J. Phys.: Condens. Matter. 21 (2009) 215302.

[JAME2001] Jamet M, Wernsdorfer W, Thirion C, Mailly D, Dupuis V, Melinon P, Perez A, Phys. Rev. Lett. 86 (2001) 4676.

[JANG2009] Jang W. L, Lu Y. M, Hwang W. S, Hsiung T. L, Wang H. P, Appl. Phys. Lett. 94 (2009) 062103.

[JANO2007] Janotti A, de Walle C. G. V, Phys. Rev. B 76 (2007) 165202.

[JANO2009] Janotti A, de Walle C. G. V, Rep. Prog. Phys. 72 (2009) 126501.

[JANS2004] Jan Svoboda, Magnetic Techniques for the Treatment of Materials, Kluwer Academic Publishers, Dordrecht (2004).

[JAME2004] Jamet M, Wernsdorfer W, Thirion C, Dupuis V, Mélinon P, Pérez L, Mailly D, Phys. Rev. B 69 (2004) 024401.

[JIAN2002] Jiang S. R, Yan P. X, Feng B. X, Cai X. M, Wang J, Mater. Chem. Phys. 77 (2002) 384.

[JILE1997] Jiles. D, Introduction to Magnetism and Magnetic Materials, Chapman and Hall, Boca Raton (1997).

[JING2006] Jing L, Xin B, Yuan F, Xue L, Wang B, Fu H, The J. Phys. Chem. B 110 (2006) 17860.

[JING2015] Jing M. J, Wang C. W, Hou H. S, Wu Z. B, Zhu Y. R, Yang Y. C, Jia X. N, Zhang Y, Ji X. B, J. Power Sources 298 (2015) 241.

[JOHN2010] Johnson L. M, Thurber A, Anghel J, Sabetian M, Engelhard M. H, Tenne D. A, Hanna C. B, Punnoose A, Phys. Rev. B 82 (2010) 054419.

[JUND2006] Jundwirth T, Sinova J, Masek J, Kucera J, MacDeonald A. H, Rev. Mod. Phys. 78 (2006) 809.

[KAKA1997] Kakazey N. G, Sreckovic T. V, Ristic M. M, J. Mater. Sci., 32 (1997) 4619.

[KALI2008] Kalita M.P.C, Perumal A, Srinivasan A, J. Magn. Magn. Mater. 320 (2008) 2780.

[KANA1959] Kanamori J, J. Phys. Chem Solids 10 (1959) 87.

[KAPI2009] Kapilashrami M, Xu J, Strom V, Rao K. V, Belova L, Appl. Phys. Lett. 95 (2009) 033104.

[KART2011] Karthik K, Selvan G. K, Kanagaraj M, Arumugam S, Jaya N. V, J. Alloys. Compd. 509 (2011) 181.

[KASU1956] Kasuya T, Prog. Thror. Phys. 16 (1956) 58.

[KAVA1996] Kavan L, Grätzel M, Gilbert S. E, Klemenz C, Scheel H. J, J. American Chem. Soc. 118 (1996) 6716.

[KAYA1988] Kayanuma Y, Phy. Rev. B 38 (1988) 9797.

[KEFF1957] Keffer F, O'Sullivan W, Phys. Rev 108 (1957) 637.

[KELL1997] Kelly S, Pollak F. H, Tomkiewicz M, J. Phys. Chem. B 101 (1997) 2730.

[KENN1987] Kenning G. G, Slaughter J. M, Cowen J. A, Phys. Rev. Lett. 59 (1987) 2596.

[KHAD2003] Khadar M. A, Biju V, Inoue A, Mater. Res. Bull. 38 (2003) 1341.

[KHAI2012] Khairya M, El-Safty S. A, Ismaela M, Kawarada H, Applied Catalysis B: Environmental 127 (2012) 1.

[KHAN2014] Khan M, Wei C, Chen M, Tao J, Huang N, Qi Z, Li L, J. Alloys Comp. 612 (2014) 306.

[KHAT2012] Khataee A, Mansoori G. A, Nanostructured titanium dioxide materials: properties, preparation and applications, World scientific, Singapore (2012).

[KHEM2011] Khemprasit J, Kaen-Ngam S, Khumpaitool B, Kamkhou P, J. Magn. Magn. Mater. 323 (2011) 2408.

[KIMD2004] Kim D. H, Hong H. S, Kim S. J, Song J. S, Lee K. S, J. Alloys Comp. 375 (2004) 259.

[KIMD2009] Kim D, Hong J, Park Y. R, Kim K. J, J. Phys.: Condens. Matter 21 (2009) 195405.

[KIMJ2003] Kim J. Y, Park J. H, Park B. G, Noh H. J, Oh S. J, Yang J. S, Kim D. H, Bu S. D, Noh T. W, Lin H. J, Hsieh H. H, Chen C. T, Phys. Rev. Lett. 90 (2003) 017401.

[KISA2013] Kisan B, Shyni P. C, Layek S, Verma H. C, Hesp D, Dhanak V, Krishnamurthy S, Perumal A, IEEE Trans. Magn. 50 (2013) 2300704.

[KITA2010] Kita E, Oda T, Kayano T, Sato S, Minagawa M, Yanagihara H, Kishimoto M, Mitsumata C, Hashimoto S, Yamada K, Ohkohchi N, J. Phys. D: Appl. Phys. 43 (2010) 474011.

[KITT2004] Kittel C, Introduction to Solid state Physics, 7th edn Wiley, Singapore (2004).

[KOCH2002] Koch C. C, Nanostructured materials: Processing, properties and potential applications, Noyes Publications, New York (2002).

[KOCH2006] Koch C. C, Mechanical Milling and Alloying, Wiley-VCH Verlag (2006).

[KODA1997] Kodama R. H, Makhlouf S. A, Berkowitz A. E, Phys. Rev. Lett. 79 (1997) 1393.

[KODA19991] Kodama R. H, Berkowitz A. E, Phys. Rev. B 59 (1999) 6321.

[KODA19992] Kodama R. H, J. Magn. Magn. Mater. 200 (1999) 359.

[KOHA2000] Kohan A. F, Ceder G, Morgan D, de Walle C. G. V, Phys. Rev. B 61 (2000) 15019.

[KRAM1934] Kramers H.A, Physica 1 (1934) 182.

[KRON2003] Kronmuller H, Fahnle M, Micromagnetism and the Microstructure of Ferromagnetic Solids, Cambridge University Press, New York (2003).

[KUDR2004] Kudrnovsky J, Turek L, Drchal V, Maca F, Weiberger P, Bruno P, Phys. Rev. B 69 (2004) 115208.

[KURI2014] Kuriakose S, Choudhary V, Satpati B, Mohapatra S, Phys. Chem. Chem. Phys. 16 (2014) 17560.

[LABA2005] Labarta A, Batle X, Iglesias O, Surface Effects in Magnetic Nanoparticles; Fiorani, D, (Edts.) Springer: Berlin/Heidelberg, Germany (2005) 105.

[LAGU2005] Laguta V. V, Slipenyuk A. M, Bykov I. P, Glinchuk M. D, Appl. Phys. Lett. 87 (2005) 022903.

[LEEH2012] Lee H. Y, Clark S. J, Robertson J, Phys. Rev. B 86 (2012) 075209.

[LEES2010] Lee S, Shon Y, Kim D. Y, Kang T. W, Yoon C. S, Appl. Phys. Lett. 96 (2010) 042115.

[LEGE1972] Leger J. M, Susse C. L, Vodar B, Phys. Rev. B 6 (1972) 4250.

[LEGE2011] Legendre B, Sghaier M, J. Thermal Analys. Calori. 105 (2011) 141.

[LEWI2001] Lewis R I, Edwards H. G. M, Handbook of Raman Spectroscopy: From the Research Laboratory to the Process Line, Chap. 12, New York (2001) 491.

[LIM2000] Li M, Hebenstreit W, Diebold U, Tyryshkin A. M, Bowman M. K, Dunham G. G, Hendersan M. A, J. Chem. Phys. B 104 (2000) 4944.

[LIBA2005] Li Bassi A, Cattaneo D, Russo V, Bottani C. E, Barborini E, Mazza T, Piseri P, Milani P, Ernst F. O, Wegner K, Pratsinis S. E, J. Appl. Phys. 98 (2005) 074305.

[LID2010] Li D, Chang P. C, Chien C. J, Lu J. G, Chem. Mater. 22 (2010) 5707.

[LIH2012] Li H, Zeng Y, Huang T, Liu M, J. Nanoparticle Res. 14 (2012) 1.

[LIL2006] Li L, Chen L, Qihe R, Li G, Appl. Phys. Lett. 89 (2006) 134102.

[LINB2001] Lin B, Fu Z, Jia Y, Appl. Phys. Lett. 79 (2001) 943.

[LINY20061] Lin Y. H, Wang J, Cai J, Ying M, Zhao R, Li M, Nan C. W, Phys. Rev. B 73 (2006) 193308.

[LINY20062] Lin Y. H, Zhao R, Nan C. W, Ying M, Kobayashi M, Ooki Y, Fujimori A, Appl. Phys. Lett. 89 (2006) 202501.

[LIUC2005] Liu C, Yun F, Mokoc H, J. Mater. Sci.: Mater. Electron.16 (2005) 555.

[LIX2007] Li X, Xia C, Pei G, He X, J. Phys. Chem. Solids 68 (2007) 1836.

[LIX2014] Li X, Zheng W, He G, Zhao R, Liu D, ACS Sustain. Chem. Engg. 2 (2014) 288.

[LIUC2016] Liu C, Li C, Ahmed K, Mutlu Z, Ozkan C. S, Ozkan M, Sci. Rep. 6 (2016) 29183.

[LIUJ2009] Liu J, Lee S, Ahn Y. H, Park J. Y, Koh K. H, J. Phys. D: Appl. Phys. 42 (2009) 095401.

[LIUH2005] Liu H. X., Stephen Y. Wu, Singh R. K., Newman N, J. Appl. Phys. 98 (2005) 046106.

[LIUH2008] Liu H, Yang J, Zhang Y, Wang Y, Wei M, Mater. Chem. Phys. 112 (2008) 1021.

[LIUX20081] Liu X. H, Cui W. B, Lv X. K, Liu W, Zhao X. G, Li D, Zhang Z. D, J. Appl. Phys. 103 (2008) 103906.

[LIUX20082] Liu X. C, Shi E. W,Chen Z. Z, Zhang T, Zhang Y, Chen B. Y, Huang W, Liu X, Song L. X, Zhou K. J, Cui M. Q, Appl. Phys. Lett. 92 (2008) 042502.

[LIUX2010] Liu X. H, Liu W, Lv X. K, Yang F, Wei X, Zhang Z. D, Sellmyer D. J, J. Appl. Phys. 107 (2010) 083919.

[LIUX2013] Liu X, Gao S, Xu H, Lou Z, Wang W, Huang B, Dai Y, Nanoscale 5 (2013) 1870.

[LLAN2010] Llandro J, Palfreyman J. J, Ionescu A, Barnes C. H. W, Med. Biol. Eng. Comput. 48 (2010) 977.

[LUIS2002] Luis F, Torres J. M, Garcaí L. M, Bartolomé J, Stankiewicz J, Petroff F, Fettar F, Maurice J. L, Vaurès A, Phys. Rev. B 65 (2002) 094409.

[LUML2011] Lu M. L, Lin T. Y, Weng T. M, Chen Y. F, Opt. Express 19 (2011) 16266.

[LUOW1991] Luo W, Nagel S. R, Rosenbaum T. F, Rosensweig R. E, Phys. Rev. Lett. 67 (1991) 2721.

[LUOX2015] Luo X, Tseng L. T, Li S, Yi J. B, Mater. Sci. Semicond Proc. 30 (2015) 228.

[LUOY2012] Luo Y. D, Lin Y. H, Feng Y. N, Zhang Y. J, Yu Song, Shen Y, Wen C, J. Appl. Phys. 112 (2012) 116101.

[LYUK2010] Lyu K. K, Phan T. L, Yu S. C, Oh S. K, Dan N. H, IEEE Trans. Magn. 46 (2010) 2028.

[MAEN2009] Maeng J, Heo S, Jo G, Choe S, Kim M, Hwang H, Lee T, Nanotechnology 20 (2009) 095203.

[MAKH1997] Makhlouf S. A, Parker F. T, Spada F. E, Berkowitz A. E, J. Appl. Phys. 81 (1997) 5561.

[MAKH2002] Makhlouf S. A, J. Magn. Magn. Mater. 246 (2002) 184.

[MAKH2008] Makhlouf S. A, Al-Attar H, Kodama R. H, Sol. State Commun. 145 (2008) 1.

[MAKO2009] Makovec D, Kodre A, Arčon I, Drofenik M, J. Nanoparticle Res., 11(2009) 1145.

[MAND2009] Mandal S, Banerjee S, Menon K. S. R, Phys. Rev. B 80 (2009) 214420.

[MAND2011] Mandal S, Menon K. S. R, Mahatha S. K, Banerjee S, Appl. Phys. Lett. 99 (2011) 232507.

[MANN2008] Manna S, Deb A. K, Jagannath J, De S. K, J. Phys. Chem. C 112 (2008) 10659.

[MART1998] Martinez B, Obradors X, Balcells L, Rouanet A, Monty C, Phys. Rev. Lett. 80 (1998) 181.

[MATS2001] Matsumoto Y, Murakami M, Shono T, Hasegawa T, Fukumura T, Kawasaki M, Ahmet P, Chikyow T, Koshihara S, Koinuma H, Science 291(2001) 854.

[MCCA1998] McCafferty E, Wightman J. P, Surf. Interface. Anal. 26 (1998) 549.

[MEAD1997] Mead D. G, Willkinson G. R, J. Raman Spec. 6 (1997) 123.

[MELO2016] Melo A. H. N, Macedo M. A, PloS one 11 (2016) e0168515.

[MENE2010] Meneses C. T, Duque J. G. S, de Biasi E, Nunes W. C, Sharma S. K, Knobel M, J. Appl. Phys. 108 (2010) 013909.

[MEUL2004] Meulenberg R. W, Jennings T, Strouse G. F, Phys. Rev. B 70 (2004) 235311.

[MHAD2010] Mhadhbi M, Khitouni M, Escoda L, Sunol J. J, Mater. Lett. 64 (2010) 1802.

[MILL1997] Miller E. L, Rocheleau R. E, J. Electron Soc. 144 (1997) 3072.

[MISH2004] Mishra S. R, Losby J, Dubenko I, Roy S, Ali N, Marasinghe K, J. Magn. Magn. Mater. 279 (2004) 111.

[MISH2017] Mishra A. K, Sol-gel based nanoceramic materials: preparation, properties and applications, Springer Nature, Switzerland (2017).

[MOHA2012] Mohanty P, Mishra N. C, Choudhary R. J, Banerjee A, Shripathi T, Lalla N. P, Annapoorni S, Chandana R, J. Phy. D: Appl. Phys 45 (2012) 325301.

[MONT2016] Montes N. R, Gorria P, Blanco D. M, Fuertes A. B, Orench I. P, Olivi L, Blanco J. A, AIP Advances 6 (2016) 056104.

[MORG20101] Morgan B. J, Watson G. W, The J. Phy. Chem. C 114 (2010) 2321.

[MORG20102] Morgan S. M, Victora R. H, Appl. Phys. Lett. 97 (2010) 093705.

[MORI1960] Moriya T, Phys. Rev. 120 (1960) 91.

[MORU2013] Mørup S, Brok E, Frandsen C, J. Nanomaterials 720629 (2013) 1.

[MOSS2011] Mossanek R. J. O, Preda I, Abbate M, Rubio-Zuazo J, Castro G. R, Vollmer A, Gutierrez A, Soriano L, Chem. Phys. Lett. 501 (2011) 437.

[MOUL1995] Moulder J. F, Stickle W. F, Sobol P. E, Bomben K. D, in Handbook of X-Ray Photoelectron Spectroscopy 89, J. Chastain, R. C. Kings (Eds.), Jr. Physical Electronics, Eden Prairie, MN (1995).

[MYDO1993] Mydosh J. A, spin glasses: an experimental introduction, Taylore and Francies Pub., London (1993).

[NADO2002] Nadolny A. J, Sadowski J, Taliashvili B, Areiszewska M, Dobrowolski W, Domukhovski V, Lusakowska E, Myeielski A, Osinniy V, Story T, Swiatek K, Galazka, Diduszko R, J. Mag. Magn. Mater. 248 (2002) 134.

[NAGA1979] Nagata S, Keesom P. H, Harrison H. R, Phys. Rev. B 19 (1979) 1633.

[NAGA1980] Nagata S, Galazka R. R, Mollin D. P, Akbarzadeh H, Khattak G. D, Furdyna J. K, Keesom P. H, Phys. Rev. B. 22 (1980) 3331.

[NAGA2010] Nagare B. J, Chacko S, Kanhere D. G, J. Phys. Chem. A 114 (2010) 2689.

[NAGA2017] Nagar S, Chakrabarti S, Optimization of ZnO thin films, Springer Singapore (2017).

[NAPH2006] Na-Phattalung S, Smith M. F, Kim K, Du M. H, Wei S. H, Zhang S. B, Limpijumnong S, Phys. Rev. B 73 (2006) 125205.

[NARL2005] Narlikar A. V, Frontiers in Magnetic Materials, Springer, New York (2005).

[NEAL1994] Neal H. B, Theory of Magnetic Recording, Cambridge University Press, New York (1994).

[NEEL1962] Néel L in: C. Dewitt, B. Dreyfus, P. D. de Gennes (Eds.), Low Temperature Physics, Gordon and Breach, New York (1962) 413.

[NIAS2012] Niasari M. S, Entesari M, Polyhedron 33 (2012) 302.

[NIBA2003] Nibarger J. P, Lopusnik R, Celinski Z, Silva T, J. Appl. Phys. Lett. 83 (2003) 93.

[NUNE1998] Nunes A. C, Yang L, Surf. Sci. 399 (1998) 225.

[OGAL2003] Ogale S. B, Choudhary R. J, Buban J. P, Lofland S. E, Shinde S. R, Kale S. N, Kulkarni V. N, Higgins J, Lanci C, Simpson J. R, Browning N. D, Sarma S. D, Drew H. D, Greene R. L, Venkatesan T, Phys. Rev. Lett. 91 (2003) 077205.

[OHAN2000] O'Handley R. C, Modern Magnetic Materials Principles and Applications, Wiley, New York (2000).

[OHNO1998] Ohno H, Science 281 (1998) 951.

[OHNO2000] Ohno H, Chiba D, Matsukura F, Omiya T, Abe E, Dietl T, Ohno Y, Ohtani K, Nature 408 (2000) 944.

[OHSA1978] Ohsaka T, Izumi F, Fujiki Y, J. Raman Spec. 7 (1978) 321.

[OHSA1980] Ohsaka T, J. Phys. Soc. Jpn. 48 (1980) 1661.

[OIWA2002] Oiwa A, Mitsumori Y, Moriya R, Slupinski T, Munekata H, Phys. Rev. Lett. 88 (2002) 137202.

[OTHM2012] Othman S. H, Rashid S. A, Ghazi T. I. M, Abdullah N, J. NanoMat. 2012 (2012) 718214.

[OULD2014] Ould-Hamouda A, Tokoro H, Ohkoshi S. I, Freysz E, Chem. Phys. Lett. 608 (2014) 106.

[OZGU2005] Özgür U, Alivov Y. I, Liu C, Teke A, Reshchikov M. A, Dogan S, Avrutin V, Cho S. J, Morkoç H, J. Appl. Phys. 98 (2005) 041301.

[PANX2013] Pan X, Yang M. Q, Fu X, Zhang N, Xu Y. J, Nanoscale 5 (2013) 3601.

[PAND2011] Pandey S. K, Chouidhary R. J, J. Phys.: Condens. Matter, 23 (2011) 276005.

[PANK2009] Pankhurst Q. A, Thanh N. T. K, Jones S. K, Dobson J, J. Phys. D: Appl. Phys. 42 (2009) 224001.

[PARA2012] Parashar S. K. S, Murty B. S, Repp S, Weber S, Erdem E, J. Appl. Phys. 111 (2012) 113712.

[PARK2002] Park Y. D, Hanbicki A. T, Erwin S. C, Hellberg C. S, Sullivan J. M, Mattson J. E, Wilson A, Spanos G, Jonker B. T, Science 295 (2002) 651.

[PARR2013] Parras M, Varela A, Gill B. C, Boulahya K, Hernando A, Clabet J. M. G, J. Phys. Chem. Lett. 4 (2013) 2171.

[PASC1978] Pascual J, Camassel J, Mathieu H, Phys. Rev. B 18 (1978) 5606.

[PATE2011] Patel S. K. S, Gajbhiye N. S, Solid State Commun. 151 (2011) 1500.

[PATE2013] Patel S. K. S, Gajbhije N. S, J. Magn. Magn. Mater. 330 (2013) 21.

[PATR2014] Patrick C. E, Giustino F, Phys. Rev. Appl. 2 (2014) 014001.

[PAOL2013] Paola A. D, Bellardita M, Palmisano L, Catalysts 3 (2013) 36.

[PAUL2006] Paulose M, Shankar K, Varghese O. K, Mor G. K, Grimes C. A, J. Phys. D: Appl. Phys. 39 (2006) 2498.

[PEAR2003] Pearton S. J, Abernathy C. R, Norton D. P, Hebard A. F, Park Y. D, Boatner L. A, Budai J. D, Mat. Sci. Engg. R 40 (2003) 137.

[PECK2011] Peck M. A, Huh Y, Skomski R, Zhang R, Kharel P, Allison M. D, Sellmyer D. J, Langell M. A, J. Appl. Phys. 109 (2011) 07B518.

[PECK2012] Peck M.A, Langell M. A, Chem. Mater. 24 (2012) 4483.

[PENG2009] Peng H, Li J, Li S. S, Xia J. B, Phys. Rev. B 79 (2009) 092411.

[PENG2012] Peng C. X, Liang Y, Wang K, Zhang Y, Zhao G, Wang Y, J. Phys. Chem. C 116 (2012) 9709.

[PHAN2010] Phan T. L, Yu S. C, Vincent R, Bui H. M, Thanh T. D, Lam V. D, Lee Y. P, J. Appl. Phys. 108 (2010) 044910.

[PHAN2013] Phan T. L, Zhang Y. D, Yang D. S, Nghia N. X, Thanh T. D, Yu S. C, Appl. Phys. Lett. 102 (2013) 072408.

[PIER2003] Piera E, Tejedor M. I, Zorn M. E, Anderson M. A, Appl. Catal. B 46 (2003) 671.

[PIGE1980] Pigenet C, Fievet F, Phys. Rev. B 22 (1980) 2785.

[PODI2010] Podila R, Queen W, Nath A, Arantes J. T, Schoenhalz A. L, Fazzio A, Dalpian G. M, He J, Hwu S. J, Skove M. J, Rao A. M, Nano Lett. 10 (2010) 1383.

[POTZ2008] Potzger K, Shengqiang Z, Grenzer J, Helm M, Fassbender J, Appl. Phys. Lett. 92 (2008) 182504.

[PRED2008] Preda I, Gutiérrez A, Abbate M, Yubero F, Méndez J, Alvarez L, Soriano L, Phys. Rev. B 77 (2008) 075411.

[PROE2011] Proenca M. P, Sousa C. T, Pereira A. M, Tavares P. B, Ventura J, Vazquez M, Araujo J. P, Phys. Chem. Chem. Phys. 13 (2011) 9561.

[PUGA2013] Pugazhenthiran N, Murugesan S, Anandan S, J. Haz. Mater. 262 (2013) 541.

[PUNN2002] Punnoose A, Seehra M. S, J. Appl. Phys. 91 (2002) 7766.

[QIY2009] Qi Y, Qi H, Lu C, Yang Y, Zhao Y, J. Mater. Sci: Mater. Electron 20 (2009) 479.

[RADO2003] Radovanovicnad P. V, Gamelin D. R, Phys. Rev. Lett. 91 (2003) 157202.

[RAJA2016] Rajagopal Reddy V, Sekhar Reddy P. R, Neelakanta Reddy I, Choi C. J, RSC Adv. 6 (2016) 105761.

[RAMC2004] Ramchandran S, Tiwari A, Narayan J, Appl. Phys. Lett. 84 (2004) 5255.

[RAOG2005] Rao G. N, Yao Y. D, Chen J. W, IEEE Trans. Magn., 41 (2005) 3409.

[RASH2000] Rashba E. I, Phys. Rev. B 62 (2000) R16267.

[RATH2009] Rath C, Mohanty P, Pandey A. C, Mishra N. C, J. Phys. D: Appl. Phys. 42 (2009) 205101.

[RAUT2011] Raut B. T, Pawar S. G, Chougule M. A, Sen S, Patil V. B, J. Alloys. Compd. 509 (2011) 9065.

[REMA2008] Remashan K, Hwang D. K, Park S. J, Jang J. H, Jpn. J. Appl. Phys.47 (2008) 2848.

[RESP1998] Respaud M, Broto J. M, Rakoto H, Fert A. R, Thomas L, Barbara B, Verelst M, Snoeck E, Lecante P, Mosset A, Osuna J, Ely T. O, Amiens C, Chaudret B, Phys. Rev. B 57 (1998) 2925.

[REVE1996] Reves A, Ungar T, Borbely A, Lendvai J, Nano. Mat. 7 (1996) 779.

[RHYD2015] Rhydderch S, Howe R. F, Molecules 20 (2015) 4055.

[RICH1956] Richardson J. T, Milligan W. O, Phys. Rev. 102 (1956) 1289.

[RINA2014] Rinaldi-Montes N, Gorria P, Martınez-Blanco D, Fuertes A.B, Fern´andez Barquın L, Rodrıguez Fernandez J, de Pedro I, Fdez-Gubieda M. L, Alonso J, Olivi L, Aquilanti G, Blanco J. A, Nanoscale 6 (2014) 457.

[RISB2003] Risbud A. S, Spaldin N. A, Chen Z. Q, Stemmer S, Seshadri R, Phys. Rev. B 68 (2003) 205202.

[ROBE1984] Roberts M. W, Smart R. S. C, J. Chem. Soc., Faraday Trans. 1, 80 (1984) 2957.

[RODE2003] Rode K, Anane A, Mattana R, Contour J. P, Durand O, LeBourgeois R, Appl. Phys. 93 (2003) 7676.

[ROSA2007] Rosa E. De la, Sep'ulveda-Guzman S, Reeja-Jayan B, Torres A, Salas P, Elizondo N, Yacaman M. J, J. Phys. Chem. C 111 (2007) 8489.

[ROTH1958] Roth W. L, Phys. Rev. 110 (1958) 1333.

[ROYA2014] Roy A, De Toro J. A, Amaral V. S, Muniz P, Riveiro Ferreira J. M. F, J. Appl. Phys. 115 (2014) 073904.

[RUDE1954] Ruderman M. A, Kittel C, Phys. Rev. 96 (1954) 99.

[RUMA2007] Rumaiz A. K, Ali B, Ceylon A, Boggs M, Beebe T, Shah S. I, Solid State Commun. 144 (2007) 334.

[RUNG2010] Rungsawang R, da Silva J, Wu C. P, Sivaniah E, Ionescu A, Barnes C. H. W, Darton N. J, Phys. Rev. Lett., 104 (2010) 255703.

[SAEK2001] Saeki H, Tabata H, Kawai T, Solid State Commun.120 (2001) 439.

[SAHO2009] Sahoo S, Arora A. K, Sridharan V, J. Phys. Chem. C 113 (2009) 16927.

[SAIT2003] Saito H, Zayets V, Yamagata S, Ando K, Phys. Rev.Lett 90 (2003) 207202.

[SAMA2006] Samanta K, Bhattacharya P, Katiyar R. S, Iwamoto W, Pagliuso P. G, Rettori C, Phys. Rev. B 73 (2006) 245213.

[SAMS2015] Samsudin E. M, Hamid S. B. A, Juan J. C, Basirun W. J, Kandjani A. E, Appl. Surf. Sci. 359 (2015) 883.

[SANC1972] Sancier K. M, J. Phys. Chem. 76 (1972) 2527.

[SANY2008] Sanyal D, Roy T. K, Chakrabarti M, Dechoudhury S, Bhowmick D, Chakrabarti A. J. Phys.: Condens. Matter. 20 (2008) 045217.

[SANZ1996] Sanz J. M, Tyuliev G. T, Surf. Sci. 367 (1996) 196.

[SATO2015] Sato K, Saitoh E, Spintronics for next generation innovative devices, Wiley Series in materials for electronic & optoelectronic applications, Willoughby A, Capper P, Kasap S (Edts). Wiley, UK (2015).

[SAVI2012] Savio A. K. P. D, Starikov D, Bensaoula A, Pillai R, L. L. de la T. Garcia, Hernandez F. C. R, Ceramics Inten. 38 (2012) 3529.

[SCAN2013] Scanlon D. O, Dunnill C. W, Buckeridge J, Shevlin S. A, Logsdail A. J, Woodley S. M, Catlow C. R. A, Powell M. J, Palgrave R. G, Parkin I. P,

Watson G. W, Keal W, Sherwood P, Walsh A, Sokol A. A, Nat. Mater. 12 (2013) 798.

[SCHA2016] Schapers T, Semiconductor spintronics, Walter de Gruyter GmbH & Co KG, Germany (2016).

[SCHW20041] Schwartz D. A, Gamelin D. R, Adv. Mater. 16 (2004) 2115.

[SCHW20042] Schwartz D.A, Kevin R. Kittilstved, Daniel R. G, Appl. Phys. Lett. 85 (2004) 1395.

[SEBE2003] Seber G. A, Wild C. J, Nonlinear Regression, John Wiler & Sons (2003).

[SEEH2005] Seehra M. S, Shim H, Dutta P, Manivannan A, Bonevich J, J. Appl. Phys. 97 (2005) 10J509.

[SEEH2007] Seehra M. S, Dutta P, Singh V, Zhang Y, Wender I, J. Appl. Phys. 101 (2007) 09H107.

[SEEP2006] Seepanovie M. J, Grujie-Brojcin M. U, Dohcevie-Mitrovie Z. D, Popovie Z. V, Mater. Sci. Forum. 518 (2006) 101.

[SEPE2012] Sepelak V, Begin-Colin S, Le Caer G, Dalton Trans. 41 (2012) 11927.

[SHAR2003] Sharma P, Gupta A, Rao K. V, Owens F. J, Sharma R, Ahuja R, Guillen J. M. O, Johansson B, Gehring G. A, Nat. Mater. 2 (2003) 673.

[SHEN2005] Shen T. D, Schwarz R. B, Thompson J. D, Phys. Rev. B 72 (2005) 014431.

[SHER1975] Sherrington D, Kirkpatrick S, Phys. Rev. Lett. 35 (1975) 1792.

[SHER1978] Sherrington D, J. Phys. A: Math. Gen. 11 (1978) L185.

[SHIM2008] Shim H, Dutta P, Seehra M. S, Bonevich J, Solid State Commun. 145 (2008) 192.

[SHIN2003] Shinde S. R, Ogale S. B, Das Sarma S, Simpson J. R, Drew H. D, Lofland S. E, Lanci C, Buban J. P, Browning N. D, Kulkarni V. N, J. Higgins, Sharma R. P, Greene R. L, Venkatesan T, Phys. Rev. B 67 (2003) 115211.

[SHIN2004] Shinde S. R, Ogale S. B, Higgins J. S, Zheng H, Millis A. J, Kulkarni V. N, Ramesh R, Greene R. L, Venkatesan T, Phys. Rev. Lett. 92 (2004) 166601.

[SIEG1967] Siegbahn K, Nordling C, Fahlman A, Nordberg R, Hamrin K, Hedman J, Johansson G, Bergmark T, Kerlsson S. E, Lindgren I, Lindberg B, Nova Acta Regiae Soc. Sci., Ser IV 20 (1967).

[SING2010] Singhal A, Achary S. N, Manjanna J, Chatterjee S, Ayyub P, Tyagi A. K, J. Phys. Chem. C 114 (2010) 3422.

[SING2011] Singhal R. K, Kumar S, Kumari P, Xing Y. T, Saitovitch E, Appl. Phys. Lett. 98 (2011) 092510.

[SOFI2014] Sofianou M. V, Boukos N, Vaimakis T, Trapalis C, Appl. Catal. B: Environ. 158 (2014) 91.

[SOLE2013] Soleimanpour A. M, Jayatissa A. H, Sumanasekera G, Appl. Surf. Sci. 276 (2013) 291.

[SONI2001] Soni P. R, Mechanical alloying: Fundamental and applications, Cambridge International Science Publishing, UK (2001).

[SORI2007] Soriano L, Preda I, Gutiérrez A, Palacín S, Abbate M, Vollmer A, Phys. Rev. B 75 (2007) 233417.

[SOWW2001] So W. W, Park S. B, Kim K. J, Shin C. H, Moon S. J, J. Mater. Sci. 36 (2001) 4299.

[SREC2008] Sreckovic T, Bernik S, Ceh M, Vojisavlevic K, J. Microscopy 232 (2008) 639.

[SRIN2011] Srinivas K, Manjunath Rao S, Venugopal Reddy P, Nanoscale 3 (2011) 642.

[STEN2011] Stengl V, Králová D, Mater. Chem. Phys. 129 (2011) 794.

[STOR1986] Story T, Galstroka-cedillazka R. R, Frankel R. B, Wolff P. A, Phys. Rev. Lett. 56 (1986) 777.

[SUJ2013] Su J, Zou X. X, Zou Y. C, Li G. D, Wang P. P, Chen J. S, Inorganic Chemistry 52 (2013) 5924.

[SUND2006] Sundaresan A, Bhargavi R, Rangarajan N, Siddesh U, Rao C. N. R, Phys. Rev. B 74 (2006) 161306.

[SUND2009] Sundaresan A, Rao C. N. R, Nano Today,4 (2009) 96.

[SURY2001] Suryanarayana C, Prog. Mater. Sci. 46 (2001) 1.

[SURY2004] Suryanarayana C, Mechanical alloying and Milling, Marcel Dekker, NewYork (2004).

[SZOR1995] Szörényi T, Laude L. D, Bertóti I, Kántor Z, Geretovszky Z, J. Appl. Phys. 78 (1995) 6211.

[TADI2011] Tadic M, Panjan M, Markovi D, Milosevi I, Spasojevi V, J. Alloys Compd. 509 (2011) 7134.

[TADI2014] Tadic M, Panjan M, Markovic D, Stanojevic B, Jovanovic D, Milosevic I, Spasojevic V, J. Alloys Compd. 586 (2014) S322.

[TAJI2015] Tajiri T, Saisho S, Mito M, Deguchi H, Konishi K, Kohno A, J. Phys. Chem. C 119 (2015) 1194.

[TANG1994] Tang H, Prasad K, Sanjinès R, Schmid P. K, Lévy F, J. Appl. Phys. 75 (1994) 2042.

[TAPI2010] Tapily K, Gu D, Baumgart H, Rigo M, Seo J, ECS Trans. 33 (2010) 117.

[TAUC1966] Tauc J, Grigorovici R, Vancu A, Physica Status Solidi (b) 15 (1966) 627.

[THAK2012] Thakur R. M. Y, Yadav P, Singh D. P, Nanosci. Nanotechnol. 2 (2012) 22.

[THAN2012] Thanh N. T. K, Magnetic nanoparticles: From fabrication to clinical applications, Taylor and Francis (2012).

[THEO2006] Theodoropouloua N, Misra V, Philip J, LeClair P, Berera G. P, Moodera J. S, Satpati B, Som T, J. Mag. Magn. Mater. 300 (2006) 407.

[THOT2007] Thota S, Kumar J, J. Phys. Chem. Solids 68 (2007) 1951.

[THOT2013] Thota S, Shim J. H, Seehra M. S, J. Appl. Phys. 114 (2013) 214307.

[TIAN2008] Tian Z. M, Yuan S. L, Wang Y. Q, He J. H, Yin S. Y, Liu K. L, Yuan S. J, Liu L, J. Phys. D: Appl. Phys. 41 (2008) 055006.

[TIAN2012] Tian F, Zhang Y, Zhang J, Pan C, J. Phys. Chem. C 116 (2012) 7515.

[TIWA2005] Tiwari S. D, Rajeev K. P, Phys. Rev. B 72 (2005) 104433.

[TOKU2000] Tokura Y, Nagaosa N, Science 288 (2000) 462.

[TONG2013] Tong T, Shereef A, Wu J, Binh C. T. T, Kelly J. J, Gaillard J. F, Gray K. A, Environ. Sci. Technol. 47 (2013) 12486.

[TSUN2000] Tsunekawa S, Ishikawa K, Li Z. Q, Kawazoe Y, Kasuya A, Phys. Rev. Lett. 85 (2000) 3440.

[TSYM2016] Tsymbal E. Y, Zutic I, Handbook of spin transport and magnetism, CRC press, New York (2016).

[UEDA2001] Ueda K, Tabata H, Kawai T, Appl. Phys. Lett.79 (2001) 988.

[UHLE1992] Uhlenbrock S, Scharfschwerdt C, Neumann M, Illing G, Freund H. J, J. Phys. Condens. Matter 4 (1992) 7973.

[UHMY2006] Uhm Y. R, Woo S. H, Kim W. W, Kim S. J, Rhee C. R, J. Mag. Magn. Mater. 304 (2006) e781.

[ULMA2007] Ulmane N. M, Kuzmin A, Steins I, Grabis J, Sildos I, Pärs M, J. Phys. Conf. series 93 (2007) 012039.

[ULMA2011] Ulmane N. M, Kuzmin A, Grabis J, Sildos I, Voronin V. I, Berger I. F, Kazantsev V. A, Sol. State Phenomena 168-169 (2011) 341.

[ULMAARTI] Ulmane N. M, Kuzmin A, Dizhbite, Sildos I, Pars M, Grabis J, Article: http://www.physics.by/e107_files/mono/2book2009_pdf/3st_33.pdf

[UNGA1991] Ungar T, Tichy G, Physica Status Solidi A 171 (1999) 425.

[UNGA1992] Ungar T, Dragomir I, Revesz A, Borbely A, J. Appl. Cryst. 32(1999) 992.

[VANH1996] Vanheusden K, Warren W. L, Seager C. H, Tallant D. R, Voigt J. A, Gnade B. E, J. Appl. Phys. 79 (1996) 7983.

[VEGA2001] Vega D, Polla G, Leyva G, Konig P, Lanza H, Esteban A, Aliaga H, Causa M. T, Tovar M, Alascio B, J. Solid State Chem. 156 (2001) 458.

[VEIS2010] Veiseh O, Gunn J. W, Zhang M, Adv. Drug Delivery Rev. 62 (2010) 284.

[VOJI2008] Vojisavljevic K, Scepanovic M, Sreckovic T, Grujic-Brojcin M, Brankovic Z, Brankovic G, J. Phys.: Condens. Matter 20 (2008) 475202.

[VOLK2001] Volkov V. V, Wang Z. L, Zou B. S, Chem. Phys. Lett. 337 (2001) 117.

[WANG2002] Wang W. Z, Liu Y. K, Xu C. K, Zheng C. L, Wang G. H, Chem. Phys. Lett. 362 (2002) 119.

[WANG20051] Wang J, Cai J, Lin Y. H, Nan C. W, Appl. Phys. Lett. 87 (2005) 202501.

[WANG20052] Wang X, Song J, Gao L, Jin J, Zheng H, Zhang Z, Nanotechnology 16 (2005) 37.

[WANG20061] Wang J. B, Huang G. J, Zhong X. L, Sun L. Z, Zhou Y. C, Liu E. H, Appl. Phys. Lett. 88 (2006) 252502.

[WANG20062] Wang Y. X, Liu H, Li Z. Q, Zhang X. X, Zheng R. K, Ringer S. P, Appl. Phys. Lett. 89 (2006) 042511.

[WANG2007] Wang X, Xu J, Yu X, Xue K, Yu J, Zhao X, Appl. Phys. Lett. 91 (2007) 031908.

[WANG2008] Wang Q, Sun Q, Chen G, Kawazoe Y, Jena P, Phys. Rev. B 77 (2008) 205411.

[WANG2011] Wang X, Wan L, Yu T, Zhou Y, Guan J, Yu Z, Li Z, Zou Z, Mater. Chem. Phys. 126 (2011) 494.

[WANG20121] Wang G, Lu X, Zhai T, Ling Y, Wang H, Tong Y, Li Y, Nanoscale 4 (2012) 3123.

[WANG20122] Wang H, Wei J, Xiang R, Shi J, J. Magn. Magn. Mater. 324 (2012) 2057.

[WANG20123] Wang G, Chen G, Wei Z, Yu T, Liu L, Wang P, Chang Y, Qi M, J. Appl. Polym. Sci. 125 (2012) 3871.

[WANG2015] Wang T, Jiang H, Wan L, Zhao Q, Jiang T, Wang B, Wang S, Acta Biomater. 13 (2015) 354.

[WEIM2005] Wei M, Braddon N, Zhi D, Midgley P. A, Chen S. K, Blamire M. G, MacManus-Driscoll J. L, Appl. Phys. Lett. 86 (2005) 072514.

[WELT2008] Welte A, Waldauf C, Brabec C, Wellmann P. J, Thin Solid Films 516 (2008) 7256.

[WEND2008] Wendt S, Sprunger P. T, Lira, Madsen G. K. H, Li Z, Hansen J. Q, Matthiesen J, Rasmussen A. B, Lægsgaard E, Hammer B, Besenbacher F, Science 320 (2008) 1755.

[WILL1953] Williamson G. K, Hall W. H, Acta Met. 1 (1953) 22.

[WINK2005] Winkler E, Zysler R. D, Vasquez Mansilla M, Fiorani D, Phys. Rev. B 72 (2005) 132409.

[WINK2008] Winkler E, Zysler R. D, Mansilla M. V, Fiorani D, Rinaldi D, Vasilakaki M, Trohidou K. N, Nanotechnology 19 (2008) 185702.

[WUJB2003] Wu J. B, Nan J, Nan C. W, Lin Y, Deng Y, Zhao S, Mater. Sci. Engg. B 99 (2003) 294.

[WUS2014] Wu S, Weng Z, Liu X, Yeung K.W.K. Chu P.K, Adv. Func. Mater. 24 (2014) 5464.

[WUY2012] Wu Y, Zhang Q, Wu X, Qin S, Liu J, J. Solid State Chem. 192 (2012) 356.

[XIAZ2011] Xia Z. B, Wang Y. W, Fang Y. J, Wan Y. T, Xia W. W, Sha J, J. Phys. Chem. C 115 (2011) 14576.

[XIEY2004] Xie Y, Blackman J. A, Phys. Rev. B 69 (2004) 172407.

[XING2010] Xing G, Wang D, Yi J, Yang L, Gao M, He M, Yang J, Ding J, Sum T. C, Wu T, Appl. Phys. Lett. 96 (2010) 112511.

[XING2011] Xing G. Z, Lu, Tian Y. F, Yi J. B, Lim C. C, Li Y. F, Li G. P, Wang D. D, Yao B, Ding J, Feng Y. P, Wu T, AIP Adv. 1 (2011) 022152.

[XUJ2010] Xu J, Shi S, Li L, Zhang X, Wang Y, Chen X, Wang J, Lv L, Zhang F, Zhong W, J. Appl. Phys. 107 (2010) 053910.

[XUY2015] Xu Y, Awschalom D. D, J. Nitta, Handbook of Spintronics, Springer Netherlands (2015).

[YADA2006] Yadav A, Prasad V, Kathe A. A, Raj S, Yadav D, Sundaramoorthy C, Vigneswaran Y, Bull. Mat. Sci. 29 (2006) 641.

[YANG2008] Yang C. C, Li S, J. Phys. Chem. B 112 (2008) 14193.

[YANG1999] Yang H. X, Dong Q. F, Hu X. H, J. Power Sources 79 (1999) 256.

[YANJ2013] Yan J, Wu G, Guan N, Li L, Li Z, Cao X, Phys. Chem. Chem. Phys. 15 (2013) 10978.

[YANH2008] Yan H. L, Wang J. B, Zhong X. L, Zhou Y. C, Appl. Phys. Lett. 93 (2008) 142502.

[YANW2008] Yan W, Weng W, Zhang G, Sun Z, Liu Q, Pan Z, Guo Y, Xu P, Wei S, Zhang Y, Yan S, Appl. Phys. Lett. 92 (2008) 052508.

[YIJB2007] Yi J. B, Ding J, Feng Y. P, Peng G. W, Chow G. M, Kawazoe Y, Liu B.H, Yin J. H, Thongmee S, Phys. Rev. B 76 (2007) 224402.

[YIJJ2008] Yi J. J. B, Ding J, Thongmee S, Feng Y. P, Chow G. M, 2nd IEEE Int. Nanoelectronic Conf , INEC (2008) 1047.

[YINW2010] Yin W. J, Chen S, Yang J. H, Gong X. G, Yan Y, Wei S. H, Appl. Phys. Lett. 96 (2010) 221901.

[YOON2006] Yoon S. D, Chen Y, Yang A, Goodrich T. L, Zuo X, Arena D. A, Ziemer K, Vittoria C, Harris V. G, J. Phys.: Condens. Matter 18 (2006) L355.

[YOON2016] Yoon K. R, Ko J. W, Youn D.Y, Park C. B, Kim I.-D, Green Chem. 18 (2016) 944.

[YOSI1957] Yosida K, Phys. Rev 106 (1957) 893.

[YUJC2002] Yu J. C, Yu J, Ho W, Jiang Z, Chem. Mater. 14 (2002) 3808.

[ZARD2009] Zardo I, Conesa-Boj S, Peiro F, Morante J. R, Arbiol J, Uccelli E, Abstreiter G, Fontcubertai Morral, Phys. Rev. B 80 (2009) 245324.

[ZHAN2000] Zhang W. F, He Y. L, Zhang M. S, Yin Z, Chen Q, J. Phys. D Appl. Phys. 33 (2000) 912.

[ZHAN20121] Zhang K. H. L, McLeod I. M, Lahti M, Pussi K, Dhanak V. R, J. Phys.: Cond. Matter. 24 (2012) 435502.

[ZHAN20122] Zhang L, Zhaoa J, Lua H, Li L, Zhenga J, Li H, Zhua Z, Sens. Act. B 161 (2012) 209.

[ZHAN2016] Zhang J, Zeng D, Zhu Q, Wu J, Huang Q, Xie C, J. Phys. Chem. C 20 (2016) 3936.

[ZHAO2009] Zhao B, Ke X. K, Bao J. H, Wang C. L, Dong L, Chen Y. W, Chen H. L, J. Phys. Chem. C 113 (2009) 14440.

[ZHEN2004] Zheng R. K, Liu H, Zhang X. X, Roy V. A. L, Djurišić A. B, Appl. Phys. Lett. 85 (2004) 2589.

[ZHOU1996] Zhou M, Lin W. Y, Tacconi N. R, Rajeshwar K, J. Electroanal. Chem. 402 (1996) 221.

[ZHOU2007] Zhou Y. Z, Chen J. S, Tay B. K, Hu J. F, Chow G. M, Liu T, Yang P, Appl. Phys. Lett. 90 (2007) 043111.

[ZHOU2009] Zhou S, Cizmar E, Potzger K, Krause M, Talut G, Helm M, Fassbender J, Zvyagin S. A, Wosnitza J, Schmidt H, Phys. Rev. B 79 (2009) 113201.

[ZHUT2006] Zhu T, Zhan W. S, Appl. Phys. Lett. 89 (2006) 022508.

[ZUOX2009] Zuo X, Yoon S. D, Yang A, Duan W. H, Vittoria C, Harris V. G, J. Appl. Phys. 105 (2009) 07C508.

[ZUTI2004] Zutic I, Fabian J, Sarma S. D, Rev. Mod. Phys. 76 (2004) 323.

[ZYSL1994] Zysler R, Fiorani D, Dormann J. L, Testa A. M, J. Magn. Magn. Mater. 133 (1994) 71.

[ZYSL2000] Zysler R. D, Ramos C. A, De Biasi E, Romero H, Ortega A, Fiorani D, J. Magn. Magn. Mater. 221 (2000) 37.

Publications

LIST OF PUBLICATIONS:

	Published:
[1].	Finite size effect in magnetic and optical properties of antiferromagnetic NiO nanoparticles **Bhagaban Kisan**, P. C. Shyni, Samar Layek, H. C. Verma, David Hesp, Vinod Dhanak, Satheesh Krishnamurthy and A. Perumal IEEE Trans. Magn. 50 (2014) 2300704.
[2].	Room temperature ferromagnetism in finite sized ZnO nanoparticles **Bhagaban Kisan** and A. Perumal Physica B: condensed matter 448 (2014) 115.
[3].	Effect of annealing on the magnetic properties of milled NiO powder **Bhagaban Kisan**, P. Sarvanam, Samar Layek, H. C. Verma, Vinod Dhanak, Satheesh Krishnamurthy and A. Perumal J. Magn. Magn. Materials 384 (2015) 296.
[4].	Structural, Vibrational, Optical and magnetic properties of NiO nanoparticles **Bhagaban Kisan**, P. Ravikumar, Arnab Das, A. Srinivasan and A. Perumal J. Sci. Lett 4 (2015) 160.
[5].	Enhanced room temperature ferromagnetism in antiferromagnetic NiO nanoparticles Patta Ravikumar, **Bhagaban Kisan** and A. Perumal AIP Advances 5 (2015) 087116.
	Under communication:
[6].	Defect induced ferromagnetism in finite sized ZnO nanoparticles **Bhagaban Kisan,** P. Saravanan and A. Perumal
[7].	Room temperature ferromagnetism in strain induced TiO_2 nanoparticles **Bhagaban Kisan**, D. Pamu and A. Perumal
	Publications outside thesis work:
[8].	Thickness dependent magnetic properties of amorphous FeTaC films A.K. Singh, **Bhagaban Kisan**, D. Mishra and A. Perumal

	Journal of Applied Physics 111 (2012) 093915.
[9].	Magnetic properties of Co doped $MgTiO_3$ ceramics S. K. Thatikonda, P. Gogoi, **Bhagaban Kisan**, A. Perumal, P. Sharma and D. Pamu Physics B: Condensed Matter 448 (2014) 330.
[10].	Thickness dependent ferromagnetism in thermally decomposed NiO thin films Patta Ravi Kumar, **Bhagaban Kisan** and A. Perumal Journal of magnetism and magnetic material 418 (2016) 86.

PAPERS PRESENTED IN CONFERENCES:

[1].	Room temperature ferromagnetism in thermally decomposed NiO thin films **Bhagaban Kisan**, Patta Ravikumar and A. Perumal Presented in the Indo-Japan Workshop on Magnetism at Nanoscale (IJWMN), January 9-12, 2015, National Institute of Science Education and Research, Bhubaneswar, India.
[2].	Finite size effects in magnetic and optical properties of antiferromagnetic NiO nanoparticles **Bhagaban Kisan**, P. C. Shyni, Samar Layek, H. C. Verma, David Hesp, Vinod Dhanak, Satheesh Krishnamurthy and A. Perumal Presented in the 3rd International Symposium on Advanced Magnetic Materials and Applications (ISAMMA 2013), 21-25 July 2013, Taichung, Taiwan.
[3].	Room temperature ferromagnetism in finite sized ZnO nanoparticles **Bhagaban Kisan** and A. Perumal Presented in the International conference on magnetic materials and application (MagMA)-2013, IIT Guwahati, 5-7 Dec 2013, Guwahati, India.
[4].	Room temperature ferromagnetism in finite sized ZnO and NiO nanoparticles prepared by Combustion method **Bhagaban Kisan**, J. Christey and A. Perumal Presented in the International conference on magnetic materials and application (MagMA)-2013, IIT Guwahati, 5-7 Dec 2013, Guwahati, India.
[5].	Role of nanostructure on the magnetic properties

	A. Perumal, Akhilesh Kr. Singh, P. C. Shyni, **Bhagaban Kisan**, and Anabil Gayen Invited for presentation in National Seminar on Nanoscience and Nanotechnology, August 31-September 01, 2012, MC College, Barpeta, India.
[6].	Magnetic properties of soft magnetic thin films in recording media for futuristic hard disk drive applications A. Perumal, A. K. Singh and **Bhagaban Kisan** Presented in International conference on nanomatrials and applications (ICNMA-2012), 28 - 29, Feb 2012, Department of Physics, Mother Teresa Women's University, Kodaikanal-624 101, India.